Full optical control of quantum fluids of light in hot atomic vapors

Tangui Aladjidi

SORBONNE UNIVERSITÉ

THÈSE DE DOCTORAT
DE SORBONNE UNIVERSITÉ

Spécialité : Physique

École doctorale nº564: Physique en Île-de-France

réalisée sous la direction de Quentin GLORIEUX

au Laboratoire Kastler Brossel

LKB

présentée par

Tangui ALADJIDI

Sujet de la thèse :

Full optical control of quantum fluids of light in hot atomic vapors

soutenue le 2 octobre 2023

devant le jury composé de :

M.	Leyronas Xavier,	Professeur,	SU / ENS Paris,	Président
M.	David Clément,	MCF,	Institut d'Optique,	Examinateur
Mme	Bouchoule Isabelle,	DR,	Institut d'Optique,	Rapporteur
M.	Dudley John,	PR,	Univ. de Franche-Comté,	Examinateur
M.	Glorieux Quentin,	MCF,	SU,	Directeur de thèse
M.	Albert Mathias,	MCF,	Univ. de Nice Côte d'Azur,	Rapporteur
M.	Baboux Florent,	MCF,	Univ. de Paris Cité,	Invité

Contents

Introduction

General context

The last thirty years have been marked by what has been dubbed the "second quantum revolution". Physicists have aimed at switching from the understanding of the foundations of quantum mechanics to actually harnessing these laws in order to control quantum systems. In this context, tremendous efforts have been made to develop platforms of controllable ensembles of quantum particles: cold gases [25; 27; 83], exciton polariton condensates [7; 9; 51], superconducting circuits [105], dye-filled cavities [55; 79; 108] or in our case hot atomic vapors [39].

Study of these systems brought experimental confirmation of many seminal effects of the many-body quantum physics like Bose-Einstein condensation [10; 51; 108], superfluidity [27], superconductivity [98] or quantum entanglement [49]. These effects were subsequently harnessed to great success bringing considerable technological advancement for medical imagery thanks to superconducting magnets [107], guidance systems with the advance of atomic clocks [65] for the GPS and communications with fully optical links [104].

In this effervescence, quantum fluids of light have emerged as a competitive option due to their relative simplicity and excellent imaging capabilities comparatively to cold gases for instance, where non destructive measurement of the system is difficult. In fluids of light, the quantum particles are directly photons whose control has been perfected by hundreds of years of optics, both classical, and more recently quantum. This grants near unlimited access to the full field, making fluids of light the only platform where the correlation functions of all moments can be computed directly. However, photons do not interact in a vacuum. In order to obtain a collective behavior in an ensemble of photons, one needs to engineer interactions between them. In a medium, photons acquire an effective mass due to the index of refraction of the medium. If in addition this medium has an intensity dependant nonlinear index, the photons will acquire effective interactions. Under the right conditions, if the interactions are repulsive, the photons will behave collectively, exhibiting fluid-like behavior.

Such a nonlinear medium can be found in hot atomic vapors that have several key advantages to other nonlinear media:

- Compared to photorefractive crystals [72; 73], they are repeatable in the sense that two cells containing the same element will behave in the same manner, while photorefractive crystals are by nature flawed by large variations of their properties between samples. Also, the non-linearity of atoms can be several orders of magnitude larger and this non-linearity can be tuned over several orders of magnitude through the exponential dependance of the atomic density on temperature.

- Compared to exciton polaritons, hot atomic vapors do not require vacuum chambers and cryostats in order to bring the samples to their working conditions. Furthermore these samples require very advanced nanofabrication techniques that forbid fast iterations between samples. While the coupling between light and excitons in polariton cavities is exceptionnal, it can hardly be tuned. Furthermore, exciton polaritons fluids are driven dissipative, meaning that there is a complex exchange between the exciton reservoir, cavity photons and polaritons. This makes interpretation of the experiments more challenging.

This platform has proven very successful allowing to probe hydrodynamical effects from vortex dynamics [12], dispersive shock waves [18] up to large scale hydrodynamical phenomena like turbulence [1]. Statistical properties of quantum fluids were also observed shedding light on the response to interaction quenches [97] as well as prethermalization [3].

These results and the fruitful collaboration between theory and experiments shows great promise for the future of our community.

Motivations

The hydrodynamical properties of fluids of light in hot atomic vapors were first demonstrated in [35] where Quentin Fontaine laid the ground work of the experiments carried out in this thesis: the first methods to measure the Bogoliubov dispersion were developped and the interference of Bogoliubov particles was evidenced. In [2], Murad Abuzarli introduced new methods to precisely characterize the nonlinear index of refraction, as well as observables in order to probe the out-of-equilibrium nature of paraxial fluids of light presenting blast wave dynamics as well as studies on the coherence properties of the fluid after a quench. The motivation of this thesis is to build on these works and mature the experimental set up into a fully controlled sandbox. In order to provide a credible alternative to the leading experimental platforms like cold atoms, we build a theoretical, numerical and experimental framework in order to be able to predict ab initio, simulate and put into practice the Hamiltonian we want to study.

The goal of reaching this full control of the system is also to address important theoretical questions of paraxial fluids of light: the system dimensionality (2D or 3D), the meaning of the space-time mapping or the limits of the Bogoliubov theory. We can thus summarize the motivation of this thesis as an attempt to from passive observation to active planning and control of a specific physical effect.

Summary

This thesis manuscript contains five chapters, structured in increasing scale order: from the lowest quantum level scale to the macroscopical large scale. The common thread across chapters is the system Hamiltonian: in each chapter, we focus on the description and control of one term. This corresponds to the degrees of freedom of the fluid (kinetic, interaction and potential energy) and we ultimately link these to experimental tuning knobs. In each chapter, we try to present the theoretical framework, numerical methods and experimental results in order to try and paint a complete picture. The first chapter is devoted to introducing the theoretical concepts and description of paraxial fluids of light. The second chapter explores

the effects arising from quantum fluctuations of vacuum and interaction quenches. The third chapter describes the atomic medium that generates the all important photon-photon interactions. The fourth chapter presents a detailed study of superfluidity. Finally the fifth chapter opens up new perspectives on energy transfer accross scales presenting results on turbulence and quantum phase transitions.

Chapter 1 The theoretical framework used to describe paraxial fluids of light starting from the description of light propagation in nonlinear media. After establishing the nonlinear Schrödinger equation, the quantum formulation is introduced and the Bogoliubov theory is presented. A detailed comparison with the Gross Pitaevskii equation of cold gases is presented. The last section presents the numerical analysis tools used to solve the evolution equation of the system.

Chapter 2 The impact of the interaction quenches on the statistical properties of the fluid is presented. The evolution equation is solved analytically and we present an experimental measurement of the predicted structure factor. We present a novel experimental technique to measure the structure factor using a balanced homodyne detection. We conclude by presenting the expected signatures of effects that highlight scattering processes between Bogoliubov excitations, going beyond the theory presented in chap.1.

Chapter 3 The structure of the Rubidium atom is presented and the interaction with the electric field is derived. A three-level model is presented, before extending it to four levels and describing optical pumping. Transit effects due to the thermal motion of atoms are then explored with Monte Carlo numerical simulations. Finally, we propose two new configurations in order to tune the atomic response using electromagnetically induced transparency (EIT).

Chapter 4 In this chapter we explore the emergence and breakdown of superfluid flow in fluids of light. We start by a comparison of the relevant observables to identify the superfluid transition. We present the scattering experiment that we will use to probe the critical velocity for superfluidity and detail the measurement methods used to characterize the defect induced in the fluid. We then derive a more refined model in order to describe the back-reaction of the fluid on the defect and use this back-reaction to obtain a time resolved measurement of the drag force. We use this coupled model to numerically predict the critical velocity for various defects and compare this to experimental results. We conclude by presenting measurements of the Bogoliubov dispersion relation hinting at nonlocal behavior in the fluid.

Chapter 5 We conclude this thesis by presenting recent results on turbulent behavior in fluids of light. We start by introducing the dynamical instability phenomenon giving rise to the turbulent behavior. We then present experimental results of vortex clustering and inverse energy cascade that are trademarks of turbulence. We then study more closely the vortex dynamics as individual objects by deriving the Berezinskii-Kosterlitz-Thouless (BKT) transition, extracting the vortex interaction potential and present experimental measurements of this interaction potential. We finish by an experimental proposal to try and evidence the BKT transition by monitoring the vortex correlations and clustering. Finally, we go back to

the fluid of light and explore the thermodynamics of the fluid by using the beyond mean field predictions of chap.2.

Remerciements

Ces trois dernières années furent sans aucun doutes les plus denses en évènements (heureux comme malheureux) de ma vie. J'ai eu la chance d'être porté par un entourage bienveillant qui m'a tant appris, sur le plan scientifique comme sur le plan humain. En premier plan, je me dois de remercier ma femme Edwige qui a supporté mes tribulations diverses à toute heure du jour et de la nuit. De la même manière, je remercie du fond du coeur mes parents, qui en m'accueillant à St-Paul-lès-Monestier m'ont toujours permis de repartir du bon pied, bien soigné (merci Catherine) et en ayant bien lu la documentation (merci Papa).

Ensuite, cette thèse n'aurait pas pu exister sans le cadre formidable du laboratoire Kastler Brossel, en particulier l'équipe "Fluides Quantiques de Lumière". Évidemment, je dois remercier Quentin Glorieux de m'avoir offert l'opportunité de poursuivre dans l'équipe pour une thèse et de m'avoir laisser beaucoup d'indépendance durant ces trois années, tout en restant disponible quand j'en avais besoin. Je remercie ensuite Quentin Fontaine dont le travail fondateur a accompagné toute ma thèse, Murad qui m'a (presque) tout appris en salle d'expérience et avec qui j'ai eu grand plaisir de partager deux belles années de cette thèse, au labo et à vélo. Merci également à Ferdinand pour ses conseils en optique et pour sa contribution à l'ambiance du bureau. Je dois remercier particulièrement Myrann Abobaker en qui j'ai trouvé plus qu'un collègue de travail, mais un ami avec qui j'ai pu partager les joies et les peines de la salle de manip et mes goûts musicaux douteux. Je remercie également tous mes autres collègues de bureau, anciens doctorants, post-doc ou stagiaires Wei Liu, Tom Binaimé, Guillaume Brochier, Quentin Valnais et Malo Joly pour les discussions passionantes que nous avons pu avoir. Je remercie particulièrement mes chers camarades doctorants, actuels garants de la croissance infinie de l'entropie dans notre bureau: Clara Piekarski, Kévin Falque, Killian Guerrero et Clément Debavelaere, qui ont aussi été un grand soutien quand il s'agissait de lever nos coudes au Buisson Ardent. Sur un thème plus sérieux, je concluerai ces remerciements au laboratoire en saluant Nicolas Cherroret avec qui nous avons collaboré étroitement et dont l'expertise m'a permis de beaucoup progresser dans la compréhension théorique de mes expériences. Je dois aussi remercier mon parrain de thèse Tarik pour ses conseils toujours avisés et son regard extérieur qui m'a aidé à prendre du recul.

Évidemment, je ne saurais limiter ma gratitude au seul laboratoire Kastler Brossel, et j'ai eu la chance d'apprendre énormément au contact des équipes avec lesquelles nous avons collaboré. Je salue chaleureusement les membres du Laboratoire de Physique des Lasers: Hélène Perrin, Aurélien Perrin, Romain Debussy et Manon Ballu. Sur le plan théorique, je dois la majeure partie de mon chapitre sur la superfluidité aux travaux de l'INPHYNI: Juliette Huynh, Mathias Albert et Pierre-Élie Larré. Nos échanges fréquents et rencontres à Lille, Nice, Rome ou Paris sont d'autant d'excellents souvenirs de cette thèse. Je me dois de remercier Iacoppo Carusotto, dont l'apport théorique à notre discipline n'a d'égal que sa

sympathie. Chacun de nos échanges fut mémorable et m'a toujours permis de repartir avec un regard nouveau sur ce que je pensais comprendre. "And last but not least", je garderai un souvenir ému du séjour de Tiago Ferreira Da Silva au sein de l'équipe. Il est rare de trouver une si bonne entente personnelle et scientifique en si peu de temps. Son apport à l'expérience de superfluidité fut déterminant et j'espère que nos chemins se recroiseront rapidement.

Enfin je tiens à dédier cette thèse tout particulièrement à ma mère Nolwenn qui nous a quitté à l'été 2022, ainsi qu'à mon grand-père Claude. Sans ma mère, je n'aurais pas quitté Grenoble et n'aurais certainement pas suivi la voie qui est la mienne. Son soutien inconditionnel et son intérêt pour ma thèse même quand elle n'y "comprenait rien" ont compté beaucoup. Par ailleurs, son intransigeance en anglais m'a beaucoup aidé au moment de la rédaction. Grâce à mon grand-père Claude, j'ai pu développer ma curiosité scientifique dès le plus jeune âge : fusées à eau, arcs, balançoires et autres palans, tout le répertoire de la mécanique y est passé ! En répondant à mes questions incessantes, et en me donnant les outils pour mettre en pratique avec mes propres mains, il a forgé mon goût pour la physique expérimentale.

À travers cette douzaine de mercis, je ne peux évidemment mentionner toutes les personnes qui m'ont aidé : je conclus donc par un grand

MERCI !

Chapter 1

Quantum fluids of light

In this chapter, we will establish the theoritical basis for the concept of fluids of light. In the last twenty years, there have been significant progress made in designing experiments where light displays collective fluid-like behavior, with a wide range of experimental platforms like micro-cavity exciton polaritons [7; 8], dye-filled cavities [52] or photorefractive crystals [72; 73]. These various platforms allowed to observe some of the most striking features of quantum fluids such as superfluidity [7; 72] or Bose-Einstein condensation [51; 52].

In order to understand these phenomena, we will first describe the propagation of light in a non-linear medium. We will then look at how we can formulate a quantum theory of light propagation, and how the collective behavior of light emerges from the photon-photon interactions. Finally we will look at the numerical methods at our disposal to solve the evolution of the field.

1.1 Propagation of light in non-linear media

1.1.1 Helmholtz equation

Let us consider the propagation equation of an electric field $\mathbf{E}(\mathbf{r}, t)$ as it passes through a medium. From the Maxwell equations, we can derive the starting point of the propagation, the so-called **Helmholtz equation**, whose source term is the electric polarization $\mathbf{P}(\mathbf{r}, t)$ in the medium:

$$\nabla^2 \mathbf{E} - \frac{1}{c^2}\frac{\partial^2 \mathbf{E}}{\partial t^2} = \frac{1}{\epsilon_0 c^2}\frac{\partial^2 \mathbf{P}}{\partial t^2} \tag{1.1}$$

with c being the speed of light and ϵ_0 the electrical permittivity of vacuum.
The polarization field $\mathbf{P}$ describes the response of the medium to the illumination of the incident field $\mathbf{E}$. Since there is no reason for this polarization to be linked linearly with the incident field, we expand this field in a power series in terms of $\mathbf{E}$ (provided the electric field is weak enough):

$$\mathbf{P}(\mathbf{r}, t) = \epsilon_0 \sum_{n=1}^{\infty} \chi^{(n)} : \mathbf{E}^n(\mathbf{r}, t). \tag{1.2}$$

We define here the $n+1$ rank tensors $\chi^{(n)}$ as the electric susceptibility of the medium. In details, the susceptibility tensor $\chi^{(n)}$ describes the temporal response function of the medium to the electric field through the following convolution and tensor product:

$$\mathbf{P}_\alpha(\mathbf{r},t)^{(n)} = \epsilon_0 \sum_{\beta_i} \int_{-\infty}^{\infty} \prod_{i=1}^{n} \mathrm{d}\mathbf{r}_i \mathrm{d}t_i \chi^{(n)}_{\alpha\beta_i}(\mathbf{r}-\mathbf{r}_1,...,\mathbf{r}-\mathbf{r}_n;t_1,...,t_n)\times \prod_{i=1}^{n} E_{\beta_i}(\mathbf{r}-\mathbf{r}_i;t_i) \tag{1.3}$$

where the $\beta_i \in \{x,y,z\}$ for $i \in [1,n]$ are the Cartesian indices for each dimension of the tensor. The picture is much simpler in frequency domain where the convolution product reduces to a simple product, and taking advantage of various symmetries, one can greatly simplify this expression[21].
In this thesis, we study the propagation of light through an atomic vapor which is thus **centrosymetric** and **isotropic**. This eliminates all even order terms in the expansion of the susceptibility χ as well as aligning the polarization over the direction of the electric field $\mathbf{E}$. Furthermore, we will assume for now that the mdeium is **local** meaning that the polarization at a position $\mathbf{r}$ only depends on the electric field at this position. This assumption is in practice not always relevant and will be discussed in chap.3 and 4. With this in mind, we will limit our expansion to the first and third orders (i.e the first non-linear order), and keep only non-linear processes that yield a polarization oscillating at ω in the degenerate four-wave mixing configuration. The higher order terms will be taken into account phenomenologically as an effective saturation intensity. Thus, the expression in frequency domain for the electric polarization simply becomes:

$$\mathbf{P}(\mathbf{r},\omega) = \epsilon_0\Big[\chi^{(1)}(\mathbf{r},\omega)\mathbf{E}(\mathbf{r},\omega) + 3\chi^{(3)}(\mathbf{r},\omega)|E(\mathbf{r},\omega)|^2\mathbf{E}(\mathbf{r},\omega)\Big]. \tag{1.4}$$

We note here that due to the dispersive nature of atoms, all suscpetibilities depend on the frequency of the impinging light field. The details of the underlying atom-light interaction mechanisms will be discsussed at length in chapter 3.
Armed with our simplified polarization, we can now recast it into eq.1.1 in frequency domain to deal with the time derivatives. Furthermore, as the polarization is only along the electric field, we can study only the amplitude E of the field. Assuming a monochromatic light field, we can also simplify this amplitude by separating envelope and carrier wave $E = \frac{1}{2}(\mathcal{E}e^{i\omega t} + \mathcal{E}^* e^{-i\omega t})$. Looking at the resulting equation for the envelope, we obtain :

$$\nabla^2\mathcal{E}(\mathbf{r},\omega) + \frac{\omega^2}{c^2}[1+\chi^{(1)}(\omega)]\mathcal{E}(\mathbf{r},\omega) = -\frac{3}{4}\frac{\omega^2}{c^2}\chi^{(3)}(\omega)|\mathcal{E}(\mathbf{r},\omega)|^2\mathcal{E}(\mathbf{r},\omega). \tag{1.5}$$

If we introduce the vaccum wavenumber $k_0 = \omega/c$ of the impinging laser light, we recover the familiar expression for the linear index of refraction : $n(\omega) = \sqrt{1+\chi^{(1)}(\omega)}$. We can thus finally reformulate the previous equation as follows:

$$\nabla^2\mathcal{E}(\mathbf{r},\omega) + k(\omega)\mathcal{E}(\mathbf{r},\omega) + i\alpha\mathcal{E}(\mathbf{r},\omega) = -\frac{3}{4}\frac{\omega^2}{c^2}\chi^{(3)}(\omega)|\mathcal{E}(\mathbf{r},\omega)|^2\mathcal{E}(\mathbf{r},\omega) \tag{1.6}$$

where we have defined the the medium wavenumber $k(\omega) = k_0 n'(\omega) = k_0 \mathtt{Re}(\sqrt{1+\chi^{(1)}})$ and the linear absorption coefficient $\alpha = k_0 n''(\omega) = k_0 \mathtt{Im}(\sqrt{1+\chi^{(1)}})$.

We would still like to simplify this equation further in order to extract meaningful physical insight. For this, we rely on the two following approximations:

- The **paraxial approximation** : the beam will **deviate only slightly from the optical axis** such that $\nabla^2\tilde{\mathcal{E}}/k^2 \sim \partial_z\tilde{\mathcal{E}}/k \ll 1$ if $\tilde{\mathcal{E}}$ is the normalized adimensional envelope $\mathcal{E} = \tilde{\mathcal{E}}\mathcal{E}_0$
- The **slowly varying envelope approximation** : the envelope $\mathcal{E}$ is a **slowly varying** function of z relative to the carrier wavelength $\lambda = \frac{2\pi}{k_0}$. This allows to decouple the transverse dynamics of the envelope and the longitudinal dynamics of the carrier such that $\mathcal{E}(\mathbf{r}, z) = \mathcal{E}(\mathbf{r}_\perp, z)e^{ik(\omega)z}$.

These two approximations are at the heart of the physics described in this thesis and highlight the 2D+1 nature of our geometry. Their detailed interpretation in terms of the resulting geometry will be discussed in section 1.2.
Now in the general case, considering that the laser beam has a certain spectral extension $\delta\omega$, we should consider the effect of **dispersion**. As the wavenumber in the medium $k(\omega)$ depends on the frequency of light due to the dispersive nature of the atoms, provided the spectral width $\delta\omega$ is small (which is experimentally always the case down to pulses of several ps), we can expand the wavenumber $k(\omega)$:

$$\nabla^2\mathcal{E}(\mathbf{r},\omega) + [k(\omega_0) + i\frac{\alpha}{2} + \frac{\partial k}{\partial\omega}\bigg|_{\omega_0}\delta\omega + \frac{\partial^2 k}{\partial\omega^2}\bigg|_{\omega_0}\delta\omega^2]\mathcal{E}(\mathbf{r},\omega) = -\frac{3}{4}\frac{\omega^2}{c^2}\chi^{(3)}(\omega)|\mathcal{E}(\mathbf{r},\omega)|^2\mathcal{E}(\mathbf{r},\omega). \tag{1.7}$$

We have now introduced two physical quantities the **group velocity** $\frac{1}{v_g} = \frac{\partial k}{\partial\omega}$ and **group velocity dispersion** $D_0 = \frac{\partial^2 k}{\partial\omega^2}$ (both evaluated at the carrier pulsation ω_0). Physically, the group velocity describes the speed of the wavepacket as it propagates through the vapor. The group velocity dispersion (GVD) describes how the spectral extent of the wavepacket will evolve with time: either shrink in the case of an anomalous GVD or broaden in the case of the normal GVD (see fig.1.1). Looking at this evolution equation, we see that the **source term** for the propagation is the **non-linear polarization** $\frac{3}{4}\frac{\omega^2}{c^2}\chi^{(3)}(\omega)|\mathcal{E}(\mathbf{r},\omega)|^2\mathcal{E}(\mathbf{r},\omega)$. This non-linear polarization is thus the crucial non-trivial term that will drive the evolution of the field.
Switching back to the time domain, we obtain finally the generic propagation equation describing our system, including the effect of spectral width:

$$i\frac{\partial\mathcal{E}}{\partial z} = -\frac{1}{2k(\omega)}\nabla_\perp^2\mathcal{E} + \frac{D_0}{2}\frac{\partial^2\mathcal{E}}{\partial t^2} - \frac{i}{v_g}\frac{\partial\mathcal{E}}{\partial t} - i\frac{\alpha}{2}\mathcal{E} + g(\mathbf{r}_\perp,t)|\mathcal{E}|^2\mathcal{E}. \tag{1.8}$$

Note that we have now introduced a non-linear interaction coefficient $g(\mathbf{r},t) = -k_0\frac{3\chi^{(3)}}{4n(\omega_0)}$ to reformulate the source term deriving from the non-linear polarization. We should also link this to the classical **non-linear index of refraction** $n_2 = \frac{3\chi^{(3)}}{4\epsilon_0 c\mathrm{Re}(n(\omega_0))}$ that has the dimension of m^2/W. Having established this, one can then derive the **non-linear index of refraction variation** $\Delta n = n_2 I$ where I is the field intensity. This allows to link experimental parameters to the interaction strength governing the evolution equation through measurement of this index of refraction change (see chap.3). If we also include a local variation of the index

of refraction $\delta n(\mathbf{r}, z)$ as will be shown in chap.3, we end up with the final general classical propagation equation, the so-called **non-linear Schrödinger equation** (NLSE):

$$i\frac{\partial \mathcal{E}}{\partial z} = -\frac{1}{2k(\omega)}\nabla_\perp^2 \mathcal{E} + \frac{D_0}{2}\frac{\partial^2 \mathcal{E}}{\partial t^2} - \frac{i}{v_g}\frac{\partial \mathcal{E}}{\partial t} + k(\omega)\frac{\delta n(\mathbf{r}, z)}{n(\omega_0)}\mathcal{E} - i\frac{\alpha}{2}\mathcal{E} + g(\mathbf{r},t)|\mathcal{E}|^2\mathcal{E}. \tag{1.9}$$

We will now detail in the following subsection the physical insight that we can gain by analyzing each term of this equation.

1.1.2 Non-linear Schrödinger equation

Having established the NLSE, let us now sit down and look at it for a bit. We first decompose the equation between all of its constituents: kinetic, potential and interaction terms.

$$i\frac{\partial \mathcal{E}}{\partial z} = \underbrace{-\frac{1}{2k(\omega)}\nabla_\perp^2 \mathcal{E} + \frac{D_0}{2}\frac{\partial^2 \mathcal{E}}{\partial t^2}}_{Kinetic} - \underbrace{\frac{i}{v_g}\frac{\partial \mathcal{E}}{\partial t}}_{Drift} + \underbrace{k(\omega)\frac{\delta n(\mathbf{r}, z)}{n(\omega_0)}}_{Potential} - \underbrace{i\frac{\alpha}{2}}_{Losses} + \underbrace{g(\mathbf{r},t)|\mathcal{E}|^2\mathcal{E}}_{Interaction} \tag{1.10}$$

Looking at eq.1.10, we identify five different terms depicted graphically in fig.1.1:

- **Kinetic energy**: This term describes kinetic effects induced by diffraction and GVD. In the transverse direction, this term corresponds to the curvature of the field and thus describes diffraction In the longitudinal dimension, GVD acts as a mass like term in a very similar manner as the diffraction term in the transverse dimension.
- **Potential energy**: A localized index of refraction change acts as a potential for the light field. Assuming a quadratic shape $\delta n \propto \mathbf{r}_\perp^2$, a negative δn will act as a diverging lens or repulsive potential, while a positive δn will lead to an converging phase profile or attractive potential. In the same fashion a negative δn will lead to an attractive potential. In the case of hot atomic vapors, we realize this potential using optical pumping of the D_1 line. This will be explained in details in chap.3.
- **Interaction energy**: This is the so-called **Kerr** term describing effects such as self focusing (resp. defocusing). It is often expressed as the non-linear index of refraction variation Δn with $\Delta n = \frac{2}{c\epsilon_0} n_2 I$. In this context, n_2 is the non-linear index of refraction in m^2/W and I the intensity in W/m^2. In the case of a positive n_2 non-linear coefficient, with a gaussian intensity profile $|\mathcal{E}|^2$, this results in a negative phase accumulated (with respect to a reference beam passing through air) at the high intensity center of the beam thus focusing it. In the case of a positive n_2, the opposite effect occurs, and a positive phase is accumulated at the center of the beam resulting in self-defocusing. In this thesis, we will not study the self-focusing case as it is not energetically stable : as the beam collapses, the intensity increases drastically until modulational instability and higher order terms split the beam. This is effect is called filamentation [28].
- **Losses**: Linear absorption coefficient due to the imaginary part of the first order susceptibility $\chi^{(1)}$. In this thesis, this describes atomic absorption.
- **Rigid drift**: This term is due to the group velocity within the medium being different than in the vacuum. This term can easily be eliminated by switching to the pulse referential and is only relevant when considering pulsed scenarii.

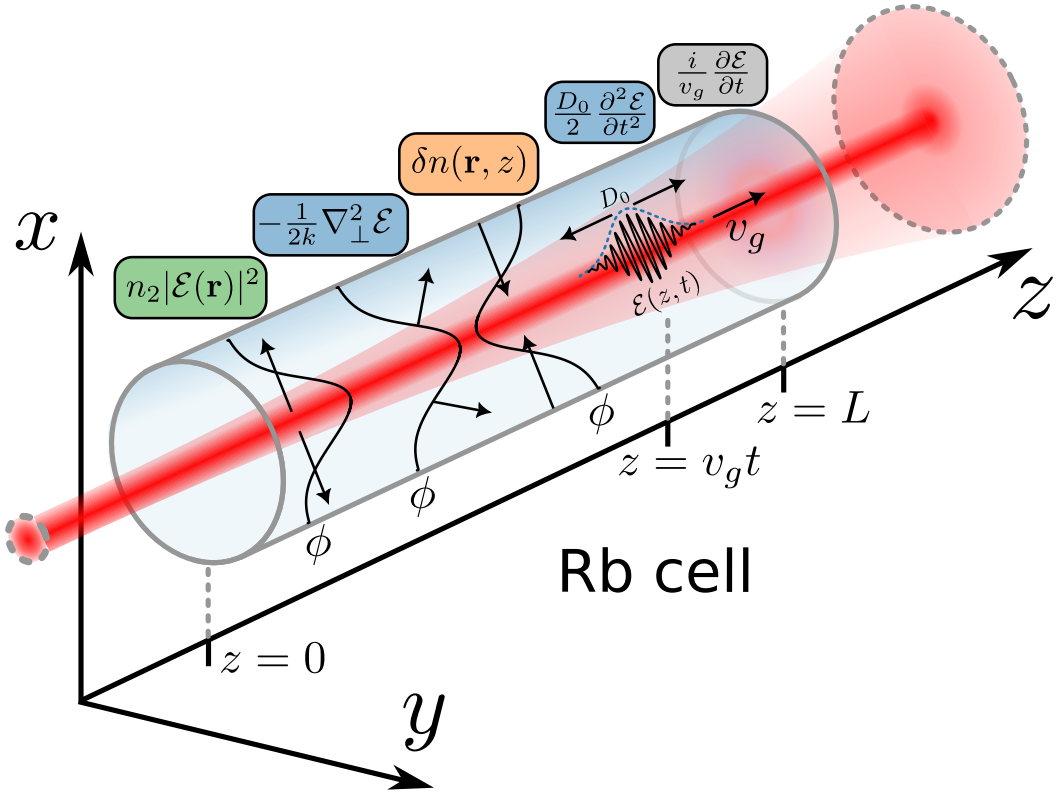

Fig. 1.1 *Effect of the different terms of the NLSE. The color-code is the same as in eq.1.10. The initial and final transverse profiles are circled by a dotted gray line: as the beam traverses the cell, due to repulsive interactions, the output profile is significantly larger. The transverse profiles represent the phase resulting of each term, labeled ϕ. Here is represented the case of a negative non-linear coefficient n_2 i.e a defocusing non-linearity thus expanding the beam. The kinetic energy term hightlights the diffraction originating from the double gradient. The potential term in orange depicts the case of a positive δn i.e an attractive potential. At the end of the cell, we represent the pulsed case where the pulse traverses through the cell at velocity v_g, expanding due to the GVD D_0.*

We will now reformulate the non-linear equation using a change of referential eliminating the rigid drift term induced by the group velocity.

1.1.3 Comoving transform

As mentioned previously, the effect of group velocity vanishes trivially when changing to the referential of the pulse [28; 59; 60]. The situation that we have is the following: we want to study the propagation of a pulse within a dispersive medium. Within the paraxial approximation, the dynamics of the field is confined to transverse planes moving at the group velocity. At the same time, the pulse elongates due to GVD, there is thus two different dynamics at play here:

- A fast dynamics governed by the group velocity along the z dimension
- Slow dynamics of pulse broadening along the time dimension, and transverse evolution of the field in the transverse (x, y) plane.

Thus, we would like to separate slow variables and fast variables in order to make the scale separation more apparent. To this extent, we are tempted to exchange the role of the *actual* time t and the third spatial coordinate z which is an **effective** time. We carry out this variable change by defining the following two new coordinates: an **effective time** $\tau = z/v_g$ and an **effective new dimension** $\zeta = v_g t - z$. By defining a new field ψ depending from the new variables such that:

$$\mathcal{E}(x, y, z, t) = \psi(x, y, v_g\tau, \frac{1}{v_g}(v_g\tau + \zeta)). \tag{1.11}$$

We thus retrieve a new evolution equation for the field ψ that reads:

$$\frac{i}{v_g}\frac{\partial\psi}{\partial\tau} = -\frac{1}{2k_0}\nabla_\perp^2\psi + \frac{v_g^2 D_0}{2}\frac{\partial^2\psi}{\partial\zeta^2} + V(\mathbf{r}, \tau)\psi + g(\mathbf{r}, \tau)|\psi|^2\psi \tag{1.12}$$

where we have substituted the potential term $k(\omega)\frac{\delta n(\mathbf{r},z)}{n(\omega_0)}$ by $V(\mathbf{r}, \tau)$ for clarity. Note that for interaction and potential terms, the comoving transform merely contracts or shift the dependence on $(z, t)/(\tau, \zeta)$ [59].

Now this is strongly reminiscent of the Gross-Pitaevskii equation (GPE) describing the evolution of interacting bosons [83] except that we here have different leading coefficients between the transverse derivatives $(\partial_x^2, \partial_y^2)$ and the longitudinal derivative ∂_ζ^2. Reformulating this as a tensor product, one can find a "mass" tensor that describes the kinetic term [59] $\mathcal{M}$ that will happen to be anisotropic contrary to the usual GPE case:

$$-\frac{1}{2k_0}\nabla_\perp^2\psi + \frac{v_g^2 D_0}{2}\frac{\partial^2\psi}{\partial\zeta^2} = (\partial_x^2\ \partial_y^2\ \partial_\zeta^2)\frac{1}{2\mathcal{M}}\begin{pmatrix}\partial_x^2\\ \partial_y^2\\ \partial_\zeta^2\end{pmatrix} \tag{1.13}$$

This highlights a peculiarity of our platform : the dynamics in the longitudinal dimension is very different from the transverse dynamics, and we can essentially consider it frozen since the typical values of the longitudinal mass term $\frac{1}{v_g^2 D_0}$ is between seven and nine orders of magnitude larger than the transverse mass term k_0 [59; 97]. Note here that we loosely use the

expression "mass term" to designate the prefactor of the second derivatives of the evolution equation in analogy with the GPE even if this term does not have the dimension of an actual mass (they are homogeneous to a wavenumber).

Furthermore, for most of the experiments described in this thesis, we work with a continuous wave (CW) laser, meaning that the spectral extent of our laser light $\delta\omega$ is completely negligible, thus our system can essentially be **considered as 2D+1** through translationnal invariance of the longitudinal dimension. A detailed physical discussion of the question of dimensionality will be presented in section 1.2 by comparing our system to cold gases.

1.1.4 Hydrodynamical formulation

The NLSE is at the heart of several of hydrodynamics effects like rogue waves, solitons[7; 31; 50; 95; 102] and vortices [68; 82]. It is then natural to recast the previous equation 1.10 to a hydrodynamics formulation. The starting point for this is the **Madelung transform** [67]. We rewrite the complex field of the electric field envelope $\mathcal{E}$ as follows:

$$\mathcal{E}(\mathbf{r}_\perp, z) = \sqrt{\rho(\mathbf{r}_\perp, z)} e^{i\Phi(\mathbf{r}_\perp, z)}. \tag{1.14}$$

Using this definition, the velocity of the field is $\mathbf{v} = \frac{c}{k_0}\nabla\Phi(\mathbf{r}_\perp, z)$ where $k_0 = k(\omega_0)$ is the wavenumber of the laser inside the cell. This is natural as this describes that the speed is essentially the instantaneous wavevector of the field i.e the direction in which it will evolve: locally the field can always be described by a plane wave of the form $e^{i\mathbf{k}_\perp\cdot\mathbf{r}_\perp}$.

We now have two hydrodynamical variables $(\rho, \mathbf{v})$ to describe the phase and amplitude degrees of freedom of the field. Plugging this relation into eq.1.10, we retrieve the celebrated quantum **Euler equations** [67]:

$$\frac{\partial\rho}{\partial z} = -\frac{1}{c}\nabla_\perp(\rho\mathbf{v}) \boxed{-\alpha\rho} \tag{1.15}$$

$$\frac{\partial\mathbf{v}}{\partial z} = -\boxed{\frac{1}{2c}\nabla_\perp\mathbf{v}^2} - \frac{c}{k_0}\nabla_\perp\Big(\boxed{g\rho} - \underbrace{\frac{1}{2k_0}\frac{\nabla_\perp^2\sqrt{\rho}}{\sqrt{\rho}}}_{\textit{Quantum pressure}} + \boxed{V}\Big) \tag{1.16}$$

As done previously we now carry a detailed study of the different terms in presence, following the same color code as in eq.1.10. This system presents two equations:

- **A "mass" rate equation** 1.15: usually this is a mass conservation term describing the conservation of current. Here as we are in the presence of linear absorption, this describes the rate of dissipation due to photon absorption.
- **A "convection" like equation** 1.16: this term describes the evolution of the velocity field $\mathbf{v}(\mathbf{r}_\perp, z)$ with different source terms.

While the equation 1.15 is essential in order to faithfully model our system, it is trivial as it describes the evolution of the density following the flow $\rho\mathbf{v}$. The "convection" term of eq.1.16 however gives valuable physical insight into the different effects at play here. The first term is **diffraction** (in blue) whose kinetic energy interpretation is now transparent: the kinetic energy of the field is proportional to $\propto \mathbf{v}^2$. Obviously if this kinetic energy is uniform, it

will mean that the energy is at equilibrium and thus there will not be any convection. We then have the **interaction** term (in green). In this formulation, it becomes more apparent that in order to have no evolution we also need to have a uniform density: because of the interactions, if the density is not uniform the fluid will want to either equalize its density (repulsive interactions), or on the contrary accumulate this density in a single point (attractive interactions). Connecting to the optics point of view, this means that plane waves will not experience geometrical effects like self-defocusing. The potential term (in orange) also only acts if it is not uniform. Then again, under this form, we recover a classical mechanical picture: the force felt by the fluid is the gradient of the potential field V. This allows to consolidate the picture showed in fig.1.1.
Finally, the last term is the **quantum pressure term** [83]. As opposed to the other terms, it has no classical counterparts, but we can gain insight by checking the effective range of this term. As a higher order derivative term, it will be effective on shorter scales. We will find in the next subsection what this relevant scale is.

1.2 Quantum formulation

Having established the classical equations for the paraxial propagation of laser light within a non-linear medium, we would like to now derive a quantum version of these equations. In order to study in depth the implication of atom-light interaction (which will be presented in chap.3), and the resulting photon-photon interactions, we need a quantum formulation of the field evolution equations. For this section, I will rely heavily on seminal works by Pierre-Élie Larré and Iacopo Carusotto who laid the theoritical foundations for the study of quantum fluids of light [23; 59; 60]. In the spirit of simplicity, we will only consider the 2D+1 case where temporal effects are ignored.

1.2.1 Quantization of the evolution equation

It can be shown [59] that it is possible to quantize the electric field envelope $\mathcal{E}$, introducing a field operator $\hat{\mathcal{E}}(\mathbf{r}, z)$ and the following "equal-time" commutation relations (in the Heisenberg picture):

$$\begin{aligned} [\hat{\mathcal{E}}(\mathbf{r}, z), \hat{\mathcal{E}}^\dagger(\mathbf{r}', z)] &= \frac{\hbar}{\mathcal{N}}\delta(\mathbf{r} - \mathbf{r}') \\ [\hat{\mathcal{E}}(\mathbf{r}, z), \hat{\mathcal{E}}(\mathbf{r}', z)] &= 0 \\ [\hat{\mathcal{E}}^\dagger(\mathbf{r}, z), \hat{\mathcal{E}}^\dagger(\mathbf{r}', z)] &= 0 \end{aligned} \tag{1.17}$$

where $\mathcal{N} = \frac{k_0}{\mu_0 \omega_0^2}$ is a normalization coefficient depending on the medium, with μ_0 is the vacuum magnetic permeability and ω_0 the central laser frequency. Now an **important caveat**: even though we ignore the temporal dimension t as we discarded the GVD terms, it is paramount to properly carry out the quantization procedure, especially the determination of $\mathcal{N}$. The details are not reproduced for clarity, but the interested reader can consult [59; 60] for the full calculation. From this, we can introduce the following Hamiltonian operator using

the usual color code:

$$\hat{H}(z) = \mathcal{N}\int \mathrm{d}\mathbf{r}\Big[\frac{1}{2k_0}\nabla_\perp\hat{\mathcal{E}}^\dagger\cdot\nabla_\perp\hat{\mathcal{E}} + V(\mathbf{x}_\perp,z)\hat{\mathcal{E}}^\dagger\hat{\mathcal{E}} + \frac{g(\mathbf{x}_\perp,z)}{2}\hat{\mathcal{E}}^\dagger\hat{\mathcal{E}}^\dagger\hat{\mathcal{E}}\hat{\mathcal{E}} + i\frac{\alpha}{2}\hat{\mathcal{E}}^\dagger\hat{\mathcal{E}}\Big]. \tag{1.18}$$

While the interpretation of the kinetic, potential and losses terms is straightforward, the interaction term carries much physical meaning: it is exactly the **four-wave mixing** Hamiltonian, or the so-called contact interaction term present in the quantum version of the Gross Pitaevskii equation. This comparison will be deepened in the next subsections, and the atomic physical origin of this term will be shown in chap.3.
In order to retrieve a propagation equation for our field operator $\hat{\mathcal{E}}$, we need only to compute its commutator with the Hamiltonian eq.1.18:

$$i\hbar\partial_z\hat{\mathcal{E}} = -[\hat{H}(z),\hat{\mathcal{E}}]. \tag{1.19}$$

Expanding this yields finally the operator version of eq.1.10:

$$i\frac{\partial\hat{\mathcal{E}}}{\partial z} = -\frac{1}{2k_0}\nabla_\perp^2\hat{\mathcal{E}} + V(\mathbf{r},z)\hat{\mathcal{E}} + g(\mathbf{r},z)\hat{\mathcal{E}}^\dagger\hat{\mathcal{E}}\hat{\mathcal{E}} - i\frac{\alpha}{2}\hat{\mathcal{E}}. \tag{1.20}$$

Now, we notice that we end up with exactly the same equation as the classical propagation equation. While this should not come as a surprise, proving this is slightly more involved than simply converting $\mathcal{E}$ to $\hat{\mathcal{E}}$.
In order to solve this equation, we start with a mean field treatment by expanding to first order in fluctuations around a mean field $\mathcal{E}_0$ described by the classical NLSE. This is the core of the Bogoliubov theory [19] that I will now present.

1.2.2 Bogoliubov theory

The obvious issue in the eq.1.20, is the non linear interaction term that prevents simple integration of this equation. In order to deal with this, we want to establish first a free field theory that studies the behavior of small amplitude quantum fluctuations on top of a classical mean field (background). We thus look simply for solutions in the form of:

$$\hat{\mathcal{E}} = \underbrace{\mathcal{E}_0}_{Mean\ field} + \underbrace{\delta\hat{\mathcal{E}}}_{Fluctuations}. \tag{1.21}$$

The flucutations operator obeys the commutation relations defined in eq.1.17. The evolution of the mean field is simply described by eq.1.10. For practical purposes, the shape of this background is usually a wide gaussian profile whose size is much larger than the scale of the fluctuations. Thus, even in the presence of non-linearity, we can (most of the time) ignore its evolution without sacrificing physical content. Absorption however cannot be ignored and its effects will be discussed in details in chap.2. For the sake of generality and simplicity, we'll ignore the potential term for now. The effect of the potential term will be discussed in chap.4.
Let us also express the field fluctuations operator in momentum space since it will greatly help us down the line when solving the evolution equation:

$$\begin{aligned}\delta\hat{\mathcal{E}}(\mathbf{r}_\perp, z) &= \int \mathrm{d}\mathbf{k}_\perp \hat{a}_{\mathbf{k}_\perp}(z) e^{i\mathbf{k}_\perp\cdot\mathbf{r}_\perp} \\ \delta\hat{\mathcal{E}}^\dagger(\mathbf{r}_\perp, z) &= \int \mathrm{d}\mathbf{k}_\perp \hat{a}^\dagger_{-\mathbf{k}_\perp}(z) e^{i\mathbf{k}_\perp\cdot\mathbf{r}_\perp}.\end{aligned} \tag{1.22}$$

Here the $\hat{a}$ operators obeying standard bosonic commutation relations:

$$\begin{aligned}\left[\hat{a}_{\mathbf{k}_\perp}(z), \hat{a}^\dagger_{\mathbf{k}'_\perp}(z)\right] &= \delta(\mathbf{k}_\perp - \mathbf{k}'_\perp) \\ \left[\hat{a}_{\mathbf{k}_\perp}(z), \hat{a}_{\mathbf{k}'_\perp}(z)\right] &= 0 \\ \left[\hat{a}^\dagger_{\mathbf{k}_\perp}(z), \hat{a}^\dagger_{\mathbf{k}'_\perp}(z)\right] &= 0.\end{aligned} \tag{1.23}$$

Plugging this into the previously established propagation equation eq.1.20 yields:

$$\begin{aligned}i\partial_z(\mathcal{E}_0 + \delta\hat{\mathcal{E}}) = -\frac{1}{2k_0}\nabla^2_\perp(\mathcal{E}_0 + \delta\hat{\mathcal{E}}) - i\frac{\alpha}{2}(\mathcal{E}_0 + \delta\hat{\mathcal{E}}) + \\ g(\mathbf{r}, z)(\mathcal{E}_0^* + \delta\hat{\mathcal{E}}^\dagger)(\mathcal{E}_0 + \delta\hat{\mathcal{E}})(\mathcal{E}_0 + \delta\hat{\mathcal{E}}).\end{aligned} \tag{1.24}$$

Assuming that $\mathcal{E}_0$ follows the eq.1.10, this allows to retrieve an equation for $\delta\hat{\mathcal{E}}$ only:

$$\begin{aligned}i\frac{\partial\delta\hat{\mathcal{E}}}{\partial z} = -\frac{1}{2k_0}\nabla^2_\perp\delta\hat{\mathcal{E}} - i\alpha\delta\hat{\mathcal{E}} + \\ g(\mathbf{r}, z)\left[\underbrace{2|\mathcal{E}_0|^2\delta\hat{\mathcal{E}} + \mathcal{E}_0^2\delta\hat{\mathcal{E}}^\dagger}_{1^{st}\ order} + \underbrace{\mathcal{E}_0^*\delta\hat{\mathcal{E}}^2 + 2\mathcal{E}_0\delta\hat{\mathcal{E}}^\dagger\delta\hat{\mathcal{E}}}_{2^{nd}\ order} + \underbrace{\delta\hat{\mathcal{E}}^\dagger\delta\hat{\mathcal{E}}^2}_{3^{rd}\ order}\right].\end{aligned} \tag{1.25}$$

We can distinguish the different orders of the expansion in fluctuations. The first order describes the ballistic evolution of the fluctuation modes. The second order describes interaction between quasi-particles and lead to the celebrated Lee-Huan-Yang corrections [62] and quantum depletion [24]: the $2\mathcal{E}_0\delta\hat{\mathcal{E}}^\dagger\delta\hat{\mathcal{E}}$ describes the process of creating two excitations from the condensate. The third order describes more complex processes involving 3 quasi-particles. As we want a free field theory, we will truncate to first order, killing the higher order terms. We are thus left with a linearized propagation for the fluctuations [59]:

$$i\frac{\partial\delta\hat{\mathcal{E}}}{\partial z} = \boxed{-\frac{1}{2k_0}\nabla^2_\perp\delta\hat{\mathcal{E}}} + \boxed{g(\mathbf{r}, z)\left[2|\mathcal{E}_0|^2\delta\hat{\mathcal{E}} + \mathcal{E}_0^2\delta\hat{\mathcal{E}}^\dagger\right]} - \boxed{i\alpha\delta\hat{\mathcal{E}}}. \tag{1.26}$$

Note that we have highlighted the physical meaning of each term using the usual color code. It is important to notice the coupling induced by the interaction term between **pairs** of quasi-particles: the evolution for a mode is coupled to its conjugate through the $\mathcal{E}_0^2\delta\hat{\mathcal{E}}^\dagger$ term. Now we can recast this equation in momentum space to a matrix form in order to hopefully integrate it. Recalling the definition of the fluctuations modes $\delta\hat{\mathcal{E}}$ eq.1.22 we obtain:

$$i\partial_z\begin{pmatrix}\hat{a}_{\mathbf{k}_\perp} \\ \hat{a}^\dagger_{-\mathbf{k}_\perp}\end{pmatrix} = \underbrace{\begin{pmatrix}-\frac{\mathbf{k}_\perp^2}{2k_0} + 2g|\mathcal{E}_0|^2 - i\frac{\alpha}{2} & g\mathcal{E}_0^2 \\ g\mathcal{E}_0^{*2} & -\frac{\mathbf{k}_\perp^2}{2k_0} + 2g|\mathcal{E}_0|^2 - i\frac{\alpha}{2}\end{pmatrix}}_{\mathcal{A}_{\mathbf{k}_\perp} - i\frac{\alpha}{2}\mathbb{I}}\begin{pmatrix}\hat{a}_{\mathbf{k}_\perp} \\ \hat{a}^\dagger_{-\mathbf{k}_\perp}\end{pmatrix} \tag{1.27}$$

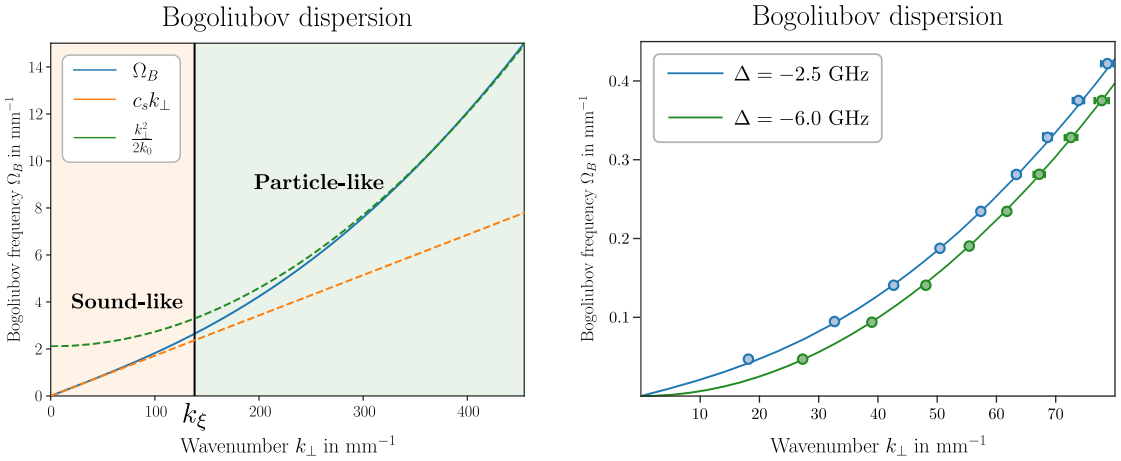

a) *Theoritical dispersion* b) *Experimental dispersion*

Fig. 1.2 *a) Analytical calculation of the Bogoliubov dispersion Ω_B for typical experimental parameters $n_2 = -5 \times 10^{-9}\ m^2/W$, $P_0 = 1\ W$ and $w_0 = 2.35\ mm$. b) Experimental measurement of this dispersion from [81]. The curves show the non-interacting (Δ=-2.5 GHz) and interacting (Δ=-6.0 GHz) case. In the non-interacting case, the dispersion is purely particle-like. In the interacting case, the dispersion shows the characteristic linear part, particularly noticeable by the vertical offset. Only the real part of the dispersion is shown here since the only imaginary part of the function is absorption.*

where the matrix $\mathcal{A}_{\mathbf{k}_\perp}$ encodes the evolution of the modes and the losses term $-i\frac{\alpha}{2}\mathbb{I}$ describes the damping due to losses. As it is, direct integration of this equation is impractical, we would want a diagonalized form. This is precisely what the celebrated **Bogoliubov transform** [83] achieves.
We introduce new operators called the **Bogoliubov quasi-particles** (sometimes "Bogolons") $\hat{b}_{\mathbf{k}_\perp}$ such that:

$$\begin{pmatrix} \hat{a}_{\mathbf{k}_\perp}(z) \\ \hat{a}^\dagger_{-\mathbf{k}_\perp}(z) \end{pmatrix} = \underbrace{\begin{pmatrix} u_{\mathbf{k}_\perp}(z) & v_{\mathbf{k}_\perp}(z) \\ v_{\mathbf{k}_\perp}(z) & u_{\mathbf{k}_\perp}(z) \end{pmatrix}}_{\mathcal{B}_{\mathbf{k}_\perp}} \begin{pmatrix} \hat{b}_{\mathbf{k}_\perp}(z) \\ \hat{b}^\dagger_{-\mathbf{k}_\perp}(z) \end{pmatrix} \tag{1.28}$$

where $\mathcal{B}_{\mathbf{k}_\perp}$ is a hyperbolic rotation: $\det(\mathcal{B}_{\mathbf{k}_\perp}) = u^2_{\mathbf{k}_\perp} - v^2_{\mathbf{k}_\perp} = 1$. The $\hat{b}_{\mathbf{k}_\perp}$ operators are the eigenmodes of the evolution and their eigenvalue is the **Bogoliubov dispersion** [34]. The spectrum of $\mathcal{B}_{\mathbf{k}_\perp}$ yields:

$$\Omega_{\mathcal{B}}(\mathbf{k}_\perp) = \sqrt{\frac{\mathbf{k}_\perp^2}{2k_0}\left(\frac{\mathbf{k}_\perp^2}{2k_0} + 2g|\mathcal{E}_0|^2\right)} - i\frac{\alpha}{2}. \tag{1.29}$$

This dispersion relation has several major features crucial to understand the dynamics of quantum fluids.
Firstly, this dispersion relation has **two regions** separated by the typical scale $k_\xi = k_0\sqrt{g|\mathcal{E}_0|^2} = \frac{2\pi}{\xi}$ where ξ is the **healing length**:

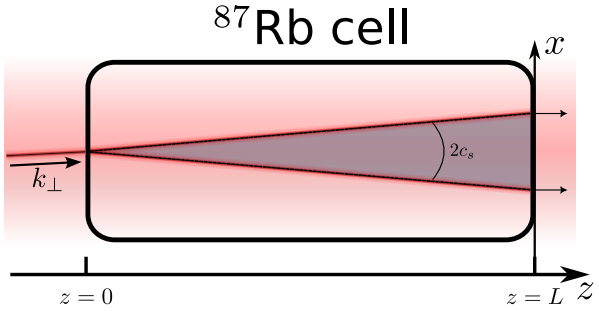

a) *Schematic view of the experiment [35]*

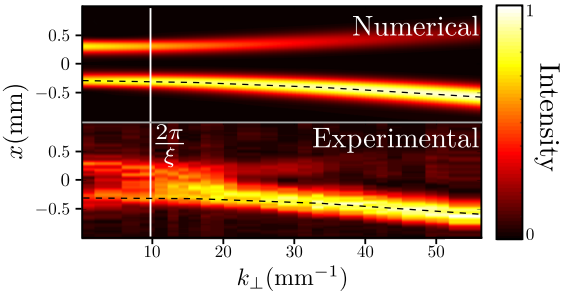

b) *Experimental results [34]*

Fig. 1.3 *a) The perturbation (dark red beam) is superimposed to a large gaussian background (in light red). Two localized excitations are generated propagating at the speed of sound as long as $k_\perp < k_\xi$. The output position of both wavepackets is recorded at the output of the cell. b) Numerical and experimental taken from [34]. The initial angle of the perturbation beam is varied and the position of the phonons is recorded. The profile is first flat until k_ξ before converging to a linear slope at high $k_\perp$*

- A **linear** sonic region under k_ξ where $\Omega_\mathcal{B}(\mathbf{k}_\perp) \approx c_s k_\perp$ with $c_s = c\sqrt{g|\mathcal{E}_0|^2}$ defining the **speed of sound**
- A **quadratic** particle-like region above k_ξ where $\Omega_\mathcal{B}(\mathbf{k}_\perp) \approx \frac{\mathbf{k}_\perp^2}{2k_0}$

The healing length ξ represents the scale under which we can no longer consider the fluid as a collective ensemble. The corresponding momentum scale k_ξ is fundamental in the context of superfluidity, where it represents the critical momentum at which superfluidity breaks down. It is also has profound meaning in atomic Bose-Einstein condensates, where excitations under the healing length kick atoms out of the condensate [83].
There is however a big caveat to this description: the evolution of the mean field driven by absorption needs to be slow with respect to the eigenvalues of $\mathcal{A}_{\mathbf{k}_\perp}$ in eq.1.27 **adiabatically** follow the evolution of $\mathcal{A}_{\mathbf{k}_\perp}$. This adiabaticity condition is fundamental when dealing with quantum aspects and will be detailed in chap.2.
The existence of sound-like excitations in fluids of light has dramatic implications that cannot be described well within the language of non-linear optics. Such a striking phenomenon is for instance the splitting of a wavepacket into two localized excitations whose propagation is independant of the initial wavepacket momentum as has been demonstrated by Quentin Fontaine in [34].

In this experiment, the dispersion relation is measured from the group velocity of the Bogoliubov excitations. Experimentally, this is measured by sending a small perturbation on top of a large gaussian background. Due to the interactions between photons, this wavepacket will split into two wavepackets, both moving at a certain group velocity. As long as the momentum of the impinging wavepacket is under k_ξ, this group velocity does not depend on the initial momentum, and is equal to the speed of sound c_s. This is easily understood since the group velocity of the Bogoliubov excitations is defined as $v_g = \frac{\partial \Omega_B}{\partial k_\perp}$. Thus it will be

constant and equal to c_s at low $k_\perp$, and linear at high $k_\perp$ where $v_g(k_\perp) = \frac{k_\perp}{k_0}$.
This behavior fails to follow either the geometrical optics, or the non-linear optics classical intuitions. Indeed, at low $k_\perp$, we expect the generation of a pair of conjugated momenta beams due to degenerate four wave mixing in the non-linear medium [21]. Within the momentum conservation, we do not expect however this effect to be independant of the incoming wavevector ! In the high $k_\perp$ limit, we hopefully recover the traditional geometrical optics limit where the beam follows a straight line that is given by the initial beam angle. There remains however another spot that is created through the four-wave mixing process (the "idler" beam in this configuration).

We have thus seen in this section that the photon-photon interactions that are mediated by the atom-light interaction within the vapor introduces effects that go beyond classical non-linear optics treatments, and rather fall in the phenomenology of cold atomic ensembles. With this in mind, I will now detail this comparison with cold Bose gases in order to extract meaningful insight from what has been a very successful experimental platform for quantum physics these last twenty years.

1.2.3 Comparison with the atomic Gross-Pitaevskii equation of cold gases

In order to compare our system to cold Bose gases, we first need to define what cold Bose gases are. Due to their bosonic nature, bosonic atoms are predicted to condense below a certain critical temperature. As the thermal wavelength approaches the typical interparticular distance, the atoms will start to behave collectively and share a single wavefunction Ψ whose evolution will be described by the Gross-Pitaevskii equation [83]. Experimentally this phenomenon is realized by cooling down atoms in optical traps using a wide range of cooling techniques pioneered by Claude Cohen-Tannoudji, Steven Chu and William Daniel Phillips granting them the 1997 Nobel prize. The first experimental observation of Bose Einstein condensation was carried out in 1995 at JILA [10] using Rubidium 87 atoms. Since this seminal work, many groups have carried out similar research using the long lifetimes and controllability of atoms to study many effects such as superfluidity In order to gain more understanding about the deep links between the physics that we have access to in our experiments and the physics of BEC, let us have a look at the description of an interacting gas of bosonic atoms. Similar to what I presented earlier in this thesis, there are three main effects at play in this problem:

- **Kinetic energy**: each atom has some energy due to thermal energy (even if the temperature is very low)
- **Potential energy**: the atoms are massive particles subjected to gravity. If we want to observe them we will need to trap them to be able to keep them at a fixed position.
- **Interaction energy**: due to the atomic potential, the atoms will scatter.

One can show [83] that the equation governing the wavefunction of the atoms in this case is the **Gross-Pitaevskii equation** (GPE):

$$i\hbar\frac{\partial\Psi}{\partial t} = -\frac{\hbar^2}{2m}\nabla^2\Psi + V\Psi + g|\Psi|^2\Psi \tag{1.30}$$

where m is the atomic mass, V is the confining potential, g the interaction constant and ∇^2 represents the kinetic term. Here, Ψ has the dimension of the square root of a density $L^{-3/2}$. Diving a bit deeper into this equation, we remark that the inter-atom interactions are simplified to a **contact interaction** meaning that the Coulombic interaction potential has been reduced to a point-like Dirac peak whose height depends on the effective s-wave scattering length: $g = \frac{4\pi\hbar^2 a_s}{m}$. This scattering length describes the typical range of the interactions. Its name is due to the dilute medium and weak interaction assumptions: we only consider the lowest energy scattering processes. When atoms scatter, there exists a range of distance in the interatomic potental within which a bound state can exist. At lowest energy, we look at the s-state bounding state (alike electronic orbitals of an atom). The higher orders that can then be considered are p-states, d-states etc ...
Thus the interaction process of atoms in BEC is qualitatively very different from the effective photon-photon interactions of fluids of light. In the case of atoms, the interaction results **directly** of the scattering of the atoms within their Coulomb potential. In the case of photons, the scattering between photons is **mediated** by the atoms due to complex atom-light interaction processes.
Having established the GPE, we can then use the Bogoliubov formalism to treat the system evolution to the first order. Without detailing the treatment (it has already been done in the previous section), we recover the Bogoliubov dispersion with its sonic part where the energy of the Bogoliubov excitations at momentum p is:

$$\hbar\omega(p) = \sqrt{\frac{p^2}{2m}\Big(\frac{p^2}{2m} + 2g\rho_0\Big)} \tag{1.31}$$

assuming ρ_0 is the condensate density. The physical meaning of the mean field in the case of BEC is the condensate fraction i.e a macroscopical occupation of a 0 momentum state. This is historically how condensation was observed for the first time [10]. We can then look at the small density fluctuations over this condensate. As shown in the previous section, this dispersion relation introduces a critical scale between linear and quadratic regimes: the **healing length** $\xi = \frac{\hbar}{\sqrt{2mg\rho_0}}$. This length owes its name to the fact that it characterizes the scale at which the collective behavior of atoms breaks down. Below this scale, a perturbation will kick atoms out of the condensate state. This establishes an equivalent momentum scale $p_\xi = \hbar\frac{2\pi}{\xi}$. In a similar fashion, the speed of sound is defined as $c_s = \sqrt{\frac{g\rho_0}{m}}$. In order to compare the platforms further, we will use these characteristic scales to adimensionalize both evolution equations. In order to do this let us go back to eq.1.12. If we alter the change of variables in the following manner, it is possible to recover an isotropic mass tensor:

$$\begin{aligned} \tau &= \frac{z}{c} \\ \zeta &= \gamma\Big(v_g t - z\Big) \end{aligned} \tag{1.32}$$

where $\gamma = \frac{\xi}{\xi_t}$ with ξ the healing length in the transverse plane (x, y) stemming from the Kerr index n_2, and $\xi_t = v_g\sqrt{\frac{-D_0 n_0}{k_0 \Delta n}}$ is the healing length in the longitudinal dimension ζ (i.e the "real time") due to group velocity dispersion. Using this new change of variable, we can reformulate eq.1.12 as:

$$\frac{i}{c}\frac{\partial\psi}{\partial\tau} = -\frac{1}{2k_0}\nabla_\perp^2\psi + \frac{v_g^2 D_0}{2}\gamma^2\frac{\partial^2\psi}{\partial\zeta^2} + V(\mathbf{r},\tau)\psi + g(\mathbf{r},\tau)|\psi|^2\psi \tag{1.33}$$

where we define the transverse gradient operator $\nabla_\perp = (\partial_x^2\ \partial_y^2)$. This reduces to :

$$\frac{i}{c}\frac{\partial\psi}{\partial\tau} = -\frac{1}{2k_0}\nabla^2\psi + V(\mathbf{r},\tau)\psi + g(\mathbf{r},\tau)|\psi|^2\psi. \tag{1.34}$$

We have here regrouped all second order derivatives in the same operator $\nabla = (\partial_x^2\ \partial_y^2\ \partial_\zeta^2)$ since $\frac{v_g^2 D_0}{2}\gamma^2 = \frac{1}{2k_0}$. This is actually the design of the change of variable 1.32 to make the mass tensor $\mathcal{M}$ presented in eq.1.13 isotropic. Introducing the photon effective mass $m = \frac{\hbar k_0}{c}$, the propagation equation reads:

$$i\hbar\frac{\partial\psi}{\partial\tau} = -\frac{\hbar^2}{2m}\nabla^2\psi + \hbar c V(\mathbf{r},\tau)\psi + \hbar c g(\mathbf{r},\tau)|\psi|^2\psi. \tag{1.35}$$

We have recovered the full 3D+1 evolution equation of the fluid of light by introducing a basis change substituting time and z dimensions. We can now already identify term by term the equivalent terms in both GPE and NLSE. For clarity, we will go further with a final step of adimensionalizing both propagation equations which will allow to compare each relevant parameter quantitatively. A natural way to adimensionalize these equation is to renormalize the time (resp. space) by some characteristic time (resp. spatial) scale. Two such obvious scales are the following:

- The healing length ξ: the length up until which the collective Bogoliubov description is valid.
- The non-linear length $z_{NL} = \frac{1}{g|E_0|^2}$ / non-linear time $\tau_{NL} = \frac{1}{cg|E_0|^2}$: intuitively, the higher the interactions are, the faster will the system will evolve since the collision rate will be higher. In the fluids of light language, the non-linear length z_{NL} wille be the length after which non-linear effects will be noticeable. Note that in order to vary the effective evolution time within the non-linear medium, we will often play with the laser power in order to change z_{NL} and such the total adimensional evolution time L/z_{NL} [1].

With these scales in mind, the NLSE recasts as follow:

$$\begin{aligned}\frac{\partial\tilde{\psi}}{\partial\tilde{\tau}} &= i\tilde{\nabla}^2\tilde{\psi} + i\frac{V(\tilde{\mathbf{r}},\tilde{\tau})}{g(\tilde{\mathbf{r}},\tilde{\tau})|E_0|^2}\tilde{\psi} - i|\tilde{\psi}|^2\tilde{\psi}, \text{ with} \\ \psi &= E_0\tilde{\psi} \quad , \quad \tilde{\tau} = \frac{\tau}{\tau_{NL}} \quad , \quad \tilde{\mathbf{r}} = \frac{\mathbf{r}}{\xi}\ .\end{aligned} \tag{1.36}$$

In the case of the GPE, $\tau_{NL} = \frac{\hbar}{g\rho_0}$ and $\xi = \frac{\hbar}{\sqrt{2mg\rho_0}}$. Note that in this case, the meaning of τ_{NL} and ξ is the same. The expression change as the link with the relevant experimental units change since the definition and dimensionality of g changes. With this in mind, we carry out the same procedure and obtain:

$$\begin{aligned}\frac{\partial\tilde{\psi}}{\partial\tilde{\tau}} &= i\tilde{\nabla}^2\tilde{\psi} + i\frac{U(\tilde{\mathbf{r}},\tilde{\tau})}{g(\tilde{\mathbf{r}},\tilde{\tau})\rho_0}\tilde{\psi} - i|\tilde{\psi}|^2\tilde{\psi}, \text{ with} \\ \psi &= \sqrt{\rho_0}\tilde{\psi} \quad , \quad \tilde{\tau} = \frac{\tau}{\tau_{NL}} \quad , \quad \tilde{\mathbf{r}} = \frac{\mathbf{r}}{\xi}\ .\end{aligned} \tag{1.37}$$

We thus finally find that one adimensionalized the GPE and NLSE are **mathematically equal**, and we can then easily compare the relevant characteristic scales quantitatively:

- **Interactions**: the relevant parameter to characterize the strength of the interactions accross different platforms is the non-linear time. In the case of BEC the interaction parameter is the **chemical potential $\boldsymbol{\mu = g\rho_0}$**. From the comparison of eqs.1.36 and 1.37 we find that the equivalent parameter for fluids of light is $\hbar cg|E_0|^2 = \hbar\omega_0\Delta n$. To give numerical orders of magnitude, in typical BEC experiments such as [27] $gn_0 = \mu$ is easily computed as it is equal to the trapping energy within the Thomas-Fermi approximation [83]. Typical trapping frequencies in 2D BEC experiments are in the kHz range [27] meaning a chemical potential in the range of 10^{-30} J. In our case, typical values of the non-linear dephasing are $\Delta n \sim 10^{-5}$, meaning an interaction energy of 10^{-24} J or a frequency in the 10 GHz range. This means that typical interactions in a photon fluid are **seven orders of magnitudes larger** than in atomic BEC's. In addition to this, the effective mass is **12 orders of magnitude** smaller. This explains why it is possible to observe much of the same physics as Bose gases even though the interaction times are much smaller. Travel time through the Rubidium cell is on the order of a few 100 ps compared to the millisecond to second time scale used in cold atoms experiments. One might argue about the relevance of travel time in CW regime, however ultimately the physical situation is that the image registered by a camera is the integration of "slices" of light that all have traveled a time L/c inside the cell.

- **Potential**: Using the same analysis as previously, one can derive relevant comparisons between the trapping of atoms and the potential engineering achievable in fluids of light (see chap.4). As for the interaction parameter $\hbar\omega_0\Delta n$, the potential energy can be written $V = \hbar\omega_0\delta n$. Typical experimental values in our system reach $\delta n \sim 10^{-4}$, meaning frequencies in the 100 GHz range. Then again, these values are much higher than in atomic condensates.

- **Kinetic energy**: Initial state of the BEC is the condensate. This means that a single momentum state gets a macroscopical occupation number, above a thermalized distribution. By its nature, the concept of BEC requires thermal equilibrium. Without a trap, the equivalent description in the context of fluids of light is a plane wave with a single $k_\perp = 0$ mode. Obviously, since plane waves require an infinite wavefront, the real state is a coherent state whose extent in Fourier domain is negligible i.e a large gaussian beam. The question of equilibrium and thermal population in the case of photon fluids is a much harder question. The fluid due to the near-instantaneous onset of interactions at the entrance of the cell is quenched far out of equilibrium, unless the input state is specifically prepared to cancel this effect. The question of thermalization and equilibrium will be detailed in the next chapter.

In order to summarize the comparison, we can build a "translation" table as follows:

BEC	Expression	Typical value	Fluids of light	Expression	Typical value
Wavefuntion	ψ	10^8 $m^{-3/2}$	Electric field	$\mathcal{E}$	10^5 V/m
Spatial coordinates	(x,y,z)	100 μm	Spatial coordinates	(x,y,ζ) with ζ comoving	1 mm
Temporal evolution	physical time t	ms to s scale	Temporal evolution	effective time $\tau = z/c$	100 ps scale
Mass	m	10^{-24} kg	Effective mass	$\bar{m} = \frac{\hbar k_0}{c}$	10^{-36} kg
Atomic density	ρ	10^{17} m^{-3}	Photon density / Intensity	$\rho = \frac{I}{\hbar\omega_0 c}$	10^{17} m^{-3}
In plane momentum (x,y)	k_x, k_y	0 to 10^6 m^{-1}	In plane wavevector $\propto$ angle	$k_\perp$	10^2 to 10^5 m^{-1}
Longitudinal momentum z	k_z	10^2 m^{-1}	Temporal frequency	$\omega \propto k_{\tilde{z}} = \frac{2\pi}{\tilde{z}}$	0.01 to 50 MHz
Speed of sound	c_s	mm/s	Speed of sound	$c_s = c\sqrt{\Delta n}$	10^7 m/s
Healing length	$\xi = \frac{\hbar}{\sqrt{2mg\rho_0}} = \frac{1}{\sqrt{8\pi a_s \rho_0}}$	100 nm scale	Healing length	$\xi = \frac{1}{k_0}\sqrt{\frac{n_0}{\lvert\Delta n\rvert}}$	5 µm to 100 µm scale
Scattering length	a_s	nm to µm scale	Scattering length	$a_s = \frac{-\hbar c^2 k_0^3 n_2}{4\pi n_0}$	0.1 nm to µm
Thermal energy	$k_b T$	100 nK	$k_\perp \neq 0$ population	speckle $\rightarrow$ $k_B T = \frac{(\hbar/\sigma)^2}{2m}$	Adjustable between 0 and 10μ

Another important question is the **dimensionality** of our system. As mentioned in the first section 1.1 of this chapter, the dynamics in our fluids of light is confined to the transverse plane due to the longitudinal mass being much larger than the transverse one due to GVD. But what are the other physical mechanisms garanteeing this interpretation ? Taking this into account, one important question arises: where does the 2D+1 geometry comes from ? Is the two-dimensional nature due to **translationnal invariance** or some **confinement mechanism along the ζ direction** ? This is particularly relevant as dimensionality plays a major role in the manifestation of effects such as superfluidity or Bose-Einstein condensation: in 2D, Bose-Einstein is not possible for instance, in opposition with the 3D case. Instead, a regime of quasi-condensation appears and the system displays the celebrated Bresinski-Kosterlitz-Thouless transition [41].

In the case of Bose Einstein condensates, in the presence of strong in plane confinement, the GPE can formally be reduced to two dimension with a renormalized interaction constant that becomes adimensional $\tilde{g} = \sqrt{8}\frac{a_s}{a_z}$ [25]. with a_s the 3d scattering length and a_z the scattering length corresponding to the confinement along the z direction. As $a_z = \sqrt{\frac{\hbar}{m\omega_z}}$ where ω_z is the trapping frequency, we easily see that $\tilde{g}$ increases with an increasing confinement.

In the typical regime of our experiments, the ζ dimension of our system is basically infinite. One limitation that we could see to the spatial extent of the fluid along the ζ dimension could

be the coherence length. As the coherence length describes the length difference after which there could be no interferences between a beam and itself, it can be understood as the typical length for which one can consider the light as belonging to the same fluid. This coherence length is on the order of several tens of meters, which is seven orders of magnitude larger than the lowest spatial scale of the system which is typically the healing length ξ. Thus, we can safely assume that our system is infinite along the ζ dimension. Now, due to this infinite dimension we can define an ansatz, very much like in the case of the 2D BEC, however in this case, as the fluid is not confined, the ansatz function will be different: in this case we factorize by a plane wave. If we include the plane wave factorizationn we can rewrite the field envelope as follows:

$$\tilde{\mathcal{E}}(\mathbf{r},\tau) = \tilde{\mathcal{E}}(\mathbf{r}_\perp,\tau)e^{i(\omega_\tau\tau+q\zeta)} \tag{1.38}$$

where ω_t and q are the conjugated variables in the comoving frame (frequency and wavenumber). Let us go back to our original equation 1.12 for the electric field envelope $\mathcal{E}$:

$$\frac{i}{v_g}\frac{\partial\mathcal{E}}{\partial\tau} = -\frac{1}{2k_0}\nabla_\perp^2\mathcal{E} + \frac{v_g^2 D_0}{2}\frac{\partial^2\mathcal{E}}{\partial\zeta^2} + V(\mathbf{r},\tau)\mathcal{E} + g(\mathbf{r},\tau)|\mathcal{E}|^2\mathcal{E} \tag{1.39}$$

Now there is an important question: the one of the normalization of the "wavefunction" i.e in this case the electric field envelope. Having established the plane wave ansatz, we want to link each factor of the ansatz to the physical quantities of the system. One natural way is to normalize such that $|\tilde{\mathcal{E}}|^2$ becomes an electric field density, closely related to the light intensity:

$$\begin{aligned}\tilde{\mathcal{E}} &= \frac{\mathcal{E}}{\mathcal{N}_0}\\ \mathcal{N}_0^2 &= \int \mathrm{d}^2\mathbf{r}|\mathcal{E}(\mathbf{r},\tau)|^2 = \frac{2P_0}{c\epsilon_0 n_0}\end{aligned} \tag{1.40}$$

where the integral carries over all of the system size and P_0 is the optical power. Plugging this into 1.12, we obtain the equation for the normalized field envelope density:

$$\frac{i}{v_g}\frac{\partial\tilde{\mathcal{E}}}{\partial\tau} = -\frac{1}{2k_0}\nabla_\perp^2\tilde{\mathcal{E}}(\mathbf{r}_\perp,\tau) + V(\mathbf{r}_\perp,\tau)\tilde{\mathcal{E}}(\mathbf{r}_\perp,\tau) + \underbrace{\overline{g}(\mathbf{r}_\perp,\tau)}_{g\mathcal{N}_0^2}|\tilde{\mathcal{E}}(\mathbf{r}_\perp,\tau)|^2\tilde{\mathcal{E}}(\mathbf{r}_\perp,\tau) \tag{1.41}$$

We recover thus a **2D+1** propagation equation, with a normalized interaction strength $\overline{g} \propto n_2 P_0$. In this case, the optical power P_0 is directly linked to the photon flux Φ: $P_0 = \hbar\omega_0\Phi$. This is a major difference with the case of 2D BEC where the **dimensionless** interaction parameter $\tilde{g}$ is obtained by normalizing by the interaction strength by the scattering length perpendicular to the confinement plane. Contrary to the case of 2D BEC, it is meaningless to try and normalize the wavefunction in a "direct" manner since integrating a plane wave on an infinite interval would only yield frustration. We overcome this by thinking about the photon **flux** and normalize with the **density** (i.e light intensity) of the fluid [35].

We conclude that the scenario in the paraxial fluids of light platform is quite different that the case of 2D BEC. While the physics accessible is comparatively very similar, the

mechanisms explaining a 2D behavior are different. In our case, the 2D+1 geometry comes from **translational invariance** instead of the direct effect of confinement. This leads to the fact that the relevant quantities in the case of the photon fluid must be the photon density in the plane i.e the **intensity** and the photon flux i.e **power**. Thus, for the rest of the thesis, we will always assume a 2D+1 geometry except in specific scenarios that will be explicitely stated.

1.3 Numerical analysis

Numerous physical effects that manifest in the experiments go beyond the perturbative analytical treatment described before. This hinders a priori the tools at our disposal to analyze experimental results. Hopefully, the recent progress in graphical processing units (GPU) allow an easy and efficient implementation of the numerical schemes I will describe in the following subsections.

1.3.1 Split-step spectral schemes

Looking back at the NLSE 1.10, we treat the following 2D+1 differential equation:

$$\frac{\partial \mathcal{E}}{\partial z} = \underbrace{-\frac{1}{2k_0}\nabla_\perp^2 \mathcal{E}}_{\mathcal{D}} + \underbrace{k_0 \delta n \mathcal{E} + \frac{k_0 n_2 c \epsilon_0}{2}|\mathcal{E}|^2 E - i\alpha\mathcal{E}}_{\mathcal{N}}. \tag{1.42}$$

If we want to solve this numerically, we discretize space and time and cast the field in the memory as a 2D array. The field is thus represented as a matrix $A_{ij} = \mathcal{E}(x_i, y_j)$ with x_i, y_j are the positions in the discretized grid of spatial coordinates such that $|x_{i+1} - x_i| = \delta x$ and $|y_{i+1} - y_i| = \delta y$ (assuming a constant sampling step). In the same fashion, we will discretize the propagation coordinate z with a sampling step δz. The most natural way to solve the equation is then to directly integrate it using a small enough discretization such that such an approximation converges. Assuming a longitudinal discretization δz small enough, we can write:

$$\mathcal{E}(z + \delta z) = \mathcal{E}(z) e^{i\delta z\left(\mathcal{D}[\mathcal{E}(z)] + \mathcal{N}[\mathcal{E}(z)]\right)}. \tag{1.43}$$

We notice that we have two types of terms:

- A non-linear operator $\mathcal{N}$ whose application is trivial in real space i.e a simple array element-wise multiplication
- A derivative operator $\mathcal{D}$ whose application is best carried out in the Fourier space as ∇^2 simply becomes $\times \mathbf{k}^2$.

We are then tempted to simply apply the $\mathcal{D}$ term in the Fourier domain, and the $\mathcal{N}$ term in the real space sequentially. However, we have to make sure that $[\mathcal{D}, \mathcal{N}] = 0$ in order to expand the exponential term as the product of each exponential. There is a priori no reason for these operators to commute, but since we use a small δz, we can use the Baker-Hausdorff formula [30] to do approximate the exponential of the sum by the product of the exponentials up to $o(\delta z^2)$. This expansion gives its name to the method presented in this subsection: **split-step** because we apply sequentially the non-linear and derivative operators, and **spectral**

because we switch to Fourier domain to apply the derivative operator.
Using this, we can define the following pseudo algorithm to solve the equation starting from some known initial state:

- Fourier transform the field: $\mathcal{E}(r,z) \rightarrow \tilde{\mathcal{E}}(k,z)$
- Apply kinetic term $\mathcal{D}$: $\tilde{\mathcal{E}}(k,z) \rightarrow \tilde{\mathcal{E}}(k,z)e^{-i\delta z\frac{k^2}{2k_0}\tilde{\mathcal{E}}(k,z)}$
- Inverse Fourier transform the field: $\tilde{\mathcal{E}}(k,z) \rightarrow \mathcal{E}(r,z)$
- Apply real space non-linear, potential and absorption terms: $\mathcal{E}(r,z) \rightarrow \mathcal{E}(r,z)e^{i\delta z\left(k_0\delta nE(r,z)+\frac{k_0 n_2 c\epsilon_0}{2}|\mathcal{E}(r,z)|^2\mathcal{E}(r,z)-i\alpha\mathcal{E}(r,z)\right)}$
- Loop over $\frac{L}{\delta z}$ times to propagate until the end of the cell

It can be shown [4] that this method converges in $\mathcal{O}(\delta z)$ in time and $\mathcal{O}(\delta r^2)$ spatially. With this in mind, the discretization steps should be chosen adequately in order to ensure a good tradeoff between performance and convergence. In order to accurately describe the physics of our system, δr should be chosen such as to be much smaller thant the healing length ξ. Modern FFT algorithms guarantee a $\mathcal{O}(N\log(N))$ complexity for all sizes. In the same manner, element-wise matrix multiplication has a $\mathcal{O}(N^2)$ complexity. Thus in general it is generally more favorable to decrease the size of the spatial discretization δr rather than increasing the number of steps i.e decreasing δz. Obviously this is highly dependant on hardware. As by essence this method is vectorized and matricial, it is particularly well suited to be implemented on GPU's. The implementation details are discussed in the Appendix A of this thesis.

1.3.2 Modelling quantum fluctuations

The previous subsection described how to solve numerically the evolution of the mean field of eq.1.36. If we wish to study effects arising from quantum fluctuations, we need to solve the evolution equation of the fluctuation modes eq.1.25. For this it can be shown [94] that we can add a classical noise to the field $\mathcal{E}(r,z) \rightarrow \mathcal{E}(r,z) + \delta\mathcal{E}(r,z)$ and by **truncating** the operators product to finite orders, identify the quantum average to an statistical averaging over realizations of this classical noise. Furthermore this can be implemented efficiently within the previous split-step scheme using vectorization: we can simultaneously propagate several realizations of the noise.

Conclusion

In this chapter we have provided an comprehensive introduction on the field of quantum fluids of light. By starting from the propagation of light in non-linear media, we developped a rigorous description of light as a novel quantum fluid and established the Bogoliubov theory of the excitations in this fluid. We deepened the analogy by establishing a quantitative comparison with cold atomic gases in order to extract meaningful experimental parameters, also settling the question of dimensionality in propagating geometry. Finally we presented numerical methods providing a simple framework to go beyond the analytical results given by

Bogoliubov theory. One of the main difference between quantum fluids of light in propagating geometry and Bose Einstein condensates is their out-of-equilibrium nature: the input state is not a thermal state and the interactions are quenched at the input and output of the cell. This leads to strong non-classical signatures [97] that will be explored in the next chapter.

Chapter 2

Interaction quenches and out-of-equilibrium dynamics

2.1 Out-of-equilibrium nature of the system

Since our non-linear medium is **finite**, a fundamental characteristic of our system is that the interactions are quenched at the input and output of the nonlinear medium. While sounding like a limitation, we can actually take advantage of this to study the effect of **interaction quenches** on the dynamics of fluids of light. This effect has been studied extensively theoretically [59; 60; 70] and it allows to explore the rich dynamics of out-of-equilibrium systems. In this chapter, we will focus on the out-of-equilibrium characteristics of the system rising from this discontinuity.

The physical situation of the problem is represented in fig.2.1. An initially non-interacting state enters a non-linear medium, undergoing an interaction quench in the process. For a spatially coherent plane wave at $k_\perp = 0$, the input state is concentrated in a $k_\perp = 0$ Dirac delta peak. This means that for all other momenta, the input state is the **vacuum**. This interaction quench generates pairs of **phonons** (Bogoliubov excitations) in the fluid of light that will evolve and interfere within the medium [36]. As the fluid exits the cell, the interactions are quenched again back to 0 and pairs of phonons are converted back into pairs of photons. This pair creation mechanism is fundamentally linked to the four wave mixing interaction hamiltonian of the system described in eq.1.18. It is rigorously equivalent to the two-body contact interaction hamiltonian of cold atomic gases. Thus, any pre-existing equilibrium momentum distribution is perturbed by these quenches. An important point, is that there is no obvious thermalization mechanisms in our system. At first order, the losses due to atomic absorption only dampen the mean field, that the fluctuations follow adiabatically (this question is detailled in subsection 2.2.7). Thus there is no physical processes that rid the system of its most energetic excitations like for instance in the case of evaporative cooling. The lack of thermalization processes will be discussed more in detail in chap.5, but this does not prevent prethermalization effects as it has been evidenced in [3]. Having established this preliminary argument about the system we will now present the analytical theory describing these quenches.

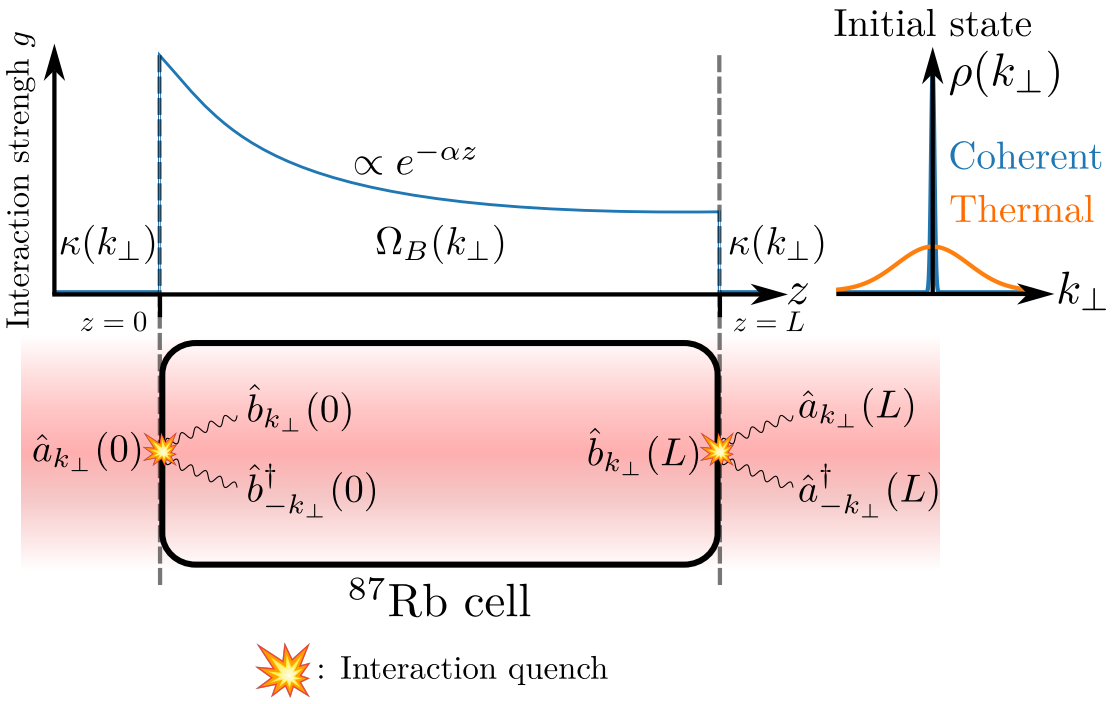

Fig. 2.1 *The initial state of the fluid is represented on the right: the blue curve represents the very narrow momentum distribution associated to a coherent state, while the orange curve represents a broad thermal profile associated with a typical temperature on the order of $k_BT \approx \mu$. The cell is represented and the creation of pair of phonons (resp. photons) is highlighted at the input and output of the cell with the orange symbols. The strength of the interaction profile is represented in parallel above the cell: within the cell the interaction strength decreases exponentially due to absorption, and the interactions are abruptly switched on and off at the input and output of the cell.*

2.2 Response to quenches

The starting point of the description of the quenches within the fluid of light is the second quantized representation of the fluctuations in eq.1.22.

2.2.1 Evolution outside the medium

We first establish the evolution equation outside of the medium. Without interactions nor potential field, the evolution of the photons is only guided by diffraction. This means that the hamiltonian of the system reduces to:

$$\hat{H} = \mathcal{N} \int \mathrm{d}\mathbf{r} \; \frac{1}{2k_0} \nabla_\perp \delta\hat{\mathcal{E}}^\dagger \cdot \nabla_\perp \delta\hat{\mathcal{E}} \tag{2.1}$$

which rewrites in momentum space as:

$$\hat{H} = \mathcal{N} \int \mathrm{d}\mathbf{k}_\perp \; \frac{\mathbf{k}_\perp^2}{2k_0} \hat{a}^\dagger_{\mathbf{k}_\perp} \hat{a}_{\mathbf{k}_\perp} \tag{2.2}$$

The evolution equation for the photon modes $\hat{a}_{\mathbf{k}_\perp}$ thus writes for $z \in [-\infty, 0] \bigcup [L, +\infty]$:

$$\begin{aligned} \frac{\partial \hat{a}_{\mathbf{k}_\perp}}{\partial z} &= i \frac{\mathbf{k}_\perp^2}{2k_0} \hat{a}_{\mathbf{k}_\perp} \\ \frac{\partial \hat{a}^\dagger_{-\mathbf{k}_\perp}}{\partial z} &= -i \frac{\mathbf{k}_\perp^2}{2k_0} \hat{a}^\dagger_{-\mathbf{k}_\perp}. \end{aligned} \tag{2.3}$$

We recognize the quadratic free-space dispersion relation $\kappa(\mathbf{k}_\perp) = \frac{\mathbf{k}_\perp^2}{2k_0}$. We can thus easily integrate these equations such that the $\hat{a}_{\mathbf{k}_\perp}$ modes pick up a phase $e^{i\kappa(\mathbf{k}_\perp)z}$ for an evolution over a distance z.

2.2.2 Evolution equation within the medium

Within the medium, we treat the evolution of the fluctuations to first order using the Bogoliubov theory presented in eq.1.29 and 1.28 such that the new eigenmodes are the $\hat{b}_{\mathbf{k}_\perp}$ modes described by:

$$\begin{aligned} \frac{\partial \hat{b}_{\mathbf{k}_\perp}}{\partial z} &= i\Omega_B(\mathbf{k}_\perp, z) \hat{b}_{\mathbf{k}_\perp} \\ \frac{\partial \hat{b}^\dagger_{-\mathbf{k}_\perp}}{\partial z} &= -i\Omega_B^*(\mathbf{k}_\perp, z) \hat{b}^\dagger_{-\mathbf{k}_\perp} \\ \begin{pmatrix} \hat{a}_{\mathbf{k}_\perp}(z) \\ \hat{a}^\dagger_{-\mathbf{k}_\perp}(z) \end{pmatrix} &= \begin{pmatrix} u_{\mathbf{k}_\perp}(z) & v_{\mathbf{k}_\perp}(z) \\ v_{\mathbf{k}_\perp}(z) & u_{\mathbf{k}_\perp}(z) \end{pmatrix} \begin{pmatrix} \hat{b}_{\mathbf{k}_\perp}(z) \\ \hat{b}^\dagger_{-\mathbf{k}_\perp}(z) \end{pmatrix} \end{aligned} \tag{2.4}$$

where the $u_{\mathbf{k}_\perp}$ and $v_{\mathbf{k}_\perp}$ are the Bogoliubov coefficients. We will assume for now that we know how to solve the evolution equation of these coefficients given by eq.1.27. This means that integration is again straightforward and we find that for an evolution over a length z, the $\hat{b}_{\mathbf{k}_\perp}$ modes pick up the following phase $e^{i\theta}$ with $\theta(\mathbf{k}_\perp, z) = \int_0^z \Omega_B(\mathbf{k}_\perp, z')\mathrm{d}z'$.

2.2.3 Final state

Now, we will compare the two evolution equations in order to link an input photon mode $\hat{a}_{\mathbf{k}_\perp}(0)$ to the final mode $\hat{a}_{\mathbf{k}_\perp}(z)$ for a certain $z > L$. In order to simplify the setting, we will take the origin of the "time" axis z at the entrance of the cell. With this in mind, let us assume assume a set of initial conditions:

$$\begin{aligned} N_{\mathbf{k}_\perp}(0) &= \left\langle \hat{a}^\dagger_{\mathbf{k}_\perp}(0)\hat{a}_{\mathbf{k}_\perp}(0)\right\rangle = N_0\delta(\mathbf{k}_\perp) \\ C_{\mathbf{k}_\perp}(0) &= \langle \hat{a}_{-\mathbf{k}_\perp}(0)\hat{a}_{\mathbf{k}_\perp}(0)\rangle = \delta(\mathbf{k}_\perp) \end{aligned} \tag{2.5}$$

These coefficients are the **normal** (N) and **anomalous** (C) correlators. The normal correlator describes the **population** of excitations. The anomalous correlator describes the **correlations** between modes. As **our initial state is assumed to be a coherent plane wave** at $\mathbf{k}_\perp = 0$, we have the vacuum as input state on all other wavevectors. This means an uncorrelated shot noise [103]. We will now rely on these two correlators to characterize the state.

In order to describe the evolution of this initial state, we diagonalize the hamiltonian of its evolution in each segment, meaning before the cell, in the cell and then finally after the cell (which are symbolized with the blue and green colors in fig.2.3). As we have established that within the cell, the Bogoliubov modes are the eigenmodes of the propagation, we merely have to transform the state to a basis of Bogoliubov modes at both faces of the cell, corresponding to the input and output quenches. Since the initial state is in a vacuum mode everywhere except for $\mathbf{k}_\perp = 0$, we will from now focus on the $\mathbf{k}_\perp \neq 0$ modes whose evolution is only seeded by quantum fluctuations. We write the correlators in the bogolon basis:

$$\begin{aligned} \left\langle \hat{a}^\dagger_{\mathbf{k}_\perp}(0)\hat{a}_{\mathbf{k}_\perp}(0)\right\rangle &= u_{\mathbf{k}_\perp}(0)v_{\mathbf{k}_\perp}(0)\left\langle \hat{b}_{-\mathbf{k}_\perp}(0)\hat{b}_{\mathbf{k}_\perp}(0)\right\rangle + v^2_{\mathbf{k}_\perp}(0)\left\langle \hat{b}_{-\mathbf{k}_\perp}(0)\hat{b}^\dagger_{-\mathbf{k}_\perp}(0)\right\rangle + \\ &\quad u^2_{\mathbf{k}_\perp}(0)\left\langle \hat{b}^\dagger_{\mathbf{k}_\perp}(0)\hat{b}_{\mathbf{k}_\perp}(0)\right\rangle + u_{\mathbf{k}_\perp}v_{\mathbf{k}_\perp}\left\langle \hat{b}^\dagger_{\mathbf{k}_\perp}(0)\hat{b}^\dagger_{-\mathbf{k}_\perp}(0)\right\rangle \\ \langle \hat{a}_{-\mathbf{k}_\perp}(0)\hat{a}_{\mathbf{k}_\perp}(0)\rangle &= u^2_{\mathbf{k}_\perp}(0)\left\langle \hat{b}_{-\mathbf{k}_\perp}(0)\hat{b}_{\mathbf{k}_\perp}(0)\right\rangle + u_{\mathbf{k}_\perp}(0)v_{\mathbf{k}_\perp}(0)\left\langle \hat{b}_{-\mathbf{k}_\perp}(0)\hat{b}^\dagger_{-\mathbf{k}_\perp}(0)\right\rangle + \\ &\quad u_{\mathbf{k}_\perp}(0)v_{\mathbf{k}_\perp}(0)\left\langle \hat{b}^\dagger_{\mathbf{k}_\perp}(0)\hat{b}_{\mathbf{k}_\perp}(0)\right\rangle + v^2_{\mathbf{k}_\perp}(0)\left\langle \hat{b}^\dagger_{\mathbf{k}_\perp}(0)\hat{b}^\dagger_{-\mathbf{k}_\perp}(0)\right\rangle. \end{aligned} \tag{2.6}$$

Using the initial populations and correlations, this readily simplifies to the following identities:

$$\begin{aligned} \left\langle \hat{b}_{-\mathbf{k}_\perp}(0)\hat{b}_{\mathbf{k}_\perp}(0)\right\rangle &= \left\langle \hat{b}^\dagger_{\mathbf{k}_\perp}(0)\hat{b}^\dagger_{-\mathbf{k}_\perp}(0)\right\rangle = -u_{\mathbf{k}_\perp}(0)v_{\mathbf{k}_\perp}(0) \\ \left\langle \hat{b}_{-\mathbf{k}_\perp}(0)\hat{b}^\dagger_{-\mathbf{k}_\perp}(0)\right\rangle &= u^2_{\mathbf{k}_\perp}(0) \\ \left\langle \hat{b}^\dagger_{\mathbf{k}_\perp}(0)\hat{b}_{\mathbf{k}_\perp}(0)\right\rangle &= v^2_{\mathbf{k}_\perp}(0). \end{aligned} \tag{2.7}$$

Let us pause and gain some physical insight of these expressions. Even **starting with a vacuum state**, the bogolon population right after the first quench is **non-zero**. In the same manner, the **correlations** between phonons are now also **non-zero**. As the photon gas enters the cell, it suddenly acquires a large amount of energy due to the interactions. The only way to dissipate this energy is to emit pairs of phonons in the photon fluid. Note that this $v^2_{\mathbf{k}_\perp}$ term is of particular significance in the context of **quantum depletion** of cold Bose gases [24]. There is a deep connection between the two phenomena as they both originate from the properties of the Bogoliubov dispersion, as well as the vacuum fluctuations. The

fact that we are able to recover a non-zero average number of bogolons directly originates from the commutation relations of the $\hat{a}_{\mathbf{k}_\perp}$ and $\hat{b}_{\mathbf{k}_\perp}$ modes. The physical interpretation of these commutation relations is that while the average photon number in the $\mathbf{k}_\perp \neq 0$ is zero, the variance is strictly positive. This means that it is really the vaccum fluctuations that seed the emission of phonons, very much like the quantum depletion process where vacuum fluctuations seed the emission of phonon pairs of non zero momenta, depleting the $k = 0$ condensate mode.

We can then continue on with the evolution of the correlators, evolving the Bogolons within the medium. As mentioned before, since the bogolons are the eigenmodes of the fluid within the cell, they only pick up a phase θ as described in eq.2.4:

$$\begin{aligned}
&\left\langle \hat{b}_{-\mathbf{k}_\perp}(L)\hat{b}_{\mathbf{k}_\perp}(L)\right\rangle = \left\langle \hat{b}^\dagger_{\mathbf{k}_\perp}(L)\hat{b}^\dagger_{-\mathbf{k}_\perp}(L)\right\rangle = -u_{\mathbf{k}_\perp}(L)v_{\mathbf{k}_\perp}(L)e^{i2\theta} \\
&\left\langle \hat{b}_{-\mathbf{k}_\perp}(L)\hat{b}^\dagger_{-\mathbf{k}_\perp}(L)\right\rangle = u^2_{\mathbf{k}_\perp}(L)e^{-\alpha L} \\
&\left\langle \hat{b}^\dagger_{\mathbf{k}_\perp}(L)\hat{b}_{\mathbf{k}_\perp}(L)\right\rangle = v^2_{\mathbf{k}_\perp}(L)e^{-\alpha L}.
\end{aligned} \tag{2.8}$$

We can then finally use the inverse Bogoliubov transform in order to retrieve the correlators in the photon basis:

$$\begin{aligned}
\left\langle \hat{a}^\dagger_{\mathbf{k}_\perp}(L)\hat{a}_{\mathbf{k}_\perp}(L)\right\rangle &= -u_{\mathbf{k}_\perp}(0)v_{\mathbf{k}_\perp}(0)u_{\mathbf{k}_\perp}(L)v_{\mathbf{k}_\perp}(L)\Big[e^{-i2\theta}+e^{i2\theta}\Big]+ \\
&\quad v^2_{\mathbf{k}_\perp}(L)u^2_{\mathbf{k}_\perp}(0)+v^2_{\mathbf{k}_\perp}(0)u^2_{\mathbf{k}_\perp}(L) \\
\langle \hat{a}_{-\mathbf{k}_\perp}(L)\hat{a}_{\mathbf{k}_\perp}(L)\rangle &= -u_{\mathbf{k}_\perp}(0)v_{\mathbf{k}_\perp}(0)u_{\mathbf{k}_\perp}(L)v_{\mathbf{k}_\perp}(L)\Big[u^2_{\mathbf{k}_\perp}(L)e^{-i2\theta}+v^2_{\mathbf{k}_\perp}(L)e^{i2\theta}\Big]+ \\
&\quad u_{\mathbf{k}_\perp}(L)v_{\mathbf{k}_\perp}(L)\Big[u^2_{\mathbf{k}_\perp}(0)+v^2_{\mathbf{k}_\perp}(0)\Big].
\end{aligned} \tag{2.9}$$

If we include an extra propagation outside the cell up to a certain position z, we need to add a simple dephasing term:

$$\begin{aligned}
&\left\langle \hat{a}^\dagger_{\mathbf{k}_\perp}(z)\hat{a}_{\mathbf{k}_\perp}(z)\right\rangle = \left\langle \hat{a}^\dagger_{\mathbf{k}_\perp}(L)\hat{a}_{\mathbf{k}_\perp}(L)\right\rangle \\
&\langle \hat{a}_{-\mathbf{k}_\perp}(z)\hat{a}_{\mathbf{k}_\perp}(z)\rangle = e^{-i2\kappa(\mathbf{k}_\perp)[z-L]}\,\langle \hat{a}_{-\mathbf{k}_\perp}(L)\hat{a}_{\mathbf{k}_\perp}(L)\rangle
\end{aligned} \tag{2.10}$$

Let us comment this result. We find that there is a complex population and correlation structure appearing from intially vacuum modes. This structure is **oscillatory** in nature and stems from the interference between the two quenches or the **interference between the two types of eigenmodes** of the system. These interferences stem from the **beating** between the free-space quadratic dispersion relation $\kappa(\mathbf{k}_\perp)$ in eq.2.9 and the Bogoliubov dispersion $\Omega_B(\mathbf{k}_\perp)$ in the θ term of eq.2.8. Within all this analysis however, we have overlooked two important points: **losses** and external **sources of noise**. As mentioned previously, we are describing effects that are seeded by vacuum fluctuations. By nature, these effects are extremely sensitive to any external noise, and one can rightfully question the robustness of such a complex structure to experimental conditions. Furthermore, up until now, we have conveniently hidden away losses as a mean-field term that dampens populations and coherences with the absorption rate α. This is why I will now detail methods to take into account these noises.

2.2.4 Modeling of noise and losses

Depending on the strength of the losses relative to the other processes during the evolution of the fluid, one may have to treat the losses as an actual **stochastic process** probabilistically

destroying photons. If the rate of losses is comparable to the energy of the Bogoliubov excitations, one cannot describe the losses as only affecting the mean-field, and the Bogoliubov dispersion will not follow the evolution of the mean-field adiabatically. This argument of adiabaticity will be detailed in the subsection 2.2.7. This is due to the **fluctuation-dissipation relations** through the Green-Kubo formulae [85]. More precisely, due to the duality of the Bogoliubov transform, destroying pairs of photons equates to creating a pairs of bogolons, and this process might give rise to significant additional contributions in the correlators of eq.2.8. This is especially relevant when going back to the physical process of absorption within the atomic vapor, that is by its very nature, stochastic since the field is quantized. This spontaneous emission process should also be included as an additional contribution to the populations within the vapor of eq.2.8.

Let us start with a modified evolution equation taking spontaneous emission into account. For this we use a Heisenberg-Langevin equation [60] and model our noise by some white quantum noise operator $\hat{\gamma}_{\mathbf{k}_\perp}(z)$ describing spontaneous photon emission such that:

$$\left[\hat{\gamma}_{\mathbf{k}_\perp}(z),\hat{\gamma}_{\mathbf{k}'_\perp}(z')\right] = \mathcal{N}\frac{\hbar\omega_0}{\epsilon_0}\alpha\delta(\mathbf{k}_\perp - \mathbf{k}'_\perp)\delta(z-z'). \tag{2.11}$$

Furthermore, we assume that this noise is completely uncorrelated with the photon or bogolon modes i.e the $\hat{a}_{\mathbf{k}_\perp}/\hat{b}_{\mathbf{k}_\perp}$ modes commute with the $\hat{\gamma}_{\mathbf{k}_\perp}$ modes. Assuming this, we will neglect stimulated emission. We then add this noise in the bogolon evolution equation as follows:

$$\frac{\partial\hat{b}_{\mathbf{k}_\perp}}{\partial z} = \underbrace{i\Omega_B(\mathbf{k}_\perp,z)\hat{b}_{\mathbf{k}_\perp}(z)}_{\textit{Bogoliubov evolution}} + \underbrace{u_{\mathbf{k}_\perp}(z)\hat{\gamma}_{\mathbf{k}_\perp}(z) - v_{\mathbf{k}_\perp}(z)\hat{\gamma}^\dagger_{-\mathbf{k}_\perp}(z)}_{\textit{Spontaneous emission}}. \tag{2.12}$$

We see that this equation exactly describes the process where a bogolon is destroyed (the $\hat{b}_{\mathbf{k}_\perp}$ operator) creating two photons (the $\hat{\gamma}_{\mathbf{k}_\perp}$ and $\hat{\gamma}^\dagger_{-\mathbf{k}_\perp}$ operators). Now we try to integrate this evolution equation:

$$\begin{aligned}
\hat{b}_{\mathbf{k}_\perp}(z) &= e^{-i\theta}\hat{b}_{\mathbf{k}_\perp}(0) + \hat{\Gamma}_{\mathbf{k}_\perp}(L)\\
\hat{\Gamma}_{\mathbf{k}_\perp}(L) &= \int_0^L \mathrm{d}z' e^{-i\int_{z'}^L \mathrm{d}z''\Omega_B(\mathbf{k}_\perp,z'')} e^{-\alpha(L-z')/2}\left[u_{\mathbf{k}_\perp}\hat{\gamma}_{\mathbf{k}_\perp}(z') - v_{\mathbf{k}_\perp}\hat{\gamma}^\dagger_{\mathbf{k}_\perp}(z')\right]
\end{aligned} \tag{2.13}$$

Injecting this into the expressions for the commutators of the $\hat{b}_{\mathbf{k}_\perp}$ modes of eq.2.8:

$$\begin{aligned}
\left\langle\hat{b}^\dagger_{\mathbf{k}_\perp}(L)\hat{b}_{\mathbf{k}_\perp}(L)\right\rangle &= \left\langle\hat{b}^\dagger_{\mathbf{k}_\perp}(0)\hat{b}_{\mathbf{k}_\perp}(0)\right\rangle + e^{i\theta}\left\langle\hat{b}_{\mathbf{k}_\perp}(0)\hat{\Gamma}_{\mathbf{k}_\perp}(L)\right\rangle +\\
&\quad e^{-i\theta}\left\langle\hat{\Gamma}^\dagger_{\mathbf{k}_\perp}(L)\hat{b}_{\mathbf{k}_\perp}(0)\right\rangle + \left\langle\hat{\Gamma}^\dagger_{\mathbf{k}_\perp}(L)\hat{\Gamma}_{\mathbf{k}_\perp}(L)\right\rangle\\
\left\langle\hat{b}_{-\mathbf{k}_\perp}(L)\hat{b}_{\mathbf{k}_\perp}(L)\right\rangle &= e^{-2i\theta}\left\langle\hat{b}_{-\mathbf{k}_\perp}(0)\hat{b}_{\mathbf{k}_\perp}(0)\right\rangle + e^{-i\theta}\left\langle\hat{b}_{-\mathbf{k}_\perp}(0)\hat{\Gamma}_{\mathbf{k}_\perp}(L)\right\rangle +\\
&\quad e^{-i\theta}\left\langle\hat{\Gamma}_{-\mathbf{k}_\perp}(L)\hat{b}_{\mathbf{k}_\perp}(0)\right\rangle + \left\langle\hat{\Gamma}_{-\mathbf{k}_\perp}(L)\hat{\Gamma}_{\mathbf{k}_\perp}(L)\right\rangle
\end{aligned} \tag{2.14}$$

Due to the commutation rules, all the cross terms vanish. We are thus left with the

computation of the correlators of the $\hat{\Gamma}_{\mathbf{k}_\perp}$ modes:

$$\begin{aligned}
\left\langle \hat{b}^\dagger_{\mathbf{k}_\perp}(L)\hat{b}_{\mathbf{k}_\perp}(L)\right\rangle &= \left\langle \hat{b}^\dagger_{\mathbf{k}_\perp}(0)\hat{b}_{\mathbf{k}_\perp}(0)\right\rangle + \left\langle \hat{\Gamma}^\dagger_{\mathbf{k}_\perp}(L)\hat{\Gamma}_{\mathbf{k}_\perp}(L)\right\rangle \\
\left\langle \hat{b}_{-\mathbf{k}_\perp}(L)\hat{b}_{\mathbf{k}_\perp}(L)\right\rangle &= e^{-2i\theta}\left\langle \hat{b}_{-\mathbf{k}_\perp}(0)\hat{b}_{\mathbf{k}_\perp}(0)\right\rangle + \left\langle \hat{\Gamma}_{-\mathbf{k}_\perp}(L)\hat{\Gamma}_{\mathbf{k}_\perp}(L)\right\rangle \\
\left\langle \hat{\Gamma}^\dagger_{\mathbf{k}_\perp}(L)\hat{\Gamma}_{\mathbf{k}_\perp}(L)\right\rangle &= \int_0^L \mathrm{d}z' e^{-\alpha(L-z')} v^2_{\mathbf{k}_\perp}(z')\mathcal{N}\frac{\hbar\omega_0}{\epsilon_0}\alpha \\
\left\langle \hat{\Gamma}_{-\mathbf{k}_\perp}(L)\hat{\Gamma}_{\mathbf{k}_\perp}(L)\right\rangle &= \int_0^L \mathrm{d}z' e^{-2i\int_{z'}^L dz'' \Omega_B(\mathbf{k}_\perp,z'')} e^{-\alpha(L-z')} - u_{\mathbf{k}_\perp}(z')v_{\mathbf{k}_\perp}(z')\mathcal{N}\frac{\hbar\omega_0}{\epsilon_0}\alpha.
\end{aligned} \tag{2.15}$$

Physically, these extra contributions express that at each slice $\mathrm{d}z'$ of the medium, losses will create $v^2_{\mathbf{k}_\perp}(z')\mathcal{N}\frac{\hbar\omega_0}{\epsilon_0}\alpha$ bogolons on average. Due to this correlated emission, the bogolons correlations will be modified by a factor proportional to $-u_{\mathbf{k}_\perp}(z)v_{\mathbf{k}_\perp}(z)$. Obviously, analytical calculation of these corrections is impossible and we have to resort to numerical integration to solve these integrals. Solving the evolution equation for the Bogoliubov coefficients as well as the correlators is detailed in subsection 2.2.8.

Looking at other sources of noise, we assume that experimental noise can be modeled with uncorrelated white noises in space. In momentum space, this will lead to a gaussian noise since we convolve with the point spread function of the system which is assumed to be a gaussian whose width is the optical resolution. Going back at the expressions for the correlators between each quench, we have to modify the calculation by adding additional populations before each quench. This models for instance the noise from the laser, or the spontaneous emission process inside the cell as described earlier. While these noises are not white noises in reality, there actual structure can be straightforwardly included by using the adequate commutators in eq.2.11. It is also the way to take into account an arbitrary initial state before the cell having some spatial noise distribution $B(\mathbf{k}_\perp)$. Assuming an extra population $B(\mathbf{k}_\perp)$ before the first quench, the populations and correlations after the first quench read:

$$\begin{aligned}
\left\langle \hat{b}_{-\mathbf{k}_\perp}(0)\hat{b}_{\mathbf{k}_\perp}(0)\right\rangle &= \left\langle \hat{b}^\dagger_{\mathbf{k}_\perp}(0)\hat{b}^\dagger_{-\mathbf{k}_\perp}(0)\right\rangle = -u_{\mathbf{k}_\perp}(0)v_{\mathbf{k}_\perp}(0)(1+2B(\mathbf{k}_\perp)) \\
\left\langle \hat{b}_{-\mathbf{k}_\perp}(0)\hat{b}^\dagger_{-\mathbf{k}_\perp}(0)\right\rangle &= u^2_{\mathbf{k}_\perp}(0)(1+B(\mathbf{k}_\perp)) + v^2_{\mathbf{k}_\perp}(0)B(\mathbf{k}_\perp) \\
\left\langle \hat{b}^\dagger_{\mathbf{k}_\perp}(0)\hat{b}_{\mathbf{k}_\perp}(0)\right\rangle &= v^2_{\mathbf{k}_\perp}(0)(1+B(\mathbf{k}_\perp)) + u^2_{\mathbf{k}_\perp}(0)B(\mathbf{k}_\perp).
\end{aligned} \tag{2.16}$$

In the same manner, at the end of the cell, we can add a momentum-dependent population $D(\mathbf{k}_\perp)$ and rewrite the population and coherences at $z = L$ in the bogolon basis:

$$\begin{aligned}
\left\langle \hat{b}_{-\mathbf{k}_\perp}(L)\hat{b}_{\mathbf{k}_\perp}(L)\right\rangle &= e^{i2\theta}\left\langle \hat{b}_{-\mathbf{k}_\perp}(0)\hat{b}_{\mathbf{k}_\perp}(0)\right\rangle \\
\left\langle \hat{b}^\dagger_{\mathbf{k}_\perp}(L)\hat{b}_{\mathbf{k}_\perp}(L)\right\rangle &= e^{-\alpha L}\left\langle \hat{b}^\dagger_{\mathbf{k}_\perp}(0)\hat{b}_{\mathbf{k}_\perp}(0)\right\rangle + D(\mathbf{k}_\perp)
\end{aligned} \tag{2.17}$$

In the next section we will see what experimental observables can be used in order to probe this complex correlation structure.

2.2.5 Structure factor

An typical observable in order to characterize the density response function [83] of the system is the **static structure factor**. It describes the density fluctuations [32] distribution

in momentum space and gives deep insight into the correlation properties of the system. It has been used in cold atomic system to study the effect of interaction quenches in multiple experiments [44; 45; 58; 91]. In cold atomic systems, looking directly at first order field correlation functions is challenging even though some form of interferometry is possible [41; 84], giving access to integrated $g^{(1)}$ functions.

In order to describe the density fluctuations of the system, we recall the Madelung transform of eq.1.14 and express the $\hat{a}_{\mathbf{k}_\perp}$ fluctuation modes of the field in terms of density fluctuations. Since $\hat{\mathcal{E}} = \sqrt{\hat{\rho}}e^{i\hat{\phi}}$, within these definitions, we define the density fluctuation operator as:

$$\delta\hat{\rho}_{\mathbf{k}_\perp}(z) = \int \mathrm{d}\mathbf{q}\hat{a}^\dagger_{\mathbf{k}_\perp+\mathbf{q}}\hat{a}_{\mathbf{k}_\perp}. \tag{2.18}$$

Note that we have expanded here only in density fluctuations since phase fluctuations can be large. This is detailed in section 2.5. For a density fluctuation operator $\delta\hat{\rho}$, the definition of the static structure factor is the following:

$$S(\mathbf{k}_\perp) = \frac{1}{N}\left\langle \delta\hat{\rho}^2_{\mathbf{k}_\perp} - |\left\langle \delta\hat{\rho}_{\mathbf{k}_\perp}\right\rangle|^2 \right\rangle, \tag{2.19}$$

where N is the total particle number. In our case the total particle number will be the photon flux depending on laser power, beam cross-section and integration time. The static structure factor is thus simply the variance of density fluctuations in momentum space. Furthermore given that the fluctuations are zero-mean, we can recast this into the expression for the static structure factor [106]:

$$\begin{aligned} S(\mathbf{k}_\perp) &= \frac{1}{N_0}\left\langle \delta\hat{\rho}_{\mathbf{k}_\perp}\delta\hat{\rho}_{-\mathbf{k}_\perp}\right\rangle \\ &= \frac{1}{N_0}\int \mathrm{d}\mathbf{q}\mathrm{d}\mathbf{q}'\left\langle \hat{a}^\dagger_{\mathbf{q}-\mathbf{k}_\perp}\hat{a}_{\mathbf{q}}\hat{a}^\dagger_{\mathbf{q}'+\mathbf{k}_\perp}\hat{a}_{\mathbf{q}'}\right\rangle. \end{aligned} \tag{2.20}$$

This formula is strongly reminiscent of the four-wave mixing hamiltonian of eq.1.18. This is of course not fortuitous and it is of particular relevance for the physical interpretation of this quantity: the structure factor is a **measure of how many momentum preserving scattering events** occur between modes at momenta $\mathbf{q}$ and $\mathbf{q}'$ going towards momenta $\mathbf{q}-\mathbf{k}_\perp$ and $\mathbf{q}'+\mathbf{k}_\perp$.

Looking at this expression, it seems that this integral is not analytical, however we can make a few approximations when by taking into account the initial state of the fluid. If we assume that the $k=0$ mode is a coherent classical state populated with $\hat{a}^\dagger_0\hat{a}_0 = N_0$ photons, and that all of the other modes are in vacuum modes, then we can consider that to lowest order in perturbation (i.e within Bogoliubov theory), **the only relevant scattering processes are between the zero momentum "condensate"** and **pairs of opposite momenta** (in order to preserve total momentum). This scattering phenomena is exactly the degenerate four-wave mixing mechanism from which the photon-photon interactions originate, thus we can interpret the static structure factor as a fingerprint of the interactions within the fluid. This means that in the four momenta integral of eq.2.20, only one momentum remains. We set q and q' to 0, thus the integral collapses and we retrieve the following simplified expression:

$$S(\mathbf{k}_\perp) = \left\langle \hat{a}^\dagger_{\mathbf{k}_\perp}\hat{a}_{\mathbf{k}_\perp}\right\rangle + \left\langle \hat{a}_{\mathbf{k}_\perp}\hat{a}^\dagger_{\mathbf{k}_\perp}\right\rangle + \left\langle \hat{a}_{-\mathbf{k}_\perp}\hat{a}_{\mathbf{k}_\perp}\right\rangle + \left\langle \hat{a}^\dagger_{\mathbf{k}_\perp}\hat{a}^\dagger_{-\mathbf{k}_\perp}\right\rangle, \tag{2.21}$$

which can reduce further using the commutation rule:

$$S(\mathbf{k}_\perp) = 1 + 2N(\mathbf{k}_\perp) + 2\mathrm{Re}\Big(C(\mathbf{k}_\perp)\Big), \tag{2.22}$$

with the populations $N(\mathbf{k}_\perp)$ and coherences $C(\mathbf{k}_\perp)$ as defined in eqs.2.5 and 2.17. Let us first stop and think about what is happening if we only consider the first quench:

- Initial state $z = 0^-$: since all populations and correlations are null aside from the $k_\perp = 0$ mode, the static structure factor describes a uniform white noise and is equal to 1.
- Right after the quench $z = 0^+$: the populations in the $\hat{b}_{\mathbf{k}_\perp}$ modes becomes non-zero due to the emission of pairs of bogolons. In this case the structure factor takes the shape $1 + 2N_0 + 2Re(C_0)$. N_0 and C_0 are the corresponding photon populations / correlations.
- At length $z < L$: the coherences have picked up a phase θ as defined in eq.2.4. Ignoring absorption, it becomes simply $\theta = \Omega_B(\mathbf{k}_\perp)z$, thus the structure factor is $S(\mathbf{k}_\perp) = 1 + 2N_0 + 2C_0\cos(2\Omega_B(\mathbf{k}_\perp)z)$.

This means that the structure factor will develop oscillations around unity driven by the Bogoliubov frequency. Since the Bogoliubov frequency is lower at low $\mathbf{k}_\perp$, the low frequency peaks will take longer to appear in the structure factor in Fourier space: the oscillations are proportional to $\cos(\Omega_B(\mathbf{k}_\perp)z)$ so as z advances, signal at low $k_\perp$ will evolve slowly since $\Omega_B(\mathbf{k}_\perp)$ is small. On the contrary, at the high $k_\perp$ end of the spectrum, the frequency $\Omega_B(\mathbf{k}_\perp)$ is high, thus $\cos(\Omega_B(\mathbf{k}_\perp)z)$ will evolve quickly. Furthermore, if we follow a peak of $S(\mathbf{k}_\perp) = 1$, it will move at the group velocity, that is equal to c_s for all modes at low $\mathbf{k}_\perp$.

In order to get some physical insight in the more general case of two quenches of this formula, one can look at a plot of this quantity for typical quench scenarii:

- **Constant interactions**: the first scenario to consider is the ideal case of two quenches separated by a constant interaction region. In this scenario, the first quench creates a population of bogolons and correlates them due to the interaction structure. These bogolons evolve harmonically at the Bogoliubov frequency within the medium. A second set of excitations is generated by the second quench, and these excitations will also evolve harmonically but this time in air (vacuum). The beatnote between these two frequencies leads to the blue pattern in fig.2.2.
- **Decreasing interactions**: Due to absorption, in practice the interactions will diminish as the fluid propagates along the cell. Provided the losses are slow enough, it will be shown in subsection 2.2.7 that the Bogoliubov frequency will slowly ramp down until some negligible value thus suppressing the output quench. As this reduction of the Bogoliubov frequency is homogeneous in $\mathbf{k}_\perp$ in virtue of eq.1.27, this will not modify the quench correlation pattern. Essentially the initial distribution is slowly "frozen" by absorption.
- **Increasing interactions**: While this situation cannot be realized with our experimental setup, it is still relevant as it is the canonical situation considered when quenches. Assuming some non-interacting system, it is often desirable to slowly ramp up the interactions to avoid exciting the system in an uncontrolled manner. In this scenario,

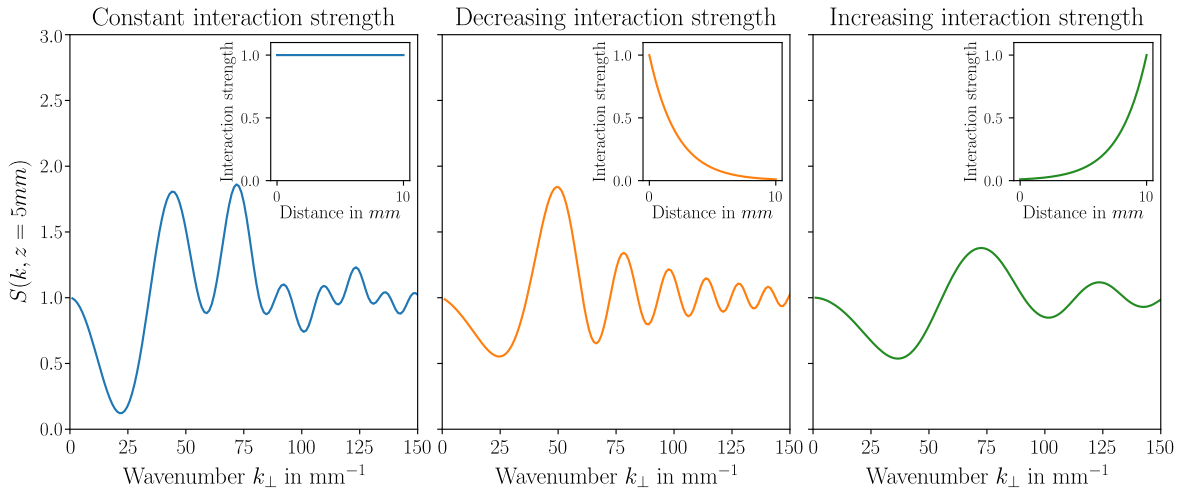

Fig. 2.2 *$S(\mathbf{k}_\perp)$ for different scenarii. In the case of constant interactions, there is a strong beating between the signals of both quenches. In the case of exponentially dampened interactions (which is the case with absorption), the signature of the second quench is strongly suppressed. Finally in the case of increasing interactions (which cannot be realized experimentally for the moment), only the second quench is visible. In all cases, the structure factor oscillates around 1 which is the value vacuum shot noise.*

the Bogoliubov frequency slowly ramps up keeping the system in its vacuum state until the quench at the output face of the cell. In the end we are left with a single set of fringes as there has been only a single quench.

It is thus clear that the evolution of the interaction strengh due to absorption is a critical element in order to accurately describe our fluid of light. In the next subsections, we will detail how we can take this into account using either analytical approximations or numerical methods.

2.2.6 Local density approximation

As explained in the last subsection, the signal in the static structure factor at the output of the cell results from the interference between created bogolons. Because we measure the fluid at the output of the cell with a camera, the system we consider is always the integrated structure factor during the exposure time. Furthermore, we'll see in the experimental results section 2.3 that we'll use a pulsed laser during the experiment. As these bogolons evolve adiabatically within the cell, it is tempting to describe the final signal as being the sum of each infinitesimal slice $\mathrm{d}\zeta$ of the pulse. Formally this means doing a **local density approximation** and equate the following integral to a sum:

$$\int_0^{L'} \mathrm{d}\zeta S(\mathbf{k}_\perp, \zeta, \tau) \approx \frac{1}{L'} \sum_\zeta S(\mathbf{k}_\perp, \zeta, \tau)\delta\zeta, \tag{2.23}$$

where L' is the length of the pulse in the ζ direction. Formally, since the equal-time commutators of the field modes defined in eq.1.17 are delta correlated, there is no "communication"

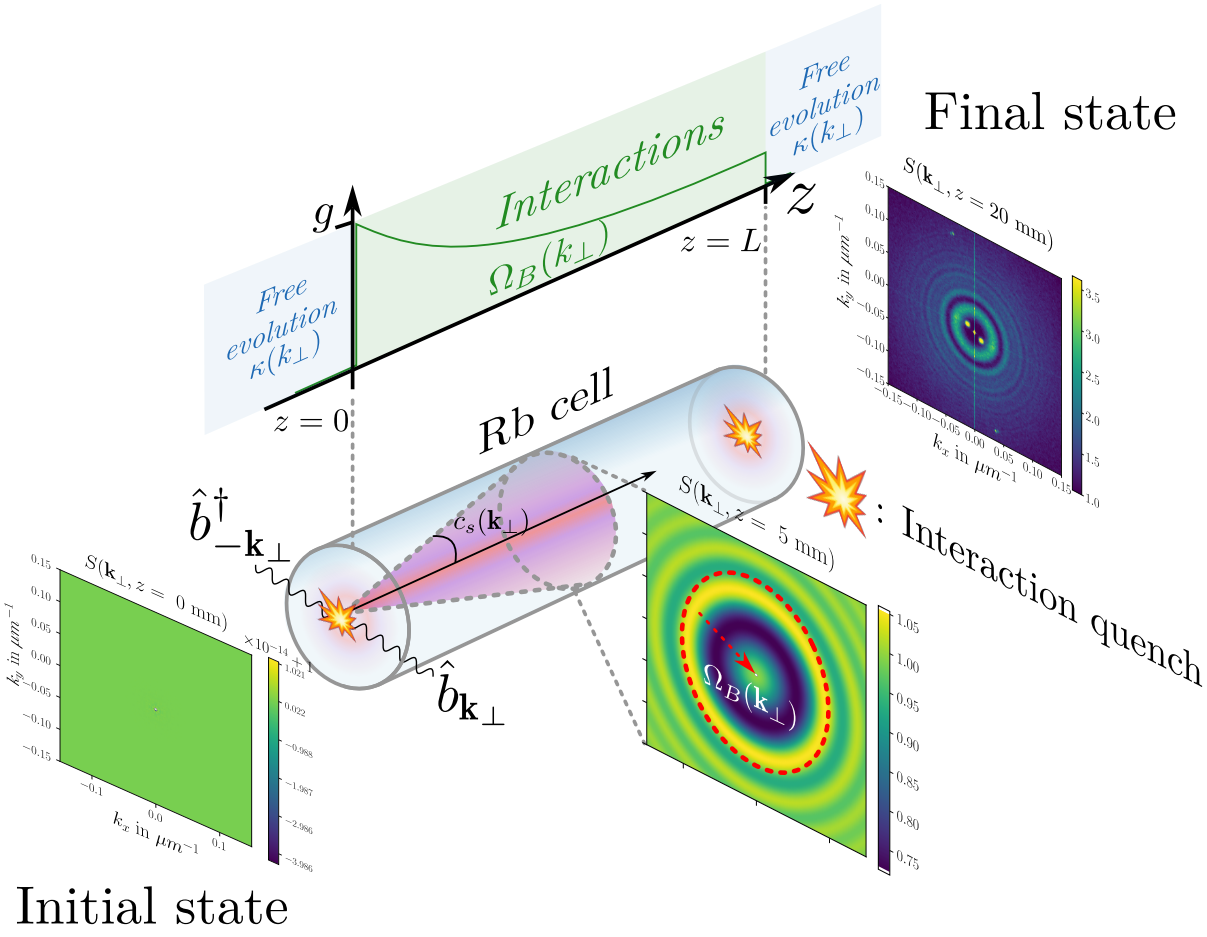

Fig. 2.3 *The physical situation of the two quenches. As the fluid traverses the cell, it undergoes a fist quench that creates a set of Bogoliubov modes $\hat{b}_{\mathbf{k}_\perp}$ highlighted with the pink cone. These modes will evolve and interfere generating an oscillary noise spectrum represented on the side of the cell. Highlighted in red is the fact that the equal-$\mathbf{k}_\perp$ peaks will shrink inwards with time driven by the Bogoliubov frequency. The final image represents the experimental spectrum obtained after the second quench and some additional free space propagation, similar to time of flight imaging [97]*

between infinitesimal slices. What happens at a position ζ only depends on the state within this plane.
Now, we would like to solve accurately the evolution of each slice $\delta\zeta$ along the cell. For this we need to question the adiabaticity hypothesis i.e the fact that the Bogoliubov dispersion follows the evolution of the mean field within eq.1.27

2.2.7 Adiabaticity criterion

In order to be quantitative on the adiabaticity approximation, one would like to derive some numerical criterion in order to quantify how much a state follows the instantaneous eigenvalues of the operator or if we need to do something more involved. To do this we follow an "Ehrenfest theorem" approach [59; 83]. Assuming some time-like evolution of a state $|\psi\rangle$ driven by some hamiltonian $\hat{H}$:

$$i\frac{\partial}{\partial z}|\psi\rangle = \hat{H}(z)\,|\psi(z)\rangle\,, \tag{2.24}$$

where $\hat{H}$ is assumed to be hermitian. We can then naturally expand our state $|\psi\rangle$ over some basis $\{|\phi_n\rangle\}_{n\in\mathbb{N}}$ of eigenvectors having a matching set of eigenvalues $\{\lambda_n\}_{n\in\mathbb{N}}$:

$$\begin{aligned} |\psi(z)\rangle &= \sum_{n\in\mathbb{N}} \alpha_n(z) e^{i\theta_n(z)}\,|\phi_n(z)\rangle \\ \theta_n(z) &= \int_0^z \mathrm{d}z'\lambda_n(z'), \end{aligned} \tag{2.25}$$

where the $\theta_n(z)$ is the integrated phase. We can then plug this into the evolution equation 2.24 in order to find the expression of the decomposition coefficients $\alpha_n(z)$:

$$\begin{aligned} \frac{\partial\alpha_n(z)}{\partial z} &= -\left\langle \phi_n(z)\middle|\frac{\partial\phi_n(z)}{\partial z}\right\rangle \alpha_n(z) + \mathcal{R}_n(z) \\ \mathcal{R}_n(z) &= -\sum_{m\neq n} \frac{\langle\phi_n(z)|\,\partial_z\hat{H}(z)\,|\phi_m(z)\rangle}{\lambda_m(z)-\lambda_n(z)} e^{i[\theta_m(z)-\theta_n(z)]}\alpha_m(z). \end{aligned} \tag{2.26}$$

$\mathcal{R}_n(z)$ is the remainder of the projection of $\partial_z\hat{H}$ the Hamiltonian derivative, between eigenvectors ϕ_m and ϕ_n. Let us precise that this remainder would be the forgotten terms during an uncareful derivation of the evolution equation. Thus, one wonders in which case this remainder could be neglected ? If this remainder is negligible, the evolution of the decomposition coefficients α_n is given by $\left\langle \phi_n(z)\middle|\frac{\partial\phi_n(z)}{\partial z}\right\rangle$, which is diagonal in the $\{|\phi_n\rangle\}_{n\in\mathbb{N}}$ basis. It is natural since this remainder quantifies the **off-diagonal terms of the derivative** of the Hamiltonian. In simpler terms, a non-adiabatic evolution will couple the instantaneous eigenvectors together. If these off-diagonal terms are zero, the Hamiltonian remains diagonal and the evolution is trivial in the eigenbasis $\{\phi_n\}_{n\in\mathbb{N}}$. Thus we have to compare these off-diagonal terms to the **smallest eigenvalue spacing** yielding the following criterion for adiabaticity:

$$\begin{gathered} \max_{z\in[0,L]}\left|\frac{\langle\phi_n(z)|\,\partial_z\hat{H}(z)\,|\phi_m(z)\rangle}{\lambda_m(z)-\lambda_n(z)}\right| \ll \min_{z\in[0,L]}|\lambda_m(z)-\lambda_n(z)| \\ \forall\ (m,n),\ m\neq n. \end{gathered} \tag{2.27}$$

As we know the evolution equation for the Bogoliubov coefficients, we can compute numerically this criterion and get quantitative information about the type of evolution by mode.

Finally, we will see how we can numerically bring everything together to solve the evolution equation for the Bogoliubov coefficients in order to get the most faithful solution in the general case where, for some modes, the evolution is not adiabatic anymore.

2.2.8 Integration of the evolution equation

In order to link experimental results and analytical calculation, a convenient numerical integration procedure needs to be developped. One goal is to isolate all contributions, enabling easy identification of the most relevant approximations.

In practice, a convenient formalism in order to do the calculations in the most general way is to introduce a particular choice of gauge. Earlier, I described the evolution of the structure factor within the adiabatic approximation assuming that the $\hat{b}_{\mathbf{k}_\perp}$ modes evolve at the Bogoliubov frequency $\Omega_B(\mathbf{k}_\perp)$. In order to consider also the non-adiabatic case, it is more convenient to deal directly with the evolution of the $u_{\mathbf{k}_\perp}$ and $v_{\mathbf{k}_\perp}$ coefficients, and choose a gauge where they vary, much like the change between Heisenberg and Schrödinger picture. In the end, it only means that the Bogoliubov coefficients will pick up the phases instead of the operators. To this end, we introduce the following new Bogoliubov coefficients $\tilde{u}_{\mathbf{k}_\perp}$ and $\tilde{v}_{\mathbf{k}_\perp}$ defined as follows:

$$i\frac{\partial}{\partial z}\begin{pmatrix}\tilde{u}_{\mathbf{k}_\perp}(z)\\ \tilde{v}_{\mathbf{k}_\perp}(z)\end{pmatrix} = \underbrace{\begin{pmatrix}\frac{i\alpha}{2}+\frac{\mathbf{k}_\perp^2}{2k_0}+k_0\Delta n(z) & k_0\Delta n(z)\\ -k_0\Delta n(z) & \frac{i\alpha}{2}-\frac{\mathbf{k}_\perp^2}{2k_0}-k_0\Delta n(z)\end{pmatrix}}_{\mathcal{A}_{\mathbf{k}_\perp}(z)-\frac{i\alpha}{2}\mathbb{I}}\begin{pmatrix}\tilde{u}_{\mathbf{k}_\perp}(z)\\ \tilde{v}_{\mathbf{k}_\perp}(z)\end{pmatrix} \tag{2.28}$$

with $\Delta n(z) = n_2 c\epsilon_0|\mathcal{E}_0|^2$. We note that it is the same equation as eq.1.27, except that the phases are now carried on the Bogoliubov coefficients themselves. The formal solution to the differential system can then be written :

$$\begin{pmatrix}\tilde{u}_{\mathbf{k}_\perp}(z)\\ \tilde{v}_{\mathbf{k}_\perp}(z)\end{pmatrix} = Z\Big[e^{-i\int_0^z \mathrm{d}z'\mathcal{A}_{\mathbf{k}_\perp}(z')-i\alpha/2}\Big]\begin{pmatrix}\tilde{u}_{\mathbf{k}_\perp}(0)\\ \tilde{v}_{\mathbf{k}_\perp}(0)\end{pmatrix} \tag{2.29}$$

where Z represents the chronological ordering. This ordering means that we should recall that this exponential should be computed in an order preserving causality. This final integral can then be evaluated by choosing a sufficiently fine discretization i.e $\delta z \ll z_{NL}$. Assuming a discretization scale δz, the integral becomes simply a product of exponentials:

$$\begin{pmatrix}\tilde{u}_{\mathbf{k}_\perp}(z)\\ \tilde{v}_{\mathbf{k}_\perp}(z)\end{pmatrix} = \prod_j e^{-\delta z(i\mathcal{A}_{\mathbf{k}_\perp}(j\delta z)-\alpha/2)}\begin{pmatrix}\tilde{u}_{\mathbf{k}_\perp}(0)\\ \tilde{v}_{\mathbf{k}_\perp}(0)\end{pmatrix} \tag{2.30}$$

Taking this into account in the expression of the field correlators, this yields the following

final expression, in its most general form:

$$\begin{aligned}&\left\langle \hat{a}^{\dagger}_{\mathbf{k}_\perp}(L)\hat{a}_{\mathbf{k}_\perp}(L)\right\rangle = -u_{\mathbf{k}_\perp}(0)v_{\mathbf{k}_\perp}(0)(1+2B(\mathbf{k}_\perp))\tilde{u}_{\mathbf{k}_\perp}(L)\tilde{v}_{\mathbf{k}_\perp}(L)+\\&|\tilde{v}_{\mathbf{k}_\perp}(L)|^2\Big[1+v^2_{\mathbf{k}_\perp}(0)(1+B(\mathbf{k}_\perp))+u^2_{\mathbf{k}_\perp}(0)B(\mathbf{k}_\perp)+D(\mathbf{k}_\perp)\Big]+\\&|\tilde{u}_{\mathbf{k}_\perp}(L)|^2\Big[v^2_{\mathbf{k}_\perp}(0)(1+B(\mathbf{k}_\perp))+u^2_{\mathbf{k}_\perp}(0)B(\mathbf{k}_\perp)+D(\mathbf{k}_\perp)\Big]\\&-u_{\mathbf{k}_\perp}(0)v_{\mathbf{k}_\perp}(0)(1+2B(\mathbf{k}_\perp))\tilde{u}^*_{\mathbf{k}_\perp}(L)\tilde{v}^*_{\mathbf{k}_\perp}(L)\end{aligned} \tag{2.31}$$

$$\begin{aligned}&\langle \hat{a}_{-\mathbf{k}_\perp}(L)\hat{a}_{\mathbf{k}_\perp}(L)\rangle = -u_{\mathbf{k}_\perp}(0)v_{\mathbf{k}_\perp}(0)(1+2B(\mathbf{k}_\perp))\tilde{u}^{*2}_{\mathbf{k}_\perp}(L)+\\&\tilde{u}^*_{\mathbf{k}_\perp}(L)\tilde{v}_{\mathbf{k}_\perp}(L)\Big[1+v^2(\mathbf{k}_\perp,0)(1+B(\mathbf{k}_\perp))+u^2(\mathbf{k}_\perp,0)B(\mathbf{k}_\perp)+D(\mathbf{k}_\perp)\Big]+\\&\tilde{u}_{\mathbf{k}_\perp}(L)\tilde{v}^*_{\mathbf{k}_\perp}(L)\Big[v^2(\mathbf{k}_\perp,0)(1+B(\mathbf{k}_\perp))+u^2(\mathbf{k}_\perp,0)B(\mathbf{k}_\perp)+D(\mathbf{k}_\perp)\Big]+\\&-u_{\mathbf{k}_\perp}(0)v_{\mathbf{k}_\perp}(0)(1+2B(\mathbf{k}_\perp))\tilde{v}^2_{\mathbf{k}_\perp}(L).\end{aligned} \tag{2.32}$$

The next section will show how we can **measure** these correlators experimentally through the measurement of the **static structure factor**.

2.3 Experimental measurement of the static structure factor

In order to probe the **static structure factor** experimentally, we aim at measuring the effect of vacuum fluctuations on the **noise spectrum** of the fluid of light. To this extent, we want the setup to stay as simple as possible in order to limit losses. The general scheme will be to:

- send light through the cell
- integrate the intensity on a camera over time
- measure the shot to shot fluctuations and compute the variance.

In order to limit losses, there should be as little optical elements between the output of the cell and the camera sensor, whose quantum efficiency is already limited. To this extent, we have to send short pulses of light in order to avoid camera saturation.

We start our experiment with a 1 cm long glass cell of ^{85}Rb heated to approximately 150°C. The experimental setup is described in fig.2.4. The laser source is a Toptica DL PRO extended cavity diode laser which allows easy laser frequency tuning and stabilization. In order to have an absolute frequency reference, we monitor the laser frequency using a Doppler free spectroscopy scheme: the saturated absorption spectroscopy or SAS highlighted in blue. In order to generate pulses of light, the beam passes in an acousto-optic modulator (AOM) in double pass configuration. This AOM is gated using an arbitrary function generator (AFG) modulating the radio frequency drive of the crystal. Pulses between 10 ms and 30 ns are generated using this method. The pulse generation part of the setup is highlighted in orange in fig.2.5. There remains the "experiment" part of the setup highlighted in green with both the cell and the imaging setup. Temperature of the cell is monitored by scanning the laser frequency over the D_2 line of Rubidium, and acquiring transmission data. A reference arm is built in Mach-Zehnder configuration (as described in chap.3) to measure the non-linear index

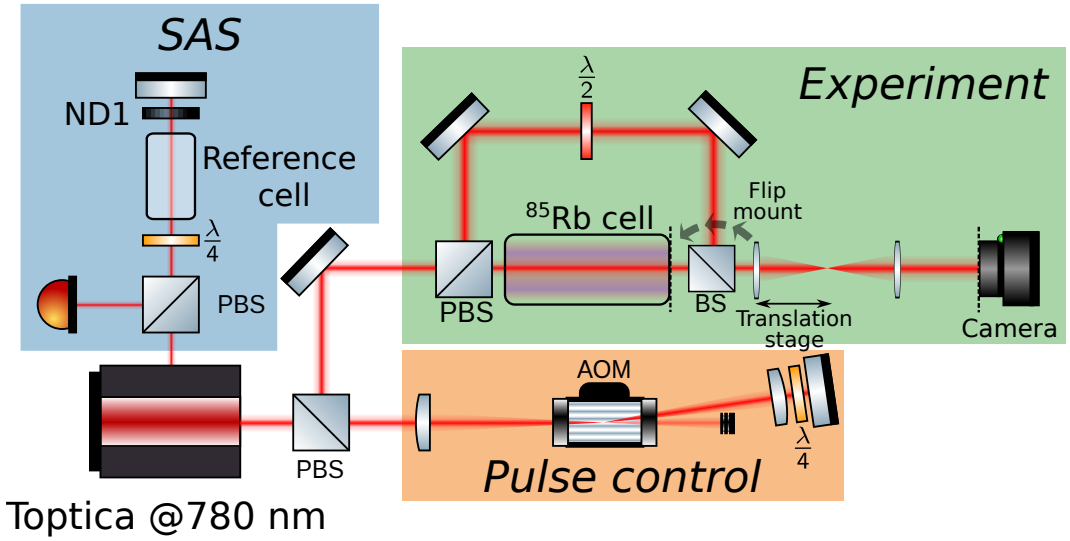

Fig. 2.4 *The different parts of the experimental setup are highlighted with the three colors. In blue, the saturated absorption spectroscopy (SAS) setup allows to monitor the laser frequency using a reference cell of naturally abundent Rubidium. In orange, the laser is pulsed using an acousto-optic modulator (AOM) in double pass configuration. In green, there is the heart of the setup with the pure ^{85}Rb cell and the imaging setup. The translation stage on the first lens of the imaging system allows to shift the imaging plane*

of refraction n_2. To avoid losses, the beam-splitter at the output of the cell is placed on a flipped mount such as to remove it when measuring $S(\mathbf{k}_\perp)$. Data acquisition is triggered by pulse generation, and a typical measurement shot will acquire 500 images. Planes at a position z after the cell between 0 and 50 mm are imaged on the camera using a $4f$ imaging system with a translation stage to shift the imaging plane.

Data processing is then as follows:

- Compute the average density $\langle\rho(\mathbf{r}_\perp)\rangle_N$
- Compute the fluctuations $\delta\rho(\mathbf{r}_\perp) = \rho(\mathbf{r}_\perp) - \langle\rho(\mathbf{r}_\perp)\rangle_N$
- Compute the fluctuations spectrum $\delta\rho(\mathbf{k}_\perp) = \mathcal{F}\left(\rho(\mathbf{r}_\perp) - \langle\rho(\mathbf{r}_\perp)\rangle_N\right)$
- Compute the variance $S(\mathbf{k}_\perp) = \frac{1}{N}\mathrm{Var}_N\left[\delta\rho(\mathbf{k}_\perp)\right]$

where the N subscript represents the averaging over the experiment realizations.

Due to the cylindrical symmetry of the system, we can improve the signal further by calculating an azimuthal average of the signal. The results are presented in fig.2.5. On the top row, we present the processed signal on a set of 500 images taken at a detuning $\Delta = -1.4$ GHz for pulses of length $\tau = 100$ ns. The temperature of Rubidium vapor is 147°C. The measured non-linear index of refraction change Δn is 8.6×10^{-6}. The optical power is

100 mW for a beam of waist w_0 of 4 mm. We observe sets of concentric rings whose contrast grows with time, and whose radii shrink with time. As explained earlier, since low $k_\perp$ modes (long wavelengths) have lower energy, large scale features take longer to develop. This is why we observe the spectra after some trivial free space evolution that allows for these low energy modes to develop. We see also two bright symetrical spots that are due to set of parasitic fringes on the imaging system. Looking at the azimuthal averages on the bottom line, we see the beating of the two quenches whose cusps allow to reconstruct the Bogoliubov frequency [97].

Another way to look at this is to convert the static structure factor into a real space density-density correlation function $g^{(2)}(\mathbf{r}, \mathbf{r}', z)$:

$$\begin{aligned} g^{(2)}(\mathbf{r}, \mathbf{r}', z) &= 1 + \int \mathrm{d}\mathbf{k} e^{i\mathbf{k}\cdot\mathbf{r}} \left[S(\mathbf{k}_\perp, z) - 1\right] \\ g^{(2)}(\mathbf{r}, \mathbf{r}', z) &= \frac{\langle \delta\hat{\rho}(\mathbf{r})\delta\hat{\rho}(\mathbf{r}')\rangle}{\rho_0^2} \end{aligned} \tag{2.33}$$

Using this identity, we can convert the curves from the second panel into the third panel of fig.2.5. In this picture, the oscillatory pattern is seen to expand with time, starting with high frequency oscillations near $\Delta r_\perp = 0$, the pattern, that slowly goes further and further inducing larger scale correlations. The frequency of the oscillations decreases, as lower frequencies take longer to appear. This is the exact reciprocal argument as the one made in the wavenumber picture. In order to model the experimental curves, we use eqs.2.21 and 2.17, and solve numerically the integral.
Starting with a pure vacuum model, we see that while the period of the oscillations matches convincingly the experimental curves, there remains a significant offset. The agreement becomes excellent however when **fitting a uniform population** of 1.34 particle per mode within the cell, in order to model at incoherent noise sources inside the cell such as spontaneous emission. This noise should originate from within the cell since the structure factor is measured to be 1 in the non-interacting case, thus confirming that the input state is indeed vacuum for all $k_\perp \neq 0$. When comparing this to the expression found in eq.2.15, this uniform population is six times higher than the one predicted by the analytical model when plugging in the experimental parameters from [97]. Furthermore, the noise spectrum from eq.2.15 is peaked at around $\mathbf{k}_\perp = 0$ from its dependence in the Bogoliubov coefficients. Comparing the 1.34 particles per mode to the typical interaction energy of the system, we can attribute an effective temperature (in terms of modes occupation) of around $2mc_s^2 \sim 30mK$ [97], which is comparable to temperatures found in cold atomic gases experiments.

We have seen that with a clean setup, it is possible to measure the fluctuations and correlations seeded by vacuum shot noise. However, in this experiment we only look at correlations on a "macroscopic" level. Indeed, we are not able to compute the noise in a single $k_\perp$ mode, and within this we are only able to measure intensity-intensity correlations. An interesting extension to get a complete picture of our experiments would be to use a homodyne detection in order to reconstruct precisely each $\hat{a}_{\mathbf{k}_\perp}$ mode, allowing to measure independently each correlator.

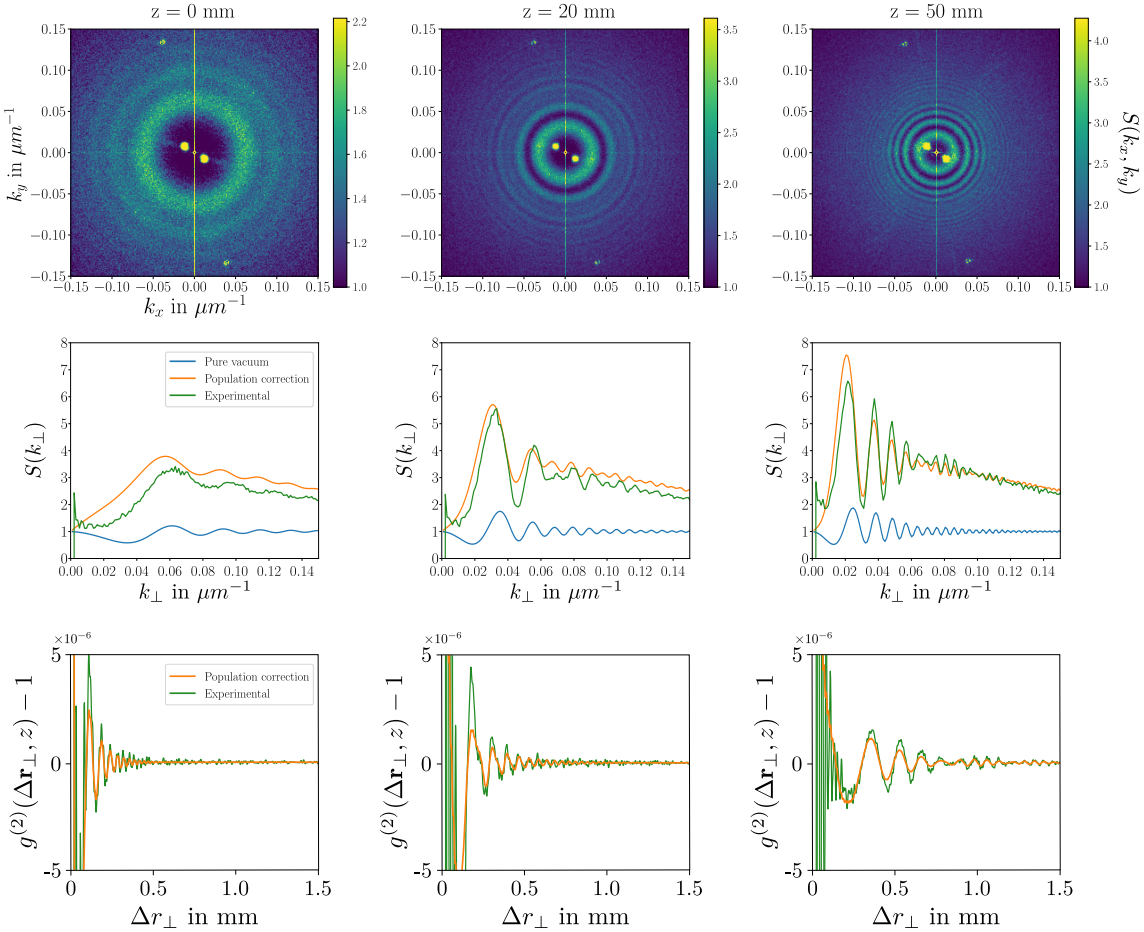

Fig. 2.5 *Experimental signal of the static structure factor for different evolution lengths after the cell. Here the z axis has its origin at the output of the cell. The laser detuning is -1.4 GHz, cell temperature is 147°C and the pulse length is 100 ns. On the bottom panel, we have azimuthal averages of the top pictures. The blue curves are the experimental signal, in blue are the analytical model described in the previous section without any added noise (pure vacuum state), and in orange with with a fitted noise value $D(\mathbf{k}_\perp)$ of 1.34 particles per mode inside the cell. The green curves are the experimental signal. On the last row, intensity correlation function extracted from the structure factor using eq.2.33*

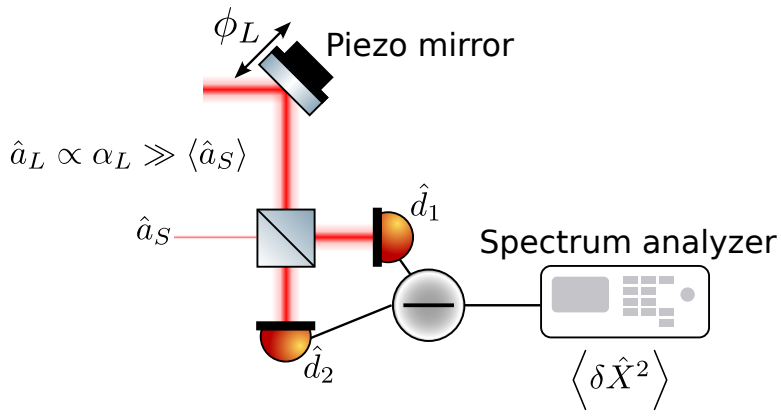

Fig. 2.6 *Canonical setup of a homodyne detection. A strong local oscillator mode $\hat{a}_L$ interferes with a weak signal mode $\hat{a}_S$ on a beam splitter. Two detectors are placed at each port of the beam splitter to record the outcoming modes $\hat{d}_1$ and $\hat{d}_2$. The detectors are coupled with a difference signal circuit. The difference is then finally sent to a spectrum analyzer that allows to measure the variance of the input signal.*

2.4 Homodyne detection

In order to measure the weak vacuum fluctuations, one would want a way to non perturbatively amplify the signal such as to bring the noise spectrum to a measurable level. This problem is a classical problem of signal processing and can be achieved using the general technique of **heterodyne** or **homodyne detection**. Let us compute the result of the aforementioned interfererence process on the field modes.

2.4.1 Balanced homodyne detection

The classical homodyne detection scheme considers the following two modes: the **signal** $\hat{a}_S$ and **local oscillator** (LO) $\hat{a}_L$ are sent on a perfect beam-splitter. Two detector, whose input modes are written $\hat{d}_1$ and $\hat{d}_2$, are placed at the outputs of the beam-splitter. Using classical input-output relations [13]:

$$\begin{pmatrix} \hat{d}_1(\mathbf{r},t) \\ \hat{d}_2(\mathbf{r},t) \end{pmatrix} = \begin{pmatrix} t & r \\ r & t \end{pmatrix} \begin{pmatrix} \hat{a}_S(\mathbf{r},t) \\ \hat{a}_L(\mathbf{r},t) \end{pmatrix} \tag{2.34}$$

where t,r are the transmission and reflection coefficients from the beam-splitter. In the case of the **balanced** (meaning a 50/50 splitting ratio) homodyne detection ($r = i/\sqrt{2}$ $t = 1/\sqrt{2}$), one can readily obtain the modes on each of the two detectors:

$$\begin{aligned} \hat{d}_1(\mathbf{r},t) &= \frac{1}{\sqrt{2}}\Big[\hat{a}_S(\mathbf{r},t) + i\hat{a}_L(\mathbf{r},t)\Big] \\ \hat{d}_2(\mathbf{r},t) &= \frac{1}{\sqrt{2}}\Big[i\hat{a}_S(\mathbf{r},t) + \hat{a}_L(\mathbf{r},t)\Big]. \end{aligned} \tag{2.35}$$

Note that we have assumed here a "perfect" beam splitter whose reflection and transmission coefficients r and t **do not depend** on position or time. In real life, this is obviously false since the splitting ratio of an ordinary glass beam-splitter cube strongly depends on the polarization and on the incident angle. Since the detector is actually measuring the intensity of the field, we are interested in the the averages $\left\langle \hat{d}_1^\dagger \hat{d}_1 \right\rangle$ and $\left\langle \hat{d}_2^\dagger \hat{d}_2 \right\rangle$:

$$\begin{aligned} \hat{d}_1^\dagger \hat{d}_1 &= \frac{1}{2}\left[\hat{a}_S^\dagger(\mathbf{r},t)\hat{a}_S(\mathbf{r},t) + \hat{a}_L^\dagger(\mathbf{r},t)\hat{a}_L(\mathbf{r},t) + i\left(\hat{a}_S^\dagger(\mathbf{r},t)\hat{a}_L(\mathbf{r},t) - \hat{a}_L^\dagger(\mathbf{r},t)\hat{a}_S(\mathbf{r},t)\right)\right] \\ \hat{d}_2^\dagger \hat{d}_2 &= \frac{1}{2}\left[\hat{a}_S^\dagger(\mathbf{r},t)\hat{a}_S(\mathbf{r},t) + \hat{a}_L^\dagger(\mathbf{r},t)\hat{a}_L(\mathbf{r},t) + i\left(\hat{a}_L^\dagger(\mathbf{r},t)\hat{a}_S(\mathbf{r},t) - \hat{a}_S^\dagger(\mathbf{r},t)\hat{a}_L(\mathbf{r},t)\right)\right] \end{aligned} \tag{2.36}$$

we then model the detection process on the photodiode as follows:

$$d_1 = \eta \int_0^T \mathrm{d}t \int_S \mathrm{d}^2\mathbf{r} \ \left|\left\langle \hat{d}_1^\dagger(\mathbf{r},t)\hat{d}_1(\mathbf{r},t)\right\rangle\right|, \tag{2.37}$$

where η is some detection efficiency parameter, S is the detector surface and T is the integration time. Looking at eq.2.36, we recognize the familiar form of an interference signal where the first two terms correspond to the intensity in the signal and local oscillator fields, and the last term is the interference term. In all generality, this interference term will be proportional to $e^{i\mathbf{k}\cdot\mathbf{r}-i\omega t}$ if $\mathbf{k}$ is the wavevector of the LO relative to the signal and ω is the difference in frequency between the signal and LO fields. It becomes then clear that the only spatial and temporal mode that is not averaged out in the crossed interference term is the one that have the same frequency ω and wavevector $\mathbf{k}$ between the signal and the local oscillator. This means that the measurement **projects** the mode of the signal onto the local oscillator mode. We can thus identify equivalently the signal modes with the variables $\mathbf{k}$ and ω. It then follows that the LO spatial mode should be tailored to match the desired signal mode, and that the norm of this projection will be limited by this **mode matching**. We can then anticipate that the information will be carried in the interference term. In order to extract the interference term, we simply take the difference of the two detectors signal:

$$\hat{D}(\mathbf{k},\omega) = \hat{d}_1^\dagger(\mathbf{k},\omega)\hat{d}_1(\mathbf{k},\omega) - \hat{d}_2^\dagger(\mathbf{k},\omega)\hat{d}_2(\mathbf{k},\omega) = i\Big[\hat{a}_S^\dagger(\mathbf{k},\omega)\hat{a}_L(\mathbf{k},\omega) - \hat{a}_L^\dagger(\mathbf{k},\omega)\hat{a}_S(\mathbf{k},\omega)\Big]. \tag{2.38}$$

The scheme is powerful in the case where the local oscillator is **much stronger** than the signal. In the strong local oscillator approximation, we can express $\hat{a}_L$ as a classical field. Assumuing a **plane wave** local oscillator, we can write $\alpha_L = |\alpha_L|e^{i\phi_L}$. ϕ_L is the local oscillator phase with respect to the signal, an important parameter that is varied in the experiment. The difference signal then reads:

$$\hat{D}(\mathbf{k},\omega) = i|\alpha_L|\Big[e^{i\phi_L}\hat{a}_S^\dagger(\mathbf{k},\omega) - e^{-i\phi_L}\hat{a}_S(\mathbf{k},\omega)\Big]. \tag{2.39}$$

Changing this phase will change the **quadrature** on which the signal is projected [13; 40]. Now this term admits two limiting cases: in the case where $\phi_L = 0$, and in the case where $\phi_L = \pi/2$. In these two limits we can identify the two conjugated quadratures of the difference signal [13; 40]:

$$\begin{aligned} \hat{D}_0 &= i|\alpha_L|\left[\hat{a}_S^\dagger(\mathbf{k},\omega) - \hat{a}_S(\mathbf{k},\omega)\right] \\ \hat{D}_{\pi/2} &= -|\alpha_L|\left[\hat{a}_S^\dagger(\mathbf{k},\omega) + \hat{a}_S(\mathbf{k},\omega)\right]. \end{aligned} \tag{2.40}$$

These conjugated quadratures allow to decompose any state of the field on this basis. Their expression can be interpreted as the **density** and **phase** of the field as is presented further in eq.2.47. Measuring this difference signal with a spectrum analyzer [13] will give access to the variance of this difference signal for frequencies within the bandwidth of the analyzer. We can the directly deduce that the variance of the difference signal operator will read:

$$\begin{aligned}\mathrm{Var}(\hat{D}) &= \left\langle |\hat{D}|^2 - \left\langle \hat{D} \right\rangle^2 \right\rangle \\ &= |\alpha_L|^2 \left\langle (e^{-i\phi_L}\hat{a}_S(\mathbf{k},\omega) - e^{i\phi_L}\hat{a}_S^\dagger(\mathbf{k},\omega))(e^{i\phi_L}\hat{a}_S^\dagger(\mathbf{k},\omega) - e^{-i\phi_L}\hat{a}_S(\mathbf{k},\omega)) \right\rangle \\ &= |\alpha_L|^2 \left\langle 1 + 2\hat{a}_S^\dagger(\mathbf{k},\omega)\hat{a}_S(\mathbf{k},\omega) + 2\mathrm{Im}(e^{i2\phi_L}\hat{a}_S(\mathbf{k},\omega)\hat{a}_S(\mathbf{k},\omega)) \right\rangle\end{aligned} \tag{2.41}$$

We find that we can directly recover the population in each $(\mathbf{k},\omega)$ signal mode by taking the sum of the variance between the two quadratures:

$$\mathrm{Var}(D_{\pi/2}) + \mathrm{Var}(D_0) = 2|\alpha_L|^2 \left(1 + 2N(\mathbf{k},\omega)\right), \tag{2.42}$$

where $\mathrm{N}(\mathbf{k},\omega) = \left\langle \hat{a}_S^\dagger(\mathbf{k},\omega)\hat{a}_S(\mathbf{k},\omega) \right\rangle$ is the population of the $(\mathbf{k},\omega)$ signal mode as defined in eq.2.49.

An advantage is that this measurement technique is based on photodiodes, which can have bandwidth reaching several GHz. This technique gives a direct access to the population of Bogoliubov excitations with both a spatial and temporal resolution. Furthermore, looking at the difference signal allows to reject any common mode noise. For this rejection to work at its full potential however, we obviously need the photodiodes to be calibrated accurately in order to have matched responsivity and electronic noise. Another crucial point is that by **changing the frequency** of the local oscillator and going to a heterodyne detection scheme, one can probe the population of excitations in the **longitudinal dimension**. Finally, compared to the previous measurement method that rely on camera images, this alleviates the limitation in resolution at **low wavevectors $\mathbf{k}_\perp$**: the resolution in $\mathbf{k}_\perp$ here is limited by the smallest possible increment achievable in angle between the LO and signal arms. This is detailed in the experimental setup section.

2.4.2 Comparison to the static structure factor

Following the derivations made in the previous section in eq.2.31, the state of the field at a position $z > L$ after the cell (L is the length of the cell, and the origin of z is taken at the front face of the cell) [36; 59; 97] is:

$$\begin{aligned}\hat{a}_S(\mathbf{k},z) &= \left[U_\mathbf{k}\hat{a}_S(\mathbf{k},0) + V_\mathbf{k}^*\hat{a}_S^\dagger(-\mathbf{k},0)\right]e^{-i\frac{\mathbf{k}^2}{2k_0}(z-L)} \\ U_\mathbf{k} &= \tilde{u}_\mathbf{k}(L)u_\mathbf{k}(0) - \tilde{v}_\mathbf{k}^*(L)v_\mathbf{k}(0) \\ V_\mathbf{k}^* &= \tilde{v}_\mathbf{k}^*(L)u_\mathbf{k}(0) - \tilde{u}_\mathbf{k}(L)v_\mathbf{k}(0),\end{aligned} \tag{2.43}$$

where the $u_\mathbf{k}(z)$ and $v_\mathbf{k}(z)$ coefficients are the Bogoliubov amplitudes defined in eq.1.28 that contain a dephasing term due to the cell, and absorption. From this we can then easily deduce the final population from the initial populations:

$$N(\mathbf{k},z) = |U_\mathbf{k}|^2 N(\mathbf{k},0) + |V_\mathbf{k}|^2(1 + N(-\mathbf{k},0)). \tag{2.44}$$

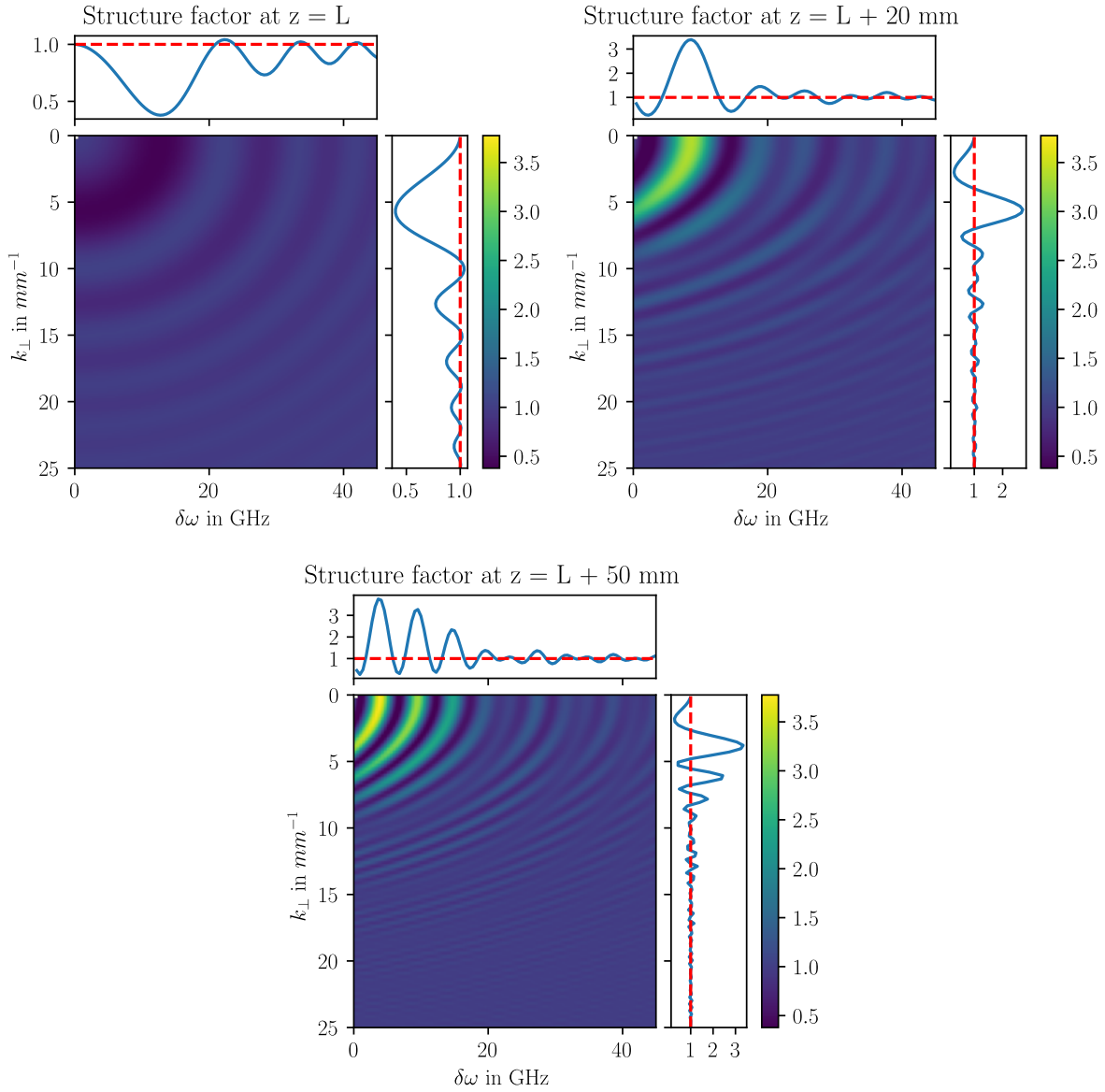

Fig. 2.7 *Static structure factor in both the spatial and temporal dimensions. The quenches produce a pattern in both dimensions whose frequency depend on the interaction strength or the GVD. The dashed line in red represents the vacuum level of the static structure factor $S(\mathbf{k}_\perp, \omega, z) = 1$. The simulated signal is plotted for a 10 cm long cell, with typical values of $\Delta n = 10^{-5}$, $v_g = 0.5c$ and the GVD $D_0 = -10^9$ fs^2/cm.*

As explained previously, this means that the quench will produce a **non-trivial** distribution of excitations [91] even when starting from pure vacuum where $N(\mathbf{k}, 0) = 0$.

Now, thanks to the temporal resolution of the homodyne detection, one can access the **three components** of the wave vector: the paraxial wave vector (k_x, k_y) by changing the angle of the local oscillator, and the longitudinal wave vector k_z by changing the LO frequency ω. To study the expected signal, it is convenient to stay in the uncompressed retarded frame moving at the group velocity. In this frame, we recall that the evolution of the Bogoliubov coefficients is given by the following equation:

$$i\frac{\partial}{\partial z}\begin{pmatrix} u_{\mathbf{k}}(z) \\ v_{\mathbf{k}}(z) \end{pmatrix} = \underbrace{\begin{pmatrix} \frac{i\alpha}{2} + \frac{\mathbf{k}_\perp^2}{2k_0} + \frac{D_0}{2}\omega^2 + k_0\Delta n & k_0\Delta n \\ -k_0\Delta n & \frac{i\alpha}{2} - \frac{\mathbf{k}_\perp^2}{2k_0} + \frac{D_0}{2}\omega^2 - k_0\Delta n \end{pmatrix}}_{\mathcal{K}(z)} \begin{pmatrix} u_{\mathbf{k}}(z) \\ v_{\mathbf{k}}(z) \end{pmatrix}. \quad (2.45)$$

We have split here explicitly the **paraxial** and **temporal** dependences. In this frame of reference, we recover the anisotropy of the mass term through two quadratic terms, one in $\mathbf{k}_\perp$, and another one in ω. As the light enters the cell, it does not only induce a quench of the non-linear index difference Δn but also a quench of the GVD. While this leads to the same phenomenology of oscillatory patterns of correlations, the physical interpretation of the origin of these patterns is quite different. In the transverse plane, we have an interaction strength quench, which is a classical scenario. In the temporal dimension, we have an **effective mass quench**. Exploring this as a testbed for field theories in the context of analogue gravity has been proposed and looks to be an exciting future for these measurements [44; 48]. We can compute the expected signal using the numerical integration eq.2.30 presented in the last section and obtain the fig.2.7. In the panels, we find the familiar oscillatory pattern in the spatial frequencies, as highlighted by the right insets. More surprising however is to find the **exact same structure in the longitudinal dimension**. We see that the total pattern in both dimension is the complex interference of the correlation patterns in both time and space induced by the quenches. The complementary pattern can be found in the populations. If we study the evolution of the $|U|^2$ and $|V|^2$ coefficients defined in eq.2.43, we find a similar oscillary pattern in both time and space, as shown in fig.2.8. Since after the cell the evolution is in vacuum, these populations are frozen after $z = L$. We thus expect the homodyne signal to reflect this evolution: when scanning the frequency of the local oscillator with respect to the fluid (i.e sweeping $\delta\omega$ in figs.2.7,2.8), we scan the different corresponding ω modes of the dispersion. Since the popultations of excitation are created from vacuum, this corresponds to observing a signal of anti-squeezing following the pattern of the top insets of fig.2.8. Interestingly, we can convert the typical pulsations at which this population is visible in the time domain ($\approx 50\ 2\pi\times$ GHz) back to longitudinal wavenumbers and realize that this corresponds to density fluctuations whose wavenumber is **at the largest** 3.3 m^{-1}. This is three orders of magnitude smaller than the typical wavenumbers $\mathbf{k}_\perp$ in the paraxial plane. This corresponds to a wavelength of 30 cm, which is much larger than the cell length, furthermore, the typical value of GVD attainable in hot Rubidium vapors used in this example is 4 orders of magnitude larger than typical values for silica fibers at the wavelength where the GVD is the most anomalous. This means that **even for large values of the GVD**, the dynamics in the longitudinal dimension is **almost negligible** if we assume an initial plane wave state. This is consistent with the assumption that we consider the system as having a two-dimensional dynamics. The advantage of the homodyne detection is that the sensitivity allows to still

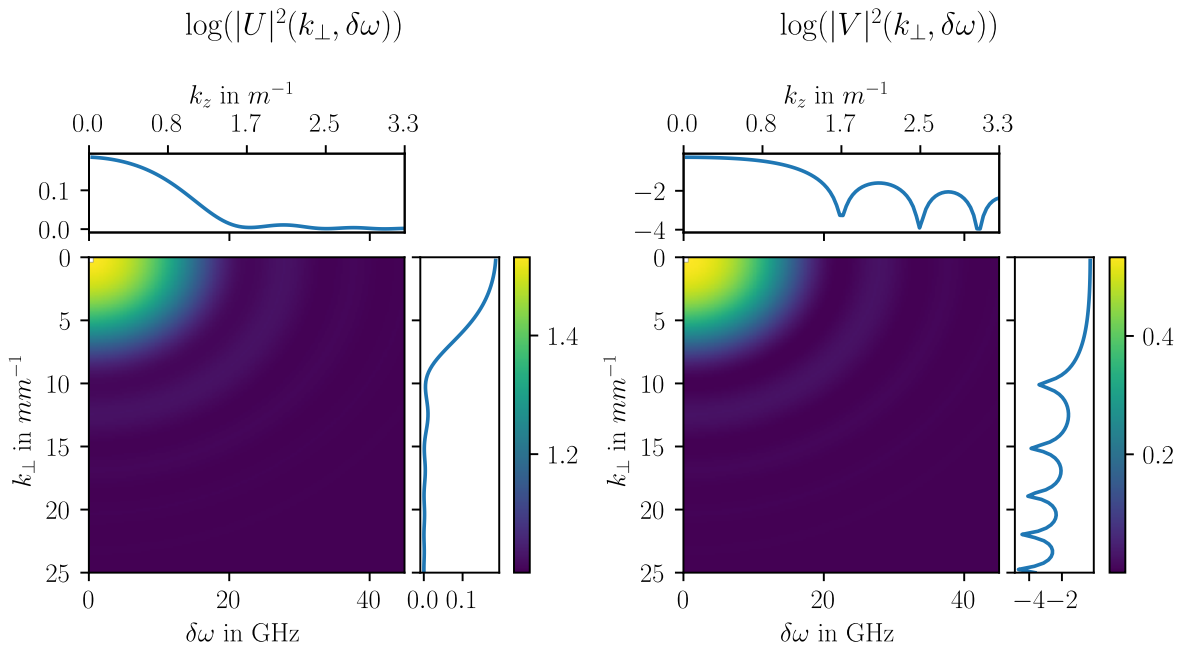

Fig. 2.8 $|U|^2$ and $|V|^2$ *coefficients of eq.2.43 in both the spatial and temporal dimensions. The quenches produce a pattern in both dimensions whose frequency depend on the interaction strength or the GVD. In the case of an initial plane wave state at* $k = 0$, $|V|^2(k, \omega) = N(k, \omega)$, *giving a prediction of the expected homodyne signal. The simulated signal is plotted for a 10 cm long cell, with typical values of* $\Delta n = 10^{-5}$, $v_g = 0.5c$ *and the GVD* $D_0 = -10^9$ fs^2/cm. *In the top insets, the longitudinal wavenumber* k_z *corresponding to the frequency* ω *is plotted.*

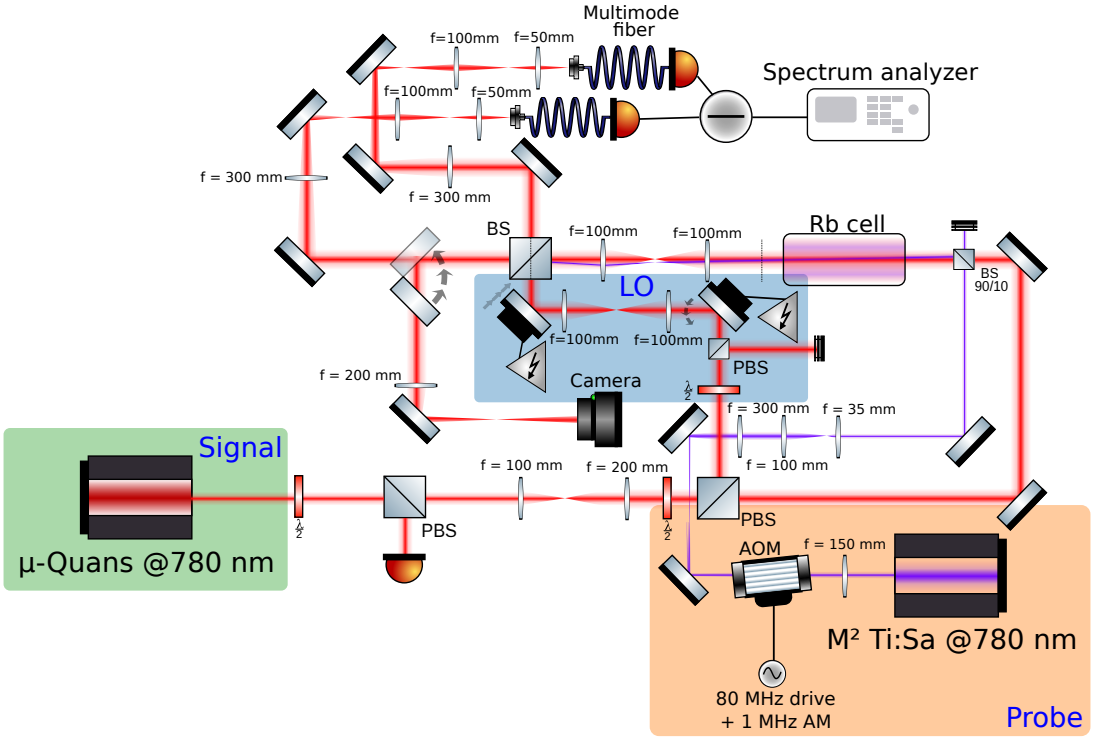

Fig. 2.9 *Experimental setup for the homodyne detection measurement. The different main parts are highlighted in color. In green, the main fluid beam, that is later split between signal and local oscillator in blue. The local oscillator can be swept in phase and angle using a piezo mounted mirror, and piezo stepping screws. This allows to select the* $\mathbf{k}_\perp$ *mode that is probed, and the quadrature that is measured. Finally in orange, an additional low noise Ti-Sa laser is used to seed fluctuations to make alignment easier and probe specific modes. This probe laser is frequency shifted with an AOM in order to be able to modulate the probe in both amplitude and frequency.*

observe this dynamics. We will now see how we can devise an experimental arrangement in order to put this homodyne detection to the test.

2.4.3 Experimental setup

In order to set up a homodyne detection, we build around the canonical interference setup around a non polarizing beam-splitter. We add $\frac{\lambda}{2}$ waveplates to ensure a 50/50 splitting ratio: even though the non-polarizing beam splitters are supposed to be polarization insensitive, they actually are, even though this dependence is weak. The experimental setup is represented in fig.2.6. In order to achieve a spatially resolved operation, we want to scan the local oscillator angle relative to the signal arm. This means that the signal and local oscillator beams need to be imaged at the inside of the beam splitter. Obviously, they will need to also be imaged on the photodiodes. Thus, we build the setup "in reverse" and start with the photodiodes

and mount the whole setup starting with the detection. Because we want to build a balanced detection, as mentioned before, we need fast balanced diodes whose electronic wiring cancels common mode. For this we use a Thorlabs PDB450A-AC balanced diode with switchable gain. As its ports are fibered, we use two wide numerical aperture fiber coupler, with multimode fibers to guide the light to the diodes. We use this unconventional setup as traditionnaly, homodyne detections are not spatially resolved. Because mode-matching between the signal and the local oscillator is paramount, this part of the detection is crucial (and will actually be its eventual downfall).
This then leads us to the LO arm. We want to both scan the phase, and scan the angle of the beam. To scan the phase, we use a piezo mounted mirror that will be driven at around 1kHz in order to scan the phase faster than typical experimental noise, but still low enough that we do not risk damaging the epoxy resin holding the mirror to the piezo. The angle of the LO is scanned thanks to Thorlabs piezo actuator screws PIA13. This provides virtually continuous adjustment range of $\mathbf{k}_\perp$, and allows to reach **low values** of $\mathbf{k}_\perp$ below 10 m^{-1}. This is 50 times lower than the minimal resolution allowed by a typical camera with a $1\times$ magnification whose minimal wavenumber resolvable is limited by the sensor size: one cannot resolve a wavelength larger than the sensor. As we do not want the position of the LO beam to change when sweeping the angle, we need to image the surface of the mirror onto the center of the beam splitter. We can then take care of the actual ^{87}Rb cell. We use a 10 cm long pure ^{87}Rb cell, and image the output of the cell on the same beam splitter. In order to monitor Δn, we use the LO arm, and a camera imaging the beam-splitter, using a flip mirror in order to minimize losses when running measurements. This camera is also used to monitor the angle between LO and signal, as well as the fringes contrast, a critical observable to asses mode-matching between signal and local oscillator.

Before measuring vacuum fluctuations, it is safe to start with weak classical signals. To this end, we also add a third beam: the probe beam. This beam is used to induce controlled fluctuations in the fluid, modulated in time in order to easily identify the fluctuations at the output of the cell. As we want to ultimately measure noise that is seeded by the purest possible fluctuation (a single $\mathbf{k}_\perp$ and ω), we want a low-noise laser. For this we use a M^2 Ti:Sa Solstis laser. Both lasers frequencies are controlled using saturated absorption spectroscopy (SAS). In order to be able to modulate the probe laser in intensity, we use a single-pass AOM setup allowing modulation frequencies up to several MHz (far away from any technical noise of the laser).

Finally analysis of the diode signal is carried out using the three outputs of the diode: each individual DC coupled diode outputs is sent to a Rigol MSO7024 oscilloscope, while the AC difference signal is sent to an Agilent E4411B spectrum analyzer. We chose this spectrum analyzer because of its bandwidth (1.5 GHz) and high sensitivity (-166 dBm). We want high sensitivity in order to measure the weak signal from the diodes, and high bandwidth because the temporal pattern in the $S(\mathbf{k}_\perp, \omega)$ / $N(\mathbf{k}_\perp, \omega)$ signal typically ranges over several tens of GHz as shown in figs.2.7, 2.8.

2.4.4 Results

Realization of this spatially resolved homodyne detection proved to be extremely challenging. I will detail in this section the different pitfalls that prevented me to measure anything more than shot noise:

- **Mode matching**: the critical parameter of the homodyne detection in order for the common mode rejection to work (at the optical level) is **mode matching**. This means that contrast of at least 98% should be reached before attempting any measurement [13]. For this, both LO and signal beam should have the exact same profile. While this requirement can be satisfied (albeit tediously) if the beams are fixed, this becomes difficult when attempting this while scanning one of the arms angle. Furthermmore, in order to keep maximal noise rejection, both arms should have as little distance difference as possible. This is why the setup comprised of equal length arms after the beam splitter where the signal and LO interfere, thus making it quite challenging to bring light to the photodiodes. Finally, due to the non-linearity, the signal beam will undergo nonlinear dephasing. In order to maintain good contrast, this dephasing needs to be applied on the LO as well, as well as any possible beam enlargment due to self defocusing.

- **Bandwidth**: From the previous calculations we have seen that the oscillations in time domain span over tens of GHz for typical nonlinear index variation Δn values. This means that in order to resolve these oscillations, we both need very high bandwidth photodiodes, as well as a high bandwidth spectrum analyzer. Even if the beatnote between LO and signal can be brought back to lower frequencies using an additional amplitude modulation, these bandwidth constrains are paramount.

Having established these shortcomings, I will now present an updated detection setup that could allow (at least partially) to resolve them.

The proposed modifications are presented in the fig.2.10. In order to reach better mode matching, we propose to simplify the detection in order to reduce the path length between the recombination cube and the photodiodes. To make alignment easier, we switch out the Thorlabs balanced diodes with a custom set of balanced diodes mounted at the corner of a right angle housing. We image the beams directly on the diodes, using high numerical aperture aspheric lenses (like fiber coupling lenses for instance). This allows to reach much tighter spot sizes, and thus ensuring that the spots fit within the active area of the diodes. In addition to this, removing the multimode fibers allows to remove the angular dependance of the coupling. The LO arm is fitted with a spatial light modulator (SLM) in order to correct the phase of the beam.

Now, this future setup could prove essential to measure **beyond mean-field effects** thanks to the **low-k resolution**. I will now present some recent theoretical results providing clear indications of where to look for signs of quantum effects that lie beyon the Bogoliubov theory presented in the first chapter.

2.5 Outlook : beyond mean-field effects

Up until this point, the attentive reader will note that the Bogoliubov theory presented in chap.1 and the calculations presented in this chapter only include effects due to the **mean-field**

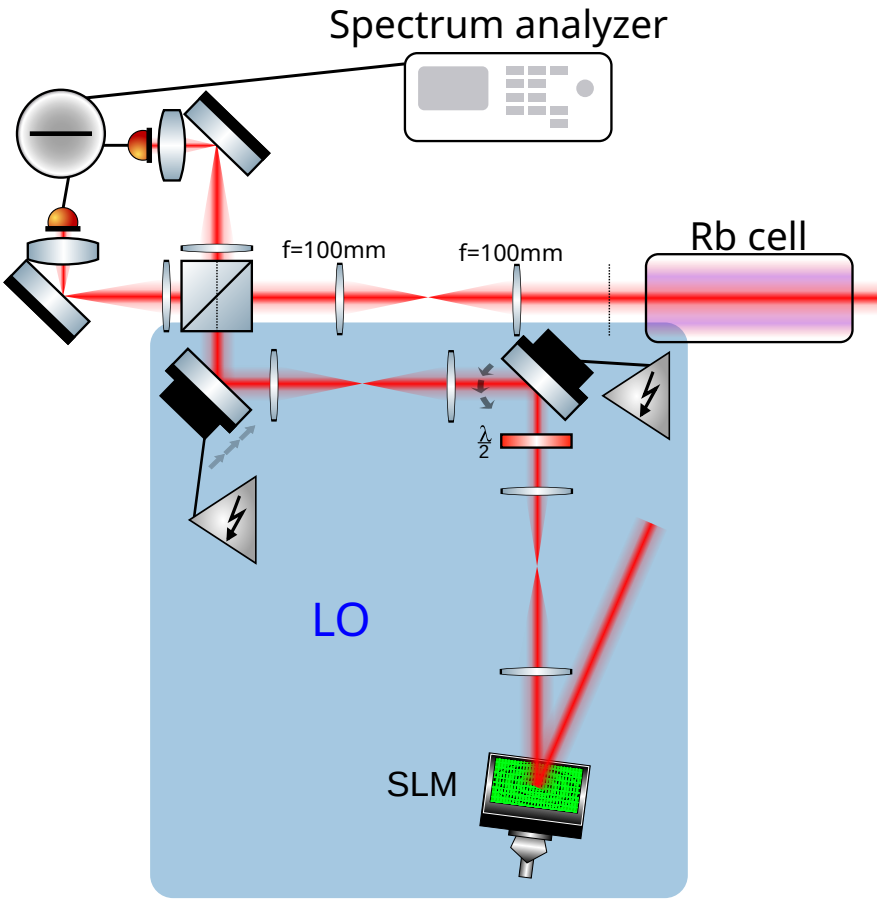

Fig. 2.10 *An updated setup in order to solve the issues encountered in the experimental realization of a spatially resolved homodyne detection. The LO arm phase can be tuned with a SLM. The detection arms after the beam-splitter are shortened and simplified by removing the fiber couplers. The diode arrangement is changed to a right angle corner to facilitate alignment.*

$\mathcal{E}_0$ of the fluid. Most of these effects can be well understood with a classical field theory. We did not describe any effect linked to the interactions between excitations or between vacuum fluctuations. In this section, I will now present an outlook towards quantum effects that manifest when considering higher order terms of the mean-field theory i.e beyond the Bogoliubov theory.

2.5.1 Kinetic equation

Recently, a more detailed picture going beyond a free particle theory describing the quench experiments has been developped by Clément Duval and Nicolas Cherroret in [29]. As we have already seen previously, the study of the kinetic equations for the correlators is of particular interest in the context of thermalization and response to quenches as it describes the structure of the system as time goes. We need these equations in order to describe the asymptotic behavior of the system as it relaxes towards equilibrium after a quench. The main idea is the following: within the Bogoliubov approximation presented in chap.1, the correlators of the bogolons in eq.2.8 evolve harmonically within the medium, and more specifically the populations **do not evolve** a part from an exponential damping due to the exponential damping of the mean field. However, if we consider inter-excitations interactions i.e the higher order terms in eq. 1.25, the kinetic equations for the correlators will change.

Let us go back to the Hamiltonian of a **2D** Bose gas in density-phase representation. If the field operator for the gas is $\hat{\psi}$, we can use the Madelung transform to represent it as a density and phase fields: $\hat{\psi} = \hat{\rho}e^{i\hat{\phi}}$. We can then write the Hamiltonian as follows:

$$\hat{H} = \hbar \int_{\mathbf{r}} \mathrm{d}r \left[\frac{\rho_0}{2m}(\nabla\hat{\phi})^2 + \frac{g}{2}(\delta\hat{\rho})^2 + \frac{1}{8m\rho_0}(\nabla\delta\hat{\rho})^2 + \frac{1}{2m}(\nabla\hat{\phi})\delta\hat{\rho}(\nabla\hat{\phi}) \right]. \tag{2.46}$$

Here we have already expanded the density operator in mean field ρ_0 and fluctuations $\delta\hat{\rho}$. The phase operator cannot be expanded this way since **phase fluctuations can be very large** especially close to phase transitions [83]. We can then introduce the familiar Bogoliubov operators in order to diagonalize the quadratic part of the Hamiltonian. In the "atomic" language within the hydrodynamic formulation, the Bogoliubov operators write:

$$\begin{aligned} \delta\hat{\rho}_{\mathbf{q}} &= -\sqrt{\frac{\Omega_B(q)}{\kappa(q)}} \left(\hat{b}^\dagger_{\mathbf{q}} + \hat{b}_{-\mathbf{q}} \right) \\ \hat{\phi}_{\mathbf{q}} &= \frac{i}{2}\sqrt{\frac{\kappa(q)}{\Omega_B(q)}} \left(\hat{b}^\dagger_{\mathbf{q}} - \hat{b}_{-\mathbf{q}} \right). \end{aligned} \tag{2.47}$$

We have written directly the operators in momentum space where q is the quasi-momentum of the mode, $\Omega_B(q)$ is the Bogoliubov dispersion defined in eq.1.31. and $\kappa(q) = \frac{q^2}{2m}$ is the kinetic dispersion. Having defined these operators, one can rewrite the Hamiltonian in momentum space in the bogolon basis under the following form:

$$\hat{H} = \underbrace{\hbar \int \frac{\mathrm{d}\mathbf{q}}{(2\pi)^2\rho_0} \Omega_B(q) \left(\hat{b}^\dagger_q \hat{b}_q + \frac{1}{2} \right)}_{\hat{H}_0} + \underbrace{\hbar \int \frac{\mathrm{d}\mathbf{p}\mathrm{d}\mathbf{q}}{(2\pi)^4\rho_0^2} \Lambda_{\mathbf{p},\mathbf{q}} \left(\hat{b}_{\mathbf{p}} \hat{b}_{\mathbf{q}} \hat{b}^\dagger_{\mathbf{p}+\mathbf{q}} + \mathrm{H.c} \right)}_{\hat{H}_{int}}. \tag{2.48}$$

Here, the Hamiltonian consists of two parts: the quadratic Hamiltonian $\hat{H}_0$ which is diagonalized by the Bogoliubov transform (by design), and the cubic interaction term $\hat{H}_{int}$ which contains three phonon scattering processes, with momentum conservation. At low energy i.e $q \ll \frac{1}{\xi}$, the vertex function writes $\Lambda_{\mathbf{p},\mathbf{q}} = \frac{3}{4m}\sqrt{\frac{g\rho_0}{2c_s}}\sqrt{|\mathbf{p}||\mathbf{q}||\mathbf{p}+\mathbf{q}|}$. Let us comment a bit the interaction term. In two dimensions, there is a range of momenta p and q for which $\Omega_B(p+q) = \Omega_B(p) + \Omega_B(q)$ i.e the scattering process is **resonant**. It can be shown that these resonant processes are dominant at low energy [29]. We can then define the correlators we want to study:

$$\begin{aligned} N_{\mathbf{q}}(\tau) &= \left\langle \hat{b}(\tau)^\dagger_{\mathbf{q}} \hat{b}(\tau)_{\mathbf{q}} \right\rangle \\ C_{\mathbf{q}}(\tau) &= \left| \left\langle \hat{b}(\tau)_{\mathbf{q}} \hat{b}(\tau)_{-\mathbf{q}} \right\rangle \right| \end{aligned} \tag{2.49}$$

where we have explicited the time dependance τ. As mentioned before, we see again that ignoring the interaction term $\hat{H}_{int}$, these correlators evolve only harmonically driven by the Bogoliubov dispersion Ω_B. Obtaining analytical equations of motion for these correlators is a priori not possible without approximations, however if we remain in the low-momentum approximation of a dilute Bose gas, it is possible to obtain the following equations of motion for the two correlators:

$$\begin{aligned} \frac{\partial N_{\mathbf{q}}(\tau)}{\partial \tau} &= 2\int_0^\infty \mathrm{d}p \mathcal{K}^L_{\mathbf{p},\mathbf{q}} \left[N_{\mathbf{p}+\mathbf{q}}(N_{\mathbf{p}} + N_{\mathbf{q}} + 1) - N_{\mathbf{p}} N_{\mathbf{q}} \right] + \\ &\quad 2\int_0^q \mathrm{d}p \mathcal{K}^B_{\mathbf{p},\mathbf{q}} \left[N_{\mathbf{p}} N_{\mathbf{q}-\mathbf{p}} - N_{\mathbf{q}}(N_{\mathbf{p}} + N_{\mathbf{q}-\mathbf{p}} + 1) \right] \\ \frac{\partial C_{\mathbf{q}}(\tau)}{\partial \tau} &= 2\int_0^\infty \mathrm{d}p \mathcal{K}^L_{\mathbf{p},\mathbf{q}} \left[N_{\mathbf{p}+\mathbf{q}} C_{\mathbf{p}} + C_{\mathbf{p}} C_{\mathbf{p}+\mathbf{q}} - N_{\mathbf{p}} C_{\mathbf{q}} \right] + \\ &\quad 2\int_0^q \mathrm{d}p \mathcal{K}^B_{\mathbf{p},\mathbf{q}} \left[C_{\mathbf{p}} C_{\mathbf{q}-\mathbf{p}} - C_{\mathbf{q}}(N_{\mathbf{p}} + N_{\mathbf{q}-\mathbf{p}} + 1) \right]. \end{aligned} \tag{2.50}$$

The "Landau" (resp. "Belaiev") collision kernels $\mathcal{K}^L_{\mathbf{p},\mathbf{q}}$ and $\mathcal{K}^B_{\mathbf{p},\mathbf{q}}$ are defined as follows:

$$\begin{aligned} \mathcal{K}^L_{\mathbf{p},\mathbf{q}} &= \frac{3\sqrt{3}c_s}{8\pi\rho_0} p(p+q) \\ \mathcal{K}^B_{\mathbf{p},\mathbf{q}} &= \frac{3\sqrt{3}c_s}{816\pi\rho_0} p(q-p). \end{aligned} \tag{2.51}$$

There is obviously no closed form solution for these functions, however it carries great physical meaning. The evolution is driven by two processes:

- The **Landau process** where one phonon of momentum $\mathbf{q}$ splits into two phonons of momenta $\mathbf{p}$ and $\mathbf{q}-\mathbf{p}$
- The **Belaiev process** where two phonons of momenta $\mathbf{q}$ and $\mathbf{p}$ recombine into a phonon of momentum $\mathbf{q}+\mathbf{p}$

Studying at the limiting cases of this equation, we can look at the long time behavior equation following a quench where the system has reached a state close to thermal equilibrium at a finite temperature (since we injected energy with the quench) and look at the evolution

of the density fluctuations on top of this thermal background. We thus linearize the evolution to first order in perturbation around a thermal state:

$$\begin{aligned} N_{\mathbf{q}}(\tau) &\to N_{\mathbf{q}}^{th} + \delta N_{\mathbf{q}}(\tau) \\ N_{\mathbf{q}}^{th} &= \frac{1}{e^{\frac{\Omega_B(\mathbf{q})}{k_B T}} - 1}. \end{aligned} \tag{2.52}$$

Linearizing then yiels two damping rates for the density fluctuations $\delta N_{\mathbf{q}}$ depending on the collision integrals that are kept:

$$\begin{aligned} \frac{\partial \delta N_{\mathbf{q}}}{\partial \tau} &= -2\gamma_{\mathbf{q}}^{L} \delta N_{\mathbf{q}} \\ \gamma_{\mathbf{q}}^{L} &= \frac{\sqrt{3}\pi}{8\rho_0 c_s} q T^2 \end{aligned} \tag{2.53}$$

$$\begin{aligned} \frac{\partial \delta N_{\mathbf{q}}}{\partial \tau} &= -2\gamma_{\mathbf{q}}^{B} \delta N_{\mathbf{q}} \\ \gamma_{\mathbf{q}}^{B} &= \frac{\sqrt{3} c_s}{32\pi\rho_0} q^3. \end{aligned} \tag{2.54}$$

The coherences $C_{\mathbf{q}}(\tau)$ follow the same damping. From eqs.2.53 and 2.54, we see that the Belaiev damping is predominant as the temperature vanishes. On the other hand, Landau damping dominates for non-zero temperatures, which should be the more relevant case after a quench.

The take away message from this treatment is that beyond-mean field effects manifest as **an evolution of the Bogoliubov excitations population**. The question is then: how can we **experimentally measure this evolution** in our fluids of light platform ? Do these effects survive in the presence of absorption ?

2.5.2 Experimental observables

In [29], a direct study of the populations is presented, as well as the dynamical static structure factor to which we can access as demonstrated in the two previous sections. We can also access directly to the population of excitations since we can measure the density fluctuations $\delta\rho$ as well as the phase ϕ. In this case, we can devise a simple experiment where we produce an initial state corresponding to a thermal state for the Bogoliubov particles. We can then slightly perturb this state and observe the relaxation of this perturbed state towards equilibrium, measuring the damping rates. This proposal is detailed in chap.5.

Conclusion

In this chapter, we have explored the quantum effects arising from the photon-photon interactions. We have described the effect of the interactions quenches on the correlation properties of the fluid of light as it enters and leaves the cell. We have presented a novel experimental arrangement allowing to reach much lower wavenumbers, and granting a direct acess to the fluid's noise spectrum with both spatial and temporal resolution. Using recent

theoritical deveopments, we discuss potential new experiments in order to probe the limits of the current description of our platform. However, we have not yet detailed how the crucial photon-photon interactions arise, nor how to control them. To this extent, we will now devote a chapter to study the atomic structure of Rubidium.

Chapter 3

Atomic medium characterization

So far we have explored the effects of photon-photon interactions in the collective behavior of photon fluids, however we never got into the specifics of the atomic structure explaining this interactions. In this chapter, we study why alkali vapors are of such interest in the context of quantum optics, starting by answering the question "is the Rubidium atom a two-level system ?" (to paraphrase William D. Philips). We will then look at how we can control the state of the atoms by considering a 4-level system. Finally, we will take a detour in the land of numerical simulation to explore transit effects.

3.1 Rubidium fine structure

One of the strengths of alkali atoms is their **fine structure** giving access to rich manifolds of hyperfine levels allowing for laser trapping and cooling. Alkali atoms are the atoms of the first column of the periodic table, they include Lithium (Li), Sodium (Na), Potassium (K), Rubidium (Rb), Cesium (Cs) and Francium (Fr). They are sometimes called Hydrogen like since their electronic structure ressembles the one of Hydrogen with one valence electron on the outermost S-shell, explaining their weak metallic bonding and thus why all of the alkali are soft metal, and highly reactive. The spin-orbit coupling of this outer-shell electron will lead to a fine structure, and the coupling between electronic angular momentum and nuclear spin will split this structure further into the so-called hyperfine structure [93]. In this thesis we will always adress only the two D line of Rubidium which are detailed in the fig.3.1:

- **The D_1 line** from the ground state manifold $5^2S^{\frac{1}{2}}$ to the $5^2P^{\frac{1}{2}}$ manifold and with a corresponding optical wavelength near **795 nm**.
- **The D_2 line** going from the ground state manifold $5^2S^{\frac{1}{2}}$ to the $5^2S^{\frac{3}{2}}$ manifold and with a corresponding optical wavelength near **780 nm**.

3.2 Electromagnetic response

We now describe the atom-light interaction process undergone by the atoms within the cell. The quantity we want to extract is the **atomic coherences** induced by the laser interaction that will drive the **electric susceptibility** of the medium.

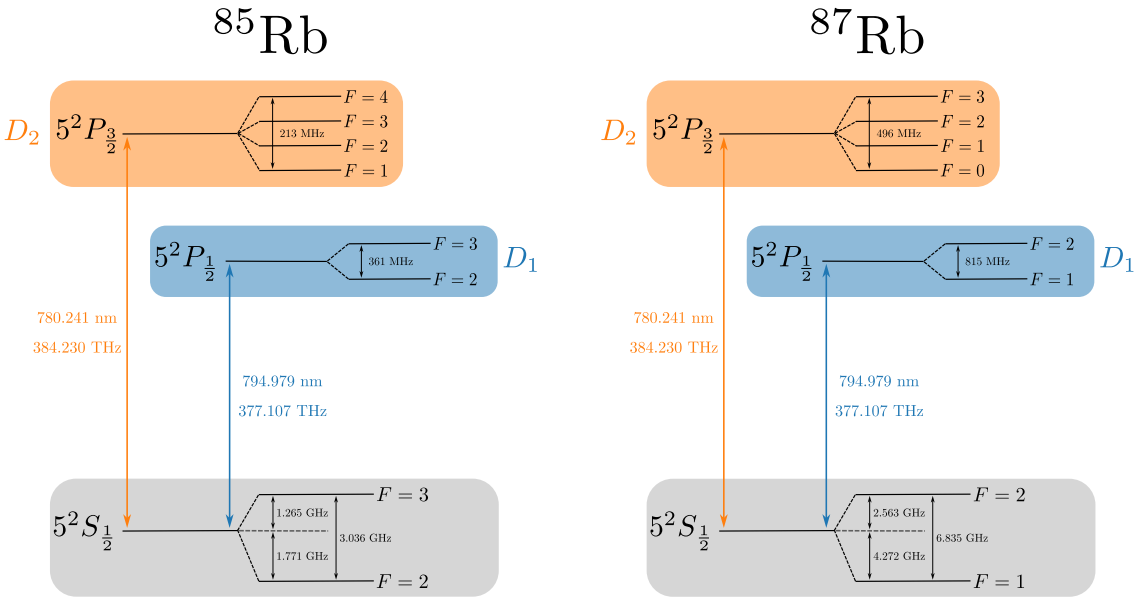

Fig. 3.1 *Rubidium D line structure from [96]. The Zeeman sublevels are not represented and each F level is split into $2F + 1$ m_F Zeeman sublevels degenerate in energy (in absence of magnetic fields).*

3.2.1 Dipole operator

Light matter interaction in the case of the atom will be described by the **dipole operator** $\hat{\mathbf{d}} = e\hat{\mathbf{r}}$, since the energy associated to the dipole in a classical electric field $\mathbf{E}$ is $\hat{W} = -\hat{\mathbf{d}}\cdot\mathbf{E}$[40]. The physical scenario here is simply that a dipole will tend to align with the electric field in order to minimize the total energy. In order to describe this dipole operator in more detail, we study the internal structure of the atom, especially reduce it by computing the **transition moments**. For this procedure [93], we compute the dipole line stengths of the transitions between a ground state $|F_g, m_{F_g}\rangle$ and an excited state $|F_e, m_{F_e}\rangle$. Here F and m_F are the two quantum numbers describing the total angular momentum of the valence electron stemming from the coupling between orbital angular momentum, electron spin and nuclear spin. It can be shown calculating Clebsch-Gordan coefficients [35; 93; 96] that the dipole matrix element reads:

$$\langle F_g, m_{F_g}| e\hat{r}_q |F_e, m_{F_e}\rangle = c_{m_F} d \tag{3.1}$$

where $\hat{r}_q$ is the projection of the position operator on the direction of the electric field polarization, and $d = \sqrt{\frac{9\epsilon_0\hbar\Gamma\lambda^3}{8\pi^2}}$ is the dipole constant for each D-line. In the end, since each F level is degenerate $2F+1$ times, we should add the c_{m_F} coefficients in order to retrieve the total line strength $f_{F_g}^{F_e}$:

$$f_{F_g}^{F_e} = \frac{\sum_{m_F} c_{m_F}^2 d^2}{2F_g + 1}. \tag{3.2}$$

Let us go back to the actual dipole operator. For a simple two-level system comprising of two levels $|1\rangle$ (ground state) and $|2\rangle$ (excited state), it reads:

$$\begin{aligned} \hat{\mathbf{d}} &= \mathbf{d}^* |2\rangle\langle 1| + \mathbf{d} |1\rangle\langle 2| \\ &= \mathbf{d}^*\rho_{21} + \mathbf{d}\rho_{12}, \end{aligned} \tag{3.3}$$

where $\rho_{ij} = |i\rangle\langle j|$ are the density matrix element $\hat{\rho} = |\psi\rangle\langle\psi|$ of the atom. We consider some electric field $\mathbf{E}(t) = \mathcal{E}\cos(\omega t)\mathbf{p}$ where ω is the field's pulsation, $\mathcal{E}$ the field envelope and $\mathbf{p}$ the polarization vector. Thus the final interaction term is:

$$\hat{W}(t) = -\frac{\hbar}{2}\left(\Omega_{12}^* |2\rangle\langle 1| + \Omega_{12} |1\rangle\langle 2|\right) \times \left(e^{i\omega t} + e^{-i\omega t}\right) \tag{3.4}$$

where $\Omega_{12} = \frac{\mu_{12}\mathcal{E}}{\hbar}$ is the **Rabi frequency** and $\mu_{12} = \langle 1|\hat{\mathbf{d}}\cdot\mathbf{p}|2\rangle$ the **dipole moment**. If we consider that $|1\rangle$ and $|2\rangle$ are single F levels, it is simply the square root of the line strength $f_{F_1}^{F_2}$. If we consider that the excited state is actually a manifold of several F levels (which will be described in the next subsection), then we should add the all the relevant line strenghts. We notice directly that the interaction between the electric field and the atom will induce a **coherence** between the ground state and excited state. The oscillating terms can be eliminated by switching to the interaction picture and using the rotating wave approximation [40].
Having defined the dipole moments of each transition, we can define the **electric susceptibility** χ from the medium polarization $\mathbf{P}(\mathbf{r}, t)$:

$$\mathbf{P}(\mathbf{r}, t) = \epsilon_0\chi(\mathbf{E}(\mathbf{r}, t))\mathbf{E}(\mathbf{r}, t). \tag{3.5}$$

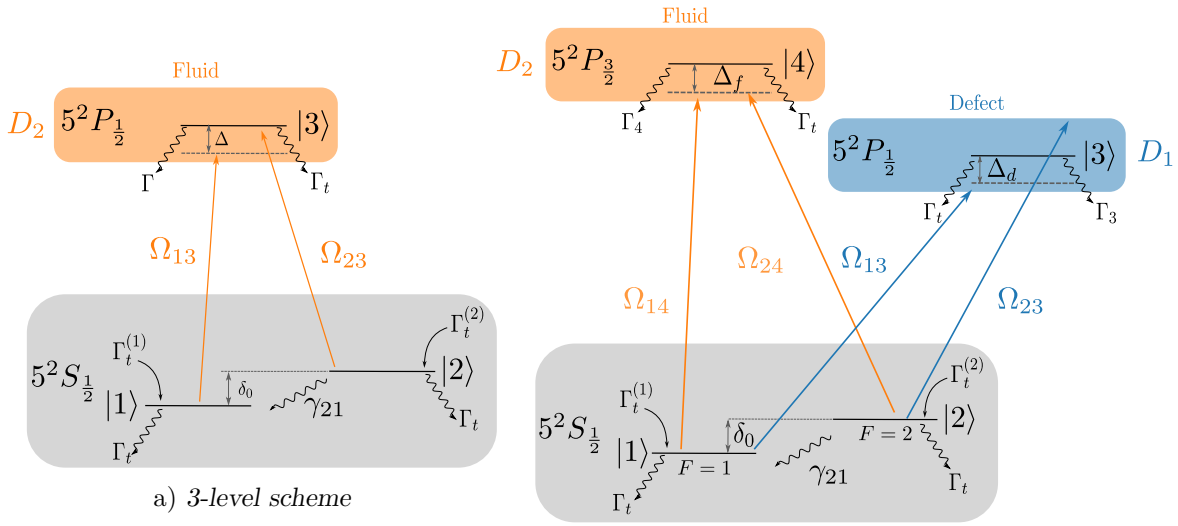

a) *3-level scheme*

b) *4-level scheme*

Fig. 3.2 *Detail of the Rubidium level structure considered in the atom-light interactions. We consider the ground state manifold in gray, and an excited state manifold in orange or blue. Wavy lines represent the various decay rates involved in the system. Each ground states receive an additional influx rate due to transit effects. In orange, we have the manifold addressed by the "fluid" beam, and in blue we have the manifold addressed by the "defect" beam.*

This susceptibility can then be expressed from the dipole moment as follows:

$$\chi(\mathbf{E}(\mathbf{r},t)) = \frac{2N}{\epsilon_0 \mathcal{E}_0(\mathbf{r},t)} \mu_{12}\rho_{21}(\mathbf{r},t) \tag{3.6}$$

where $\mathcal{E}_0$ is the electric field amplitude, and N is the atomic density. In general, this susceptibility will depend on the field's strength, and what will be of particular interest for us are the two first order of the power expansion of the susceptibility $\chi^{(1)}$ and $\chi^{(3)}$.

3.2.2 Three level model

In this subsection, we first describe the scenario where a single linearly polarized beam $\mathcal{E}(\mathbf{r}_\perp,t)\mathbf{x}$ couples the two ground states to an excited state. We focus on this structure as it is common among all alkali. From now on, **we will consider only Rubidium** since it is the atom we use in our experiment. We chose Rubidium because of the history of our research team, as well as the fact that it has been extensively studied in the laboratory. Rubidium is still at the heart of many cold and hot atoms experiments within our laboratory.

In the context of hot vapors, due to the high temperature of the vapor, we will ignore the hyperfine structure of the excited state manifold since they span over 496 MHz, which is comparable with the Doppler broadened linewidth $\Gamma_D = k_0\sqrt{\frac{2k_BT}{m}}$ where k_B is the Boltzmann constant, T the temperature and m the mass of a Rubidium atom. In the case of ^{87}Rb at typical temperatures of 140°C (413 K), Γ_D=360 MHz. We thus consider the following system of levels within the D_2 line as depicted in fig.3.2 a):

- Two ground states: $F = 1$ and $F = 2$
- One excited state manifold: $F' = \{0,1,2,3\}$

This structure is called a **lambda level scheme** and is typical of alkali atoms. In this case, we consider a bundle of excited states. We will thus take into account the effect of the driving field on both transition. Furthermore, due to the high temperature of the vapor, even at large detunings some atoms might end up interacting resonantly with the laser field. From this, it follows that we should consider two Rabi frequencies $\Omega_{13} = \frac{\mu_{13}\mathcal{E}}{\hbar}$ and $\Omega_{23} = \frac{\mu_{23}\mathcal{E}}{\hbar}$. The dipole moment of each transitions reads:

$$\begin{aligned} |\mu_{13}|^2 &= \sum_{F'=0}^{F'=3} f_1^{F'} \\ |\mu_{23}|^2 &= \sum_{F'=0}^{F'=3} f_2^{F'}. \end{aligned} \tag{3.7}$$

In practice, these values are tabulated and allow quick identification of the relevant transitions [96]. We can then write the Hamiltonian of our system, consisting of a bare Hamiltonian $\hat{H}_0$ describing the atom at rest and the interaction Hamiltonian $\hat{W}(t)$ describing the light-matter coupling:

$$\begin{aligned} \hat{H} &= \hat{H}_0 + \hat{W} \\ \hat{H}_0 &= \hbar\delta_0 \left|2\right\rangle\!\left\langle 2\right| - \hbar(\Delta - \delta_0) \left|3\right\rangle\!\left\langle 3\right| \\ \hat{W} &= -\frac{\hbar}{2}(\Omega_{23}^* \left|3\right\rangle\!\left\langle 2\right| + \Omega_{23} \left|2\right\rangle\!\left\langle 3\right|) - \frac{\hbar}{2}(\Omega_{13}^* \left|3\right\rangle\!\left\langle 1\right| + \Omega_{13} \left|1\right\rangle\!\left\langle 3\right|). \end{aligned} \tag{3.8}$$

Here we have directly made the generic assumptions of switching to the interaction picture and making the rotating wave approximation in order to eliminate fast terms at 2ω. In this picture, we thus introduce $\Delta = \omega - \omega_0$ the laser **detuning** to the central frequency of the transition ω_0, and δ_0 is the hyperfine splitting between the two ground states ($2\pi\times$6.835 GHz for ^{87}Rb).
In order to establish the **optical Bloch equations** of the system, we then use the Lindblad master equation for the density matrix of the system $\hat{\rho}$:

$$\frac{\partial\hat{\rho}}{\partial t} = -\frac{i}{\hbar}\left[\hat{H}, \hat{\rho}\right] + \sum_{\nu}\left[\hat{L}_\nu\hat{\rho}\hat{L}_\nu^\dagger - \frac{1}{2}\{\hat{L}_\nu^\dagger\hat{L}_\nu, \hat{\rho}\}\right] \tag{3.9}$$

where $\hat{\rho} = \left|\psi\right\rangle\!\left\langle\psi\right| = \sum_{i,j\in[1,3]} \rho_{ij} \left|i\right\rangle\!\left\langle j\right|$ is the density matrix of the system. The set of operators $\hat{L}_\nu$ are called jump operators and describe relaxation with the exterior of the system. Finally, $\{.,.\}$ is the Poisson bracket or anti-commutator. In order to solve, we now need to detail the expression of the jump operators. We can define two types of relaxation:

- **Spontaneous emission**: this will affect the populations i.e the diagonal terms of the density matrix $\hat{\rho}$. These terms will be modelled with a rate Γ_{mn} such that $\hat{L}_{mn} = \sqrt{\Gamma_{mn}} \left|m\right\rangle\!\left\langle n\right|$.
- **Dephasing noise**: this will induce random dephasing for each state leading to a loss of coherence i.e affecting the off-diagonal terms of $\hat{\rho}$. Such terms will be modelled with a rate γ_{mn} such that $\hat{L}_m = \sqrt{\gamma_m} \left|m\right\rangle\!\left\langle m\right|$.

Applying this to the lambda scheme considered of the D_2 line, we should take the following rates into account: the relaxation rate Γ from the excited state towards the ground states with equal rates $\Gamma/2$ and a dephasing rate between states γ_{21}. This implies the following jump operators in the $\{|1\rangle, |2\rangle, |3\rangle\}$ basis:

$$\hat{L}_{31} = \sqrt{\frac{\Gamma}{2}} |1\rangle\langle 3| = \sqrt{\frac{\Gamma}{2}} \begin{pmatrix} 0 & 0 & 1 \\ 0 & 0 & 0 \\ 0 & 0 & 0 \end{pmatrix} \tag{3.10}$$

$$\hat{L}_{32} = \sqrt{\frac{\Gamma}{2}} |2\rangle\langle 3| = \sqrt{\frac{\Gamma}{2}} \begin{pmatrix} 0 & 0 & 0 \\ 0 & 0 & 1 \\ 0 & 0 & 0 \end{pmatrix} \tag{3.11}$$

$$\hat{L}_{21} = \sqrt{\gamma_{21}}(|2\rangle\langle 2| - |1\rangle\langle 1|) = \sqrt{\gamma_{21}} \begin{pmatrix} -1 & 0 & 0 \\ 0 & 1 & 0 \\ 0 & 0 & 0 \end{pmatrix} \tag{3.12}$$

In the same way we express the Hamiltonian into matrix form in order to gain some graphical insight:

$$\hat{H} = \hbar \begin{pmatrix} 0 & 0 & -\frac{\Omega_{13}}{2} \\ 0 & \delta_0 & -\frac{\Omega_{23}}{2} \\ -\frac{\Omega_{13}^*}{2} & -\frac{\Omega_{23}^*}{2} & -(\Delta - \delta_0) \end{pmatrix} \tag{3.13}$$

we find the familiar shape where the **off-diagonal** terms represent the **couplings** and the **diagonal** terms represent the **bare energies**. Using the closure relation $\mathrm{Tr}(\hat{\rho}) = 1$, we can then compute the evolution equation using eq.3.9 under matrix form:

$$\frac{\partial \hat{\rho}}{\partial t} = A\hat{\rho} + b \tag{3.14}$$

where $\hat{\rho}$ is represented here as a vector:

$$\hat{\rho} = \begin{pmatrix} \rho_{11} \\ \rho_{22} \\ \rho_{21} \\ \rho_{12} \\ \rho_{31} \\ \rho_{13} \\ \rho_{32} \\ \rho_{23} \end{pmatrix} \tag{3.15}$$

and thus yielding the following matrix A:

$$A = \begin{pmatrix} -\frac{\Gamma}{2} & -\frac{\Gamma}{2} & 0 & 0 & \frac{i\Omega_{13}}{2} & -\frac{i\Omega_{13}^*}{2} & 0 & 0 \\ -\frac{\Gamma}{2} & -\frac{\Gamma}{2} & 0 & 0 & 0 & 0 & \frac{i\Omega_{23}}{2} & -\frac{i\Omega_{23}^*}{2} \\ 0 & 0 & -\tilde{\gamma}_{21}^* & 0 & \frac{i\Omega_{23}}{2} & 0 & 0 & -\frac{i\Omega_{13}^*}{2} \\ 0 & 0 & 0 & -\tilde{\gamma}_{21} & 0 & -\frac{i\Omega_{23}^*}{2} & \frac{i\Omega_{13}}{2} & 0 \\ i\Omega_{13}^* & \frac{i\Omega_{13}^*}{2} & \frac{i\Omega_{23}^*}{2} & 0 & -\tilde{\gamma}_{31}^* & 0 & 0 & 0 \\ -i\Omega_{13} & -\frac{i\Omega_{13}}{2} & 0 & -\frac{i\Omega_{23}}{2} & 0 & -\tilde{\gamma}_{31} & 0 & 0 \\ \frac{i\Omega_{23}^*}{2} & i\Omega_{23}^* & 0 & \frac{i\Omega_{13}^*}{2} & 0 & 0 & -\tilde{\gamma}_{32}^* & 0 \\ -\frac{i\Omega_{23}}{2} & -i\Omega_{23} & -\frac{i\Omega_{13}}{2} & 0 & 0 & 0 & 0 & -\tilde{\gamma}_{32} \end{pmatrix} \tag{3.16}$$

where $\tilde{\gamma}_{21} = 2\gamma_{21} + i\delta_0$, $\tilde{\gamma}_{31} = \frac{1}{2}(\Gamma + \gamma_{21}) + i(\Delta - \delta_0)$ and $\tilde{\gamma}_{32} = \frac{1}{2}(\Gamma + \gamma_{21}) + i\Delta$. And an additional vector b:

$$b = \begin{pmatrix} -\frac{\Gamma}{2} \\ \frac{\Gamma}{2} \\ 0 \\ 0 \\ \frac{i\Omega_{13}^*}{2} \\ -\frac{i\Omega_{13}}{2} \\ \frac{i\Omega_{23}^*}{2} \\ -\frac{i\Omega_{23}}{2} \end{pmatrix}. \tag{3.17}$$

Under this form, there is little physical insight that we can extract from this, at least analytically. However, it makes it convenient to solve numerically. There are now two ways to extract some solutions of this equation:

- set the left-hand side to zero and solve the **steady-state**
- plug the full equation into a **numerical differential equation solver** [5] in order to get a full numerical solution at the cost of computation time.

The generic treatment presented in this subsection can readily be extended to arbitrary level structures, especially using modern formal calculation tools like Sympy [71] allowing for fast obtention of the A and b matrices. An example of this workflow is presented in the Appendices of this thesis.

3.2.3 Four level model

In general, there are cases where we want to drive both D-lines at the same time in order to modulate the response of the medium with a control field, while having a fluid field on the other line (see Chap.4). In this case we need to include two excited states manifolds, in addition to the aforementioned two ground states. This scenario is presented in panel b) of fig.3.2. We consider in this case a double lambda scheme where the ground state pair is coupled to each excited state manifold. To describe the problem we take the following convention: the D_2 line is driven by the **fluid** beam, and the D_1 line is driven by the **defect** beam. The excited states manifold of the D_2 line is level $|4\rangle$ and the one of the D_1 line is $|3\rangle$,

numbering the states in increasing order of energy. We thus consider four Rabi frequencies Ω_{13}, Ω_{23}, Ω_{14} and Ω_{24} and define two detunings Δ_f and Δ_d representing the detuning to the D_2 (resp D_1) line. This yield the following Hamiltonian in the $\{|1\rangle, |2\rangle, |3\rangle, |4\rangle\}$ basis:

$$\hat{H} = \hbar \begin{pmatrix} 0 & 0 & -\frac{\Omega_{13}}{2} & -\frac{\Omega_{14}}{2} \\ 0 & \delta_0 & -\frac{\Omega_{23}}{2} & -\frac{\Omega_{24}}{2} \\ -\frac{\Omega_{13}^*}{2} & -\frac{\Omega_{23}^*}{2} & -(\Delta_d - \delta_0) & 0 \\ -\frac{\Omega_{14}^*}{2} & -\frac{\Omega_{24}^*}{2} & 0 & -(\Delta_f - \delta_0) \end{pmatrix}. \tag{3.18}$$

The jump operators are in this case very similar to the three level case, except that we need to distinguish between the two excited states decay rates. Introducing the rates Γ_3 and Γ_4, we now have four relaxation operators:

$$\begin{aligned} \hat{L}_{31} &= \sqrt{\frac{\Gamma_3}{2}} |1\rangle\langle 3| \\ \hat{L}_{32} &= \sqrt{\frac{\Gamma_3}{2}} |2\rangle\langle 3| \\ \hat{L}_{41} &= \sqrt{\frac{\Gamma_4}{2}} |1\rangle\langle 4| \\ \hat{L}_{42} &= \sqrt{\frac{\Gamma_4}{2}} |2\rangle\langle 4| \end{aligned} \tag{3.19}$$

In this case, following the same procedure as above, we can extract the evolution equation for the density matrix (having included the closure relation):

$$A = \begin{pmatrix} -\frac{\Gamma_4}{2} & -\frac{\Gamma_4}{2} & \frac{\Gamma_3}{2} - \frac{\Gamma_4}{2} & 0 & 0 & \frac{i\Omega_{13}}{2} & -\frac{i\Omega_{13}^*}{2} & \frac{i\Omega_{14}}{2} & -\frac{i\Omega_{14}*}{2} & 0 & 0 & 0 & 0 & 0 & 0 \\ -\frac{\Gamma_4}{2} & -\frac{\Gamma_4}{2} & \frac{\Gamma_3}{2} - \frac{\Gamma_4}{2} & 0 & 0 & 0 & 0 & 0 & 0 & \frac{i\Omega_{23}}{2} & -\frac{i\Omega_{23}^*}{2} & \frac{i\Omega_{24}}{2} & -\frac{i\Omega_{24}^*}{2} & 0 & 0 \\ 0 & 0 & -\Gamma_3 & 0 & 0 & -\frac{i\Omega_{13}}{2} & \frac{i\Omega_{13}^*}{2} & 0 & 0 & -\frac{i\Omega_{23}}{2} & \frac{i\Omega_{23}^*}{2} & 0 & 0 & 0 & 0 \\ 0 & 0 & 0 & -\tilde{\gamma}_{21}^* & 0 & \frac{i\Omega_{23}}{2} & 0 & \frac{i\Omega_{24}}{2} & 0 & 0 & -\frac{i\Omega_{13}^*}{2} & 0 & -\frac{i\Omega_{14}^*}{2} & 0 & 0 \\ 0 & 0 & 0 & 0 & -\tilde{\gamma}_{21} & 0 & -\frac{i\Omega_{23}^*}{2} & 0 & -\frac{i\Omega_{24}^*}{2} & \frac{i\Omega_{13}}{2} & 0 & \frac{i\Omega_{14}}{2} & 0 & 0 & 0 \\ \frac{i\Omega_{13}^*}{2} & 0 & -\frac{i\Omega_{13}^*}{2} & \frac{i\Omega_{23}^*}{2} & 0 & -\tilde{\gamma}_{31}^* & 0 & 0 & 0 & 0 & 0 & 0 & 0 & 0 & -\frac{i\Omega_{14}^*}{2} \\ -\frac{i\Omega_{13}}{2} & 0 & \frac{i\Omega_{13}}{2} & 0 & -\frac{i\Omega_{23}}{2} & 0 & -\tilde{\gamma}_{31} & 0 & 0 & 0 & 0 & 0 & 0 & \frac{i\Omega_{14}}{2} & 0 \\ i\Omega_{14}^* & \frac{i\Omega_{14}^*}{2} & \frac{i\Omega_{14}^*}{2} & \frac{i\Omega_{24}^*}{2} & 0 & 0 & 0 & -\tilde{\gamma}_{41}^* & 0 & 0 & 0 & 0 & 0 & -\frac{i\Omega_{13}^*}{2} & 0 \\ -i\Omega_{14} & -\frac{i\Omega_{14}}{2} & -\frac{i\Omega_{14}}{2} & 0 & -\frac{i\Omega_{24}}{2} & 0 & 0 & 0 & -\tilde{\gamma}_{41} & 0 & 0 & 0 & 0 & 0 & \frac{i\Omega_{13}}{2} \\ 0 & \frac{i\Omega_{23}^*}{2} & -\frac{i\Omega_{23}^*}{2} & 0 & \frac{i\Omega_{13}^*}{2} & 0 & 0 & 0 & 0 & -\tilde{\gamma}_{32}^* & 0 & 0 & 0 & 0 & -\frac{i\Omega_{24}^*}{2} \\ 0 & -\frac{i\Omega_{23}}{2} & \frac{i\Omega_{23}}{2} & -\frac{i\Omega_{13}}{2} & 0 & 0 & 0 & 0 & 0 & 0 & -\tilde{\gamma}_{32} & 0 & 0 & \frac{i\Omega_{24}}{2} & 0 \\ \frac{i\Omega_{24}^*}{2} & i\Omega_{24}^* & \frac{i\Omega_{24}^*}{2} & 0 & \frac{i\Omega_{14}^*}{2} & 0 & 0 & 0 & 0 & 0 & 0 & -\tilde{\gamma}_{42}^* & 0 & -\frac{i\Omega_{23}^*}{2} & 0 \\ -\frac{i\Omega_{24}}{2} & -i\Omega_{24} & -\frac{i\Omega_{24}}{2} & -\frac{i\Omega_{14}}{2} & 0 & 0 & 0 & 0 & 0 & 0 & 0 & 0 & -\tilde{\gamma}_{42} & 0 & \frac{i\Omega_{23}}{2} \\ 0 & 0 & 0 & 0 & 0 & 0 & \frac{i\Omega_{14}^*}{2} & -\frac{i\Omega_{13}}{2} & 0 & 0 & \frac{i\Omega_{24}^*}{2} & -\frac{i\Omega_{23}}{2} & 0 & -\tilde{\gamma}_{43}^* & 0 \\ 0 & 0 & 0 & 0 & 0 & -\frac{i\Omega_{14}}{2} & 0 & 0 & \frac{i\Omega_{13}^*}{2} & -\frac{i\Omega_{24}}{2} & 0 & 0 & \frac{i\Omega_{23}^*}{2} & 0 & -\tilde{\gamma}_{43} \end{pmatrix} \tag{3.20}$$

in the $(\rho_{11}, \rho_{22}, \rho_{33}, \rho_{21}, \rho_{12}, \rho_{31}, \rho_{13}, \rho_{41}, \rho_{14}, \rho_{32}, \rho_{23}, \rho_{42}, \rho_{24}, \rho_{43}, \rho_{34})$ basis.
The dephasing rates are defined as follows: $\tilde{\gamma}_{21} = 2\gamma_{21} + i\delta_0$, $\tilde{\gamma}_{31} = \frac{\Gamma_3}{2} - \frac{\gamma_{21}}{2} + i(\Delta_d - \delta_0)$, $\tilde{\gamma}_{41} = \frac{\Gamma_4}{2} - \frac{\gamma_{21}}{2} + i(\Delta_f - \delta_0)$, $\tilde{\gamma}_{32} = \frac{\Gamma_3}{2} - \frac{\gamma_{21}}{2} + i\Delta_d$, $\tilde{\gamma}_{42} = \frac{\Gamma_4}{2} - \frac{\gamma_{21}}{2} + i\Delta_f$ and $\tilde{\gamma}_{43} = \frac{\Gamma_3}{2} - \frac{\Gamma_4}{2} + i(\Delta_d - \Delta_f)$.
Of course, one might lose hope when looking at this matrix. However, this is more to highlight the usefulness of developping an easily extendable analytical framework, and the corresponding

numerical methods. When building the two hand in hand from the beginning, it becomes tractable to include the more realistic picture of considering individual transitions, which will hopefully yield to better results. This is mandatory when considering effects like non-linear birefringence, crucial to go towards mixtures of fluids of light [69].

3.2.4 Optical pumping

The critical phenomenon to describe the physics of controlling the response of the atoms with the "defect" beam is **optical pumping**. It is possible to simplify greatly the previous situation if we consider the following particular case: if we drive **resonantly** the $|2\rangle \rightarrow |3\rangle$ transition, we will strongly modulate the populations in the ground states $|1\rangle$ and $|2\rangle$. Essentially, this means that we can increase or decrease the number of atoms available for the fluid transition. This in turn creates a difference of refractive index between the regions where the defect beam is on, and where it is not. Let us study the two limit cases [35]:

- If $\Delta_d = 0$, we pump atoms from $|2\rangle$ to $|1\rangle$ thus reducing the number of atoms seen by the fluid beam in $|2\rangle$. This means the index seen by the fluid beam will be reduced thus $\delta n < 0$, meaning an **repulsive** defect.
- If $\Delta_d = \delta_0$, we pump atoms from $|1\rangle$ to $|2\rangle$ thus increasing the number of atoms seen by the fluid beam in $|2\rangle$. This means the index seen by the fluid beam will be increased thus $\delta n > 0$, meaning an **attractive** defect.

Furthermore, the index of refraction change δn will not depend on the fluid power in this case. Of course since we drive the defect on resonance, this is at the expanse of self-effects for the defect beam: self-focusing (resp. defocusing) and absorption. We will see how we can mitigate these in chap.4.

3.3 Transit effects

A crucial aspect of hot atomic vapors is that they are **hot**. The high temperature of our typical experiments (between 130°C and 150°C) leads to Doppler effect, and **transit effects**. The average speed of the atoms is on the order of several hundreds meters per second leading to Doppler shifts of up to the GHz range. This means that the dynamics of the interaction will be drastically different between two atoms from one side to the other of the velocity distribution. On the other hand, this will also lead to very different interaction times within the beam. These are the so-called **transit** effects refering to the transit of the atoms across the beam. In this section we will consider the 3-level model.

3.3.1 Kinetic model

The first step is to simply model the atoms using classical thermodynamics. We consider a Boltzmann distribution of atoms velocity. The vapor density can be computed from the vapor pressure using the Eldèn [6] and perfect gases formulae:

$$\begin{aligned} \log_{10}(P_v) &= 15.88253 - \frac{4529.635}{T} + 0.00058663 \times T - 2.99138 \times \log_{10}(T) \\ N(T) &= \frac{133.23 \times P_v}{k_B T} \end{aligned} \tag{3.21}$$

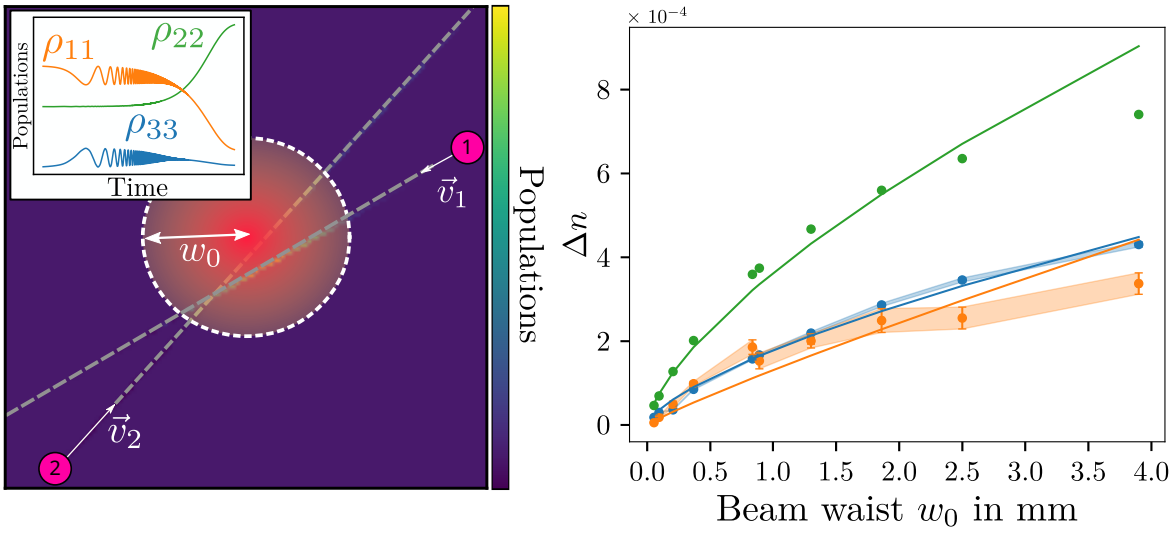

Fig. 3.3 *Visualization of the beam cross section over the population in the excited state* $|3\rangle$*. Two atoms highlighted in pink will have different trajectories (dashed lines) through the beam, and their different initial velocities* ($\vec{v}_1$, $\vec{v}_2$) *will lead to different detunings. In inset, there is a depiction of the evolution of the populations of one atom when interacting with the beam. On the right, non-linear index of refraction variation is represented as a function of the beam waist. In green, the stationary solution of the one coupling 3-level model including transit rates, in orange the experimental results, and in blue the Monte-Carlo model. The shaded areas represent the experimental error or the statistical error of the Monte Carlo method. The solid lines represent a fit by a power law. The model computes the response ab initio, without any fitting parameter.*

We can then infer the velocity distribution of the atoms at thermal equilibrium using the Maxwell-Boltzmann distribution:

$$f(\mathbf{v})\mathrm{d}^3\mathbf{v} = \left(\frac{2k_BT}{m}\right)^{\frac{3}{2}} e^{-\frac{m\mathbf{v}^2}{2k_BT}} \tag{3.22}$$

In first approximation, one might introduce a rate that describes atoms coming in and out of the beam due to thermal motion. This rate describes the atoms leaving the beam thus depopulating each level, but also adding contributions to the ground states: atoms from outside the beam will "refresh" the populations of the ground states. A simple way to take this into accound is to compute the average rate at which atoms come in and out of the beam. This is given by the average time spent in the beam meaning the beam waist divided by the average atom velocity [35]:

$$\Gamma_t = \frac{\langle v \rangle}{w_0} = \sqrt{\frac{8k_BT}{\pi m w_0^2}} \tag{3.23}$$

Modelling influx rates is a much more delicate subject, since we quickly need to take into account **collisions** between atoms, in order to describe atoms that leave the beam for some time before diffusing back to the beam without having lost their "memory" of the interaction [20; 63]. A detailed discussion of these mechanisms can be found in [35]. For simplicity, we will assume here that the atoms quickly lose their coherence outside the beam such that the influx rates repopulate the states with the ground state equilibrium populations in $|1\rangle$ and $|2\rangle$:

$$\begin{aligned} \Gamma_t^{(1)} &= G_1\Gamma_t \\ \Gamma_t^{(2)} &= G_2\Gamma_t \end{aligned} \tag{3.24}$$

where $G_1 = \frac{g_1}{2g_1+1}$ (resp. $G_2 = \frac{g_2}{2g_2+1}$) is the degeneracy factors of each ground states. For ^{87}Rb they are respectively $G_1 = \frac{3}{8}$ and $G2 = \frac{5}{8}$. In order to include this into the optical Bloch equations previously defined, we need to modify eqs.3.10,3.11, 3.12 and define additional relaxation operators:

$$\hat{L}_{31} = \sqrt{\frac{\Gamma + \Gamma_t}{2}}\,|1\rangle\langle 3| = \sqrt{\frac{\Gamma + \Gamma_t}{2}} \begin{pmatrix} 0 & 0 & 1 \\ 0 & 0 & 0 \\ 0 & 0 & 0 \end{pmatrix} \tag{3.25}$$

$$\hat{L}_{32} = \sqrt{\frac{\Gamma + \Gamma_t}{2}}\,|2\rangle\langle 3| = \sqrt{\frac{\Gamma + \Gamma_t}{2}} \begin{pmatrix} 0 & 0 & 0 \\ 0 & 0 & 1 \\ 0 & 0 & 0 \end{pmatrix} \tag{3.26}$$

$$\hat{L}_{21} = \sqrt{\Gamma_t}(|2\rangle\langle 2| - |1\rangle\langle 1|) = \sqrt{\Gamma_t} \begin{pmatrix} -1 & 0 & 0 \\ 0 & 1 & 0 \\ 0 & 0 & 0 \end{pmatrix} \tag{3.27}$$

We explicit here that the dephasing mechanism between the two ground states is effectively the transit rate meaning $\gamma_{21} = \Gamma_t$. We add influx rates phenomenologically as an additional operator $\hat{\Gamma}_t$:

$$\frac{\partial \hat{\rho}}{\partial t} = -\frac{i}{\hbar}\left[\hat{H}, \hat{\rho}\right] + \sum_{\nu} \hat{L}_\nu \hat{\rho} \hat{L}_\nu^\dagger - \frac{1}{2}\{\hat{L}_\nu^\dagger \hat{L}_\nu, \hat{\rho}\} + \hat{\Gamma}_t. \tag{3.28}$$

Where $\hat{\Gamma}_t$ in matrix form in the $\{\rho_{ij} | (i,j) \in [1,3]^2\}$ basis is written:

$$\hat{\Gamma}_t = \begin{pmatrix} \Gamma_t^{(1)} & 0 & 0 \\ 0 & \Gamma_t^{(2)} & 0 \\ 0 & 0 & -\Gamma_t \end{pmatrix}. \tag{3.29}$$

Note that we might worry at first that adding these terms is unphysical. However one can readily check that the evolution equation remains **symplectic** (i.e the total density is conserved / the trace is preserved) since we "lose" atoms at a rate $\Gamma_t/2$ towards each ground state from $|3\rangle$, but "recover" a total rate of Γ_t with the influx rates $\Gamma_t^{(1)}$ and $\Gamma_t^{(2)}$. Retrieving the A and b matrices for numerical solving can be obtained with the Jupyter notebook in the Appendices. We will now check how we have developped an easily extendable numerical framework to complement the analytical results we have presented so far. From the moment we establish the evolution equation, we are tempted to explore transit and other stochastic effects using numerical methods like **Monte-Carlo** type modelling.

3.3.2 Numerics : Monte-Carlo modelling

I will now present the numerical side of the models I have exposed so far. In the same manner as before, the goal of these methods is to make a modular model in order to extract the relevant physical ingredients for each experimental scenario. The generic spirit of the following subsection will be simple: since we have **many** different atoms with many different velocities and trajectories, we will solve the evolution equation **for each** simulated atom. We will thus have the following workflow for each atom:

- Generate a random initial velocity norm from the 3D Maxwell-Boltzmann distribution $|\mathbf{v}|$.
- Generate a random velocity vector (v_x, v_y, v_z) respecting the total velocity vector. This will also set the Doppler shift through the longitudinal velocity v_z.
- Choose a random starting position (x_0, y_0) at the edge of the computational window.
- Choose a random end position (x_1, y_1) at the edge of the computational window.
- Solve the evolution of the atom over this trajectory for a high intensity and low intensity to extract both linear and non-linear susceptibilities: $\chi^{(3)} \approx \frac{\chi_{high} - \chi_{low}}{|E_{high}|^2}$, $\chi^{(1)} \approx \chi_{low}$.

This workflow is summarized in the left pannel of fig.3.3. The initial positions of the atoms are highlighted in pink, with their velocity vector $\vec{v}_1$ and $\vec{v}_2$. The trajectory across the beam is in dashed lines. We then extract the overall response of the medium by averaging over the velocity classes and the atoms.

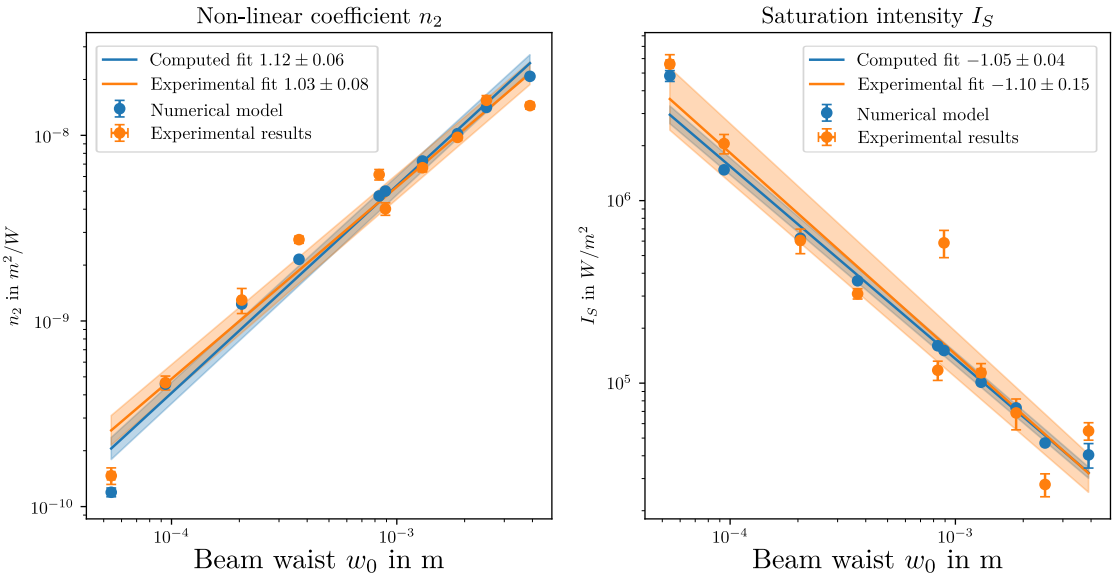

Fig. 3.4 *Evolution of the non-linear coefficient n_2 and saturation intensity I_S as a function of beam waist size. The points in blue represent the numerical model, and in orange we have the experimental points. The area in the corresponding color represent the 1σ confidence interval. Both sets of data are fitted using a power law model to extract trends in the variation of these quantities.*

The choice of the trajectories is crucial since a proper choice of probability has a great impact on convergence speed of stochastic methods. With this in mind one might question then the relevance of starting all atoms on the edge of the computational window, and not with atoms at random positions in the window. We choose this distribution in order to cover all available trajectories across the beam, and because only at the edge of the computational window can we safely assume that the atoms are in their ground state: if we were to pick an atom's initial position within the beam, defining the initial state of the atom would be challenging. Finally during the averaging process, we will average the response at **different times** and for different initial positions. In this sum, it will be as if we had solved for different realizations with random initial positions within the computational window.

While this approach might seem infeasible in practice due to its "brutal" computational complexity, recent advances in modern high performance languages like Julia [87] and hardware make it tractable in a reasonable time [5].
The technical implementation details will be discussed in Appendix A. We will now have a look at the results of this study concerning the two critical quantities in our context of fluids of light: the **non-linear index** and the **saturation intensity** that describe the strengh of photon-photon interactions.

3.3.3 Non linear index n_2 and saturation intensity I_{sat}

In order to study the effect of transit on the critical quantities of our experimental platform, we test our models with respect to a measurement of the non-linear coefficient n_2 and saturation

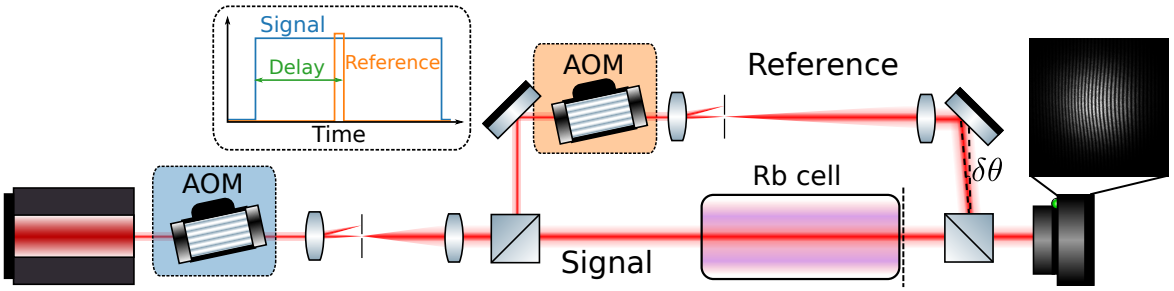

Fig. 3.5 *Time resolved off-axis interferometry setup. The signal and reference beams can be gated using either the blue (resp. orange) Acousto Optic Modulators (AOM). The interference signal is imaged at the output of the cell using a camera. In inset, the sequence of the experiment in time-domain is represented: if the reference is gated much faster than the signal beam, one can sample the dynamics of the system.*

intensity I_S for different beam waist sizes. We chose this tuning knob since this is the one of the most accessible (and controllable) parameters that allow to change the transit rate. We are interested in these quantities since the total interaction term is guided by the **non-linear index of refraction** $\Delta n = n_2 \frac{I}{1+\frac{I}{I_S}}$.

To this extent we devise a simple experimental setup as represented in fig.3.5. Since we want to characterize the response of the medium, we only need a Rubidium cell, and a reference arm in Mach-Zehnder configuration. Using the off-axis interferometry technique (described in details in Appendix A), we measure the non-linear dephasing $\Delta\phi$, and from there, extract both the non-linear index n_2 and saturation intensity. Thanks to the time gating of the beams, we are also able to describe the time response of the medium. This time resolved measurement will be described in the next subsection. The Rubidium cell is a pure ^{87}Rb cell of length L=10 mm. The short cell allows to not worry about geometrical effects such as self-defocusing when measuring n_2 (we fall within the thin medium approximation [21]). The temperature is controlled with heating Kapton tapes, and monitored fitting the low power transmission spectrum when scanning the laser frequency across the D_2 line (see Appendix A for the details). The temperature is set at 150 ± 2°C. The laser detuning is set to -2.2 GHz with respect to the crossover resonance between the $F = 3 \rightarrow F' = 2$ and $F = 3 \rightarrow F' = 3$ of ^{85}Rb, on the D_2 line. The usual reference point for laser detuning on the D lines of Rubidium is the line center, however it is experimentally more accurate to measure the detunings from a crossover resonance in the saturated absorption spectrum as it is a spectrally narrow feature. The optical power is scanned between 0 and 560 mW. Looking at the results presented in fig.3.4, we find excellent agreement between our ab-initio model and the experimental results. By fitting the waist dependence of the non-linear coefficient n_2 and the saturation intensity I_S with a power law $n_2 \propto w_0^p$, we can compare the qualitative behavriors of these quantities. When choosing the frequency of the laser to optimize the losses to interaction ratio, it is challenging to get an intuition in which scenario we want to be in:

- **Large detuning** $\rightarrow$ high saturation intensity, low n_2, low losses and high intensity / small beam waists.

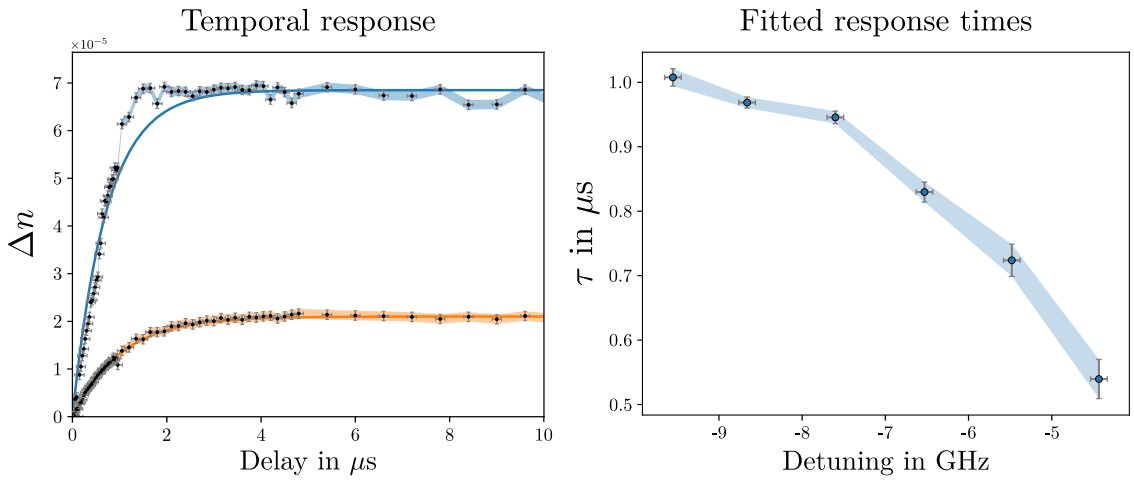

Fig. 3.6 *Left: temporal onset of the non-linear index variation Δn for different delays between pulse and reference. The curve in blue represents the response at a detuning of -5.5 GHz, in orange is the response at -9.6 GHz. Each curve is fitted with an exponential response function with characteristic time τ such that $\Delta n \propto 1 - e^{-\delta t/\tau}$. Right: fitted response time τ for different detunings. The shaded area represents the 1σ confidence interval.*

- **Small detuning** → low saturation intensity, high n_2, high losses and low intensity / large beam waists.

We find that the non-linear coefficient has a linear dependence on waist size with a fitted power-law exponent $p = 1.03 \pm 0.08$. Conversely, the saturation intensity I_S displays an inverse dependence with a fitted exponent of $p = -1.10 \pm 0.15$. We find thus that the product $n_2 I_S$ **is a constant**. This represents the intrinsic maximal non-linear index variation that can be generated by the atoms, and it is ultimately the figure of merit of the interaction strengh. Taking this equality into account allows to drastically reduce the parameter space thus allowing for easier working point identification. Furthermore, these results highlight that **the ballistic transit of atoms across the beam is the dominant effect** to describe the interaction parameter. Essentially, as the beam size increases, the atoms will spend a longer time inside the beam, and will be more saturated. The counterpart being that they accumulate more coherence thus increasing n_2. This is quite intuitive when we think that the total linewidth of the transition is $\gamma = \frac{\Gamma+\Gamma_t}{2}$. The center line saturation field is proportional to $\frac{\hbar\gamma}{\mu_{23}}$ [35] thus as $\Gamma_t \propto \frac{1}{w_0}$, we expect this inverse dependence. More surprising maybe is the fact that **transit alone** describes well this dependence, even when $\Gamma_t \ll \Gamma$ which is generally the case: for a 1 mm beam at 150°C, $\Gamma_t/\Gamma = 8 \times 10^{-3}$, and the ballistic mean free path is on the order of 8 μm at 400K [35], so one could expect some effect of the collisions (which so far have been completely ignored).

3.3.4 Time-resolved response of the atomic medium

Another application of the off-axis interferometry setup is the time resolved operation of the setup. This allows to measure the characteristic time of the medium response. To this order, we measure the non-linear index of refraction Δn at different times by adjusting the delay δt between the signal pulse and reference pulse as shown in the inset of fig.3.5. We chose a 100 ns wide pulse for the reference in order to maintain sufficient exposure on the camera: we want the fringes pattern to be above the noise floor of the camera. We find that the response of the medium follows an exponential onset, which can readily be fitted in order to extract the characteristic response time of the medium τ which can also be interpreted as the time needed to reach the atomic steady state. We find that the typical atomic response times are in the μs range, giving a limit bandwidth for the atomic medium steady state in the MHz range. Since we operate most often in the continuous regime, the response time of the vapor is not as relevant as a interpreting it as low-pass filter: effects whose frequency are lower than $1/\tau$ will have known a medium that can be assumed to be constant.

It is also useful as it allows to measure the characteristic "memory time" of the medium which is of particular interest in the context of the transit broadening of optically induced defects (see chap.4).

3.4 Going beyond: electromagnetically induced transparency

We have described in the previous subsections, ways to modulate the atomic response using optical pumping. However, this is done in an incoherent way, and is limited practically since we can only modify the linear response reliably with this technique. There is however means to achieve much stronger non-linear response using **Electromagnetically Induced transparency** (EIT) [42], even at the **few photons level** [43]. In this case, we use interferences between the different transition probabilities in order to strongly enhance the coherence of the atoms using a probe and control field.

3.4.1 EIT in the lambda scheme

Let us start with the typical level schemes considered in Rubidium vapors, the Λ (lambda) and **N** type schemes. These are the schemes already presented in fig.3.2, except that in this case we will work much closer to resonance. The typical detunings presented before were in the GHz range, here we will work at a few Γ from the transitions or detunings in the 10 MHz range. We thus need to modify a bit our treatment and adapt our definitions. This is represented in fig.3.7. The advantage of these near-resonant drives, is that we can greatly simplify the tedious treatment presented in the previous sections and obtain analytical expressions for the response of any lambda and N level schemes. The response of such systems has been researched extensively, especially in Rubidium vapors in previous works as it is of peculiar interest in the context of **quantum memories** (store light as collective atomic excitations i.e polaritons) [66].
I will thus directly give the relevant results for the atomic susceptibilities. For the Λ type

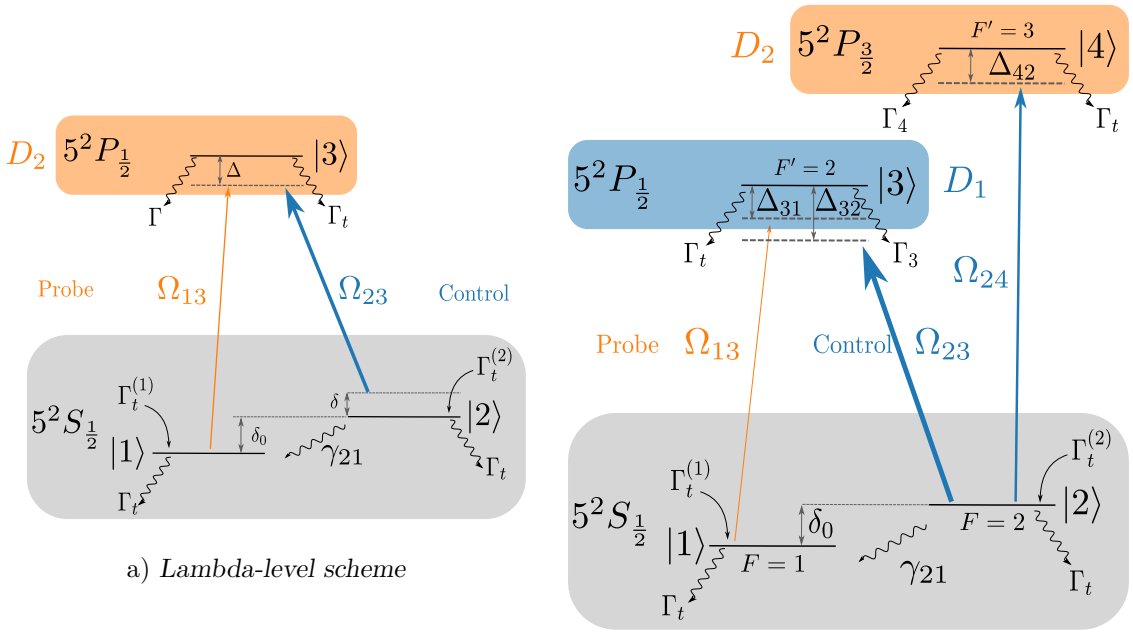

a) *Lambda-level scheme*

b) *N-level scheme*

Fig. 3.7 *The different definitions in the context of EIT. In the lambda scheme, there is a strong control field (as indicated by the thickness of the arrow), and a weaker probe beam. The detuning Δ is called the one-photon detuning, while the detuning δ is the two-photon detuning. For the N-level scheme, we have two control field. A strong field drives the $|2\rangle \rightarrow |3\rangle$ transition, and another very weak control field drives the $|1\rangle \rightarrow |3\rangle$ transition. The remaining definitions are the same as in fig.3.2.*

system, the steady state (at first order in probe power) atomic coherence reads:

$$\rho_{31}^{(1)} = \frac{\Omega_{13}}{\Delta - \delta - i\frac{\Gamma}{2} + \frac{|\Omega_{23}|^2}{\delta + i\gamma_{21}}}. \tag{3.30}$$

We notice directly the two familiar resonances involved in the EIT profile:

- A wide resonence corresponding to the $|1\rangle \rightarrow |3\rangle$ transition highlighted in blue. Its width is controlled by the bare linewidth of the transition $\Gamma/2$.
- A narrow transparency window highlighted in red whose width is controlled by the total dephasing rate between the two ground states $|1\rangle$ and $|2\rangle$.

3.4.2 EIT in the N scheme

For the N-type, we get from [92]:

$$\rho_{31}^{(1)} = \frac{i\Omega_{13}\left(|\Omega_{24}| + 4\tilde{\gamma}_{21}\tilde{\gamma}_{41}\right)}{2\left(\tilde{\gamma}_{31}|\Omega_{24}|^2 + \tilde{\gamma}_{41}|\Omega_{23}|^2 + 4\tilde{\gamma}_{21}\tilde{\gamma}_{31}\tilde{\gamma}_{41}\right)} \tag{3.31}$$

where $\tilde{\gamma}_{21} = \gamma_{21} - i(\Delta_{31} - \Delta_{32})$, $\tilde{\gamma}_{31} = \gamma_{31} - i\Delta_{31}$ and $\tilde{\gamma}_{41} = \gamma_{41} - i(\Delta_{31} - \Delta_{32} + \Delta_{42})$. In the context of hot vapors, the decoherence rates γ_{ij} are including a pure dephasing rate taken to be the transit rate of the beam driving the $|i\rangle \to |j\rangle$ transition:

$$\begin{aligned}
\gamma_{31} &= \Gamma_3 + \underbrace{\frac{2}{\sqrt{\pi}}\max\left(\frac{u}{w_0^{23}}, \frac{u}{w_0^{13}}\right)}_{\gamma_3^\phi} \\
\gamma_{32} &= \Gamma_3 + \underbrace{\frac{2}{\sqrt{\pi}}\max\left(\frac{u}{w_0^{23}}, \frac{u}{w_0^{13}}\right)}_{\gamma_3^\phi} + \underbrace{\frac{2}{\sqrt{\pi}}\frac{u}{w_0^{23}}}_{\gamma_2^\phi} \\
\gamma_{21} &= \gamma_2^\phi \\
\gamma_{42} &= \frac{\Gamma_4}{2} + \underbrace{\frac{2}{\sqrt{\pi}}\frac{u}{w_0^{24}}}_{\gamma_4^\phi} + \gamma_2^\phi \\
\gamma_{41} &= \gamma_{42}
\end{aligned} \tag{3.32}$$

where u is the most probable speed and w_0^{ij} is the waist of the beams driving each transition. Note that we consider here a situation where all of the beams overlap spatially.

Now we already see the interest of the EIT setup since the different coupling fields will allow to spatially or temporally pattern the response of the medium. However, we are especially interested in the non-linear response of the atoms, thus we need to look at further powers of the expansion. More specifically, we need to look at the third power since we want to be able to recover the third order non-linear susceptibility. We recall the expression of the electric susceptibility $\chi = \frac{2N\mu_{13}}{\epsilon_0 \mathcal{E}_{13}}\rho_{31}$, and the expansion of the susceptibility $\chi = \chi^{(1)} + 3\chi^{(3)}|\mathcal{E}_{13}|^2$ as defined in eqs.1.4 and 3.6. Note here that we consider the electric field amplitude $\mathcal{E}_{31}$ driving the $|1\rangle \to |3\rangle$ transition (i.e as the "fluid" / probe beam). Going back to the lambda scheme, we get the following expression for the non-linear susceptibility:

$$\chi^{(3)}(\Delta, \delta) = \frac{2\mu_{23}^2\mu_{13}^2 N}{3\epsilon_0\hbar^3}\frac{2}{\Delta}\frac{1}{|\Omega_{23}|^2 + (\gamma_{31} + i2\Delta)(\gamma_{21} - i2\delta)}. \tag{3.33}$$

Finally, in the N scheme, the non-linear susceptibility reads:

$$\chi^{(3)}(\Delta_{31}, \Delta_{32}, \Delta_{42}) = -\frac{iN|\mu_{13}|^4}{12\epsilon_0\hbar^3}\frac{2\gamma_{21} + \frac{\Gamma_3}{2}}{\gamma_{21}\Gamma_3}\frac{1}{F}\left(\frac{1}{F} + \frac{1}{F^*}\right). \tag{3.34}$$

Where F is defined as follows:

$$F = \tilde{\gamma}_{31} + \frac{|\Omega_{23}|^2}{4\left(\tilde{\gamma}_{21} + \frac{|\Omega_{24}|^2/4}{\tilde{\gamma}_{41}}\right)} \tag{3.35}$$

In the case of the N-level scheme, it is challenging to form an intuition, and we anticipate that the susceptibility will have a complex structure, however we make some reasonable assumptions that will reduce the parameter space. We want to keep the two-photon detuning close to zero in order to maximize the interference between the two-lambda level schemes.

Ideally, we would like to find the regime where the sign of the interactions can be switched by varying the Rabi frequencies (i.e intensity) of the various beams to allow for both spatial and temporal patterning of the interactions and potentials. For this purpose we draw sets of "maps" for different combinations of the parameters near resonance. We choose typical experimental values for the temperature of the cell T=140°C, leading to an atomic density of $N \approx 5 \times 10^{19}$ atoms/m^3. We first explore the detuning dependance of the indices by plotting eq.3.34 for three values of the fluid detuning Δ_{13} ranging from -10 MHz to 10 MHz. We then vary continuously the detunings from the two control and signal fields Δ_{23} and Δ_{24} between -50 MHz and 50 MHz. The results are presented in figs.3.8, 3.9 and 3.10. Let us first look at the limiting cases:

- $\Delta_{24} \gg \Gamma_3$: a transparency window is opened at the the fluid detuning $\Delta_{13} = \Delta_{23}$. This is the typical EIT scheme where the two-photon detuning is brought to zero on the lambda level scheme of the D_1 line. When scanning the control beam frequency, we clearly see the transparency window highlighted in red in figs.3.8, 3.10 and 3.9 shift following Δ_{23}.

- $\Delta_{24} \approx 0$: when the signal beam is brought closer to resonance, the $|2\rangle \rightarrow |4\rangle$ transition on the D_2 dresses the lambda scheme of the D_1 line [35]. This dressing is strongly indicated by the avoided crossing between the red line $\Delta_{13} = \Delta_{23}$ and the $\Delta_{24} = 0$ line. One can interpret the disappearance of the transparency window at the $\Delta_{24} = 0$ as a consequence of the AC Stark shift induced that shifts the energy of the ground state $|2\rangle$ thus destroying the constructive interference between the $|1\rangle \rightarrow |3\rangle$ and $|2\rangle \rightarrow |3\rangle$ transitions.

Looking at what happens when changing the signal field detuning Δ_{24}, one might think that its interest is limited since it kills EIT on resonance, however looking at what happens when we vary the intensities of the beams i.e the different Rabi frequencies, we see that it provides a useful tuning knob. The Rabi frequencies map is presented in fig.3.11.

The same observables are presented as previously, as a function of the Rabi frequencies the two control and signal beams Ω_{24} and Ω_{23}. We see that one can switch the sign of both the linear and non-linear indices n_1 and n_2 by changing Ω_{24} or Ω_{23}.

More quantitatively, one can note that the resulting non-linear index n_2 is one order of magnitude larger than the typical highest values of 10^{-8} m^2/W reached in our experiments. Furthermore, within the transparency window, it is possible to virtually eliminate losses. It is not trivial to be able to find a region of the parameter space allowing some decoupling of the control of n_1 and n_2, however more careful exploration and a finer treatment of the atomic susceptibility should allow to identify relevant working points.

Another critical point is the **dephasing rate**. Because EIT effects are an interference effect between transitions, dephasing rates will hinder the contrast of these interferences. For this we carry on the same analysis by plotting eq.3.34. We place ourselves in the most favorable regime of fig.3.8 i.e at large signal beam detuning $\Delta_{24} = 40$ MHz.

We can extract great physical insight from the study of the variation of the susceptibilities with the decoherence rates γ_{21} and γ_{31}. Since the total decoherence rate γ_{31} is limited by the the natural linewidth of the transition Γ_3, we want to study the influence of the pure dephasing rate γ_3^ϕ. On the other hand, γ_{21} is already a pure dephasing rate so we will carry on our study over $\gamma_2 1$ and γ_3^ϕ. The behavior between the linear (top rows of figs.3.8, 3.9, 3.10

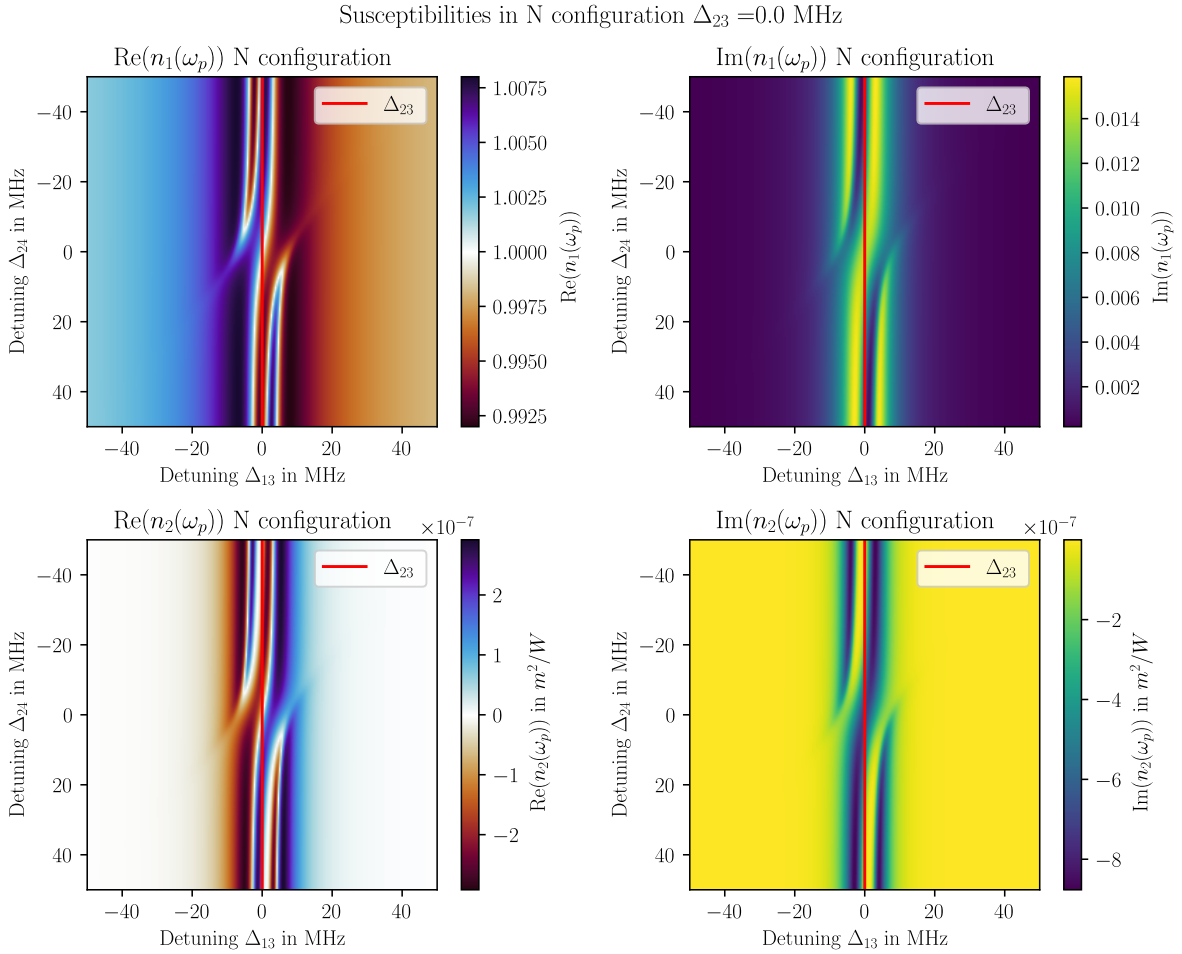

Fig. 3.8 *Susceptibilities as a function of the signal and probe detuning Δ_{24} and Δ_{13}. On the top panel, the linear index at the probe frequency $n_1(\omega_p)$ is represented with the real part of the index on the left, and the imaginary part on the right. On the bottom panel, we have the same representation for the non-linear index of refraction $n_2(\omega_p)$. The susceptibilities are here represented with a control field detuning $\Delta_{23} = 0$ MHz. In red, we hightlight the transparency window opened by the control field at the probe detuning $\Delta_{13} = \Delta_{23}$. Below the pannels, the slider bar indicates the control detuning Δ_{23}.*

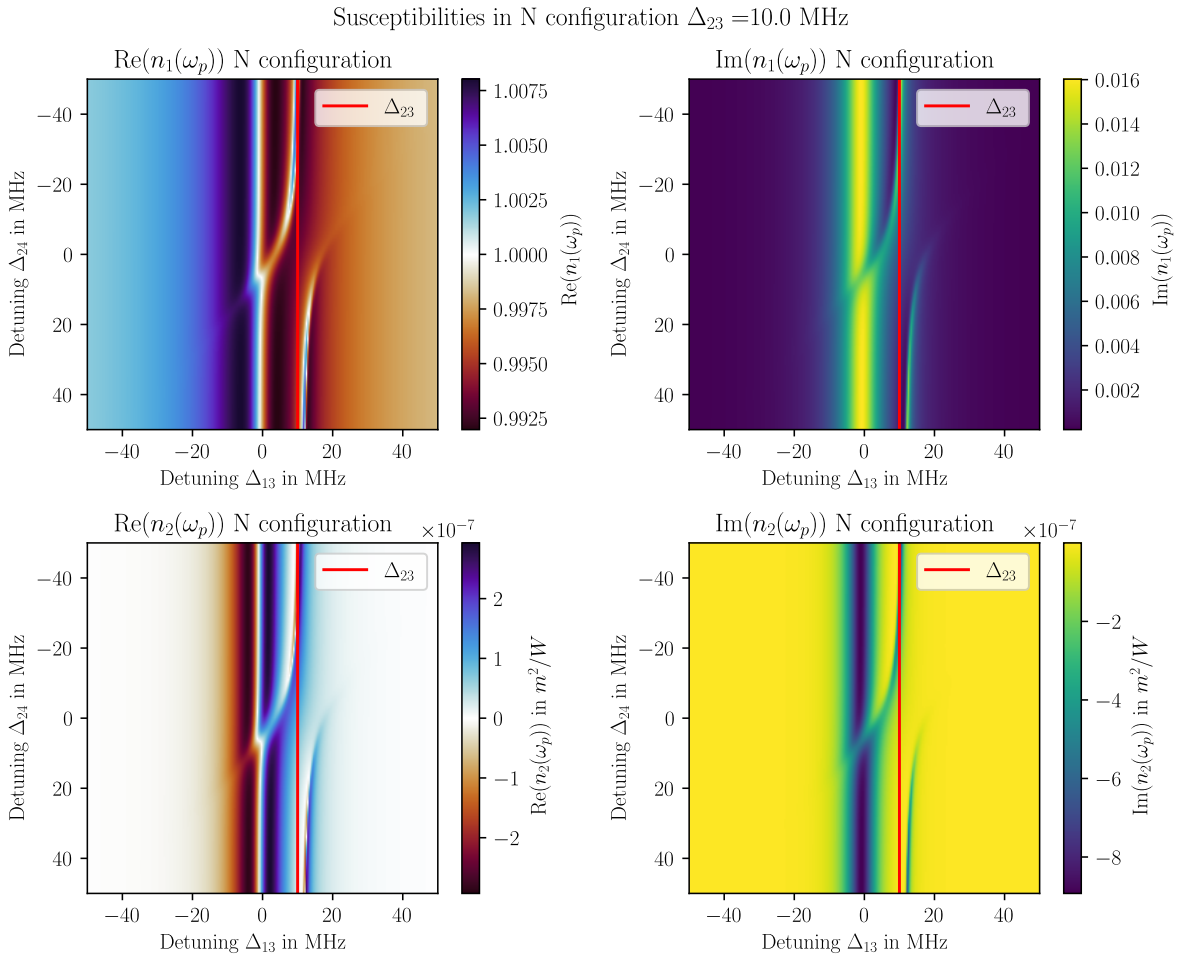

Fig. 3.9 *Susceptibilities as a function of the signal and probe detuning Δ_{24} and Δ_{13}. On the top panel, the linear index at the probe frequency $n_1(\omega_p)$ is represented with the real part of the index on the left, and the imaginary part on the right. On the bottom panel, we have the same representation for the non-linear index of refraction $n_2(\omega_p)$. The susceptibilities are here represented with a control field detuning $\Delta_{23} = 10$ MHz. In red, we hightlight the transparency window opened by the control field at the probe detuning $\Delta_{13} = \Delta_{23}$. Below the pannels, the slider bar indicates the control detuning Δ_{23}.*

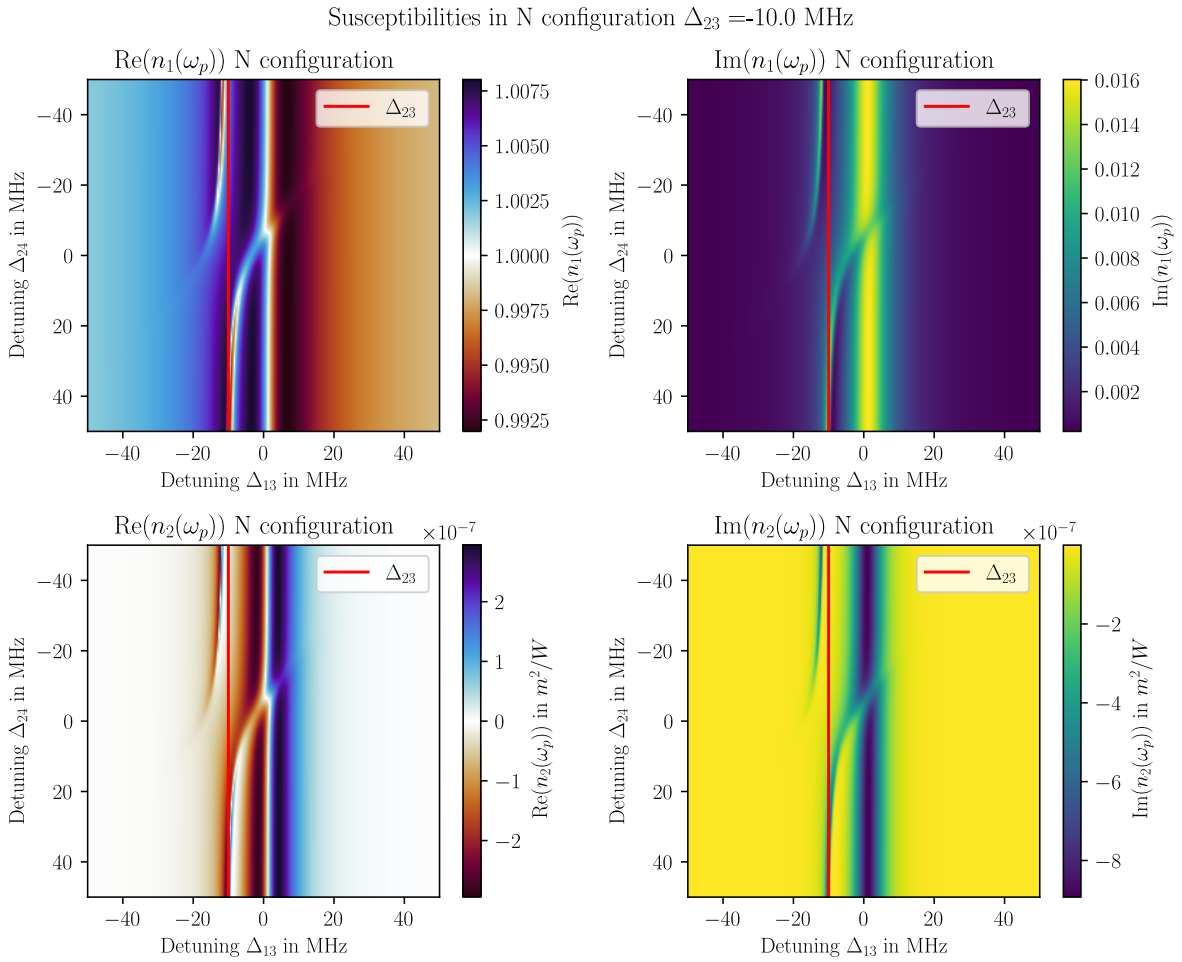

Fig. 3.10 *Susceptibilities as a function of the signal and probe detuning Δ_{24} and Δ_{13}. On the top panel, the linear index at the probe frequency $n_1(\omega_p)$ is represented with the real part of the index on the left, and the imaginary part on the right. On the bottom panel, we have the same representation for the non-linear index of refraction $n_2(\omega_p)$. The susceptibilities are here represented with a control field detuning $\Delta_{23} = -10$ MHz. In red, we hightlight the transparency window opened by the control field at the probe detuning $\Delta_{13} = \Delta_{23}$. Below the pannels, the slider bar indicates the control detuning Δ_{23}.*

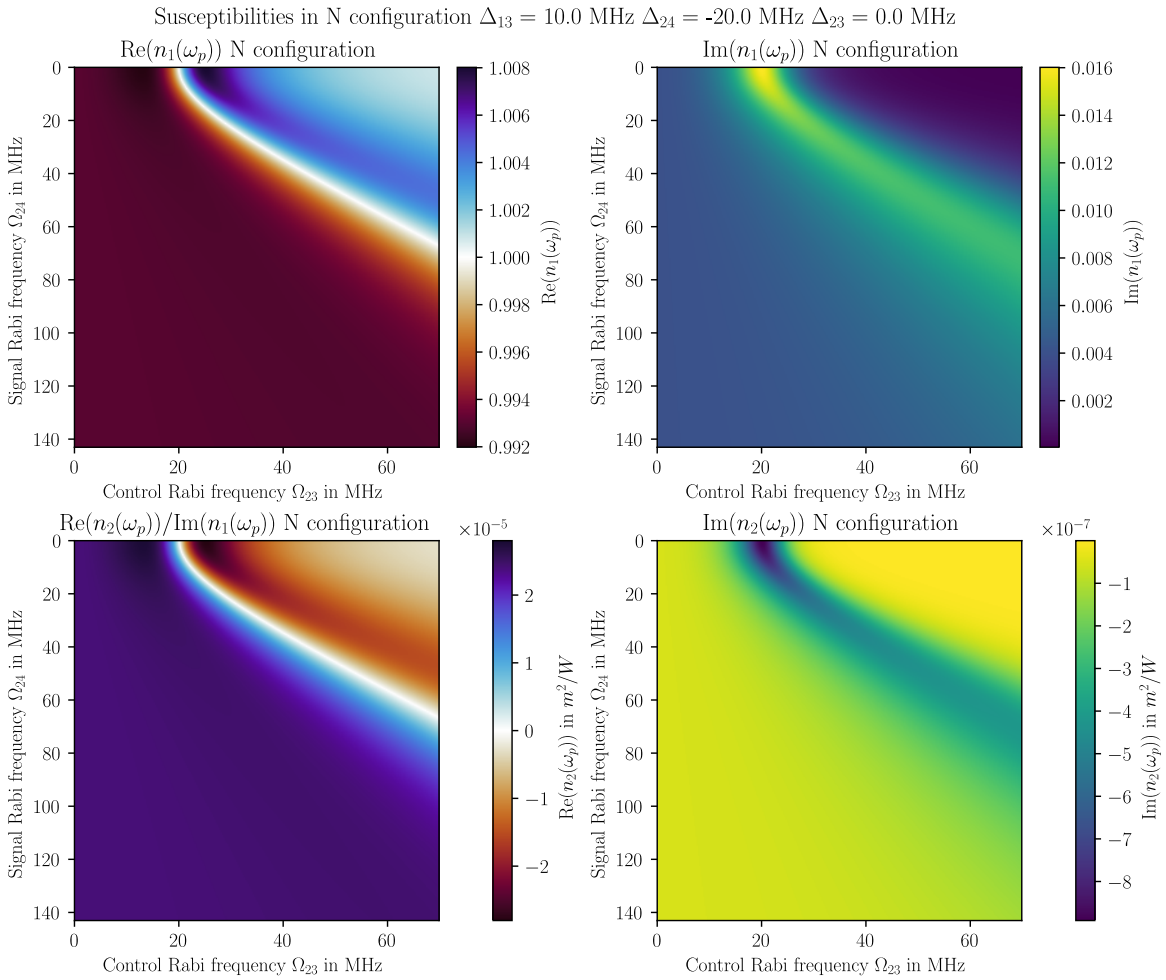

Fig. 3.11 *The susceptibilities are represented for a resonant probe / fluid $\Delta_{13} = 0$ MHz, control field $\Delta_{23} = 0$ MHz and a $\Delta_{24} = -20$ MHz detuned signal beam. Variation of the indices of refraction (linear and non-linear) with the control and signal Rabi frequencies. Playing with the balance of these two Rabi frequencies allows to change signs of the interactions.*

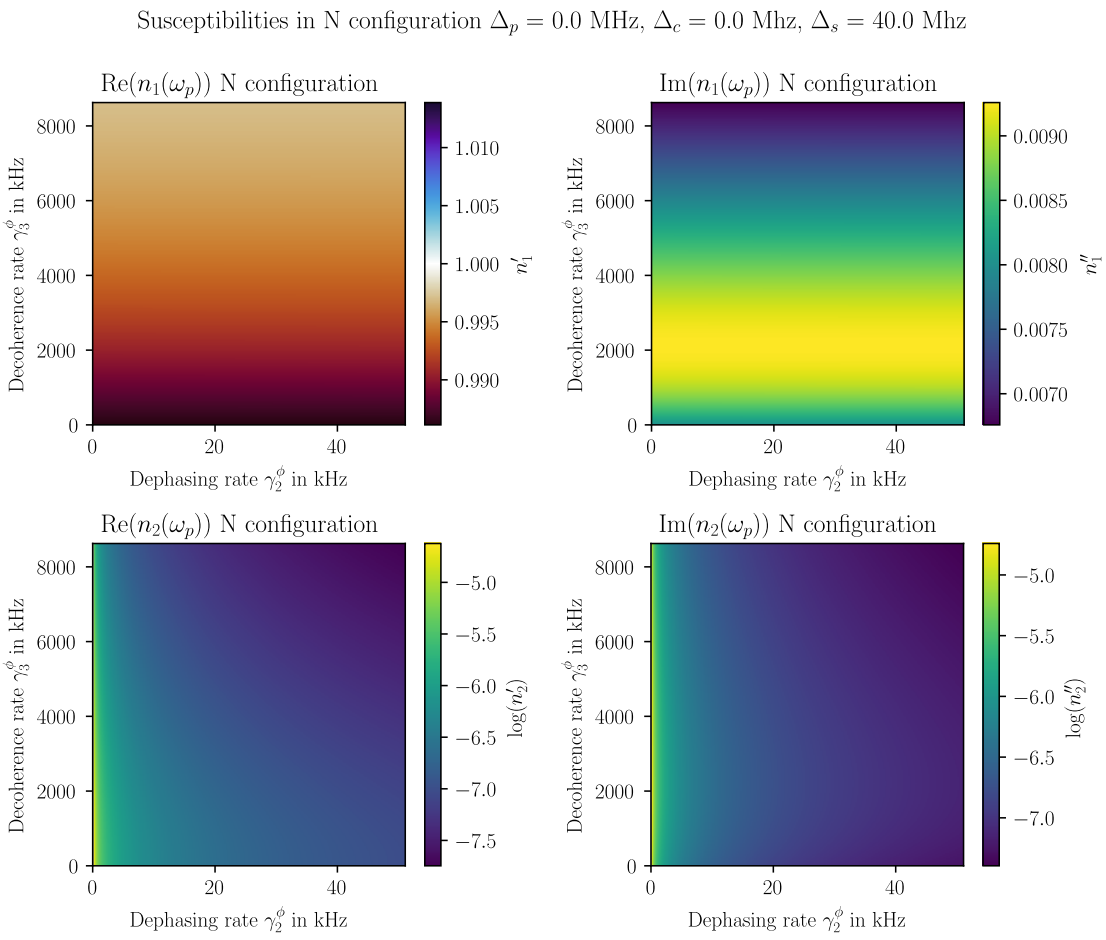

Fig. 3.12 *Effect of the decoherence rates on the different components of the susceptibility. On the top line, the linear susceptibility is depicted as a function of γ_2^ϕ the pure dephasing rate between the two ground states, and γ_3^ϕ the pure dephasing rate of the excited state of the probe (fluid) beam. On the bottom panel, the non-linear index is represented (in log scale).*

and 3.11) and non-linear (bottom row of figs.3.8, 3.9, 3.10 and 3.11) indices is quantitatively different: the linear index only varies with γ_{31} while the non-linear index depends on both γ_{31} and γ_{21} with a strong dependence on the latter. The lower the decoherence rate γ_{31} between ground and excited states, the higher the linear index, both real and imaginary parts. The linear index of refraction originates from the "main" lambda scheme of the atomic structure considered i.e the $|1\rangle$, $|2\rangle$ and $|3\rangle$ levels. Since the decoherence rate γ_{31} will govern the lifetime of the atomic coherence ρ_{31}, it is no surprise that low decoherence rates will lead to stronger atomic response. Since the linear index describes the leading order of the atomic response, it is not surprising that the decoherence between the two ground states γ_{21} does not play a role. For the non-linear index however, the most impacting parameter is the decoherence rate γ_{21} between the two ground states. Since EIT is a direct consequence of the interferences between the transitions within the D_1 and D_2 lines [33], the dephasing induced between the two ground states quickly destroy these interferences. This effect is strong since an order of magnitude change in γ_{21} yields three orders of magnitude change in $\mathrm{Re}(n_2)$.

In hot atomic vapors, these **decoherence terms are dominated by transit rate**, thus going towards a **cold atoms** setup could potentially yield significant improvements in terms of non-linearity and tunability, at the expanse of experimental simplicity. One can also enhance further the response by going to the Rydberg regime using the giant electronic moment provided by Rydberg atoms [86] in a ladder scheme.

Conclusion

In this chapter, we have detailed how the atomic structure of Rubidium induces photon-photon interactions. We have presented both analytical and numerical methods in order to understand, predict and measure the atomic response within our medium, enabling control of both the linear and nonlinear indices of refraction. Finally, we presented a possible extension to electromagnetically induced transparency in order to reach stronger interactions and finer control of the atomic response. Using this control on the atomic response, we will now probe the superfluid behavior of a fluid of light in a scattering experiment on a defect beam.

Chapter 4

Superfluidity of light

One of the most striking feature arising from the effective photon-photon interactions induced by the atomic medium is the emergence of a **superfluid behavior for light**, consequence of the existence of a spectrum of phononic collective excitations called Bogoliubov excitations [35; 36; 72; 73] (see chap.1). However, a complete description of superfluidity in the context of quantum fluids of light remains elusive. Over the last ten years, there have been several seminal works investigating superfluidity in experiments or from a theoretical point.

4.1 Superfluid transition and critical velocity study

One of the main questions is the characterization of the **critical velocity** for superfluidity above which the fluid of light will behave as a classical fluid. It has been known for decades that the upper bound fixed by the **Landau criterion** greatly overestimates this critical velocity. There have been theoretical efforts in order to yield analytical forms, however limited to special geometries, or special types of nonlinearities. Recently, a series of two papers by J.Huynh et al. [46; 47] presents a set of general analytical formulae yielding critical velocities in 1D and 2D for arbitrary defect geometries and several generic types of nonlinearities. This lead to an intense and stimulating exchange between our groups the goal of this chapter is to present the experimental realization probing the superfluid transition in order to compare our experimental platform to this theoretical framework.

4.1.1 Starting point : the Landau criterion

I will first present the canonical approach to superfluidity developed by Landau in his historical work of 1941 [57]. Let us consider the physical situation of a fluid obeying the Gross-Pitaevskii equation 1.30. We have shown how we can obtain a **dispersion relation** 1.31 for the small amplitude fluctuations on top of some static background. Now let us depict some **scattering** process between the fluid and a defect. For convenience, we will consider that the fluid is moving at a velocity $\mathbf{v}$, and that the defect is immobile. Assuming the defect is small enough to remain within the realm of the Bogoliubov approximation, if there is some scattering between the defect and the fluid, then we this will nucleate some excitations within the fluid. For the sake of simplicity, let us assume that we emit a single excitation of momentum $\mathbf{p}$. It will have energy $\varepsilon(\mathbf{p}) = \hbar\omega(\mathbf{p})$ with $\omega(\mathbf{p})$ following 1.31. In the fluid

reference frame, the total energy will thus be Doppler shifted as follows [83]:

$$\varepsilon'(\mathbf{p}) = \varepsilon(\mathbf{p}) + \mathbf{p} \cdot \mathbf{v}. \tag{4.1}$$

Now, in order for this process to happen, it needs to be **energetically favorable** for the fluid thus $\varepsilon'(\mathbf{p}) < 0$. This straightforwardly put a lower bound on the velocity norm v_c for this condition to be realized as follows:

$$v_c = \min_{\mathbf{p}} \frac{\varepsilon(\mathbf{p})}{\|\mathbf{p}\|} \tag{4.2}$$

Now, in the case of the Bogoliubov dispersion, we readily see that this minimum is realized at low wave-vector where $\frac{\varepsilon(\mathbf{p})}{\|\mathbf{p}\|} \approx c_s$. Thus in first approximation we may say that the **critical velocity** under which **no excitations might be nucleated** is $\boldsymbol{c_s}$. This is precisely the so-called **Landau criterion** for superfluidity. Since no excitations can be nucleated under the critical velocity, the fluid will not display any viscosity since it cannot dissipate energy. Thus a superfluid **will not interact with small defects**. We anticipate that this *Gedankenexperiment* might be far from the reality in an actual Bose-Einstein condensate or light superfluid since a lot of other mechanisms might induce dissipation and reduce this critical velocity, however it is a good concepetual starting point to understand why excitations are forbidden. Note that in this argument, the "size" of the defect is critical and has so far only be very loosely defined. I will come back to this in the following sections in order to rigorously quantify the defects in terms of relative energy scales.

4.1.2 Scattering on a gaussian defect

The simplest experiment one might want to do is to look at the scattering on a gaussian defect. In this experiment represented in fig.4.1, we devise a defect using a small gaussian beam to optically pump the vapor on the D_1 line of ^{87}Rb according to the scheme presented in the last chapter 3. The defect beam is a small gaussian beam of variable size but the typical waist w_0^d is around 200μm. The laser source is an amplified Toptica TA Pro ECDL. The optical power of the defect can be adjusted up to 1.2 W. The fluid is a wide gaussian beam of waist $w_0^f =$ 2.23 mm on the D_2 line generated by a MuQuans SML780. This diode laser is amplified with an Erbium doped fibered amplifier that delivers up to 1.3 W of optical power. This setup is almost identical to the experiment of [72]. We use a 10cm long isotopically pure ^{87}Rb, heated to approximately 140°C. We use detunings of between -5GHz and -3GHz (relative to the D_2 line center), corresponding to transmissions between 50% and 10%. The velocity of the fluid is controlled via a mirror whose plane is imaged in the middle of the cell in order to be able to change the angle of the beam without changing its position. This mirror is actuated using piezo stepper screws (Thorlabs PIA13). We can image both the fluid and defect beams at the input and output of the cell in order to control the experiment. Finally, as usual we have a reference arm allowing to retrieve the phase of the fluid beam. We set up the detuning of the defect beam such as to create a **repulsive** defect, and stabilize its size by being in a slightly **self-focusing** regime. For this we place ourselves at around $\Delta_d =$ -500 MHz of the D_1 line center. A typical measurement is to scan the velocity of the fluid beam to try and cross the superfluid transition. We anticipate naively that under the critical velocity, "nothing will happen", and over the critical velocity "something will happen". Of course the definition of these terms will be crucial, and thus I will detail them in the next subsection.

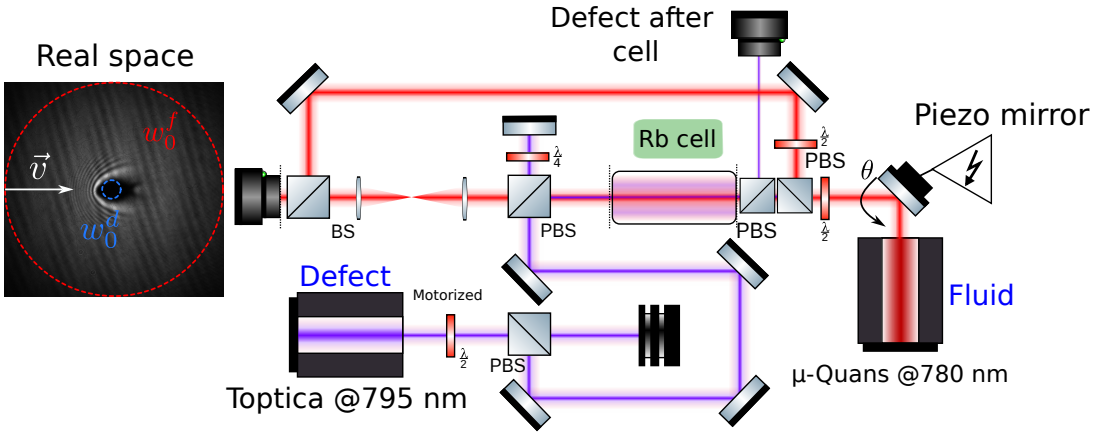

Fig. 4.1 *Simplified experimental setup of the defect scattering experiments. Each laser adresses one of the D lines: the Toptica defect beam adresses the D_1 line at 795 nm and the MuQuans adresses the D_2 line for the fluid at 780nm. The velocity of the fluid is controlled using a piezo actuated screw on the rightmost mirror. A reference arm allows to monitor the phase, and two cameras allow to monitor the fluid at the output of the cell, and the defect after it has passed through the cell (in the counter propagating geometry here). The defect beam is imaged at the output of the cell (entrance of the cell for the defect) using a mirror in the image plane of the fluid imaging $4f$ system. Power of the defect beam is controlled with a motorized $\frac{\lambda}{2}$ waveplate. On the inset, we display a sample image showing the fluid beam waist (in red) relative to the defect beam waist (in blue).*

4.1.3 Relevant observables

Several observables have been used in the previous works to try and characterize the breakdown of superfluidity in quantum fluids: thermometry [27], nucleation of vortices, drag force measurements [72] or scattering measurements [8]. Since thermometry is poorly defined in our system (as has been explained in chap.1), we are left with the remaining techniques. We can divide these measurements in two big categories: in situ observables like drag force or nucleation of vortices, and indirect observables like scattering measurements. I will now detail our experimental implementations of these techniques.

Drag force measurement Let us assume a local index of refraction change $U(\mathbf{r})$. I use this notation as in the context of fluids of lights, a local index of refraction change will equate to some local potential U. We can formally derive the force felt by an electromagnetic field across this index of refraction change [15; 61]. If the electric field is denoted as $E(\mathbf{r})$, then the drag force is:

$$\mathbf{F}_D \propto -\int \nabla U(\mathbf{r})|E(\mathbf{r})|^2 \tag{4.3}$$

Assuming we have some way to measure the potential field imprinted with the defect beam (which we have through phase measurement, and that will be detailed in the next section),

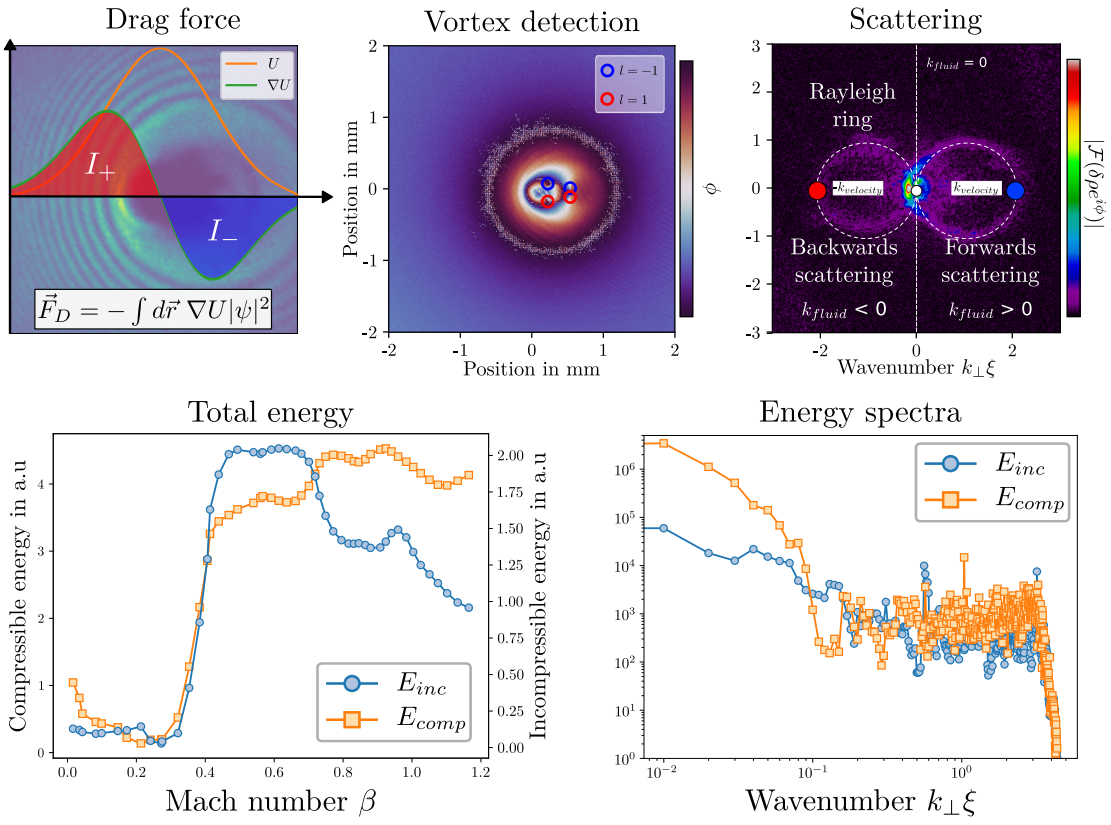

Fig. 4.2 *Sample examples of the different observables. Each observable is labeled, the drag force is calculated using the potential profile V and the formula in the white frame. The access to the phase allows to spot the vortices. Vortex charge l is highlighted with the circles color. Scattering is computed by Fourier transforming the density fluctuations $\delta\rho$ and the phase ϕ. The two scattering rings of forward and backwards scattering are represented in dashed white lines. After Helmholtz decomposing the $\sqrt{\rho}\nabla\phi$ field, one can extract the compressible and incompressible energy spectra, as well as the total energies.*

we can then numerically compute this quantity.

Vortices Using the phase measurement made possible by off-axis interferometry, one can compute the circulation of the phase in order to detect vortices. For a vortex field $\varphi(\mathbf{r})$ of charge $l \in \mathbb{Z}$, we have:

$$\mathcal{C} = \oint_{\mathcal{A}} \mathrm{d}\mathbf{r}_\perp \varphi(\mathbf{r}_\perp) = 2l\pi \tag{4.4}$$

where $\mathcal{A}$ is any closed contour enclosing the vortex singularity. The exact numerical procedure allowing a fast computation of this quantity is detailed in Appendix A.

Scattering In order to study the scattering mechanisms at play when the fluid interacts with the defect, we need to look at the Fourier transform of the **field** in order to gain access to the spatial spectral density which is $\rho(\mathbf{k}_\perp) = |\mathcal{F}(\sqrt{\rho}e^{i\phi})|^2$. Note here that we use the fluctuations field $\delta\rho$ retrieved from taking the difference between the fluid with and without the defect beam on. We could also directly image the Fourier plane of some lens, however as the signal has an extremely broad dynamic range (10 to 14 order of magnitudes) in the Fourier domain, reconstruction through this method usually yields much better results as it allows to circumvent the limited dynamic range of a typical camera. In the Fourier domain, we expect symetrical structures like a Rayleigh ring [38] reflecting the momentum conservation during the scattering properties.

Hydrodynamics observables: compressible and incompressible flows From the phase field $\phi(\mathbf{r}_\perp)$ and the density field $\rho(\mathbf{r}_\perp) \propto |\mathcal{E}(\mathbf{r}_\perp)|^2$, one can define the density weighted velocity field $\mathbf{u}(\mathbf{r}_\perp) = \sqrt{\rho(\mathbf{r}_\perp)}\nabla\phi(\mathbf{r}_\perp) = \sqrt{\rho}\mathbf{v}(\mathbf{r}_\perp)$. One can then decompose this field in rotational and irrotational parts using a Helmholtz decomposition [1]:

$$\mathbf{u}(\mathbf{r}_\perp) = \underbrace{\nabla\varphi(\mathbf{r}_\perp)}_{\mathbf{u}_{comp}} + \underbrace{\nabla \times \mathbf{A}(\mathbf{r}_\perp)}_{\mathbf{u}_{inc}} \tag{4.5}$$

where $\varphi(\mathbf{r}_\perp)$ is a scalar field and $\nabla\varphi(\mathbf{r}_\perp)$ thus constitutes the **irrotational** part of $\mathbf{u}(\mathbf{r}_\perp)$. Similarly, $\mathbf{A}(\mathbf{r}_\perp)$ is some vector potential and $\nabla \times \mathbf{A}(\mathbf{r}_\perp)$ constitutes the **solenoidal** or rotational part. We can then identify the **compressible** part to the irrotational part, and the **incompressible** part to the solenoidal part. From the classical vector analysis theorems, one can prove that for any sufficiently fast decaying field (which is assured through the regularization of the veclocity field $\nabla\phi(\mathbf{r}_\perp)$ by the density), we have the following expressions for φ and $\mathbf{A}$:

$$\begin{aligned} \varphi(\mathbf{r}_\perp) &= \frac{1}{4\pi}\int \mathrm{d}\mathbf{r}'_\perp \frac{\nabla\mathbf{u}\cdot(\mathbf{r}'_\perp)}{|\mathbf{r}_\perp - \mathbf{r}'_\perp|} \\ \mathbf{A}(\mathbf{r}_\perp) &= \frac{1}{4\pi}\int \mathrm{d}\mathbf{r}'_\perp \frac{\nabla\times\mathbf{u}(\mathbf{r}'_\perp)}{|\mathbf{r}_\perp - \mathbf{r}'_\perp|} \end{aligned} \tag{4.6}$$

These are familiar formulae from classical electromagnetism textbooks. At first, it might be surprising to look for an incompressible rotational flow within the normalized velocity field since $\mathbf{u}(\mathbf{r}_\perp) \propto \nabla\phi(\mathbf{r}_\perp)$. However, this decomposition will on the contrary allow to extract all the singularities of the field as for example vortices.

Compressible and incompressible kinetic energies From the hamiltonian in density-phase representation (see eq.2.46) we can decompose the energy of the system in the following components [22]:

$$\begin{aligned} E_K &\propto \int \mathrm{d}\mathbf{r}_\perp \rho(\mathbf{r}_\perp)|\mathbf{v}(\mathbf{r}_\perp)|^2 \\ E_P &\propto \int \mathrm{d}\mathbf{r}_\perp \rho(\mathbf{r}_\perp) V(\mathbf{r}_\perp) \\ E_I &\propto \frac{g}{2}\int \mathrm{d}\mathbf{r}_\perp \rho(\mathbf{r}_\perp)^2 \\ E_Q &\propto \int \mathrm{d}\mathbf{r}_\perp \left|\nabla\sqrt{\rho(\mathbf{r}_\perp)}\right|^2 \end{aligned} \tag{4.7}$$

where E_K is the kinetic term, E_P is the potential energy, E_I is the interaction energy and E_Q is the energy deriving from the quantum pressure term (eq.1.14). From this, we can define trivially the **compressible** and **incompressible** kinetic energies as follows:

$$\begin{aligned} E_{inc} &= \int \mathrm{d}\mathbf{r}_\perp |\mathbf{u}_{inc}|^2 \\ E_{comp} &= \int \mathrm{d}\mathbf{r}_\perp |\mathbf{u}_{comp}|^2. \end{aligned} \tag{4.8}$$

It means that the incompressible energy will start to be non-zero as soon as there are singularities i.e vortices. On the other hand, the compressible energy will quantify the phononic excitation of the fluid.

There is now the question of the relevance of each observable in the physical processes we want to look at namely: which is the observable which will display the most dramatic change across the superfluid transition ? On paper, we anticipate that emergence of vortices in the wake of the defect is a definite proof of the loss of superfluidity. However, we look at our fluid of light at a finite time, and thus precisely identifying the transition velocity might prove challenging since close to the transition, vortices take longer and longer to detach from the defect. Furthermore, close to a strong repulsive defect, the fluid density is zero, thus complicating further the identification of vortices. In the same fashion, the scattering signal has been used in a lot of studies, but the very strong zeroth order often makes quantitative exploitation of these spectra difficult in the experimental setting. We will thus present a comparison of these different observables in numerical simulations in order to try and distinguish in a controlled environment where to focus our attention.

4.1.4 Numerical analysis

In order to simulate the scattering of the fluid on a gaussian defect we use the split- step spectral scheme presented in chap.1. We develop a numerical framework in Python `NLSE` whose implementation is detailed in Appendix A.
We set up beams, defect and fluid which have waists w_0^d and w_0^f. The fluid beam has a gaussian profile and the defect beam has a Lorentzian profile. This is in order to take broadening effects due to the temperature of the vapor (see next section). The interaction strength for the fluid is controlled by the non-linear index n_2 and the fluid power $\mathcal{P}_f$. The strength of the defect is controlled by the local index of refraction change $\delta n(\mathbf{r}_\perp)$. In first approach, the backreaction

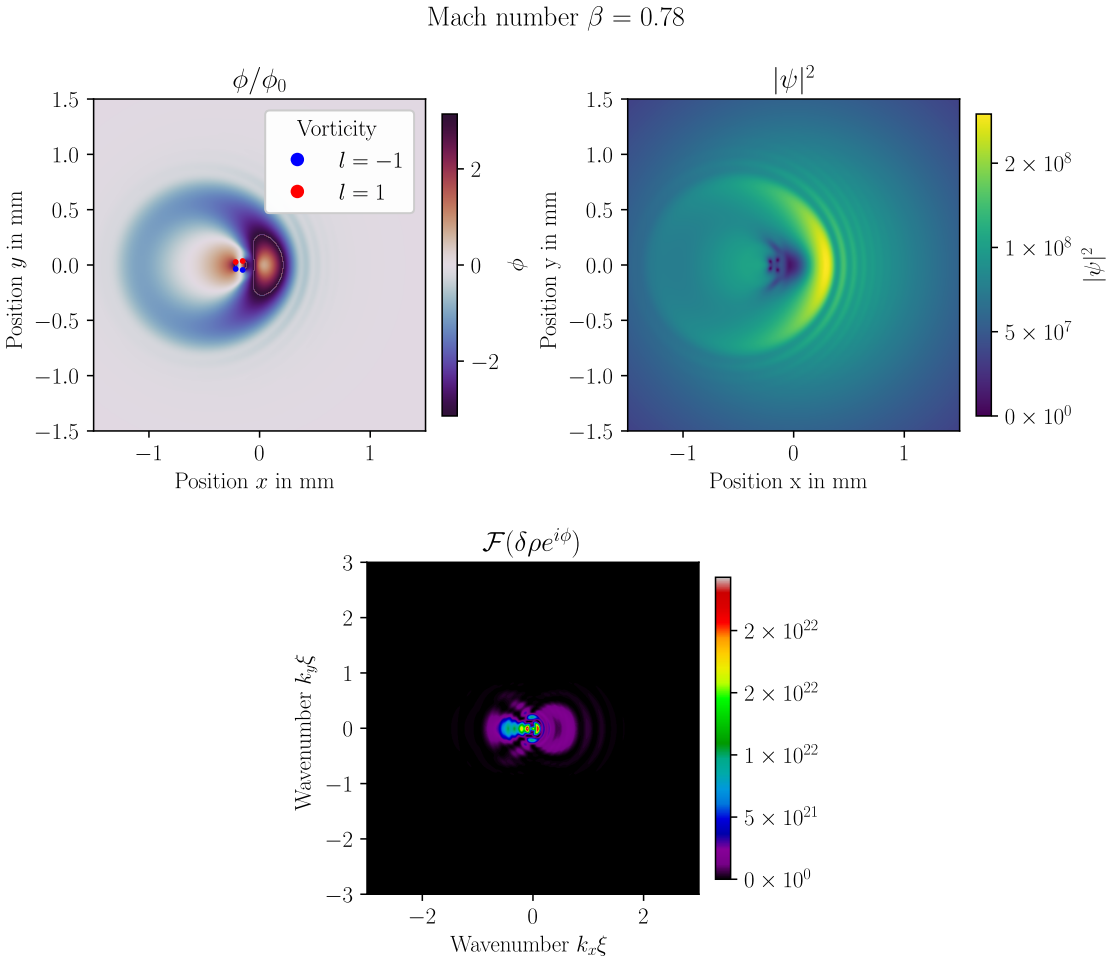

Fig. 4.3 *Typical realization of a simulation run for the parameters described in the main text. The Mach number is 0.78. The phase is displayed renormalized by the phase without the defect. Vortices are represented with red and blue dots (with resp. charge 1 and -1). The density of the fluid shows characteristic dips indicating the vortices position, as well as a bunching of density in front of the defect. Finally, in the bottom panel, the scattering spectrum is represented in the fluid's referential. The scattering occurs in a ring-like structure, indicative of the Rayleigh type scattering.*

of the fluid on the defect is not modelled. We also take into account linear absorption through the parameter α. The goal is to remain as close as possible to the experimental parameters in order to easily compare experimental results to the numerics. We solve the evolution of the fluid through the cell for different initial fluid velocity by changing the fluid's initial phase. For each realization, we compute all of the aforementioned observables. We find the results of a typical run presented in figs.4.3 and 4.4.

The simulated setup is the following:

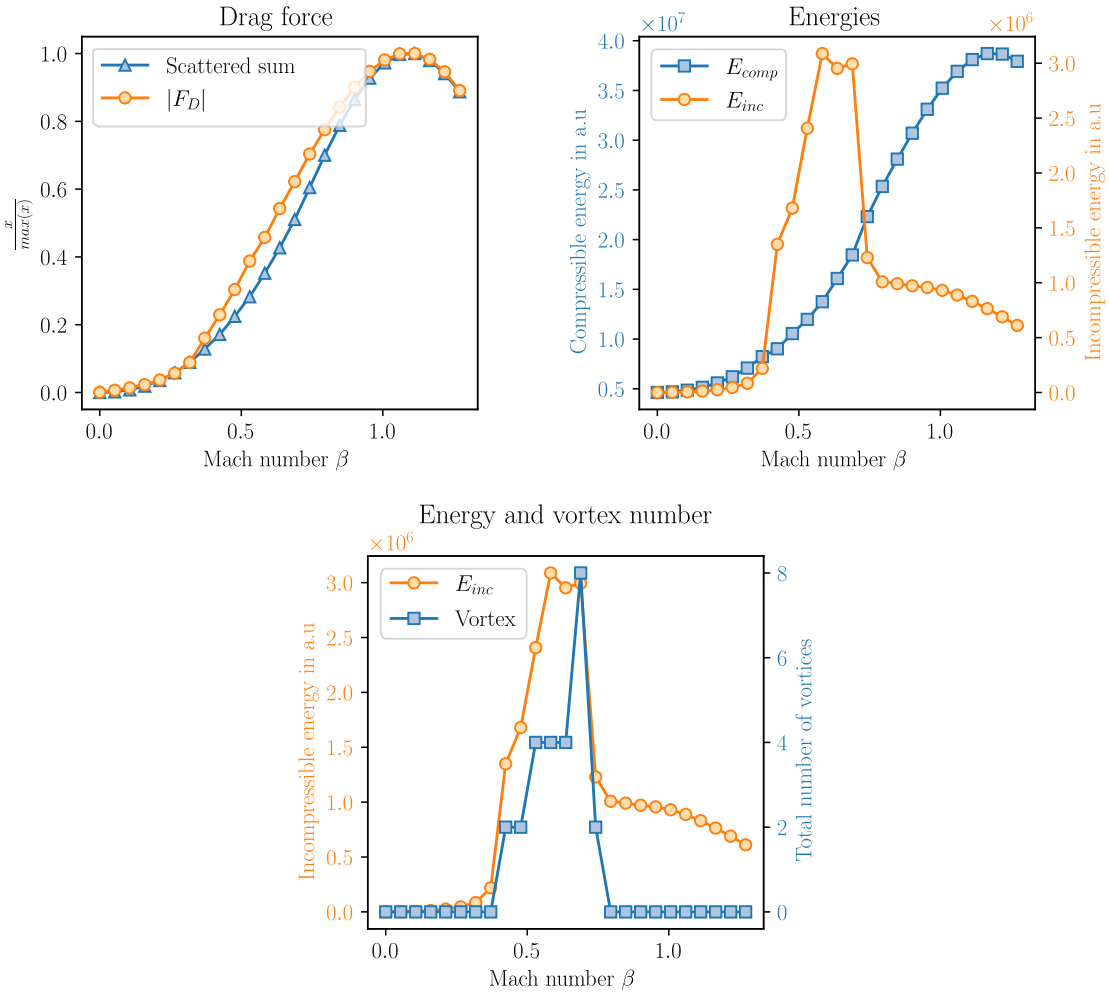

Fig. 4.4 *Comparison of the different observables for different Mach numbers. In the drag force pannel, the drag force and total scattering signals are displayed, normalized to their maximal value. In the energies panel, the total compressible and incompressible energies are displayed. We note that the compressible energy can be almost perfectly superposed with the drag force. The incompressible energy on the other hand displays a dependance that is very Similar to the vortex number (bottom panel).*

- Beam waists $w_0^d = 110$ μm, $w_0^f = 2.3$ mm
- Non-linear index $n_2 = -4.4 \times 10^{-9}$ m^2/W
- Fluid power $P_f = 1.0$ W
- Defect height $\delta n = -10^{-4}$
- Cell length $L = 10$ cm
- Linear absorption coefficient $\alpha = 20$ m^{-1}
- Saturation intensity $I_s = 3.28$ W/cm^2

As mentioned before, these parameters replicate the parameters **measured** in the experiment. These parameters can be abreviated by defining the following relevant adimensional quantities:

- $\frac{\delta n}{\langle \Delta n \rangle}$ the ratio of the defect's height to the interaction strength. For the previous parameters, this is 1.7.
- $\frac{z}{z_{NL}}$ the total evolution time with $z_{NL} = \frac{1}{k_0 \langle \Delta n \rangle}$. For the previous parameters, this is 47.
- $\frac{w_0^d}{\langle \xi \rangle}$ and $\frac{w_0^f}{\langle \xi \rangle}$ designating the sizes of the beam in units of the average healing length over the cell $\langle \xi \rangle = \left\langle \frac{1}{k_0 \sqrt{\Delta n}} \right\rangle$. For the previous parameters, they are respectively 6.8 and 142.
- $\beta = \frac{v}{c_s}$ with $c_s = \sqrt{\langle \Delta n \rangle}$ the sound velocity is the Mach number.

Essentially, we express all relevant quantities in the natural units of the system. From this, what can we extract ? A value of the defect height $\frac{\delta n}{\langle \Delta n \rangle} = 1.7$ tells us that the defect will be on the order of the interaction energy. This means that while the defect is not perturbative, it is not so strong that its mere presence might break superfluidity around it through a quench process. The adimensional time is $\frac{z}{z_{NL}} = 47$, meaning that while we study the transition at a finite time, and not at infinite time, the evolution time is still significant. The typical maximum evolution times that we can reach for a 10 cm cell are on the order of $\frac{z}{z_{NL}} = 200$. Finally, we still want to work within the Bogoliubov theory, thus the spatial scales need to be (much) bigger than the healing length ξ. With $\frac{w_0^f}{\xi} = 142$ we can safely ignore finite size effects. In the same fashion $\frac{w_0^d}{\xi} \approx 7$ ensures that the defect is not too small while remaining much smaller than the fluid, allowing to ignore boundary effects.

The results are presented in figs.4.3 and 4.4. Let us start with the phenomenology of a single realization presented in fig.4.3. From the density plot, we can clearly see the pair of opposite signed vortices being nucleated at the poles of the defect. To conserve angular momentum, only pairs of opposite signed vortices can be emitted. In the phase plot, their presence can be checked by computing the circulation of the phase. Note here that we consider the phase renormalized by the phase of the fluid without the defect (ϕ_0). This allows to remove the constant phase linked to the velocity field imprinted on the fluid, as well as the gaussian phase due to the defocusing of the beam. Essentially, it simply means going in the fluid's reference frame. Similarly, we look at the fourier transform of the fluctuation field

$\delta\rho e^{i\phi}$, with the phase in the reference frame of the fluid. This allows to get the excitation spectrum of the fluctuations. As the vortices appear, a complex scattering structure emerges with the appearance of a typical ring-like structure in the forward scattering direction: the Rayleigh ring [23] originating of the scattering of the long wavelength phononic modes on the comparatively small defect. By definition, there are no phononic modes under a wavelength of ξ, thus most of the Bogolons have a wavelength on the order of or larger than the defect. This typical symmetrical structure is especially visible at high velocities.

To go beyond phenomenology, we compare several realizations for various Mach numbers. This is the subject of fig.4.4. Computing the drag force, we see that the drag force displays an inflexion point at around $\beta \approx 0.5$. We do not expect a very sharp transition as we look at finite time, and two main factors limit the cancellation of the drag force: losses as well as the fact that the defect in our case is turned on violently. As the fluid enters the cell, it undergoes an interaction quench, but it also undergoes a potential energy quench with the sudden appearance of the defect beam. Furthermore, experimentally, we see that as the defect gets dragged by the fluid after the transition, this complicates further the measurement of the drag force when measuring it at the output plane of the cell. This is discussed further into this chapter in section 4.3. The drag force correlates very well with the total compressible energy on the top right. Looking at the incompressible energy however, we see a sharp transition that correlates near exactly to the emergence of vortices. This is the strength of the Helmholtz decomposition as it allows to discriminate between the regular irrotational part, and the singularities. Now on to the scattering signal. Integrating the scattering signal yields two important informations: since we are in the fluid's reference frame, any population outside the $\mathbf{k}_\perp = 0$ mode will indicate scattering due to the defect. If we integrate over the whole k-space, we will recover the amount of the fluid that has been scattered by the defect.ial scattering displays a sharp cusp at the same Mach number as the other observables. From this preliminary study, we can conclude that while drag force displays a "softer" transition, the incompressible energy, total scattering and the vortex number all display very sharp changes at the same Mach number strongly indicating the loss of superfluidity. We will thus focus on these observables to try and extract some predictions for the critical velocity in our system, especially the dependance in terms of the adimensional parameters described above: height of the defect, and size. This will also allow easier comparisons to the analytical results presented in [46; 47].

Looking at several realizations varying only the defect strength, we can extract several important physical features. The different observables are presented in fig.4.5. We can distinguish two qualitatively different regimes:

- When $\frac{\delta n}{\langle \Delta n \rangle} < 1$: in this case, the defect is "penetrable" meaning that the fluid enters the defect. No observable display a sharp transition. While the incompressible energy displays a marked increase at roughly $\beta \approx 0.8$ for small defects, no vortices are emitted suggesting that in this case, the loss of superfluidity is caused through other mechanisms.

- When $\frac{\delta n}{\langle \Delta n \rangle} > 1$: in this case, the defect goes towards the "impenetrable" limit where the region inside the defect is forbidden to the fluid for all velocities. In this case, the picture is quite different and all observables show a coinciding sharp transition. This transition either corresponds to the emission of the first vortex pair, the sudden increase of the incompressible energy, or the onset of scattering outside the $k_\perp = 0$ mode. The

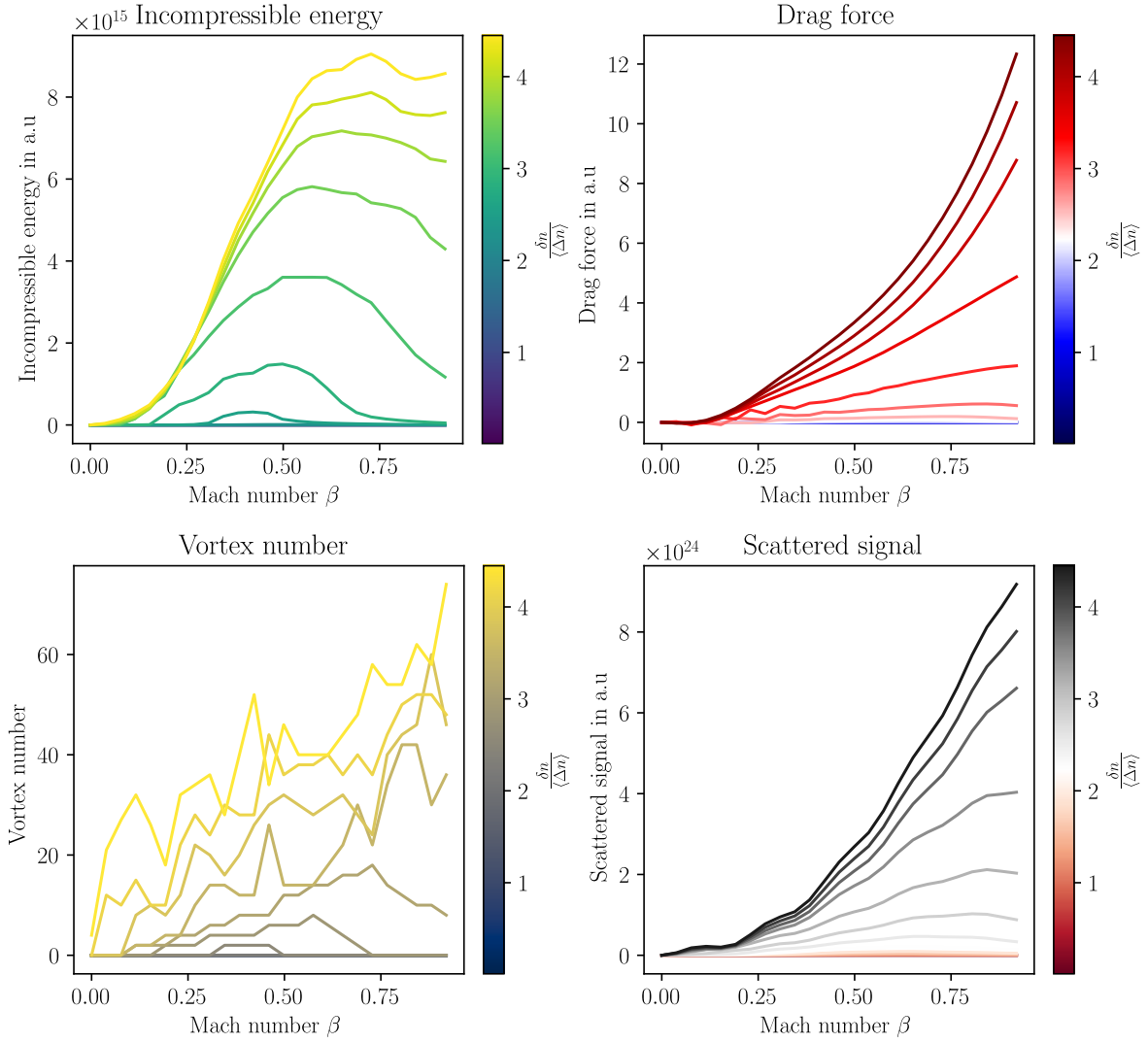

Fig. 4.5 *Behaviour of the different observables for different defect heights. Top left: incompressible energy. Top right: drag force. Bottom left: vortex number. Bottom right: scattered signal. The defect height* $\frac{\delta n}{\langle \Delta n \rangle}$ *is varied between 0.01 and 5.*

transition is the clearest in the vortex number, however actual experimental detection might be challenging in noisy environment.

We can carry the same analysis when varying the defect size $\frac{w_0^d}{\langle\xi\rangle}$. Keeping all other parameters fixed, for a defect height of $\frac{\delta n}{\langle\Delta n\rangle} = 1.7$, we vary the defect size between 0.5ξ and 15ξ. We present the same observables in fig.4.6. As the defect size increases, the different observables show a more and more marked transition, up until a certain point where the fluid does not seem to display a sharp transition anymore. We can interpret that as the defect becomes large (meaning $w_0^d \gg \xi$), the fluid sees as smooth slope when approaching the defect. Thus it would seem the fluid actually adiabatically follows the potential landscape thus suppressing the sharp nucleation of vortices. While we might deduce from the vortex number and incompressible energy that the superfluidity is not broken anymore, when we look at the scattering signal, the evolution is continuous and follows the expected path [46; 47]: the larger the defect waist, the sooner the superfluidity is broken. It goes to show that in the same way as in the case of low defects ($\frac{\delta n}{\langle\Delta n\rangle} < 1$), the superfluidity is broken by other processes than vortex nucleation.

One can then try to estimate the critical velocity for superfluidity from these different observables. Using the vortex number is straightforward since we can readily take the first velocity where the vortex number is not zero. In the same fashion, detecting the first non-zero point of drag force allows to retrieve the threshold velocity. The case of the incompressible energy and scattering signal, it is more challenging since the transition is softer for low defects. In this case we try to detect a cusp in the energy or scattering signal, corresponding to a maximum of the second derivative of this signal. The results of this criteria are presented in fig.4.7

We confirm in fig.4.7 that the higher / larger the defect the lower the critical velocity. All criteria however do not predict the same critical velocity. In the case of the potential height, the vortex number cannot be used below a certain height since it superfluidity in this case in not broken by emitting vortices anymore. The incompressible energy and drag force are seen to coincide nicely up to high defects where it seems that the discrete number of velocities might trump calculation of the second derivative. Interestingly, the critical velocity infered from the drag force displays a dip at around $\frac{\delta n}{\langle\Delta n\rangle}$ as predicted in [47]. The same remarks apply to the critical velocity infered from the scattering signal in red, where it seems that the discretization in velocity is more visible, as can be seen also in figs.4.5 and 4.6. The picture is very similar for the defect size, where there exists regions where multiple observables coincide.

As a conclusion, we have identified **four observables** that indicate the superfluid transition, and explored their behavior with respect to the defect parameters. Furthermore, these observables do not make asumptions on the system geometry. This is especially important in the case of the scattering signal where usually this signal is integrated on a carefully chosen contour such as to improve signal to noise ratio [9]. We will now present the experimental techniques used to measure the induced potential by the defect beam, something that is critical to compute the drag force.

4.2 Measurement of the induced potential

A critical measurement in order to control our experiment is to measure the potential we are able to produce with the defect beam. Recalling that the effect of the optical pumping

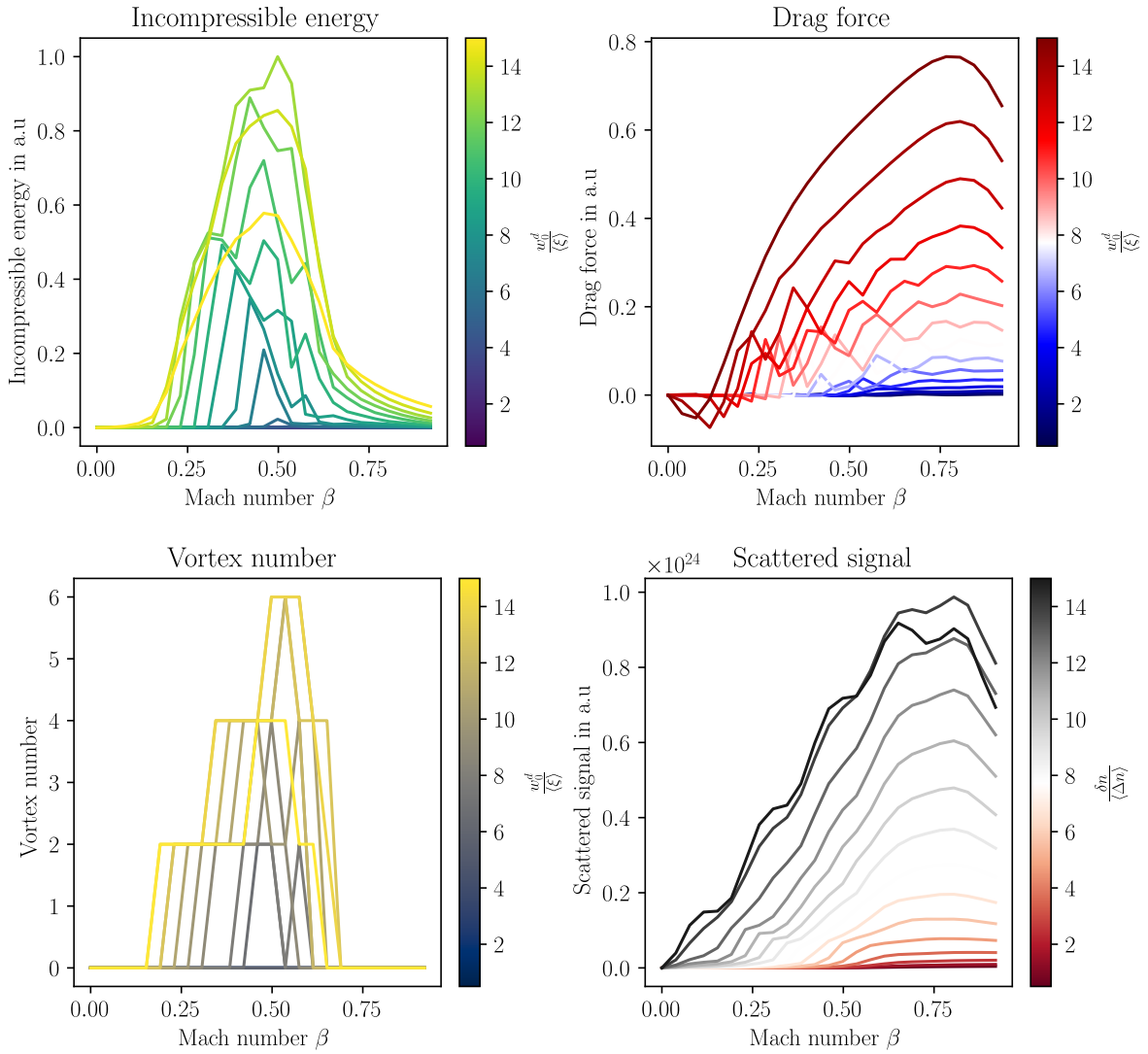

Fig. 4.6 *Behaviour of the different observables for different defect sizes. Top left: incompressible energy. Top right: drag force. Bottom left: vortex number. Bottom right: scattered signal. The defect height* $\frac{w_0^d}{\langle\xi\rangle}$ *is varied between 0.5 and 15.*

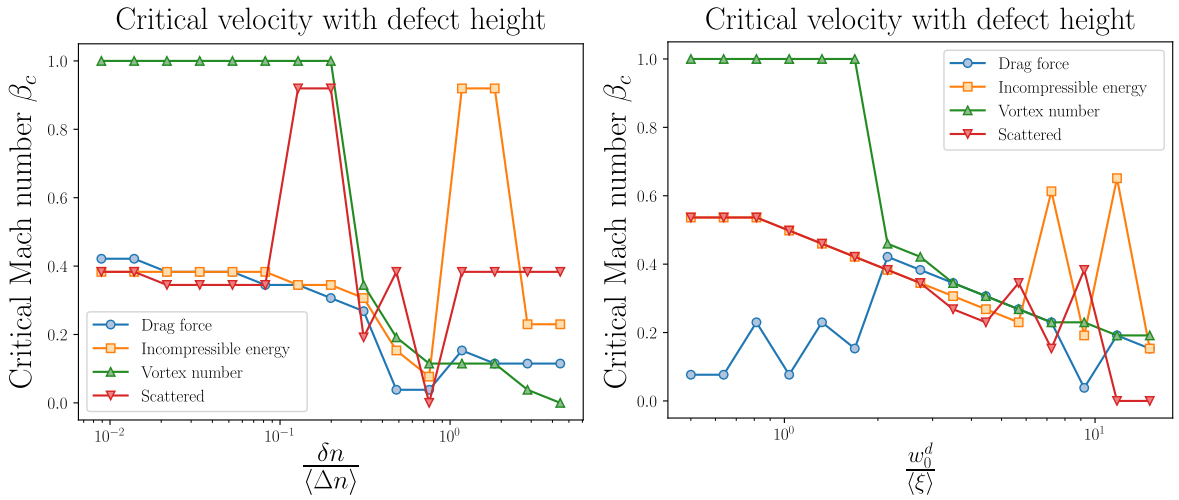

Fig. 4.7 *Left: Variation of the estimated critical Mach number* $\beta_c = \frac{v_c}{\langle c_s \rangle}$ *with defect height. Right: Variation of the estimated critical Mach number with defect waist. The inset describes the observables from which this critical velocity was infered. In blue, the velocity is infered from the zero of the drag force. In orange, the maximum of the second derivative of the incompressible energy. In green, the first velocity where the vortex number is non-zero. In red, the maximum of the second derivative of the incompressible energy.*

induced by the defect beam is to locally modulate the index of refraction, we are naturally tempted to use our phase imaging capability to measure directly the defect induced dephasing.

4.2.1 Defect dephasing

In order to measure the dephasing undergone by the fluid when interacting with the defect, we use the now usual off-axis interferometry technique. Taking the difference between the fluid's phase without defect $\phi_0(\mathbf{r}_\perp)$ and the fluid's phase with defect $\phi(\mathbf{r}_\perp)$, we recover a dephasing map $\delta\phi(\mathbf{r}_\perp)$. One can then recover the index variation (assuming it is constant along the cell) after unwrapping the phase:

$$\delta n(\mathbf{r}_\perp) = \frac{\delta\phi(\mathbf{r}_\perp)}{k_0 L}. \tag{4.9}$$

We anticipate that losses on the defect beam will induce a variation of $\delta n(\mathbf{r}_\perp)$ with the position along the cell z. However, this formula still yields the average index of refraction variation which is ultimately the relevant quantity. Fitting the index of variation map $\delta n(\mathbf{r}_\perp)$ allows to recover the effective defect size. This procedure is presented in fig.4.8

As for sufficiently strong defects, the fluid is repelled out of the defect area, the contrast becomes null in a small region at the core of the defect. This induces aliasing at the center of the recovered phase. However, we found that this aliasing was easily erased when azimuthally averaging and did not affect the fitting.

4.2.2 Transit : broadening and geometrical effects

Starting from a gaussian defect beam, one might expect that the resulting index of variation change $\delta n(\mathbf{r}_\perp)$ should also follow a gaussian profile. However, we found that experimentally the defect profile was best fitted by a Lorentzian profile. This means that the low value wings of the defect extend further than a gaussian would. The physical explanation for this broadening of the generated index of refraction variation is transit. We can understand this by thinking about what happens to a single atom being optically pumped by the defect beam: as the atom interacts with the defect beam, it will move within the vapor, and then will leave the defect beam still being in the pumped state ($|2\rangle$ in our case). As this induced population increase (resp. decrease) exponentially decays back to its equilibrium level, it will have time to diffuse away from the beam, thus broadening the effective size of the defect. In order to be a bit more quantitative, we should try and consider the convolution of the gaussian beam profile with the exponential time decay of the optical pumping and averaged over the velocity distribution. Let us assume to first order that the population in $|2\rangle$ ρ_{22} depends linearly on the defect beam power, then one can write the instantaneous population for a velocity class $\mathbf{v}$ as follows:

$$\rho_{22}(\mathbf{r}, t, \mathbf{v}) \propto \mathcal{E}_d(\mathbf{r} - \mathbf{v}t)e^{-\gamma t} f(v) \tag{4.10}$$

where $f(v)$ is the Maxwell-Boltzmann distribution and $\mathcal{E}_d$ is the normalized amplitude of the defect. Now, if we want to obtain some steady state value, we need to average. Assuming a gaussian defect of waist w_d and a temperature of the vapor T, this writes:

$$\langle\rho_{22}\rangle(\mathbf{r}) \propto \iint \mathrm{d}^3\mathbf{v}\mathrm{d}t\mathcal{E}_d e^{-\frac{2(\mathbf{r}-\mathbf{v}t)^2}{w_d^2}} e^{-\gamma t} e^{-\frac{mv^2}{2k_B T}}. \tag{4.11}$$

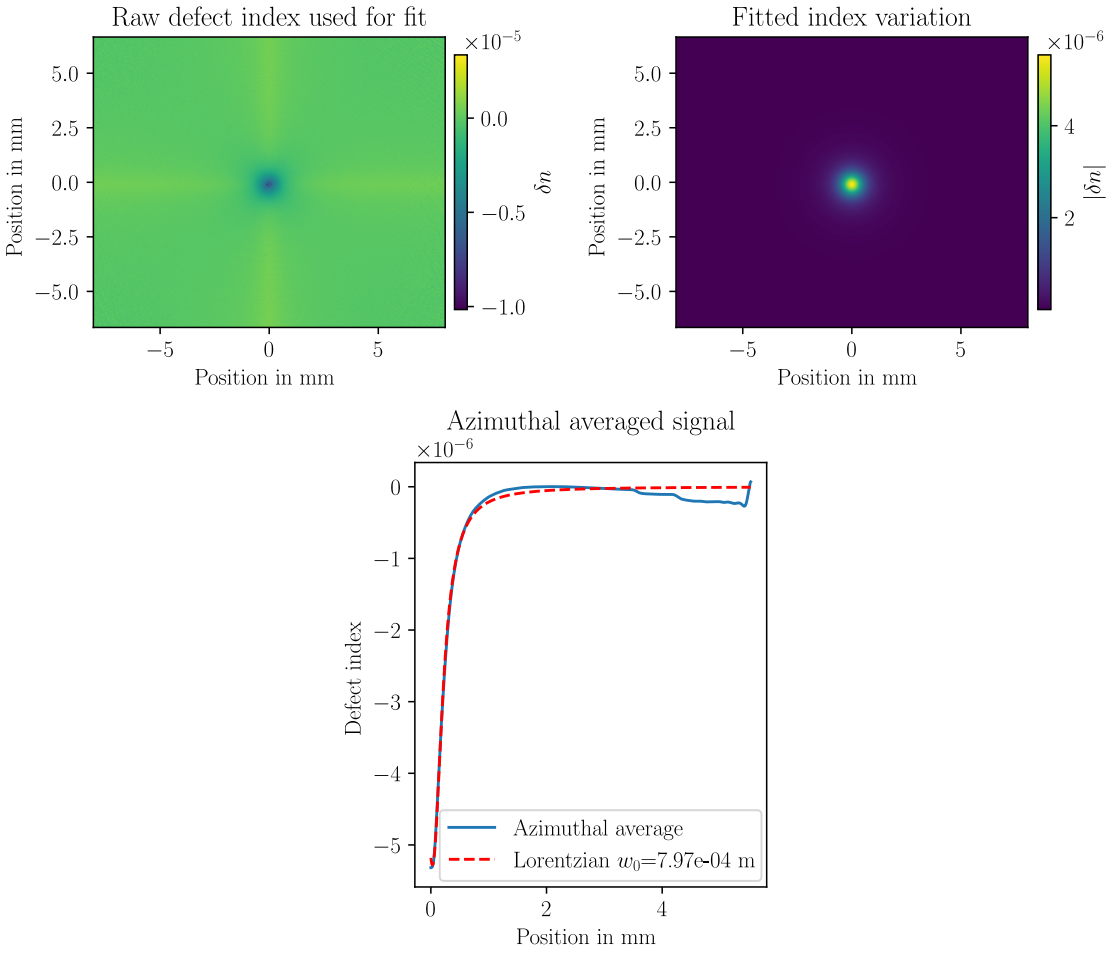

Fig. 4.8 *Defect characterization procedure. The phase is first unwrapped, then divided by $k_0 L$ in order to retrieve the index. This index is then azimuthally averaged in order to cancel phase aberrations and ease the fit by a Lorentzian profile. From the fit we can extract the maximum index variation and defect size w_0^d*

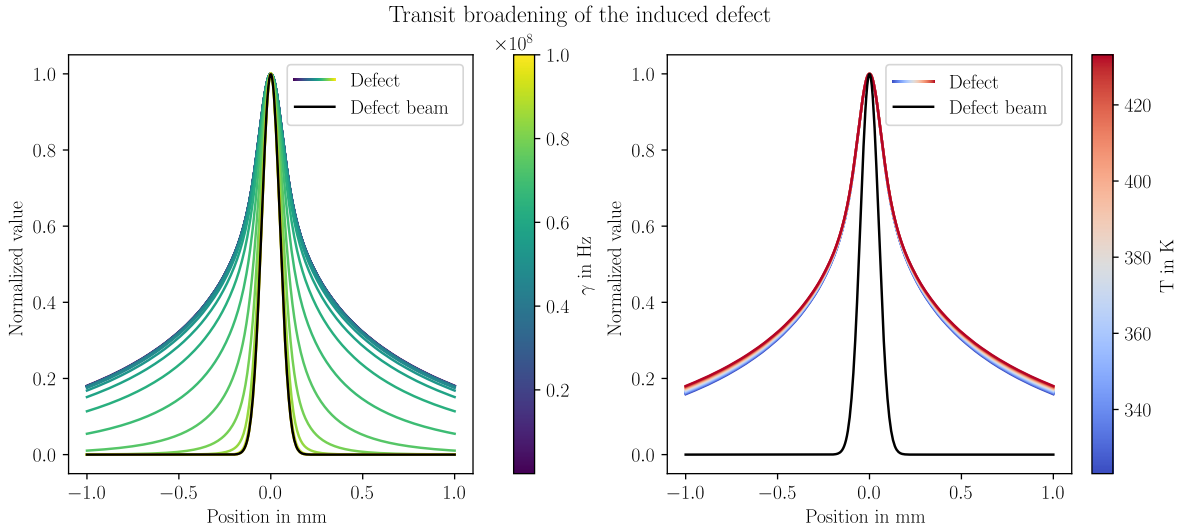

Fig. 4.9 *Effect of the lifetime of optical pumping and the temperature on the effective induced index profile. Left, the effective lifetime of the pumped state γ is varied for a constant temperature of T=152 °C. Lower lifetime lead to a more local response, and thus a smaller effective defect. Right, temperature is varied for a constant effective linewidth of γ=1 kHz: as the temperature rises, the average speed increases thus transporting pumped atoms further from the defect beam.*

Now unfortunately this expression has no closed form, however one can easily compute it numerically. The results are presented in fig.4.9.

We see that the longer-lived the pumped state is, the larger the effective defect will be. This is quite intuitive in the sense that if we think about a single atom being pumped when traversing the beam, it will be able to reach a further point if the lifetime is longer. Similarly a higher temperature will also mean a larger defect, even though in our toy-model, it has less influence as the lifetime for realistic temperature values between 50 and 160 °C. The two parameters actually merge into a single temperature dependance if we go back to the mechanism explaining the lifetime of the pumped state: the phenomenological rate γ used for the calculation is actually $\gamma_{21} = \Gamma_t$ the effective decay rate between the two ground states $|1\rangle$ and $|2\rangle$ that is dominated by the transit rate through the beam. This effect is strongly reminiscent of the profiles reported in [101] that report the broadening effects induced by thermal nonlocality in a thermo optic medium. This convolution with the exponential decay explains the final Lorentzian profile and yields excellent agreement with experimental profiles as examplified in fig.4.8.

4.2.3 Experimental setup for arbitrary potentials

In order to be able to study the effect of the defect geometry, we must be able to get full control of the defect's intensity as well as its phase. While the optical pumping mechanism is phase insensitive, controlling the phase allows to have some control over the evolution of the defect profile evolution along the propagation axis z. In order to get this simultaneous control, we use a combination of two optical paths:

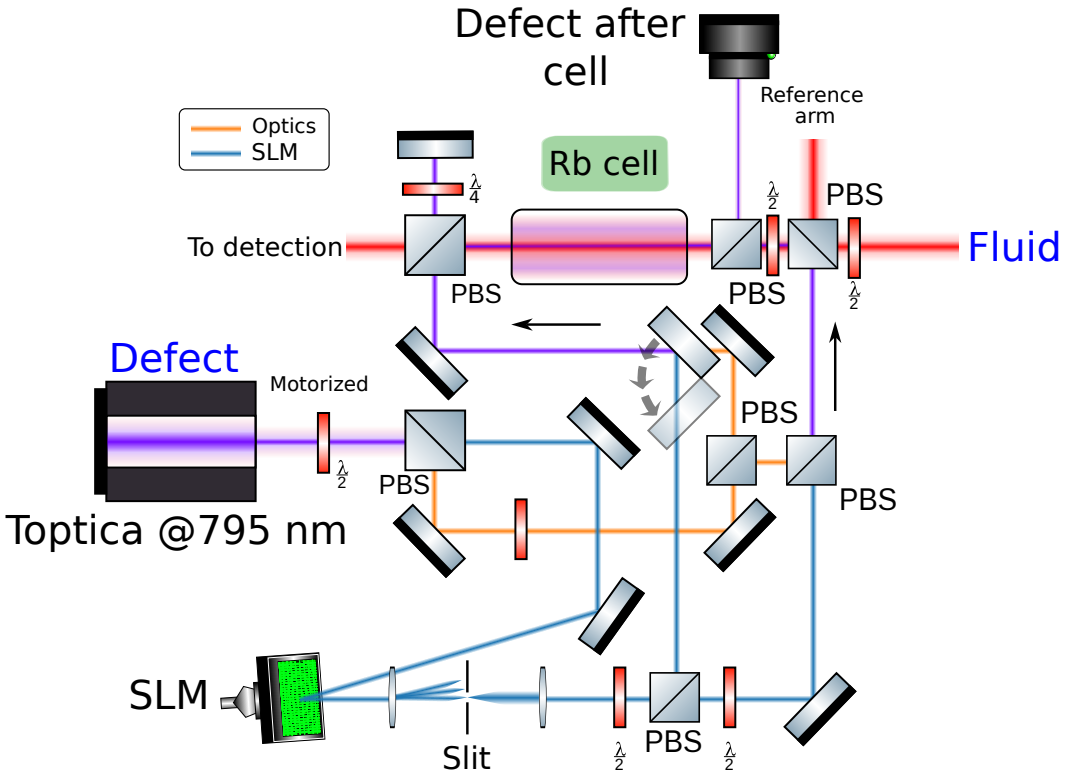

Fig. 4.10 *Experimental setup of the defect shaping arm of the experiment. The two possible paths are highlighted in orange (simple optics path) and blue (SLM shaping path). Both of these paths can either be copropagating with the fluid or counterpropagating. For simplicity the different optics in the orange path are not represented but we can add cylindrical or regular plano-convex lenses in order to reach the desired transverse and longitudinal intensity profile.*

- The "normal" path: this is the path where we will place lenses (regular plano-convex or cylindrical lenses) in order to shape the beam.
- The "SLM" path where we use a modulated diffraction grating [26] to control separately intensity and phase at the expanse of limited power efficiency.

Furthermore, we also want to be able to have a copropagating or countrapropagating beam in order to use absorption of the defect beam to our advantage to modulate the strength of the potential field as the fluid evolves along the cell. The experimental arrangement allowing this is presented in 4.10.

The defect beam is first separated in two with a polarizing beam splitter. One transmitted output is sent to the SLM (as it is aligned with the polarization axis of the SLM). The SLM plane is imaged with a $4f$ telescope, and the first order of the SLM reflected light is selected with a filter in the Fourier plane of the telescope. A half waveplate and a PBS is used to

switch between copropagation and counterpropagation. The same scheme is used for the path that does not reflect on the SLM. Examples of the achievable defect shapes are presented in fig.4.11: using a vertically arranged cylindrical lens, one can devise a one dimensional defect. We test the limits of this configuration by trying to achieve the narrowest defect beam possible. In order to keep the defect size as constant as possible along the cell, we set the lower bound of the beam waist such that the Rayleigh length is no shorter than the cell i.e 10 cm. This gives a lower bound of $w_0^d = 160\ \mu m$. Smaller defects can be achieved in transient self-focusing regimes where the interactions compensate diffraction as will be presented in the next section. We also check that we can achieve both attractive and repulsive defects as presented in fig.4.11. Furthermore, the achieved defects can be strong enough to either totally repell the fluid (top pane of fig.4.11) or attractive in a "waveguide" configuration (bottom pane of fig.4.11). This will allow to build confinement into our system. The implications of this are discussed in chap.5.

For the SLM path, we use the modulated grating approach as presented in [26] in order to achieve both amplitude and phase control of the defect beam. In this case however, we are limited in resolution since by its nature, the modulated grating technique allows phase and intensity modulation at the expense of a tradeoff in resolution since **we cannot produce details that are close to the grating's spatial frequency**. Since we use the grating to steer the beam: modulating the height of the grating for intensity and its phase to shift the phase, one needs at least one period of the grating in order to achieve this. Another way to think about this is that the grating spacing will command the spacing between diffractions orders in the Fourier plane. The achieved resolution is inversely proportional to the radius of the aperture used to select the relevant diffraction order. The **maximum radius is half the spacing between orders**, leading to a corresponding pitch in the real plane of twice the grating spacing d_G. From this, we also understand that it is best to impose a diagonal grating such as to balance the impact on resolution on both axis. The produced phase map is exemplified in fig.4.12.

From these sampling considerations, this leads to a maximal theoretical resolution of $2d_G$ if d_G is the grating pitch. For the SLM model that we use, a Holoeye Pluto-2.1-NIR-113, the pixel pitch is d_{SLM} is 8 μm. Due to pixel crosstalks effects, peak diffraction efficiency is obtained at a grating pitch of $d_G = 8$ pixels or 64 μm. After elimination of the zeroth order (as displayed in the blue arm of fig.4.10), we reach 76% light utilization efficiency. Note that contrary to the specifications provided by SLM manufacturers that often quote diffraction efficiencies above 90%, but these are **total** diffraction efficiency of all the diffraction orders. Taking this into account, one can thus realistically replicate details only up to two times the pixel pitch $2d_G = 128\ \mu$m (assuming an optical magnification factor of unity).

Having established the relevant observables, characterized the defect evolution due to the atomic medium and see how we can experimentally tailor it as we wish, I will now present the experimental results putting it all together.

4.3 Defect displacement

In this section, we will focus on the simple scattering experiment presented in the first section. A large gaussian fluid is sent into the cell, and we punch a small hole into it by generating a spatially small defect using optical pumping with a gaussian beam. We will then vary the velocity of the fluid with respect to the defect by changing the relative angle between the two

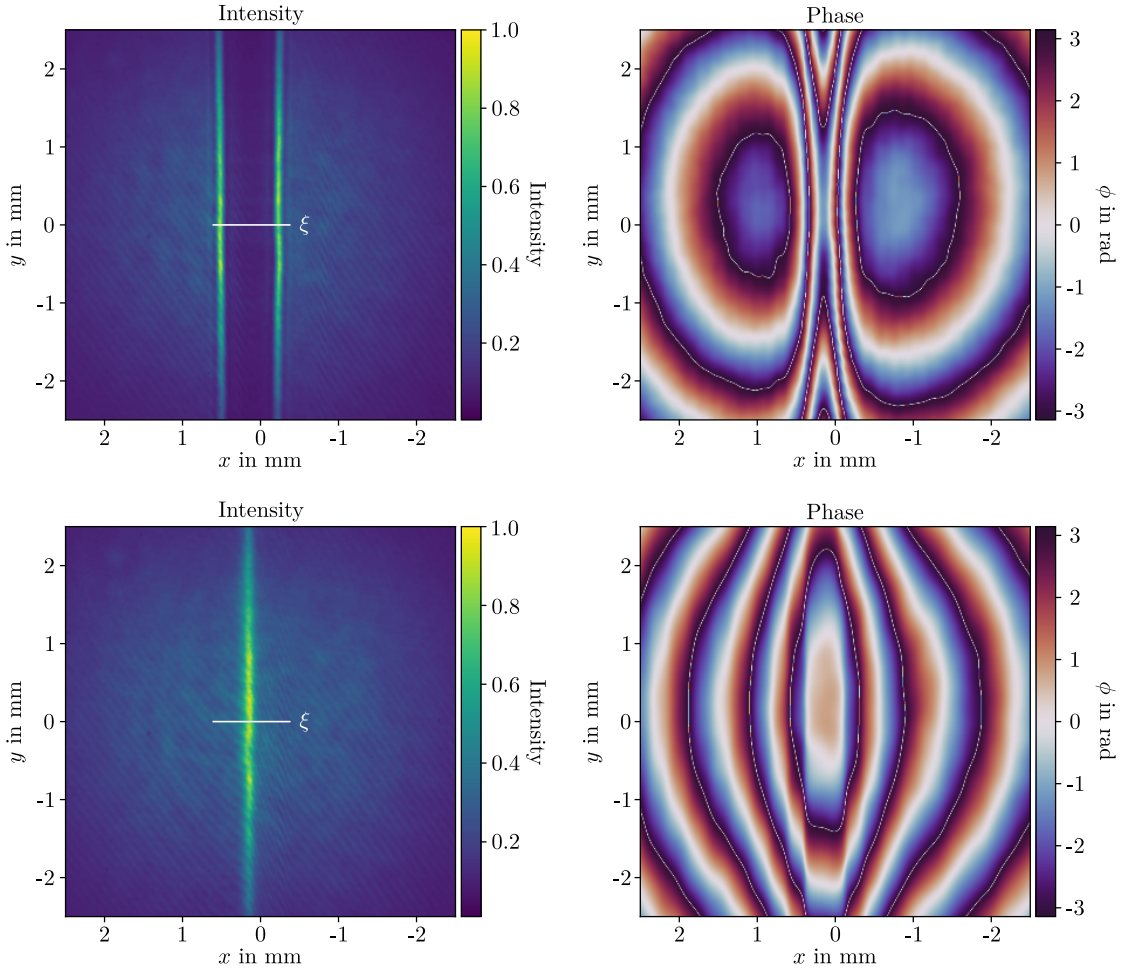

Fig. 4.11 *Example of a 1D defect in repulsive (top) or attractive configuration (bottom). The white line displays the scale of the healing length for this experimental realization. The defect is shaped with a vertical cylindrical lens. The achieved defect waist is* $w_0^d \approx 160$ *μm along the x direction. The corresponding Rayleigh length is 10cm.*

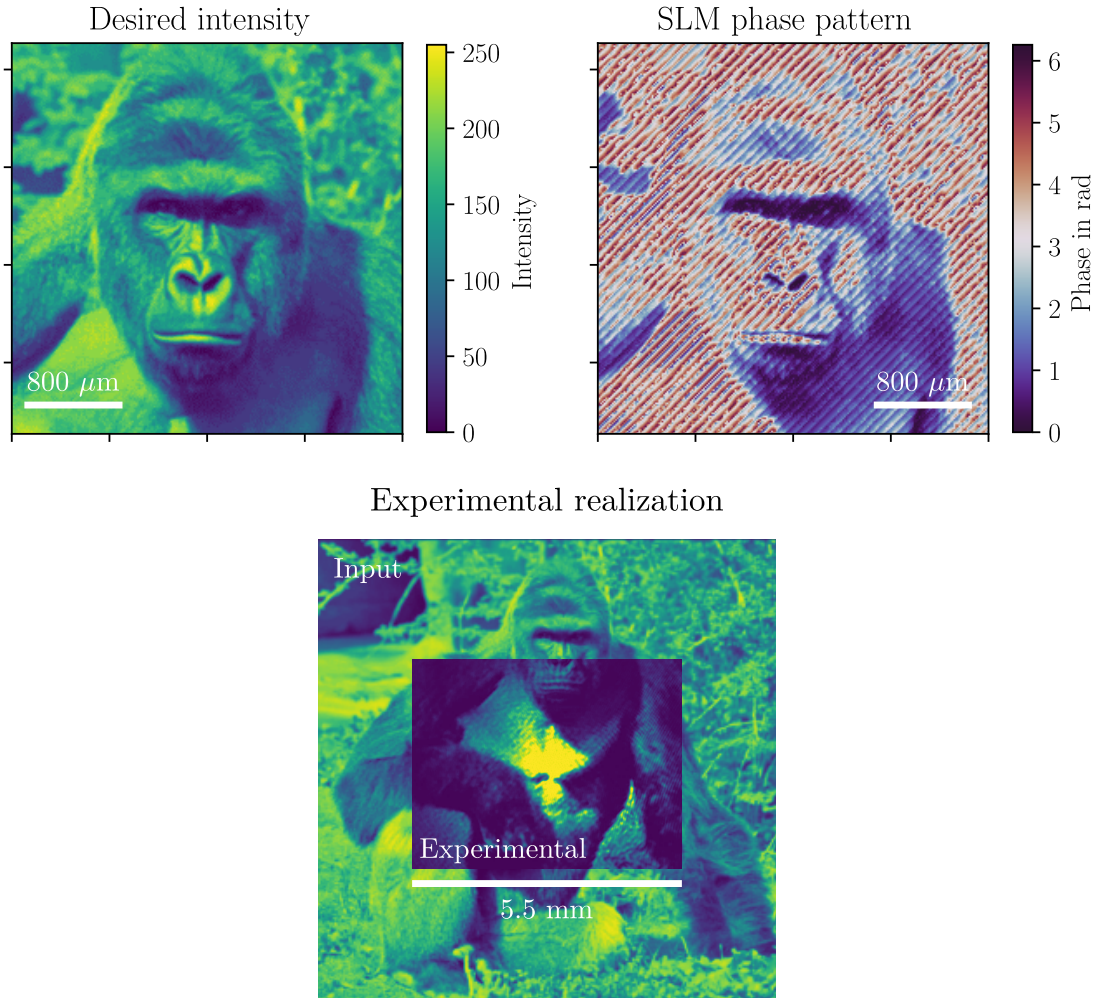

Fig. 4.12 *Example of arbitrary intensity modulation using the modulated grating technique. For readability, only the intensity is modulated here. On the left, the intensity pattern target is Harambe the gorilla. On the right, the resulting phase modulation displayed on the SLM with a diagonal grating. From the modulated phase, the sampling requirements appear clearly: the spatial details reproduced must not lie at a scale comparable to the grating. On the bottom image, we see an experimental realization with a gaussian input beam and a 2.5× optical magnification. The experimental signal is superimposed on the input to facilitate the identification of Harambe's features.*

beams using an actuated mirror.

4.3.1 Coupled model

Up until now, we have considered a static defect beam i.e we have ignored the back reaction of the fluid onto the defect beam. To take this into account, we need to introduce a coupled non-linear Schrödinger equation (CNLSE). Each beam is propagating through a non-linear medium, and the resulting system of equation is thus two time eq.1.41 with a coupling term:

$$\begin{aligned} i\frac{\partial \mathcal{E}_f}{\partial z} &= -\frac{1}{2k_f}\nabla^2\mathcal{E}_f - \frac{1}{2}n_2^f k_f c\epsilon_0|\mathcal{E}_f|^2\mathcal{E}_f + k_f n_2^{fd} c\epsilon_0|\mathcal{E}_d|^2\mathcal{E}_f - \frac{i\alpha_f}{2}\mathcal{E}_f \\ i\frac{\partial \mathcal{E}_d}{\partial z} &= -\frac{1}{2k_d}\nabla^2\mathcal{E}_d - \frac{1}{2}n_2^d k_d c\epsilon_0|\mathcal{E}_d|^2\mathcal{E}_d + k_d n_2^{fd} c\epsilon_0|\mathcal{E}_f|^2\mathcal{E}_d - \frac{i\alpha_d}{2}\mathcal{E}_d \end{aligned} \tag{4.12}$$

where k_f (resp. k_d) is the wavenumber at the frequency at the fluid beam, n_2^f is the non-linear index of the fluid (resp. defect), α_f and α_d are the linear absorption coefficients and finally n_2^{fd} is the coupling term between the two beam. In this case, this coupling term originates from the four-wave mixing process between fluid and defect beams rather than from the degenerate four-wave mixing between the fluid beam and itself (resp. the defect beam and itself). We represent the physical situation of this displacement in fig.4.13. Due to absorption, as the intensity of the fluid decreases, the critical Mach number β_c will decrease up until the point where $\beta_c \approx 0$. After this point, it means that **superfluidity will be lost at all velocities**. This means that the defect will always be displaced by the fluid due to the low intensity region at the end of the cell (in orange in fig.4.13). However, past the critical velocity at the begining of the cell (in blue in fig.4.13) the defect will be displaced from the begining of the cell, leading to an amplified defect displacement. From these simple geometrical considerations, we thus anticipate that if we monitor the displacement of the defect δr at the output of the cell when varying the fluid velocity, there should be two regimes between the part where the defect displacement is only due to the "normal" fluid, and a regime where the defect displacement is due both the "normal" and superfluid parts of the cell.

In order to check this, we can first solve the coupled equation numerically following the same split-step scheme presented in chap.1. In order to ignore geometrical effects that might be due to the fluid's profile that will be discussed in the last paragraph of this subsection, we simulate a flat fluid density profile (unless stated otherwise). We will also study the effect of fluid and defect absorption.

Effect of the defect non adiabaticity A first preliminary step that is needed is to study whether or not the brutal onset of the defect potential can induce some defect instability. In [27; 46; 47], the defect is ramped adiabatically in order to not excite the fluid. This is not the case in our setup since the potential is turned on abruptly upon entering the cell. We start without losses in order to isolate the effect of this defect "quench". For this experiment, we compare the behavior of the defect displacement at low velocities for a flat fluid density profile, as well as for a Thomas-Fermi like profile [83] corresponding to the defect profile. This profile is obtained by propagating the equation without losses, and extracting the equilibrium density profile around the defect. We vary the velocity between $\beta = 0$ and $\beta = 0.25$. We measure both the defect displacement along the propagation within the cell. The results are plotted in fig.4.14. The displacement difference between the uniform density (left) and

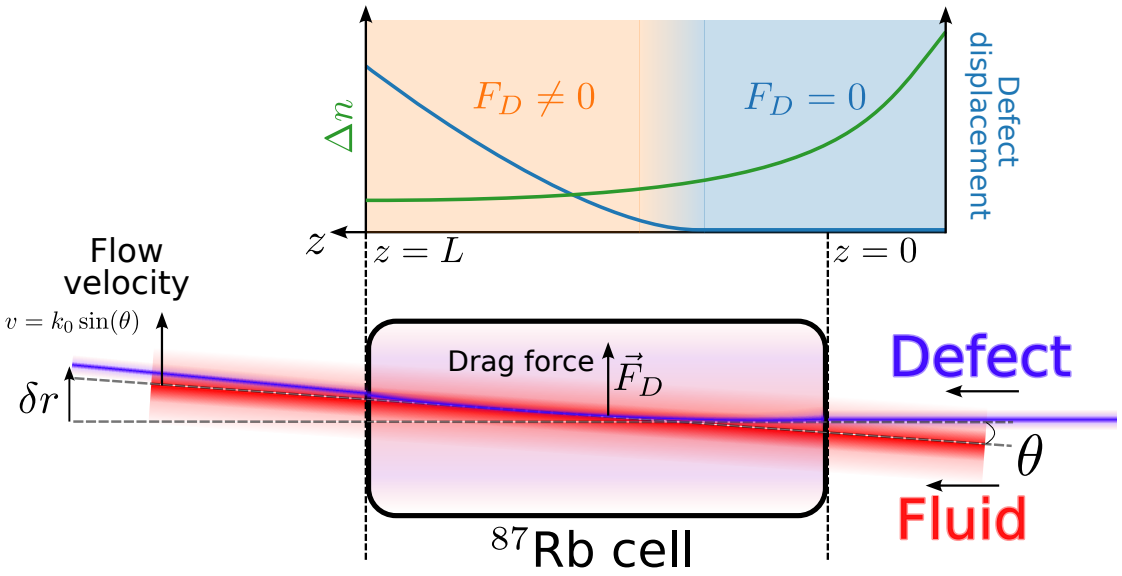

Fig. 4.13 *Physical situation of the defect displacement measurement. Using side-access through the cell, we can reconstruct z-evolution of the drag force. At some point through the cell, the interaction strength Δn drops enough such that the critical velocity for superfluidity is lower than the initial fluid velocity. The drag force can then be measured at each point of the cell by measuring the slope of the defect displacement.*

the "Thomas-Fermi" (right) if less than 20% and the qualitative behavior is very similar. Adding absorption yields surprising results, strongly enhancing this effect: with absorption, the "Thomas-Fermi" profile **halves** the defect displacement as displayed in fig.4.15

The physical interpretation of this is that the initial "shock" of the potential suddenly being turned on will tend to get "frozen" by absorption, leading to initial motion to be amplified instead of dissipating away from the defect.

Effect of fluid density profile Due to the $|\mathcal{E}_f|^2\mathcal{E}_d$ term in eq.4.12, the defect will feel an index of refraction change induced by the fluid density profile. Since the fluid beam is given an angle, its relative position with respect to the defect will change along the cell. The situation is represented in fig.4.13: the fluid beam starts at $z = 0$ below the defect and passes above the defect after the cell midpoint. We check this effect by scanning the initial position of the fluid beam waist relative to the defect between -0.5 mm and 0.5 mm. We find that the effect is significant for gaussian beams, is almost not affected by absorption. We also check that it is indeed cause by the beam profile by testing several hypergaussian profiles $\propto e^{-r^a/(w_0^f)^a}$ (with $a \in \mathbb{N}$): the higher a is, the more uniform the beam profile, and the effect is almost completely resorbed for $a = 14$. I present the results in fig.4.16 For the regular gaussian profile $a = 2$, the defect displacement induced by a shift of 0.5 mm is 8 μm, adding, losses, this displacement is almost identical just below 8 μm. This means that the **uniformity** of the beam is a **crucial element** to take into account in order to discriminate the causes of defect

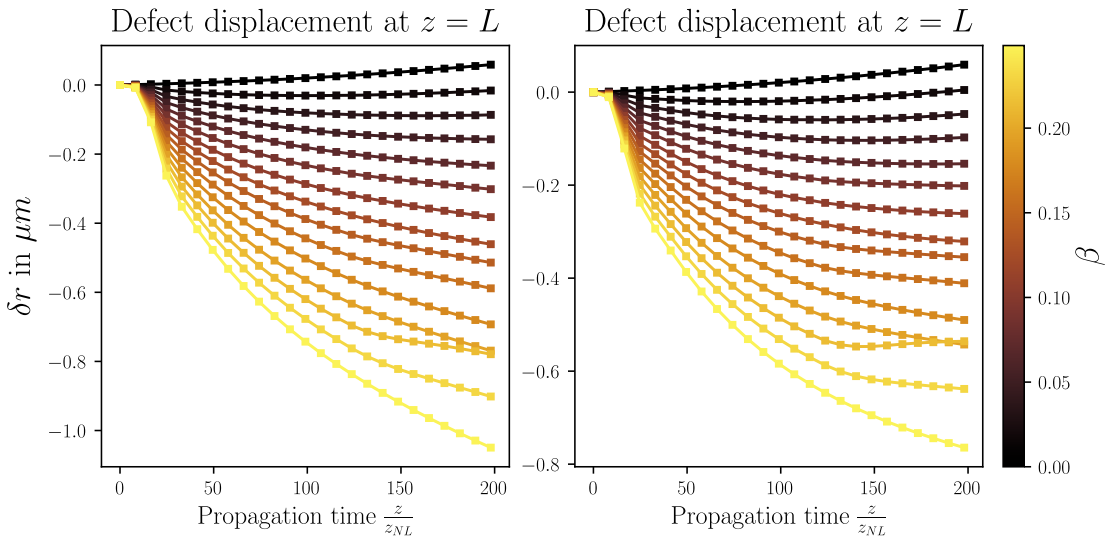

Fig. 4.14 *Left: defect displacement at low Mach number between 0 and 0.25 with a flat density profile. Right: defect displacement at low Mach number between 0 and 0.25 with a "Thomas-Fermi" density profile.*

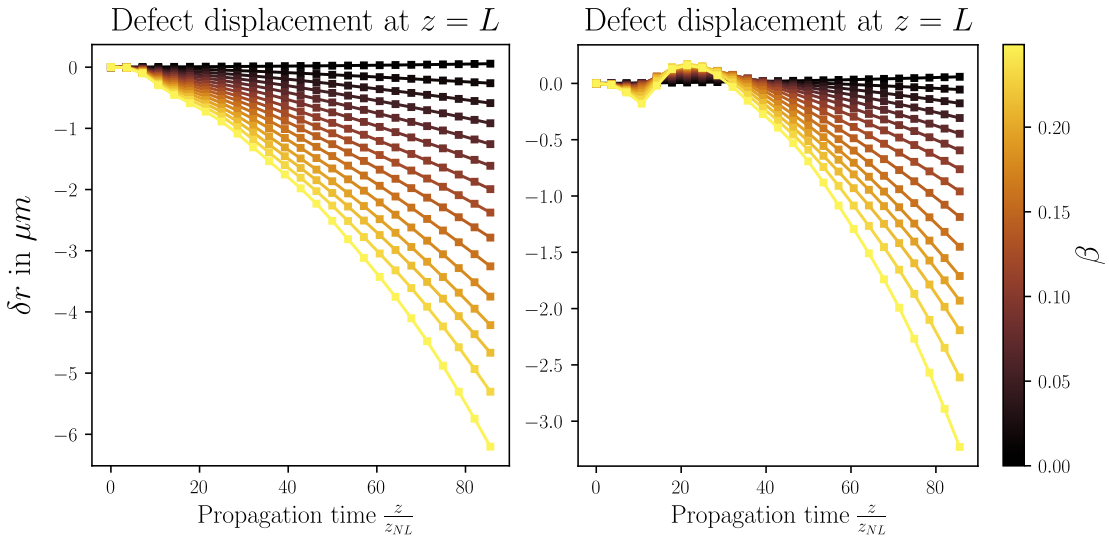

Fig. 4.15 *Left: defect displacement at low Mach number between 0 and 0.25 with a flat density profile, with absorption of the fluid. Right: defect displacement at low Mach number between 0 and 0.25 with a "Thomas-Fermi" density profile.*

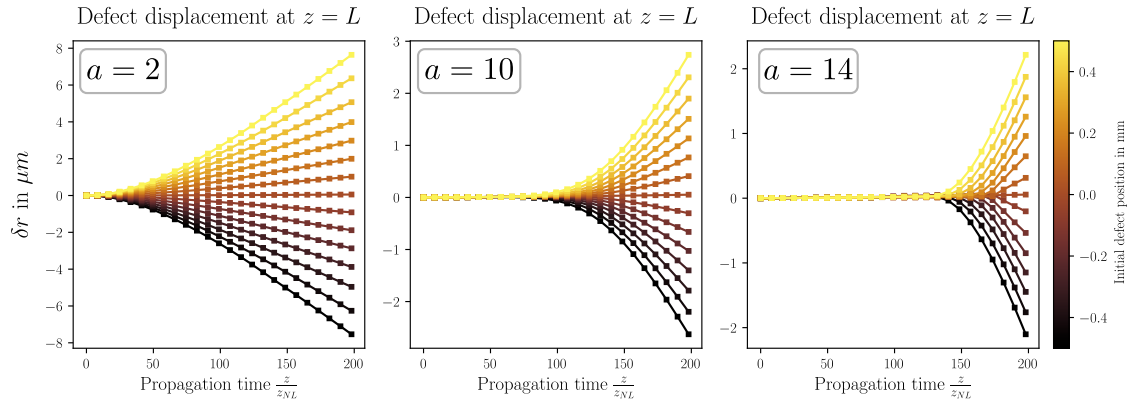

Fig. 4.16 *Displacement of the defect beam δr for different initial positions of the fluid beam center. The exponent a of the beam profile represents the exponent of the hypergaussian distribution i.e $a = 2$ is a regular gaussian beam.*

displacement.

Infered drag force: time resolved measurement The advantage of gaining access to a time resolved measurement of the defect displacement is that we can infer an estimation of the drag force from the defect curvature. Since the defect displacement is proportional to the drag force, the second derivative of the defect position with the propagation length will be proportional to the drag force:

$$F_D^{infered} \propto \partial_z^2 \delta r \tag{4.13}$$

We thus test this estimation by comparing the direct measurement of the drag force done using eq.4.3 with the two beam profiles, to the infered measurement. For this we treat a realization of the experiment by simulating the propagation through the cell as done previously in fig.4.17 .

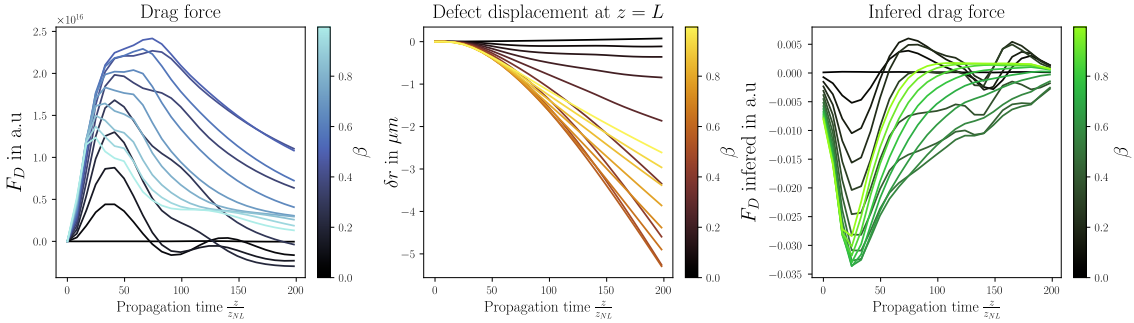

Fig. 4.17 *Comparison of the drag force measured with the two beam profiles and the infered drag force from the defect displacement. The infered drag force is computed by calculating the curvature of the defect displacement.*

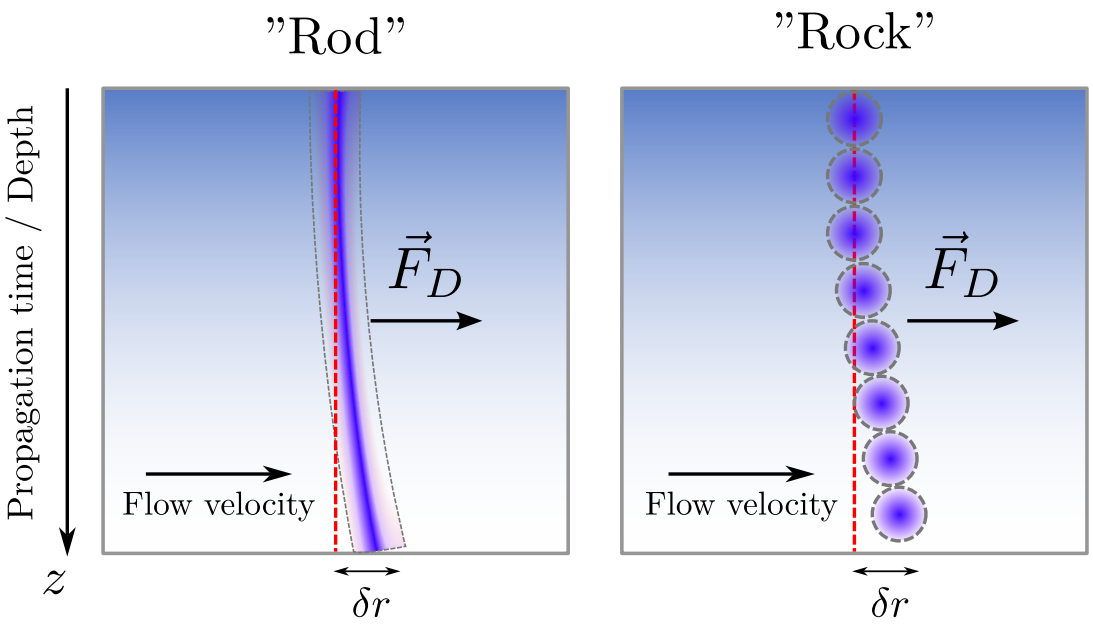

Fig. 4.18 *Figurative representation of the two possible views on the defect. Either the defect is a 3D object like a "rod" that is plunged in the stream and that bends as the fluid flows around, or the defect can be seen as a 2D object that evolved with the flow and that is dragged by the flow. The final defect displacement is represented with δr.*

We find that provided there is a sufficiently fine sampling of the evolution through the cell in order to estimate accurately the second derivative, there is an excellent agreement between the infered drag force in green, and the actual drag force in blue. Thus, we can safely use this estimation in the experiment.

Interpretation of the defect displacement Looking at the evolution of the defect displacement when increasing the fluid velocity β, an important question arises in order to properly interpret the results of our experiments (both numerical and physical). We recall the physical situation of the experiment represented in fig.4.13. The question is whether we should consider the defect as a **3D object in a stream** or rather a **2D object moving with the stream**. In simpler terms, we can think about this *Gedankenexperiment*: we identify the fluid of light with a stream of water whose velocity we can vary, of a certain depth. The depth will represent the z dimension where we monitor the evolution. We represent this in fig.4.18.

Does the defect behave more like a **"rod"** that we stick in the fluid of light that gets bent by the drag force, or rather like a **"rock"** that sinks in the fluid with a friction coefficient depending on its size (defect beam waist and height). If we think about the limiting cases of each possible interpretation, we can identify two scenarios:

- In the "rod" case, there should be a limit velocity at which it will not bend anymore when increasing the flow velocity due to its intrinsic "stiffness". This maximum velocity

will depend on the size of the defect and height of the defect. Past a certain velocity, the fluid has enough kinetic energy and does not "see" the obstacle created by the defect anymore, thus the drag force saturates as does the defect displacement, that should then decrease since the drag force gets lower and lower with increasing velocity.

- In the "rock" case, when the drag force cancels, following the same reasoning on energy, when the drag force cancels, we interpret this as the defect being displaced at the fluid velocity. There is a critical velocity at which the defect will end up at the same velocity of the fluid and get carried away in the flow, thus cancelling the drag force. In this case however, if the defect moves at the flow velocity, we do not expect the fluid displacement to saturate, but rather follow the velocity of the fluid meaning $\delta r \propto \beta L$.

Looking at the results highlighted in fig.4.17, we see that the defect displacement increases with β before saturating and decreasing. This tends to indicate that **we should rather interpret the defect experiment as a "rod"** being placed in the stream.

We have seen in this section the different subtleties induced when considering a more realistic coupled model where the defect is not considered as immobile anymore. We will now study how the critical velocity is affected by the back-reaction on the defect of the fluid. This interplay between fluid and defect will induce energy exchange that will reduce the critical velocity for superfluidity. The next section presents a detailed numerical and experimental study of this critical velocity for the two defect parameters: defect size $\frac{w_0^d}{\langle\xi\rangle}$ and height $\frac{\delta n}{\langle\Delta n\rangle}$.

4.4 Critical velocity measurement

In this section, I will present measurements of the critical velocity in the realistic coupled model, harnessing the measurement of the defect displacement to get allow for time resolution, unprecedented so far in our experiments.

4.4.1 Comparison with the uncoupled model

We first compare numerically the critical velocity infered from the observables presented in section 4.1. We study a single canonical realization: computing the drag force at $z = L$ for different Mach numbers β in fig.4.19. We compare the two models with the same parameters, adjusting the coupling term n_2^{fd} to reproduce the same δn.

Looking at the drag force, it displays a clear transition which can be fitted using a bimodal fit $F_D(\beta) = a\beta \mathrm{H}(\beta - \beta_c)$ with $(a, \beta_c) \in \mathbb{R} \times [0, 1]$ and H is the Heaviside function. We find that the critical velocity β_c reported by the coupled model is 0.31 and 0.36 for the uncoupled model, confirming that taking into account the defect displacement will lead to lower critical velocities.

We then repeat this study for different defect heights in fig.4.20 We confirm the same behavior of a reduced critical velocity. More interestingly in the coupled case, we recover very good **agreement between all of the observables**. This allows us to pick and choose the easiest observable to measure and ensures a reliable prediction of the critical velocity. Finally, the loss of superfluidity at all velocities is predicted for sufficiently high defects of $\frac{\delta n}{\Delta n} \approx 8$ in good agreement with the predictions of [46]. More quantitatively, the critical velocity in the typical regimes of our experiment in the center of the range i.e $\frac{\delta n}{\langle\Delta n\rangle} \approx 5$ hovers between 0.3 and 0.2 and is predicted to be rather around 0.37 in [47]. We attribute this to the losses.

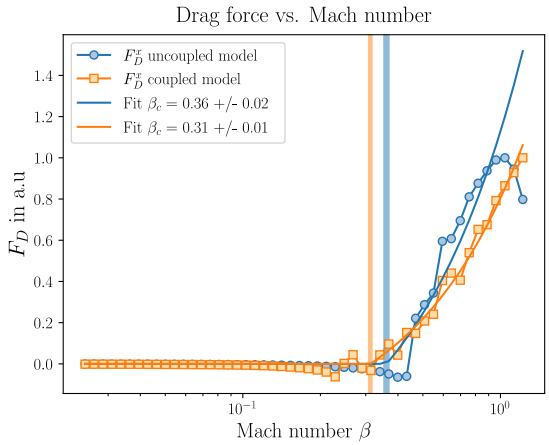

Fig. 4.19 *Drag force calculated for the uncoupled model (in blue) and for the coupled model (in orange). The solid lines represent a bimodal fit by a linear slope after some critical Mach number β_c. The shaded area indicates the 2σ confidence interval of the fit.*

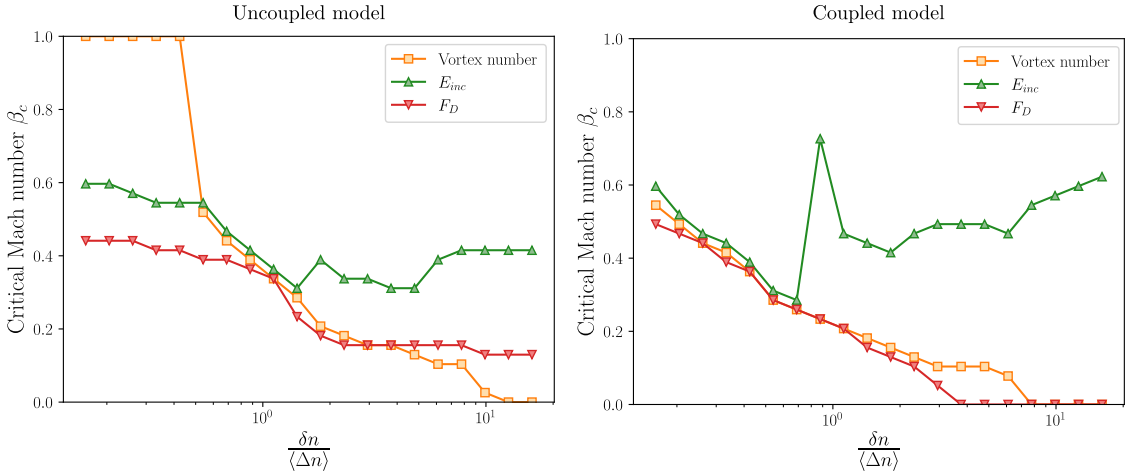

Fig. 4.20 *Comparison of the critical velocities for the uncoupled model (right) and coupled model (right). The critical velocities are extracted from the vortex number (orange), the incompressible energy (green) and the drag force (red).*

Having confirmed the sanity of the estimation of the critical velocity with different observables, wa can now comment on the experimental results.

4.4.2 Experimental setup

The complete experimental setup is depicted in fig.4.21. The fluid beam is a $w_0^f = 2.3$ mm waist beam red-detuned from the D_2 line of ^{87}Rb by $\Delta_f \approx -3$ GHz. The cell used in this experiment is an isotopically pure ^{87}Rb cell of length $L = 10$ cm and of diameter $D = 25.4$ mm. The cell temperature is maintained at around $T \approx 140^oC$ using Kapton heating tapes. The fluid laser is a MuQuans SML780 and the defect laser is a Toptica TA pro on the D_1 line. The defect beam waist is $w_0^d = 120$ μm. Both beams can be structured with an SLM using the modulated contrast technique. The fluid beam is imaged at the output face of the cell, with a band-pass interferential filter to selectively block the defect beam in co-propagating geometries. Using the reference arm in off-axis interferometry configuration, we retrieve both phase and amplitude of the phase. The defect is imaged at the output of the cell on the same camera in co-propagating geometry, and using another camera at the entrance of the cell in counter-propagating geometry. Finally, the defect can be imaged **inside** the cell by collecting the fluorescence from the side of the cell using a high numerical aperture microscope objective. The microscope objective is an infinitely conjugated objective with a $\times 5$ magnification when paired with a 200 mm focal length lens. Using a motorized translation stage, we can reconstruct the evolution of the defect beam inside the cell.

In order to probe the fluid-defect scattering, the first experiment we carry out is to vary the fluid velocity for a given defect. The velocity is varied with piezo stepped actuated screws on a mirror that is imaged at the middle of the cell to be able to change the angle of the beam with minimal change on the beam's position. Using the phase imaging provided by off-axis interferometry one can devise a servo loop in order to reach any desired angle, and more importantly, zero the mirror back to its resting position. The angle can be swept between paraxial wavenumbers such that $\frac{k_\perp}{k_0} \in [0, 0.1]$. This means that the highest angle that we can reach is at the limit of the validity of the paraxial approximation and corresponds to typical Mach numbers of several tenths. For each velocity, we measure:

- the fluid field (density and phase, with and without the defect beam)
- the defect density
- the fluid transmission
- the defect transmission.

With these measurements, we can recover all of the observables presented in the first section, as well as monitor the stability of the experiment.

I will now present the results of these measurements obtained in the co-propagating geometry.

4.4.3 Experimental results

We first attempted the experiments in the counterpropagating geometry because it was easier to extract the defect displacement for technical reasons. We subsequently switched to the

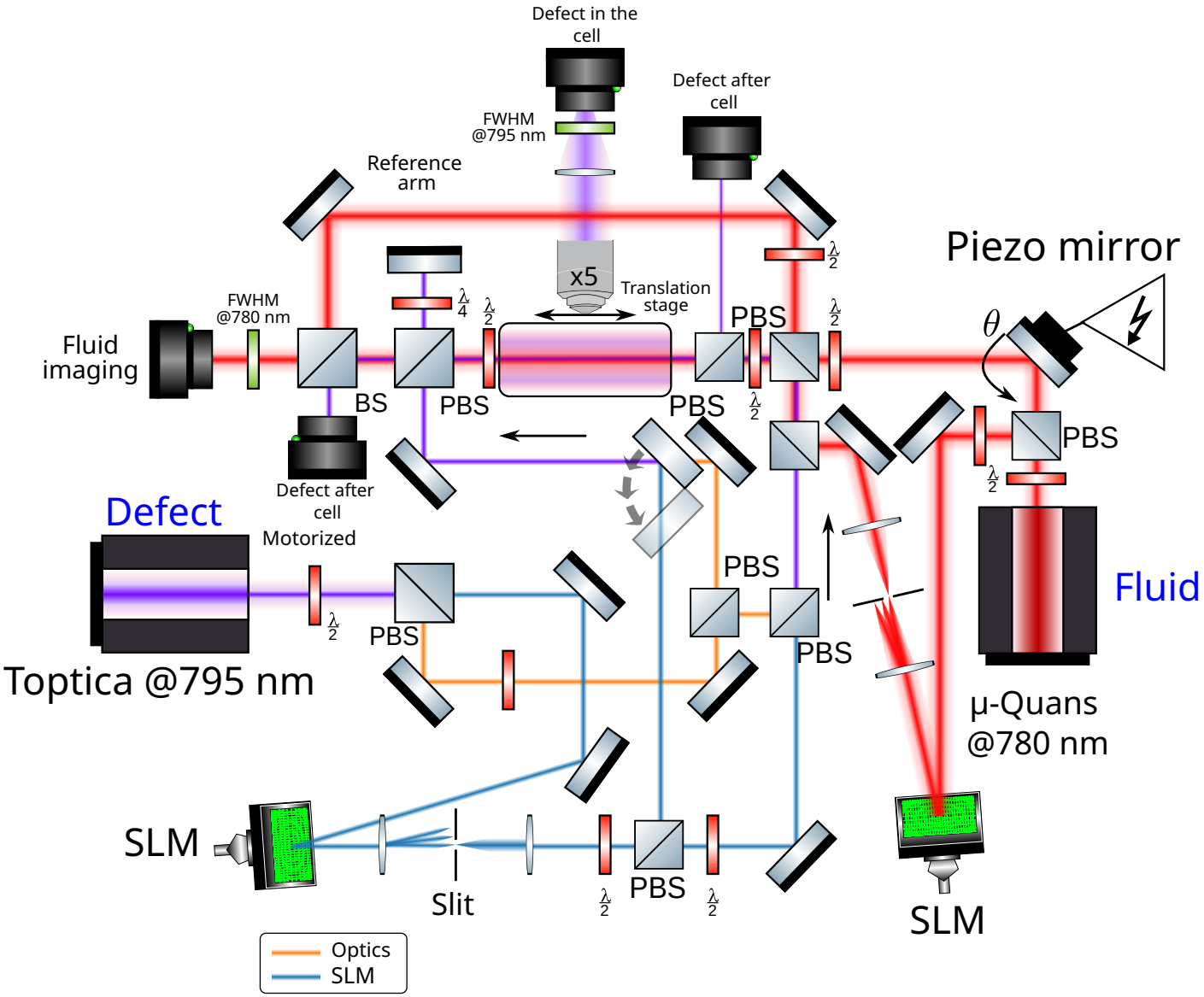

Fig. 4.21 *The full experimental setup of the defect scattering experiment. The defect beam color conventions are defined in fig.4.10. The fluid beam can be modulated with an SLM to control phase and amplitude. The evolution of the defect beam inside the cell is monitored by imaging the fluorescence of the vapor with a high numerical aperture microscope objective mounted on a translation stage.*

copropagating geometry as it yielded better results as well as being possible to simulate numerically. We start by ramping the fluid velocity and try to observe the transition at the cell output. At each velocity, cameras record both the fluid phase and amplitudes, with and without defect beam, as well as the defect beam output position. Capturing the fluid with and without the defect allows to compute the **density variation** $\delta\rho$ induced by the defect, as well as cancelling the phase induced by defocusing thereby allowing to carry out calculations

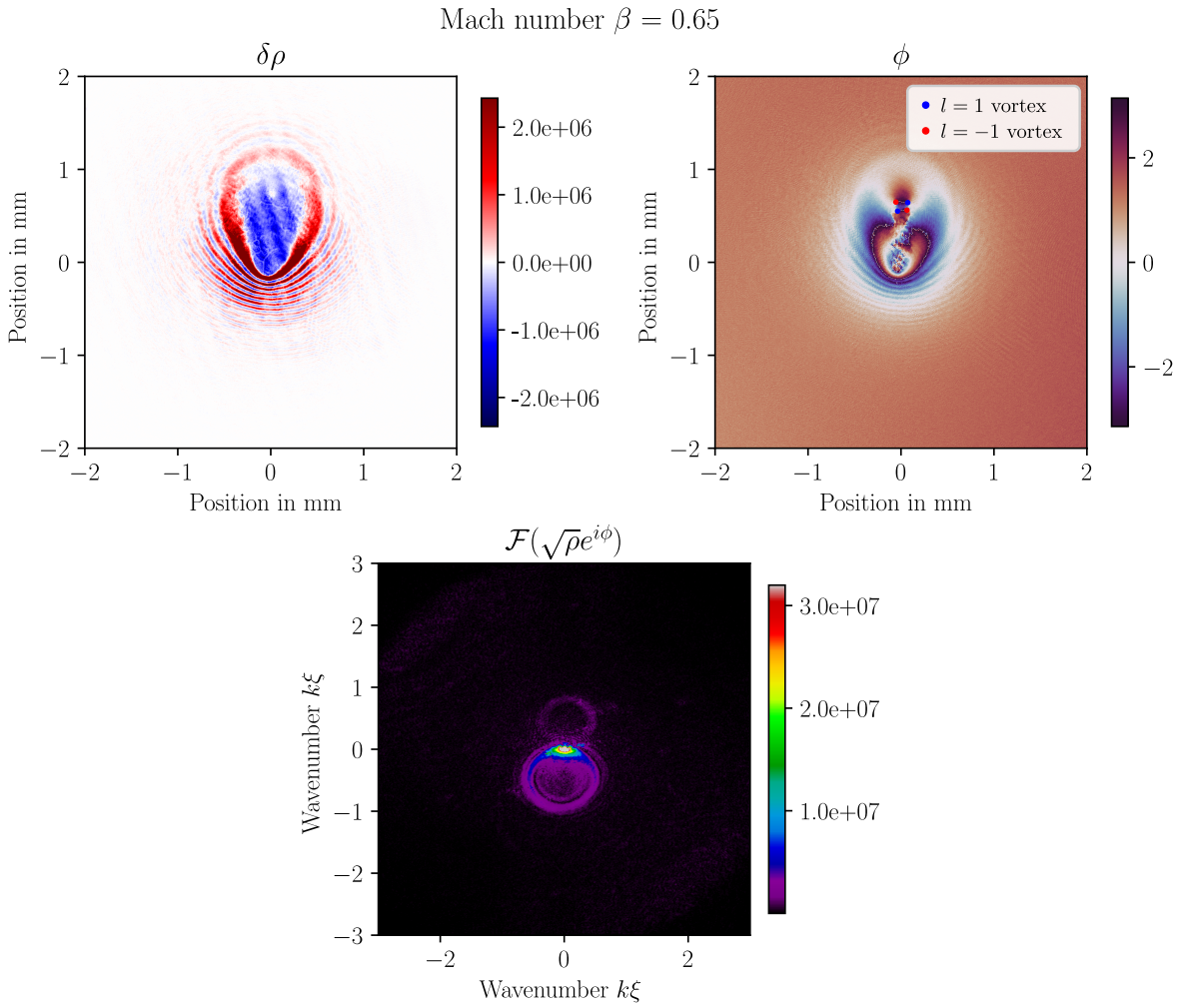

Fig. 4.22 *Fluctuation field $\delta\rho$ for a Mach number of $\beta = 0.65$. In the phase field, one can identify four vortices arranged in two dipoles that are emitted in the wake of the defect. The corresponding momentum distribution $Ae^{i(\phi-\phi_0)}$ is represented in the bottom panel. The characteristic Rayleigh rings are clearly visible.*

in the referential of the fluid. If the field obtained with the defect is denoted $Ae^{i\phi}$, and the reference field is $A_0e^{i\phi_0}$, we define the field $\sqrt{\delta\rho}e^{i(\phi-\phi_0)}$ and thus $\delta\rho = |A|^2 - |A_0|^2$. From this we can then compute the different observables in section 4.1 as a function of the Mach number β. The resulting fluctuation field is presented in fig.4.22.

The defect height is $\delta n = -4.0 \times 10^{-6}$, and the average non-linear index variation is $\langle \Delta n \rangle = -5.5 \times 10^{-5}$ measured from the dephasing of the field, leading to a relative defect height of $\frac{\delta n}{\Delta n} \approx 10^{-1}$. While this is in agreement with the simulation yielding similar results, this is enough to totally deplete the center of the fluid in fig.4.22, where one could assume that we would need $\frac{\delta n}{\langle \Delta n \rangle}$ in order to achieve this. This might be caused by non local effects reducing the effective interaction energy and will be discussed in the next subsection. Looking at the phase, we find the expected [72] pairs of vortices in the wake of the defect. The momentum distribution displays the familiar Rayleigh ring [38] indicative of the scattering

between defect and fluid. We can then infer the following observables from these fields:

- Drag force from the measured defect profile
- Compressible and incompressible energies using the density and phase
- Total scattered amplitude from the momentum distribution

We can finally plot the defect displacement as a function of the Mach number and obtain fig.4.23.

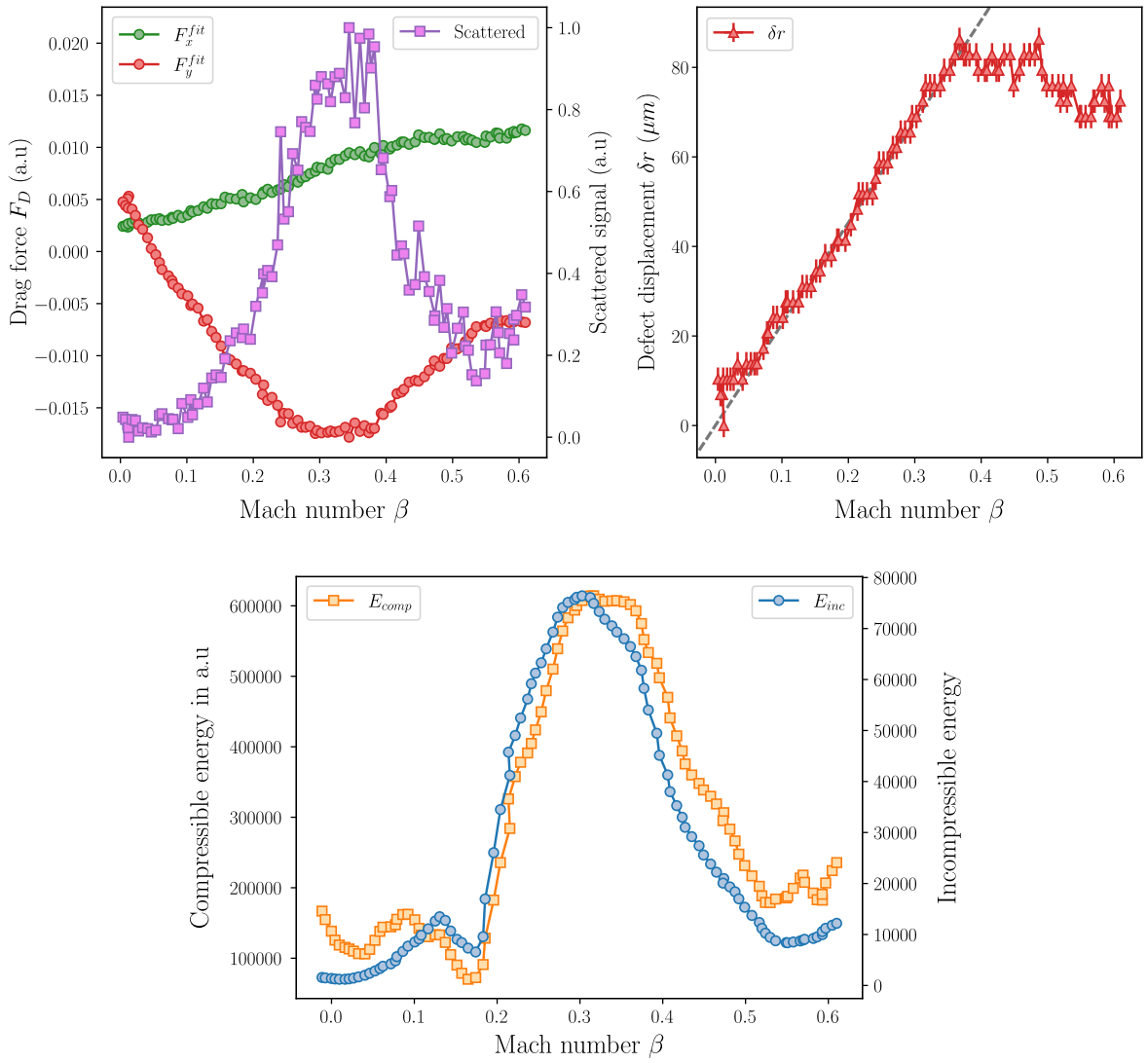

Fig. 4.23 *Top left: drag force along both axes (velocity is along y) infered from the fitted potential. In green, along x, in red along y. In violet, the total scattered amplitude is represented. Top right: the defect displacement measured at the output of the cell. The dashed line is a linear fit to highlight the deviation at low Mach numbers. Bottom: The total compressible (orange) and incompressible (blue) energies as a function of the Mach number.*

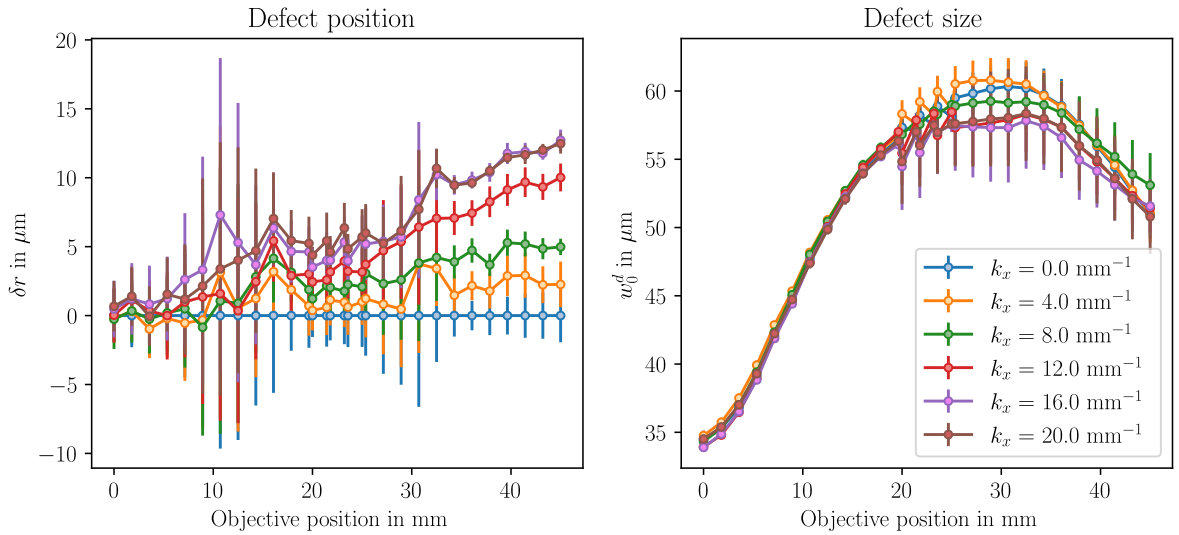

Fig. 4.24 *Left: Defect displacement as measured from the side, normalized by the zero velocity profile. Right: defect beam waist w_0^d measured from the side. The fluid input momenta are indicated in the inset.*

Looking at the results of fig.4.23, we find an excellent agreement with the numerical results: both the scattered amplitude and incompressible energies show a sharp transition at around $\beta = 0.2$ indicative of the superfluid transition. The **defect displacement** and **drag force** however do not display a measurable transition, which is surprising. For the drag force, this is not exceedingly surprising since we compute the drag force on the potential that was infered at zero velocity. If this potential changes due to the fluid back-reaction, not only in position (that we can correct since we measure the output position) but also in shape, then we do not actually compute the drag force when using the zero velocity profile. Attempts were made to use the output profile of the defect beam, however this yielded unsatisfactory results due to the broadening effects desribed in section 4.2.

On the other hand, concerning the ouptut defect beam position, this is most probably due to geometrical effects, and the input quench of the potential in the fluid. However, the defect displacement saturates at $\beta = 0.35$, before going down, confirming the "rod" point of view discussed in section 4.3. In order to explore these hypothesis, we can try to solve these short comings by looking at the beam profile from the side of the cell, in order to both try to estimate the "instantaneous" drag force, as well as distinguish geometrical effects.

For this, we set the fluid velocity using the phase of the beam in a servo loop to achieve a repeatable operation of the piezo actuated screws. We then scan the position of the microscope objective along the cell. The velocity is set along the vertical axis y such that the defect displacement occurs on this axis since the optical access is on the side of the Rubidium cell (see fig.4.21). From each beam profile, we can extract the beam position in y using a gaussian fit as well as recovering the defect beam waist w_0^d. The method is detailed in Appendix A. We present the results of this scan in 4.24.

The velocity of the fluid beam is scanned between 0 and 20 mm^{-1}, the objective is scanned over 50 mm in two phases using a motorized stage of 25 mm travel, as well as a manual 25 mm stage. Each velocity and position is repeated three times. The beam displacement is

seen to be increasing with the velocity as expected, however the mechanical stability of the translation stage is very poor. This instability is lower for positions after 30 mm where the manual stage is at its lowest extension, indicating that this is certainly the limiting component. This prevents any definitive conclusions to be reached from this data, especially infering the drag force as presented in eq.4.13. Estimation of the beam waist is on the contrary substantially more robust, and shows a rapid expansion of the beam before a contraction. This is consistant with the fact that the defect beam is in a slightly self-focusing regime, and we can use this information in order to tune the size of the defect **temporally**. Interestingly, it also shows that we can reach beams that propagate well under the limitations imposed by their Rayleigh length in vacuum: the defect beam is seen to have expanded of 15mm after 50mm, whereas the corresponding Rayleigh length for a 35 μm beam is 3.6 mm.

As a conclusion, the experimental results allow to measure the critical velocity for several coinciding observables, in good agreement with the values of the litterature [46; 47] as well as the numerical simulations. Further developments of the defect beam imaging should allow to reconstruct more reliably beam profiles, allowing to distinguish displacements induced by geometrical effects from the displacements induced by the drag force, as well as estimaging the drag force all along the fluid evolution. Another important fact is that we find that in order to replicate the experimental defect displacements in our simulations, we need to lower substantially the nonlinear index of refraction. To reconcile the numerical and experimental results, we now present a direct measurement of the dispersion relation to extract the effective interaction strength Δn.

4.5 Dispersion relation measurements

In order to probe the discrepancy between the measured values of n_2 and the observed phenomenology during the experiments, we want to **directly** measure the Bogoliubov dispersion relation. Measuring this dispersion relation allows to probe the actual interactions between photons instead of relying on a global phase shift. Let us first present the measurement technique.

4.5.1 Bragg spectroscopy

In order to measure the Bogoliubov dispersion relation, we could employ the group velocity measurement presented in [34]. However, a more direct measurement technique inspired from the cold gases has been since developped in [81]. The principle of this technique is to probe the dispersion by directly seeding a density fluctuation at a single $\mathbf{k}_\perp$ momentum, and observing the evolution of the structure factor $S(\mathbf{k}_\perp)$ defined in eq.2.19 as $\mathbf{k}_\perp$ is varied. It can be shown [81] that the contrast of the obtained fringes on our camera $C = \frac{I_{max}-I_{min}}{I_{max}+I_{min}}$ is:

$$C(\mathbf{k}_\perp) = |US(\mathbf{k}_\perp)\sin\left[\Omega_B(\mathbf{k}_\perp)L\right]|, \tag{4.14}$$

where L is the cell length, and U is the maximum of the contrast fixed by the imagery and that can be calibrated by scanning $\mathbf{k}_\perp$ without a cell in the non-interacting case (since $S(\mathbf{k}_\perp) = 1$ in this case). By retrieving the minima of contrast, we find the points at which $\Omega_B(\mathbf{k}_\perp) = p\frac{\pi}{L}$ with $p \in \mathbb{N}$. If we want to get the best resolution at low $\mathbf{k}_\perp$ where the effects of the interactions are the most visible, it is paramount to have a **large uniform** beam along

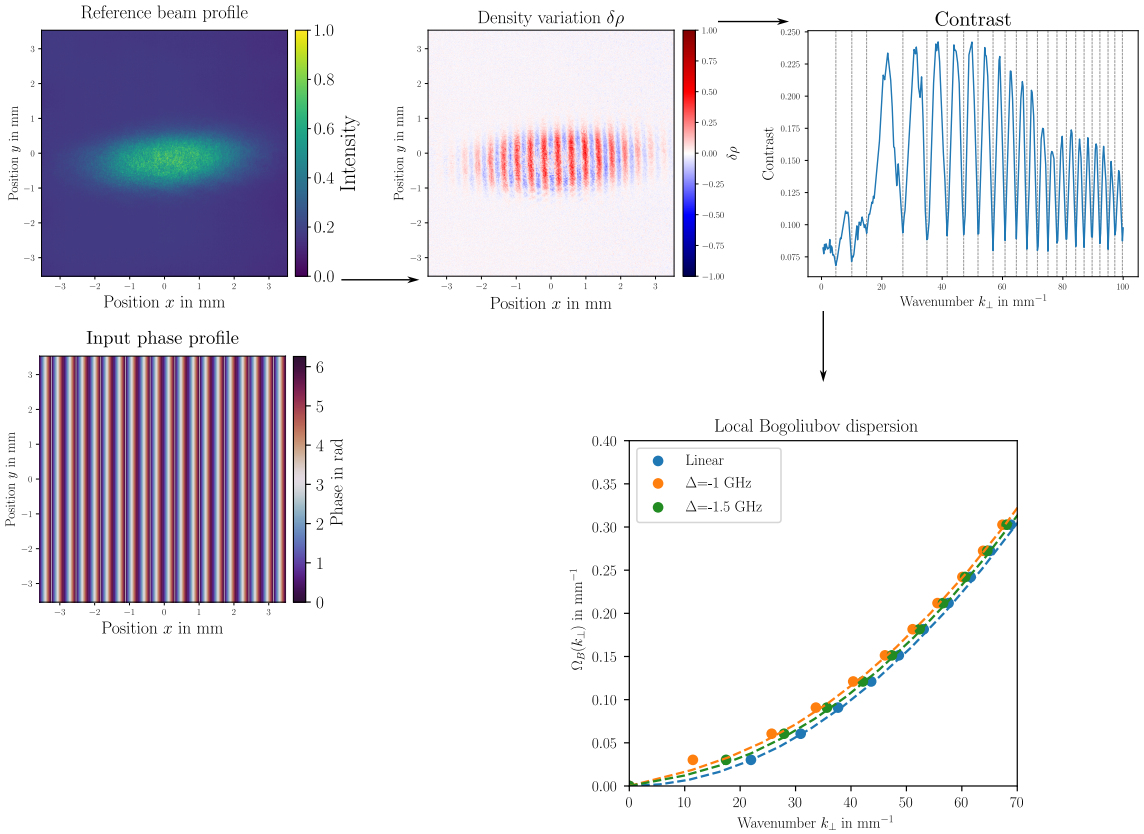

Fig. 4.25 *Bragg spectroscopy measurement. The density profile is elliptical to increase the uniformity along x. The fluid is modulated by a sinusoidal phase pattern in order to generate a density modulation. Contrast is recovered through Fourier analysis. By fitting the local maxima of the contrast, we recover the Bogoliubov dispersion. The dispersion is plotted for different values of the laser detuning Δ, as well as in the non-interacting case. The dashed line represent the fit of the non-linear dephasing Δn by a local model of eq.1.29.*

the direction of modulation. In [81], the beam is an elongated elliptical beam along x and the modulation is applied along this direction in order to have a nearly uniform fluid at the center. The perturbation is imposed in the fluid by using an SLM which allows to measure the dispersion of the fluid using the SLM arm of the fluid in fig.4.21, without changing the configuration of the experiment. Furthermore, we can also use the SLM flatten the density profile of the beam in order to get better results.

In fig.4.25, we present a typical experiment run. The modulation imposed on the fluid is a sinusoidal phase modulation applied with the SLM. This generates a density modulation. By **Fourier transforming the density**, we can **monitor the intensity of the satellite peak** appearing, and thus extract the contrast. We then fit the local minima of the contrast in order to extract the Bogoliubov dispersion. The orange and green curves represent the dispersion for a laser detuning (with respect to the $F = 2 \rightarrow F'$ $F = 3 \rightarrow F'$ crossover resonance of ^{87}Rb) of -1 and -1.5 GHz respectively. The blue curve was taken without cell, and we notice the typical

shift of the orange and green curves with respect to the blue curve: this is due to the linear part of the dispersion, indicative of the photon-photon interactions. We see in fig.4.25 the limitation of this technique: with the current setup, the low $k_\perp$ values are not accessible since for large wavelengths, it becomes challenging to measure the contrast, since the satellite peak becomes to close to the zeroth order. Furthermore, since the structure factor is expected to go to zero at low $k_\perp$ [81], the low $k_\perp$ region is by definition less accessible, and limited by the length of the cell.

However, these measurements still allow for a quantitative assessment of the interaction strength. When fitting the dispersions, we find that the recovered Δn values are quite low compared to the values extracted from the non-linear dephasing. This can be explained when taking into accound **nonlocality** that will modify the Bogoliubov dispersion.

4.5.2 Effect of non-locality on the Bogoliubov dispersion

One obvious phenomenon in the context of hot atomic vapors that can reduce the effective non-linearity is **non-locality**. Due to the atomic motion, the response at one point of the fluid will not only depend on the density at this point, but rather the density within a certain radius σ:

$$\Delta n(\mathbf{r}) = G * \Delta n(\mathbf{r}) = \int \mathrm{d}\mathbf{r}' G(\mathbf{r}-\mathbf{r}')\Delta n(\mathbf{r}'), \tag{4.15}$$

where $G(\mathbf{r})$ is the Green function representing the nonlocal response of the medium, and $\Delta n \propto n_2|\mathcal{E}|^2$ is the nonlinear index of refraction change. This nonlocal response has already been observed in [101] and has been proven to be a crucial stabilizing phenomenon in the study of collapse instabilities [11]. It can be shown [35; 101] in this case that the Bogoliubov dispersion relation is modified as follows:

$$\Omega_B(\mathbf{k}_\perp) = \sqrt{\frac{k_\perp^2}{2k_0}\left(\frac{k_\perp^2}{2k_0} + \Delta n G(\mathbf{k}_\perp)\right)}. \tag{4.16}$$

In our case, this nonlocality can be modeled either by taking into account the **diffusive** motion of the atom through the vapor or the **ballistic** motion of the atoms. This leads to the following nonlocal kernels:

$$\begin{aligned} G_B(k_\perp) &= \sqrt{\pi}\frac{1}{k_\perp\sigma_b} e^{\frac{1}{(k_\perp\sigma_b)^2}}\,\mathrm{Erfc}\left(\frac{1}{k_\perp\sigma_b}\right) \\ G_D(k_\perp) &= \frac{1}{1+\sigma_D^2 k_\perp^2}, \end{aligned} \tag{4.17}$$

where G_D and G_B are the diffusive and ballistic kernels. The ballistic kernel is obtained when solving the evolution equation of the excited state population taking into account the atomic velocity distribution [35]. In this sense it is the crudest model. A more refined model is the diffusive kernel that is obtained when solving the diffusion of the Rubidium atoms within the vapor. However quantitative predictions of the associated nonlocal lengths are very challenging since they need to simultaneously predict the internal state of the atoms in order to obtain their diffusion cross-section, and solve the atomic motion with this given cross-section. It however allows to link measurements to an effective diffusion length. We can then try to fit these nonlocal kernels to the experimental dispersions.

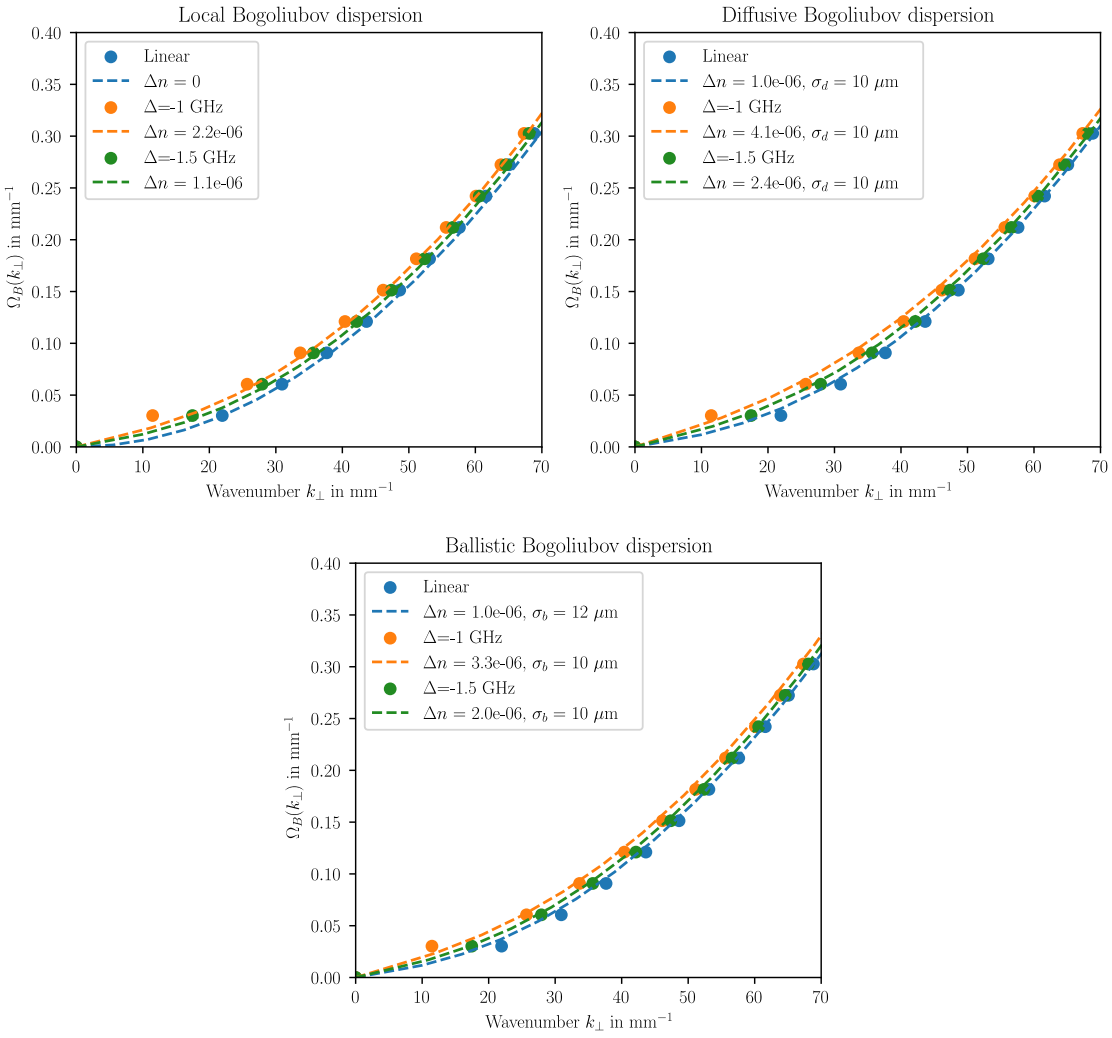

Fig. 4.26 *Effect of non-locality on the Bogoliubov dispersion. The experimental dispersions (dots) are fitted with either local or nonlocal models with the dashed lines. The extracted values of both Δn and σ_b or σ_d are displayed in the inset.*

We present the results of this comparison in fig.4.26. The same experimental results (dots) are fitted with either a local (top left), diffusive nonlocal model (top right) or ballistic nonlocal model (bottom). The fitted values of the nonlinear index of refraction variation Δn and nonlocal lengths σ_d or σ_b are indicated in the inset, as well as the laser detuning. The local model yields values of Δn significantly lower than the two nonlocal models. The diffusive model reports the highest value of Δn but the fitting procedure of the two nonlocal models yields the same nonlocal lengths. This is certainly due to the limited number of points that are available at low $k_\perp$ since this is where the deviation between the models is the most visible. In the case of a high non-locality, we expect the Bogoliubov dispersion to display an inflexion point at low k as reported in [100]. The first point of the orange curve does seem to indicate such an inflexion point, but the resolution is too limited to be able to conclude.

As a conclusion, future implementations of this measurement will include a flat top beam, a large beam size in order to achieve better better low-k resolution. This will allow to accurately characterize the nonlocal response of the medium and allow us to conclude on which model most accurately describes the non-locality in our medium.

Conclusion

In this chapter, we have carried out an extensive study of the **superfluid behavior** of light, focusing on reconciling the different observables that had been used in previous works [9; 72] in order to extract definite criteria for the superfluid transition. We have presented a scattering experiment as a testbed for the critical velocity for superfluidity, recovering theoretical results [46; 47] for the behavior of the critical velocity as a function of defect size and height. With a novel experimental technique, we presented preliminary **time-resolved** measurements of the defect beam evolution inside of the cell, allowing for time-resolved measurements of the drag force. This experiment also highlighted the important role of **non-locality**, and future developments of the experiment will aim at increasing the fluid uniformity using beam shaping techniques in order to improve the spatial resolution of dispersion relation measurements, as well as mitigating the geometrical effects polluting the defect displacement. We will now conclude this manuscript by presenting recent results employing these beam shaping techniques to study ensembles of vortices and turbulence.

Chapter 5

From turbulence to quantum phase transitions

What can we simulate with our platform ?

Throughout this thesis, we have progressively presented how we can measure, predict and control the different degrees of freedom of the system. These degrees of freedom are the colored terms of eq.1.10 that have accompanied us all along this manuscript. In this chapter, I will now present several on-going or future experiments that address these tuning knobs simultaneously in order to explore new physics like turbulence or quantum phase transitions.

5.1 Hydrodynamics and quantum turbulence

Having demonstrated the striking superfluid behavior of light in the previous chapter 4, and particularly the appearance of quantized vortices, a natural question then arises: what about turbulent behavior ? What happens when we inject more kinetic energy into the system such that a large number of vortices are nucleated ? Can we describe their trajectories and extract relevant hydrodynamical quantities from this study ?

5.1.1 From dynamical instabilities to turbulence

It is predicted [90] that when two components of a quantum fluid collide, the Doppler shift due to the velocity difference between the two components shifts the Bogoliubov dispersion such that an imaginary branch appears, seeding a **dynamical instability** leading to turbulent behavior. In the case of a fluid with two counter streaming components colliding each other at a relative velocity v, the dispersion relation Ω_B for a momentum q is modified as follows [90]:

$$\Omega_B(q)\xi^2 = \frac{1}{2}q\xi\left[\beta \pm \sqrt{2+\beta^2+(q\xi)^2 \pm 2\sqrt{1+2\beta^2+\beta^2(q\xi)^2}}\right], \tag{5.1}$$

where $\beta = \frac{v}{c_s}$ is the Mach number or in this context the **stream parameter** and ξ is the healing length. In this dispersion relation, the $\pm$ sign distinguishes the two components. This is what explains the emergence of the imaginary branch of the dispersion. Depending on the value

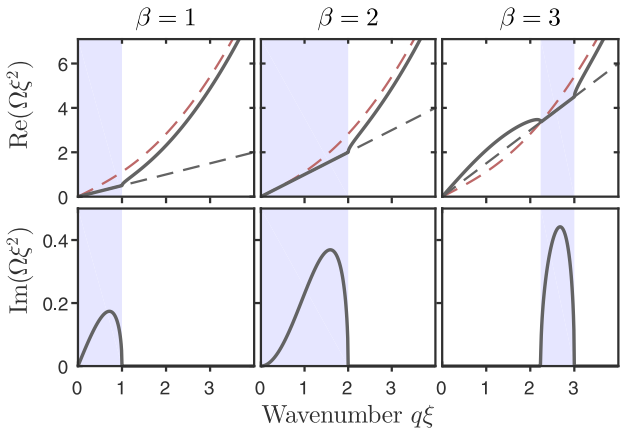

Fig. 5.1 *Bogoliubov dispersion of the fluids in the counter-streaming configuration from [90]. The top row is the real part of the dispersion of eq.5.1, the bottom row is the imaginary part. The shaded area represents the region in momentum space where the imaginary part is non-zero. The red dashed line represents the asymptotic quadratic particle-like regime, and the gray dashed line represents the asymptotic linear sonic-like regime.*

of β, there will be different roots to this dispersion relation, shifting the momentum region where the imaginary part is non-zero. A positive imaginary part will mean an **amplification** of the Bogoliubov excitations, i.e initial fluctuations will grow larger with time: this is a **dynamical instability**. This dispersion is plotted for different stream parameters in fig.5.1 taken from [90]. There are two cases:

- "Slow" flows $\beta < 2$: the imaginary branch spans over the momenta q satisfying $0 < q\xi < \beta$, meaning for all momenta q below the forcing momentum q_f corresponding to the stream velocity v.
- "Fast" flows $\beta > 2$: the imaginary branch is limited to a region $\sqrt{\beta^2 - 4} < q\xi < \beta$. In this case the dispersion displays an inflexion point at $q\xi = \sqrt{\beta^2 - 4}$, with an "anomalous" region at low momenta where the linear part of the dispersion indicated by the grey dashed line is above the quadratic part in red.

It is natural that the "critical" stream parameter should be 2 since it corresponds to a velocity of each component equal to the speed of sound c_s, speed of sound that delimitates the two regions of the Bogoliubov dispersion, and that is the upper bound for superfluid behavior in the Landau criterion (see chap.4).

We thus devise an experiment where two counter-streaming components are generated with the help of an SLM [1]. The experimental setup is represented in fig.5.2.

We use a 7.5 cm long cell of isotopically pure ^{87}Rb. In order to reach long evolution times i.e high values of $\frac{z}{z_{NL}}$, the cell is heated to 150°C, and a small beam waist w_0^f of 500μm is employed to reach a high intensity. The pattern used on the SLM is two linear ramps of phase, in order to send the two halves of the beam at an opposite angle. A grating is added

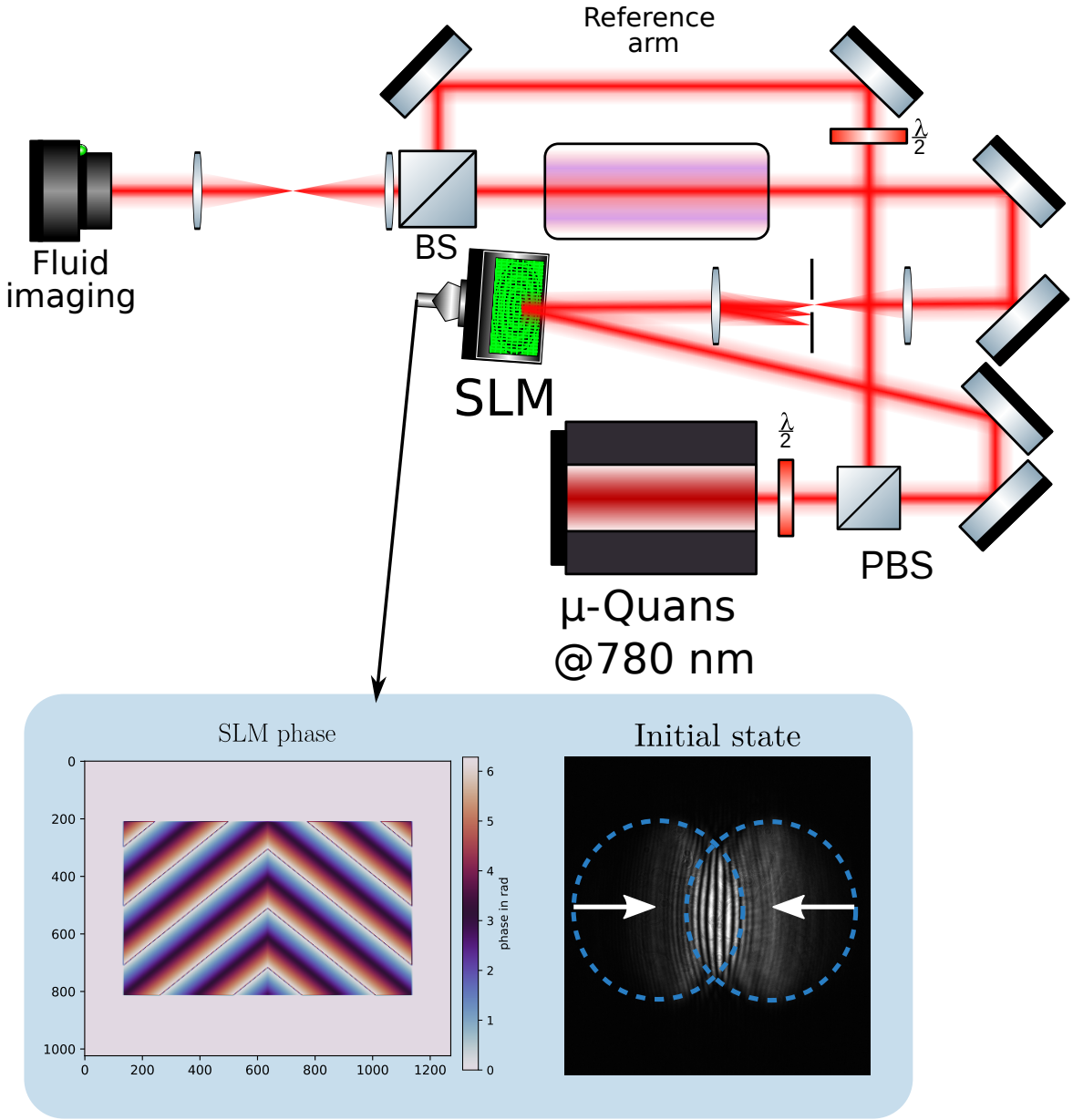

Fig. 5.2 *Experimental setup for the counter-streaming configuration. The phase profile is represented in the blue box: a grating is used to separate the 1^{st} order of the SLM, and is modulated with two opposite linear phase ramps. These ramps act like a biprism and send two components in "collision", generating fringes in the initial state. The blue dashed lines highlight the two components generated by the SLM.*

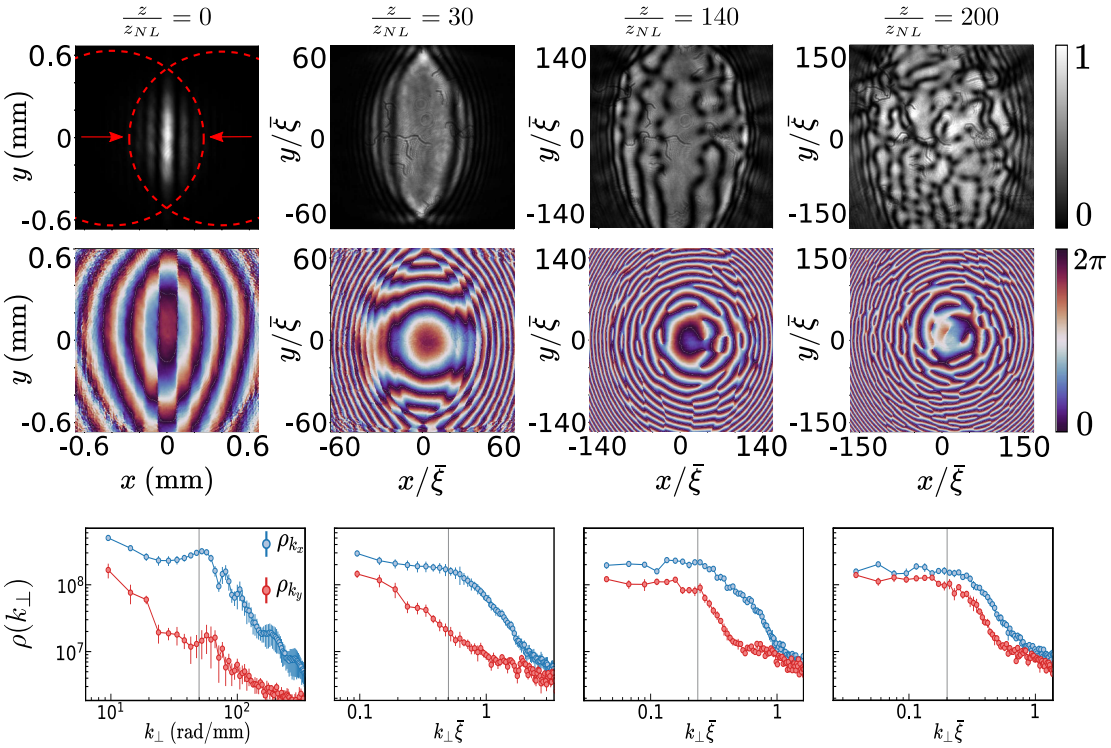

Fig. 5.3 *Emergence of turbulent behavior and isotropy. On the top row, the density of the fluid for different times* $\frac{z}{z_{NL}}$ *indicated on top of the images. The middle row displays the corresponding phase. The bottom row represents the fluid momentum space density* $\rho(k_\perp)$ *along* x *in blue (direction of the forcing) and* y *in red. The forcing spatial frequency is indicated by the gray line.*

in order to separate the SLM first order (see Appendix A). The resulting input state displays fringes at the center, indicative of the interference between the two components. To recover temporal evolution, we study the adimensional system of eq.1.36 presented in chap.1: in order to reach different evolution times $\frac{z}{z_{NL}}$, the power of the fluid is ramped between 1 and 500 mW.

Looking at the time evolution in fig.5.3, we see the fringes snaking and then splitting into a large number of vortices. One strong condition for observing turbulence is the **emergence of isotropy** [75]. While the real space density already indicates a process of uniformization of the system from an initially highly anisotropic state, one can get more quantitative information by analyzing the momentum density distribution. This is allowed by the fact that we recover the whole field, thus we can access not only to $\mathcal{F}(\rho) \propto \mathcal{F}(|\psi|^2)$ but $\rho(k_\perp) \propto |\mathcal{F}(\psi)|^2$.

We see that the initial momentum distribution depicted in the bottom pane of fig.5.3 is strongly anisotropic: the blue curve representing $\rho(k_x)$ is one order of magnitude larger than the red curve representing $\rho(k_y)$. This means that the fluid initially populates modes mostly along x. It is peaked at the forcing frequency (indicated by the gray line). As the fluid evolves, the two curves collapse and the initial peak disappears meaning that the system

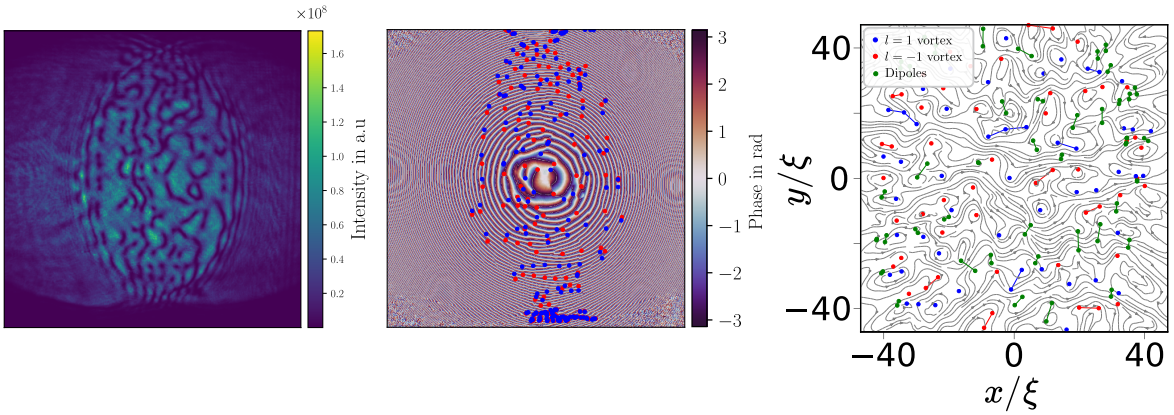

Fig. 5.4 *Example of a vortex configuration detected from the phase field (center) and the extracted incompressible flow (right). The density is also represented on the left panel. The vortices are clustered according to the algorithm from [89] and we see dipoles as well as clusters of several same sign vortices.*

"lost" the memory of its initial state. This is indicative of energy transport allowed by the dynamical instability supporting this turbulent behavior. This energy transport seeds vortices that redistribute the momenta. I will now present how we can characteristize the vortex distribution and extract meaningful physical insight.

5.1.2 Vortex statistics : clustering

The starting point of the vortex detection is the phase field. Access to this field is done by off-axis interferometry [64] (see Appendix A for implementation). The vortex detection is then carried out by computing the circulation of the phase on four-pixel plaquettes. This computation is done through a convolution. The details of the implementation is in the Appendix A of this thesis. Once the vortex distribution is obtained, one can decompose it according to a simple algorithm presented in [89]:

- Each vortex pair of opposite sign that are mutual closest neighbors are considered as dipoles
- Each vortex pair of same sign that are closer to each other than any opposite sign vortex are put in the same cluster

We first apply the first rule to isolate dipoles and we then apply the second rule recursively to cluster the remaining vortices. While these rules are very simple, their practical implementation was challenging even with existing snippets of code made available by Ashton Bradley [22], especially in order to obtain a fast enough implementation that could deal with the comparatively large vortex numbers that our experiments produce (several thousands) compared to the litterature [75; 80; 89]. The details can be found in the Appendices. An example of this clustering algorithm is presented in fig.5.4.

We find that the vortex distribution contains mostly dipoles, but clusters of same sign vortices can also be found. The change of composition of these clusters and their sizes gives insight into the energy transfers within the fluid as the turbulent flow develops. As the

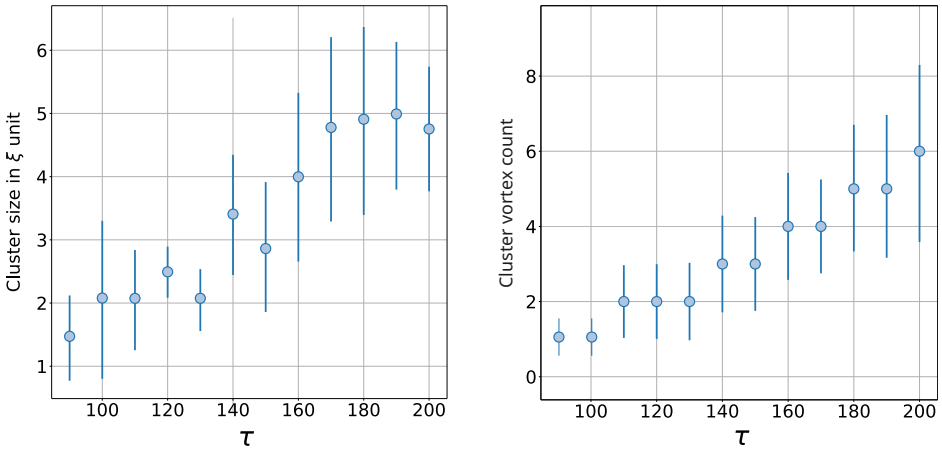

Fig. 5.5 *Left: evolution of the average vortex cluster size in units of the healing length ξ with propagation time $\tau = \frac{z}{z_{NL}}$. Right: evolution of the average vortex count within the clusters with propagation time. The error bars represent two standard deviations over 20 realizations of the experiment. As the fluid evolves, the clusters grow larger, and their vortex count grows as well.*

adimensional time $\tau = \frac{z}{z_{NL}}$ grows, we can plot the typical size of these clusters, as well as the number of vortices they contain. This is represented in fig.5.5.

The clusters are seen to start with a typical size close to the healing length for $\tau = 90$, which grows nearly five fold at $\tau = 200$. Coincidently, the average number of vortices within the clusters starts from below 2, meaning a majority of free vortices. At later times for $\tau = 200$, the average number of vortices increases to 6. This shows a significant reconfiguration of the vortex distribution, driven by an **energy transfer**: the energy is redistributed from small scales by the vortices and their interactions, to large scales as the clusters grow in size and vortex numbers forming larger and larger structures within the fluid.

This behavior is predicted in classical turbulence [22; 89], where the energy is predicted to **cascade** accross scales in a system, with a universal power law exponent in the incompressible energy distribution. I will now present how these cascades are observed in this experiment.

5.1.3 Kolmogorov cascades and power law scaling

The possibility of **inverse energy cascade** in 2D quantum fluids has been debated [77] and several seminal works have explored these ideas in the context of cold gases [74; 75]. The key observable of an isotropic energy cascade is the emergence of a **power law** dependance of the incompressible energy distribution with momentum. This power law dependance will depend on dimensionality and is indicative of the turbulence regime of the system [54; 76].

In our experiment, we study the evolution of the incompressible energy spectrum as the adimensional time $\tau = \frac{z}{z_{NL}}$ is ramped. The experimental results are presented in the fig.5.6.

Analyzing the results of fig.5.6, we find that at low momentum, the incompressible energy follows a $k_\perp$ scaling linked to the fact that at large scales, the vortex configuration is neutral and thus the velocity fields cancel [22]. At high momenta a $k_\perp^{-3}$ scaling indicative of the vortices internal structure [22]. More interestingly, we find that around the forcing frequency

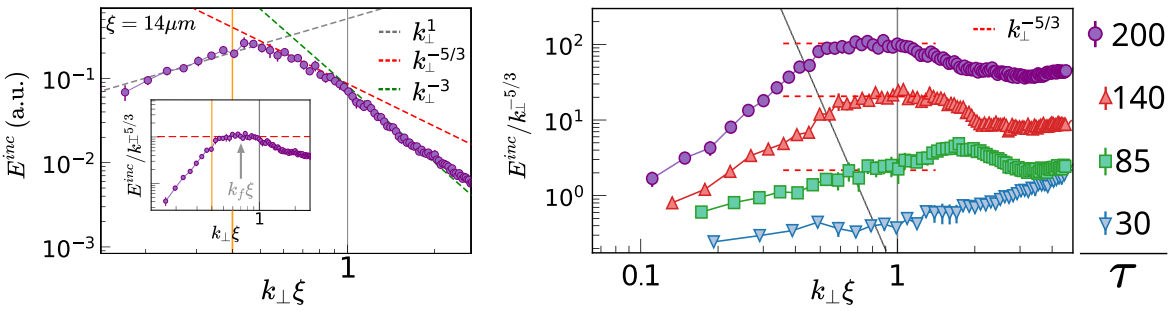

Fig. 5.6 *Emergence of an energy cascade in the incompressible energy spectrum [1]. Left: incompressible energy spectrum for $\beta = 1.6$ and $\tau = 200$. The different dashed line display the power laws for different exponents. The inertial range is delimited by the two solid orange and grey lines. They are located at the inverse of the mean cluster size (here 35 μm) and the inverse of the vortex core size i.e $k_\perp\xi = 1$. Right: Time evolution of the incompressible energy spectrum, rescaled by the power law $k_\perp^{-\frac{5}{3}}$. A plateau is seen to be developping in the inertial range as time progresses. This plateau is highlighted by the red dashed line and the grey dashed line, hinting at an inverse cascade: the plateau develops from high to low momenta.*

k_f, there exists a region where the incompressible spectrum follows a $k_\perp^{-\frac{5}{3}}$ scaling. This exponent is predicted in the case of the **2D inverse energy cascade** within the Kolmogorov theory. Further insight on the inverse energy transfer is obtained when looking at the **time evolution** of the energy spectrum. In the right panel of fig.5.6, the incompressible energy is seen to grow as vortices develop, and a plateau appears starting from $k_\perp\xi = 1$ towards lower momenta (as indicated by the gray dashed line). This confirms that energy is indeed transported from small to large scales.

In conclusion we have seen in this section how dynamical instabilities inherited from the Doppler shifted Bogoliubov dispersion lead to a rich turbulent dynamics, in accordance with the classical 2D wave turbulence. These results open exciting perspectives on turbulence, especially at low momenta i.e large scales and longer times in order to study the dissipation effects of the vortex interactions [74].

5.2 BKT transition

In the previous section 5.1, we evidenced the significance of vortices as indicators of the energy transport through the system. However we did not adress the vortices themselves, especially their thermodynamics properties as an ensemble of interacting "particles". The clustering dynamics described in the last section is strongly reminiscent of the transition between a regime of **free vortices** and **vortex pairs** that is the marker of the superfluid transition [83]. This is the celebrated **Berezinskii-Kosterlitz-Thouless transition** [17; 53] (BKT).

5.2.1 The canonical Berezinskii-Kosterlitz-Thouless transition

I will now present the **XY spin model** in which the BKT transition was initially evidenced. I follow a classical field theory approach (as what can be found in [99]). Let us assume the

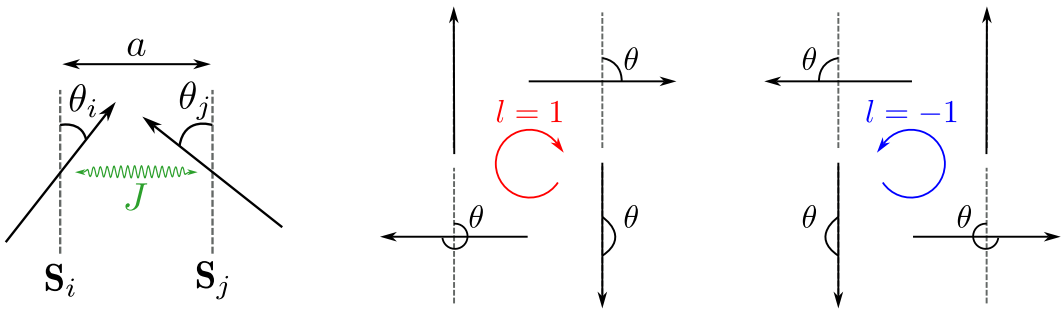

a) b) c)

Fig. 5.7 *Physical situation of the XY spin model. a) Visualization of the XY model Hamiltonian with the coupling constant J and the lattice spacing a. b) Clockwise rotating vortex (charge $l = 1$). c) Anti-clockwise rotating vortex (charge $l = -1$).*

following Hamiltonian for a 2D lattice of interacting spins $\mathbf{S}_i$ of spacing a:

$$H = -J \sum_{\langle i,j \rangle} \mathbf{S}_i \cdot \mathbf{S}_j = -J \sum_{\langle i,j \rangle} \cos(\theta_i - \theta_j) \tag{5.2}$$

where the $\langle i, j \rangle$ sum represents the sum on the first nearest neighbors, and θ_i represents the angle of one spin. The physical meaning of this field in the context of Bose gases (or quantum fluids of light) is the phase of the matter field (light). It is more clearly understood when looking at a graphical representation of the physical situation of the XY model in fig.5.7. In the context of the Ising model, the **phase** of the field is the **angle** of each spin (with respect to the vertical in fig.5.7). It is clear that formulated in this manner, the system will minimize its energy by **aligning** the spins. In the context of fluids of light, since the kinetic energy is $\propto \mathbf{v}^2 = (\nabla\phi)^2$, it translates to minimizing the phase gradient. As we are interested in the low-energy behavior of the system, we will expand around the low angle differences:

$$H \approx -\frac{J}{2} \sum_{\langle i,j \rangle} (\theta_i - \theta_j)^2 \tag{5.3}$$

where we have here absorbed the zeroth order term as it is an energy constant. From there, we can switch to a classical field theory representing the system by taking the continuous limit of the angle difference $\theta_i - \theta_j$ and identifying it with the derivative of some scalar field $\phi(\mathbf{r})$ such that eq.5.3 becomes:

$$H = \int \mathrm{d}\mathbf{r} \nabla\phi(\mathbf{r}) \cdot \nabla\phi(\mathbf{r}) \tag{5.4}$$

where the derivative is $\nabla = (\partial_x, \partial_y)$. If we identify the field gradient to a velocity as done in the hydrodynamical representation of eq.2.46, we notice that under this form, eq.5.4 is strongly reminiscent of the kinetic term of eq.2.46. In order to retrieve the state of the field $\phi(\mathbf{r})$ around its minimum energy to continue the expansion, we first identify the local minima

of the Hamiltonian (5.4). These minima are reached for a cancellation of the functionnal differentiation:

$$\frac{\delta H}{\delta \phi} = 0 \Rightarrow \nabla^2 \phi = 0. \tag{5.5}$$

This condition is readily satisfied for constant fields, however it is also realized for **vortices**. These configurations are depicted in panels b) and c) of fig.5.7. For these solutions, we get the following boundary condition: assuming a vortex at position $\mathbf{r}_0$, for all closed contours encircling $\mathbf{r}_0$, $\oint \nabla\phi(\mathbf{r}) \cdot \mathrm{d}\mathbf{l} = 2\pi l$ (with l the vortex winding number) and for the other contours not enclosing $\mathbf{r}_0$, $\oint \nabla\phi(\mathbf{r}) \cdot \mathrm{d}\mathbf{l} = 0$. We can then solve the circulation integral in order to retrieve the shape of the vortex field:

$$2\pi l = \oint \nabla\phi(\mathbf{r}) \cdot \mathrm{d}\mathbf{l} = 2\pi r |\nabla\phi| \Rightarrow |\nabla\phi| = \frac{l}{r}. \tag{5.6}$$

Substituting this into eq.5.4 allows to retrieve the energy of a vortex configuration:

$$\begin{aligned} E_{vortex} &= \frac{J}{2} \int \mathrm{d}\mathbf{r} \left(\nabla\phi(\mathbf{r})\right)^2 \\ &= \frac{Jl^2}{2} \int_0^{2\pi} \int_a^L r \mathrm{d}\mathbf{r} \frac{1}{r^2} \\ &= \pi l^2 J \ln(\frac{L}{a}). \end{aligned} \tag{5.7}$$

Let us pause for a moment and discuss this result.
In order to regularize the logarithmically diverging integral, we have introduced 2 cutoff scales:

- The **system size** L at large scale. This is obvious in the experimental setting.
- The **lattice spacing** a at small scale. It is not immediately apparent where this scale comes from physically when we try to make the parallel with quantum fluids. In the case of quantum fluids, this short scale cutoff is assured by the **healing length** ξ. It is again natural since ξ is the distance below which we cannot consider anymore the system as some macroscopic ensemble sharing the same wavefunction, but rather individual particles.

Another important point is that the vortex energy scales **quadratically** with the vortex charge l [83]. This means that it is not energetically favorable to nucleate higher charged vortices.

From now on we can thus focus on the singly charged configurations. I will now present some energy scaling argument on the free energy introducing a critical temperature separating two regimes. Let us assume that the system is at thermal equilibrium at a low temperature T. Low temperature in this setting means low enough that the expansion realized in eq.5.3 is still valid. We can define the **free energy** of the system $F = E - TS$ where E is the total energy, T the temperature and S the entropy. The energy is given by the hamiltonian 5.4. For the entropy, we can make the following argument if we consider a single vortex: the number of positions we can place the vortex is $\frac{L^2}{a^2}$, thus the entropy is $S = 2k_B \ln(\frac{L}{a})$ [99]. Combining all the terms we have the following expression for the free energy of a single vortex:

$$F = (\pi J - 2k_B T) \ln\left(\frac{L}{a}\right). \tag{5.8}$$

If we consider N_{vort} singly charged vortices instead of one, the free energy is simply multiplied by N_{vort}. It is clear that the stability of the system is conditioned by the sign of the prefactor $(\pi J - 2k_B T)$:

- If $T < \frac{\pi J}{2k_B}$: the free energy will diverge to $+\infty$ as $L \to \infty$. It means that the system cannot have any vortex.
- If $T > \frac{\pi J}{2k_B}$: the free energy will tend to $-\infty$ as $L \to \infty$, and thus the free energy will decrease further when nucleating vortices.

This means that there is a qualitatively very different behavior above and below $T_{BKT} = \frac{\pi J}{2k_B}$. This behavior is due to the logarithmic dependance of **energy** on system size, which in two dimensions coincides with the logarithmic dependance of **entropy**. This really highlights the **crucial role of dimensionality** in this transition. In practice, the system will switch between a regime of tightly bound vortex pairs, and a gas of free vortices. The full derivation of the BKT temperature is beyond the scope of this manuscript, however most of the power of the scaling argument induced by dimensionality remains in this simple heuristic treatment. I will now propose experimental procedures to measure the vortex interactions in a fluid of light and ascertain the energy calculations we have made up until now.

5.2.2 Vortices collisions and sound emission

The first experiment we have carried is to study the behavior of energy within the fluid of light as we inject pairs of vortices. We want to check what happens when we tune the initial distance between the vortices that are injected, and ultimately studying the vortex recombination mechanisms. This dynamics has already been explored in the context of Bose gases [56], or exciton polaritons [80], but the lack of access to the field or the dissipative nature of the fluid are obstacles to get a complete picture.

We start our experiment with wide gaussian beam, on which we imprint two vortices at a distance Δr of one another. We use a 10 cm long cell of isotopically pure ^{87}Rb heated to 140°C. We use the experimental configuration presented in fig.5.16 with an SLM to imprint vortices. The non-linear index is $n_2 = -4.0 \times 10^{-9}$ m^2/W, the linear losses coefficient $\alpha = 20.1$ m^{-1} and the saturation intensity is $I_{sat} = 4.0$ W/cm^2. Unless stated otherwise, we will compare distances to the **average** healing length along the cell $\langle \xi \rangle = \left\langle \frac{1}{k_0 \sqrt{\Delta n}} \right\rangle$: due to absorption the healing length of the fluid will grow as it propagates through the cell. We take the average value in order to get a good figure of merit. We have two scenarii: the **"opposite signs"** and **"same signs"** configurations i.e where the two vortices have charge (l_1, l_2) equal to $(1, -1)$ or $(1, 1)$ respectively.

Opposite signs An experimental realization of the "opposite signs" or dipole configuration is represented in fig.5.8. The phase discontinuity is clearly visible in the top right panel, connecting the vortex pair. When scanning the initial distance between vortices, there is a critical distance at which, after evolution through the cell, the vortices merge together. When recombining, the vortices **emit a sound wave** dissipating their core energy as defined in eq.5.7. In the phase field, the discontinuity has resorbed. There is also an upwards displacement of the vortex pair. Using the Helmholtz decomposition presented in eq.4.5, it is possible to highlight this behavior more clearly still. This decomposition allows to decouple the sound-like

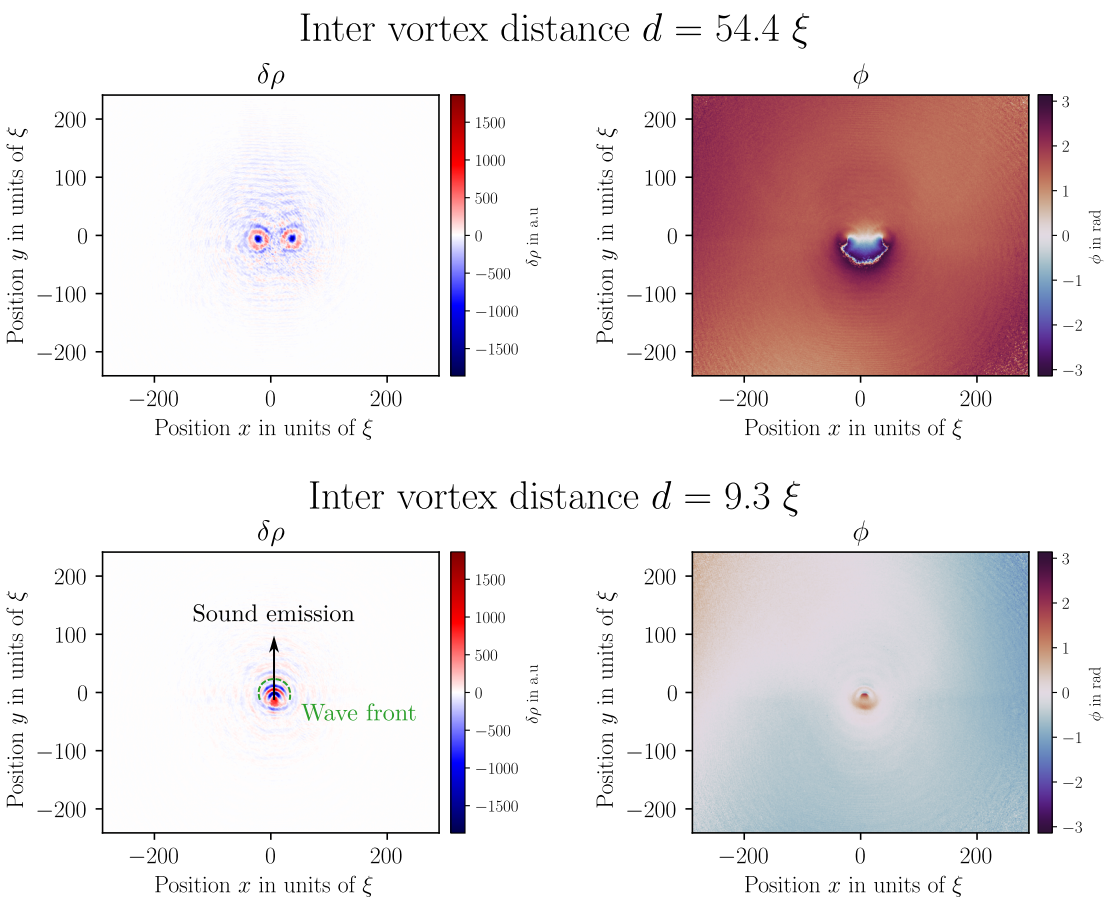

Fig. 5.8 *Experimental realization of the interaction between a singly charged vortex and an opposite signed vortex. The density variation $\delta\rho$ is represented (density with, and without vortices). The phase is the corresponding phase of the fluid i.e the relative phase where the defocusing phase is substracted. In the top panel, the initial distance between vortices is 54.4ξ, in the bottom panel it is 9.3ξ. In the bottom panel, the vortex are seen to merge dissipating energy by emitting a sound wave whose direction is highlighted by the black arrow. The sound front is indicated by the green dashed line.*

behavior of the compressible part of the density weighted velocity, from the singular (in the mathematical sense) behavior of vortices that appear in the incompressible part.

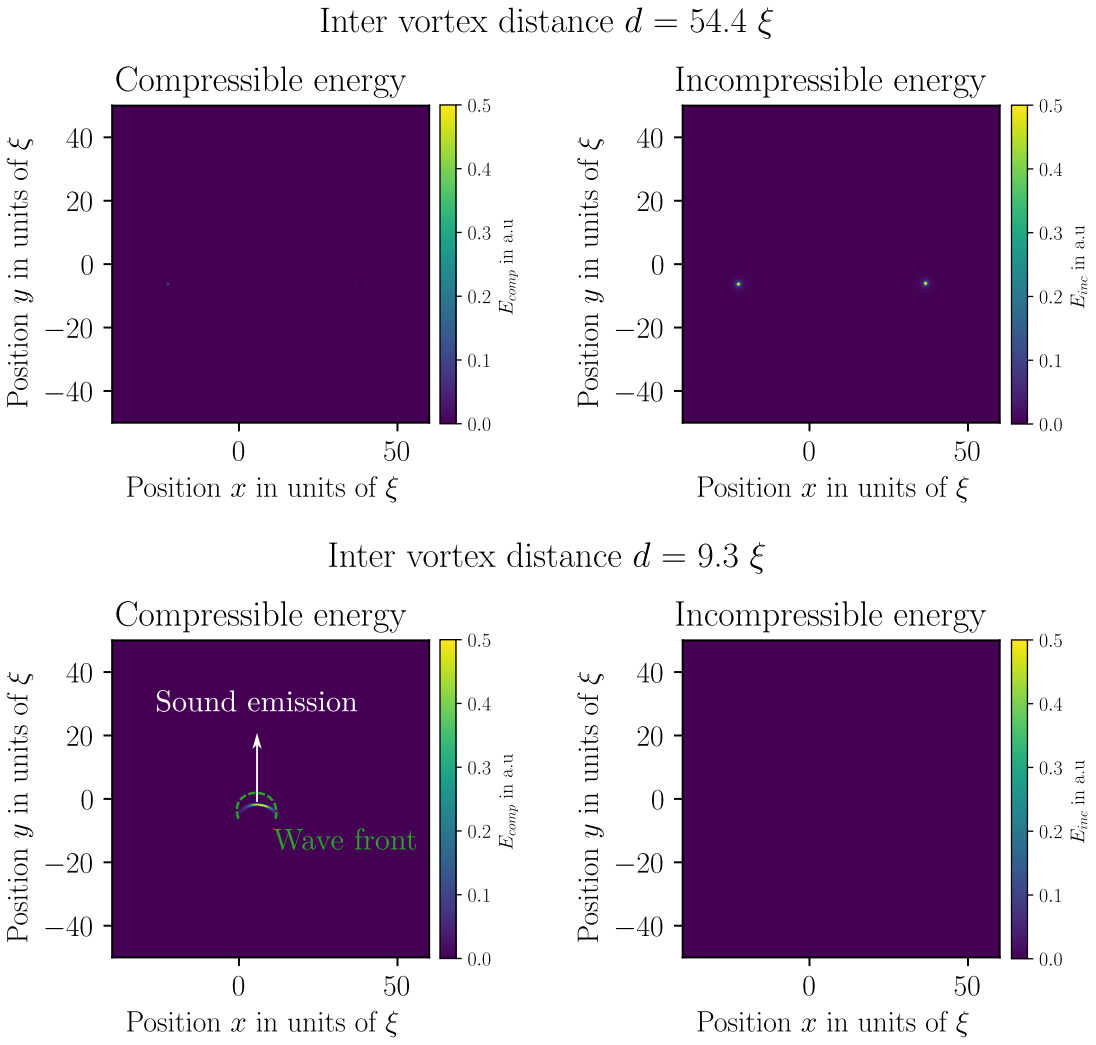

Fig. 5.9 *Compressible and incompressible kinetic energies corresponding to fig.5.8. The two peaks in the incompressible energy on the top panel correspond to the two vortices. In the bottom panel, the vortices have disappeared in the incompressible energy and there is a strong crescent shape emission of compressible kinetic energy propagating upwards. The wavefront shape is reproduced from fig.5.8.*

From the Helmholtz decomposition, one can also extract the corresponding **kinetic energies** from the density weighted velocity $\mathbf{u} = \sqrt{\rho}\mathbf{v} = \sqrt{\rho}\nabla\phi$ as follows:

$$\begin{aligned} E_{inc} &\propto |\mathbf{u}_{inc}|^2 \\ E_{comp} &\propto |\mathbf{u}_{comp}|^2. \end{aligned} \tag{5.9}$$

The resulting energy maps are represented in fig.5.9, that correspond to the experimental realization of fig.5.8. In these energy maps, the vortices appear very clearly as peaks of incompressible energy. The sound emission also appears visibly in the bottom left panel, showing a wave of compressible kinetic energy being emitted upwards. We can then integrate this energy in order to extract the total kinetic energy for both compressible and incompressible components and analyze the evolution of the total kinetic energies as a function of initial vortex separation: we anticipate that the incompressible energy containing the singular behavior of the field should encapsulate the vortex interaction energy. This curve is represented in fig.5.10.

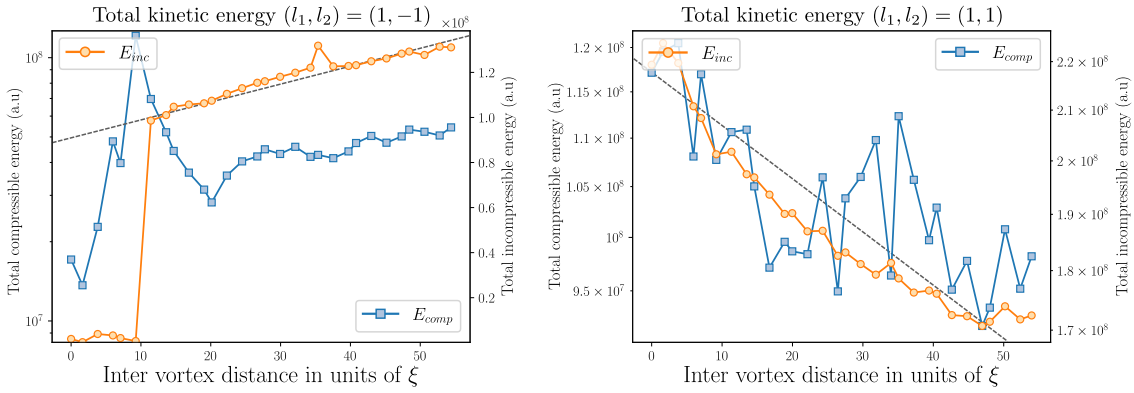

Fig. 5.10 *Total kinetic energy for the compressible and incompressible components. Left: the opposite signs scenario. Right: the same sign scenario. The compressible energy is represented in blue, and the incompressible energy in orange. The dashed line indicates a logarithmic trend that the incompressible energy follows (incompressible energy is represented in logarithmic scale). For the dipole case, the compressible energy displays a sharp peak corresponding to the sound mode emission following the vortex recombination at $\Delta r = 9.3\xi$. The incompressible energy is seen to follow closely a logarithmic scale. In the same sign scenario, the both energies incease as the vortices initial position grow closer. The logarithmic trend is also indicated with the dashed line.*

Looking at the left panel of fig.5.10 seems to confirm the physical scenario of the two vortices anihilating each other: as the starting distance between vortices grows smaller and smaller, there will be a point within the cell where the vortices will cancel out each other. While it is challenging to capture this exact moment without adimensionalizing our system like in the turbulence experiment of section 5.1, varying the initial separation will still allow some form of "temporal" resolution by changing the position at which this cancellation occurs. This means that while our observation position is fixed by imaging the cell output at $z = L$, we change the propagation distance between the anihilation position z_a and the cell output face. We wee in fig.5.10 that there is a sharp peak in compressible energy, and a sudden drop of the incompressible energy around $\Delta r = 9.3\xi$. The drop of incompressible energy is due to the loss of vortices as they cancel out, and the peak in compressible energy corresponds to the emission of this energy in the form of a sound wave. With the dashed line, we check that the incompressible energy displays a **logarithmic dependance** with the vortex separation,

with a decreasing trend as the distance reduces which is in agreement with eq.5.10. Echoing to the dimensionality discussion of chap.1, this logarithmic dependance is a strong indication of the **2D behavior** of the fluid of light in our propagating geometry. We check that this cancellation is not due to the limited imaging resolution of the SLM imposed phase since without interactions (cell), the vortices reamain clearly visible even when their intervortex separation is minimal i.e 2 SLM pixels. In order to get a better insight, we solve numerically this situation and study the adimensionalized evolution of the fluid i.e varying z/z_{NL} as well as replicating the variation of the initial position of the vortices.

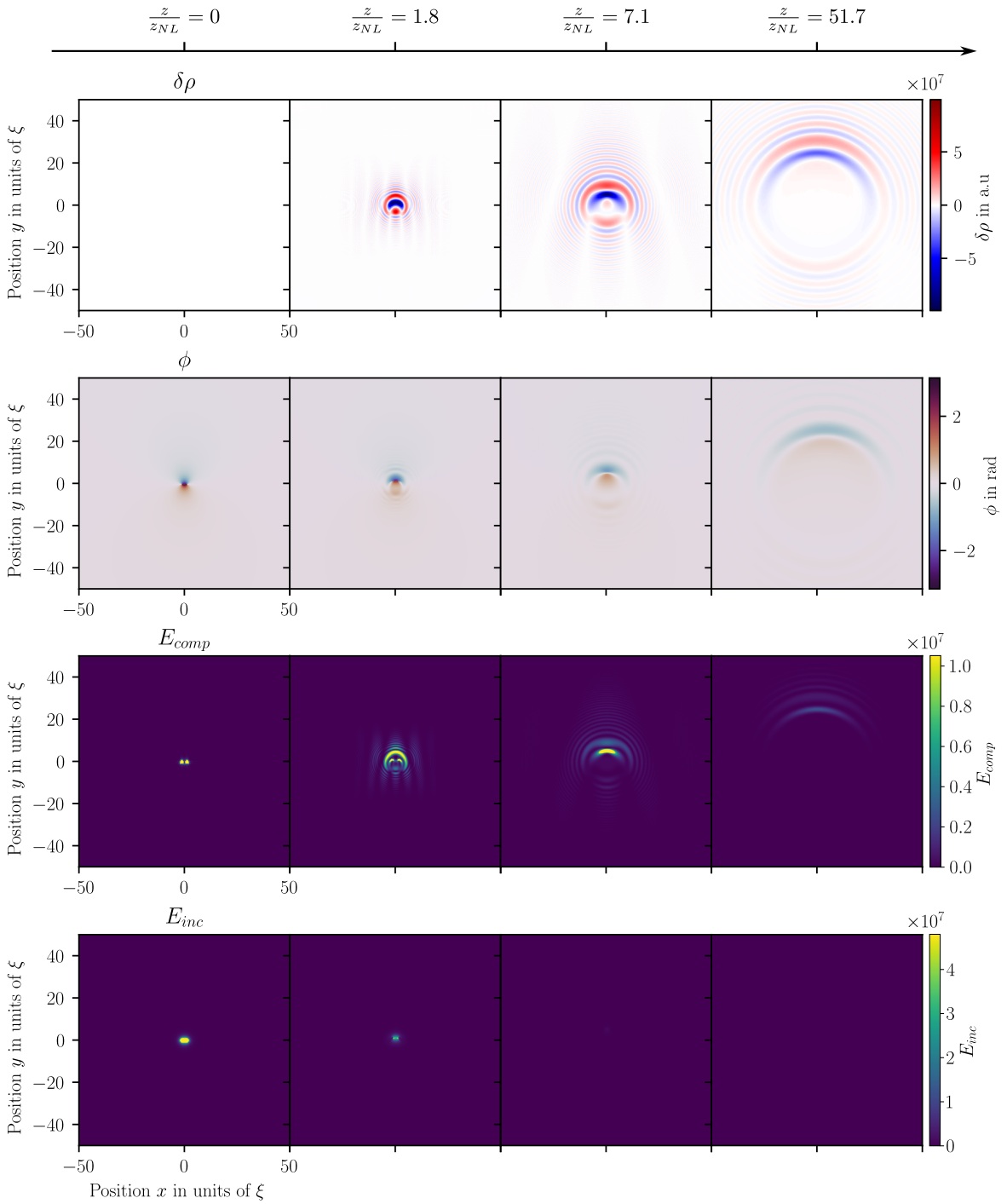

Fig. 5.11 *Numerical simulation of the time evolution of the system. The field is propagated using the* `NLSE` *library developed during this thesis (see Appendix A A). Samples of the field are taken during the propagation through the cell and the density fluctuations, phase, compressible and incompressible kinetic energies are computed. We start with an initial intervortex distance of* $2\langle\xi\rangle$*. At each snapshot, the window is adjusted such as to follow the "instantaneous" healing length in order to remain in the adimensional units. The vortices anihilate each other emitting a sound wave that propagates upwards, in excellent agreement with the experimental data.*

We record the time evolution of the fluid and follow the density fluctuations, the phase, compressible and incompressible energies in fig.5.11. As time passes, the vortices grow closer then merge emitting a sound wave propagating upwards in a nearly identical scenario as the experimental scan of the inter-vortex distance. This confirms that changing the initial distribution of vortices leads to an almost identical dynamics as varying $\frac{z}{z_{NL}}$. Replicating the experimental sequence, we then vary the initial distance and compute the total kinetic energies. In the left panel of fig.5.12, we find very good agreement with the experimental curve of fig.5.10. There is however a discrepency of the critical separation at which the two vortices anihilate each other. In the experiment, the two vortices seem to anihilate when starting closer than $10\,\langle\xi\rangle$, while in the simulation, the anihilation occurs just before a separation of $2\,\langle\xi\rangle$. This could be explained by uncertainties in the measurement of the non-linear index or non-local effects increasing the healing length (as demonstrated in chap.4). Another intriguing fact is that the interaction energy does not seem to follow as well a logarithmic dependance. This deviation is is common to both the same signs, and different signs configurations. Further testing will be carried out in order to check whether or not the interaction energy is totally described by the incompressible energy.

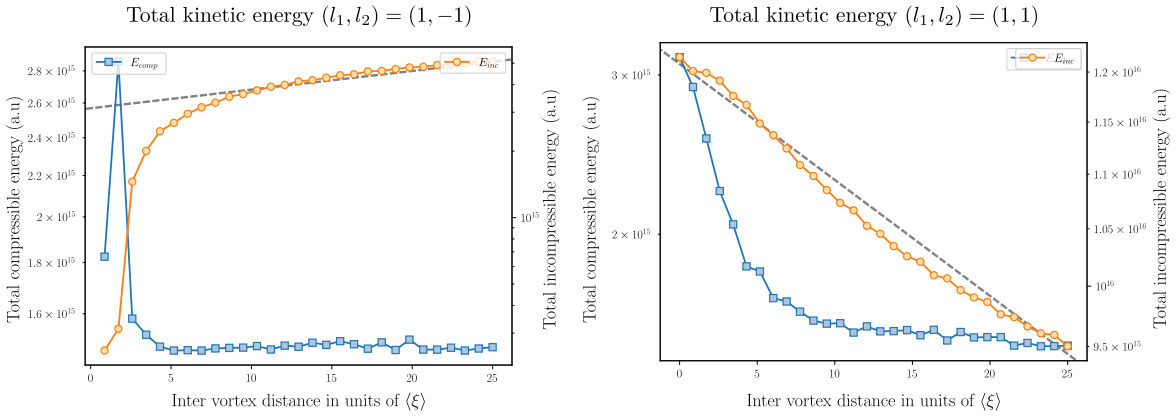

Fig. 5.12 *Numerical simulation for different initial inter-vortex distances. Left: Opposite sign / dipole configuration. The incompressible energy decreases in accordance to the experiment. Below an inter-vortex distance of 2.1$\langle\xi\rangle$, the vortices merge within the cell and we record the sharp peak in compressible energy corresponding to the emission of the sound wave. Right: Same sign configuration. The dashed lines indicate a logarithmic dependance.*

Same signs In the same signs configuration, we do not expect the vortex to anihilate. However, we anticipate that the repulsive force between same sign vortices should lead to interesting dynamics like and orbital movement around each other [56]. Following the same procedure as the previous paragraph, we are interested in the field dynamics, as well as the behavior of the compressible and incompressible energies.

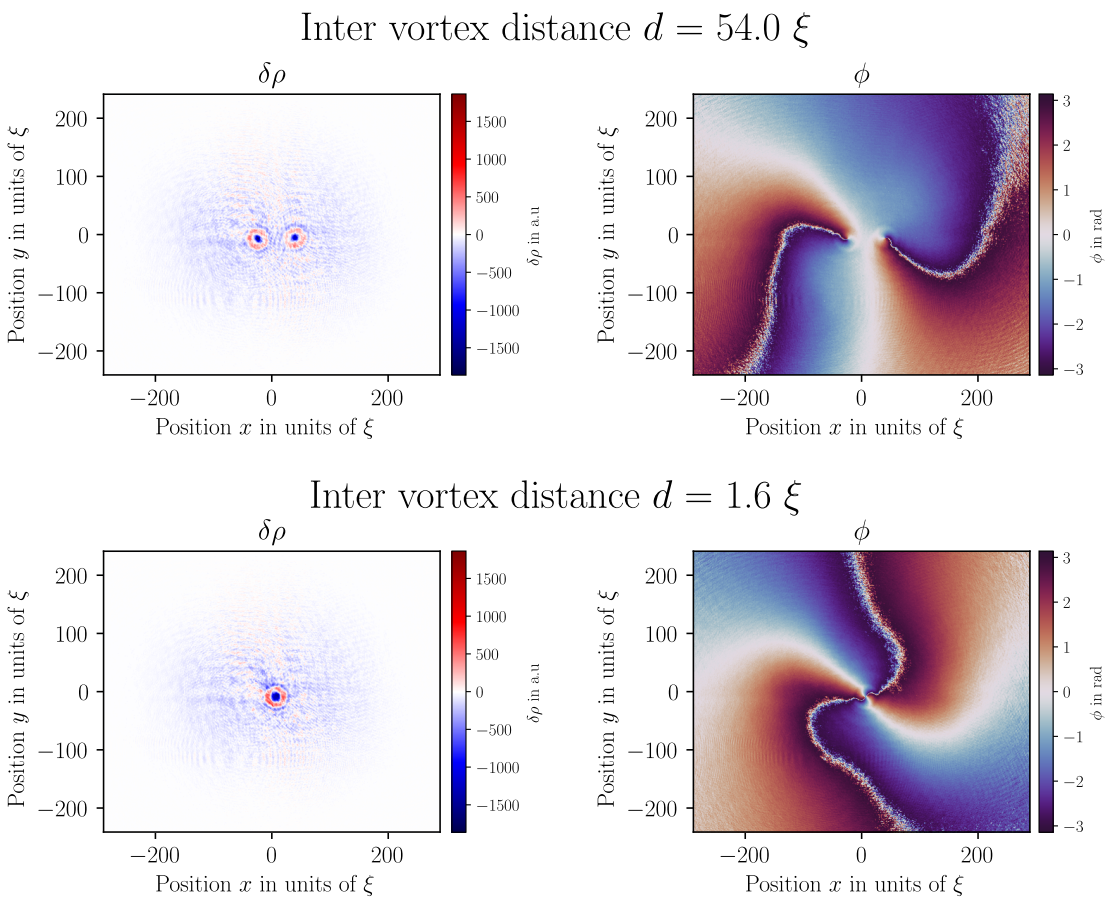

Fig. 5.13 *Experimental realization of the interaction between a singly charged vortex and an same signed vortex. The density variation $\delta\rho$ is represented (density with, and without vortices). The phase is the corresponding phase of the fluid i.e the relative phase where the defocusing phase is substracted. In the top panel, the initial distance between vortices is 54.0ξ, in the bottom panel it is 1.6ξ. In the bottom panel, the vortex are seen to show a displacement with respect to the horizontal line due to the repulsive interaction between same charge vortices.*

In the case of the same signs experiment, the vortices remain visible for all initial distances and they deviate from their initial positions as can be seen in fig.5.13. This is more visible in the incompressible energy in fig.5.14 where the peak in incompressible energy precisely locates the vortex cores: as the vortices grow closer, they initiate a rotating movement around one another.

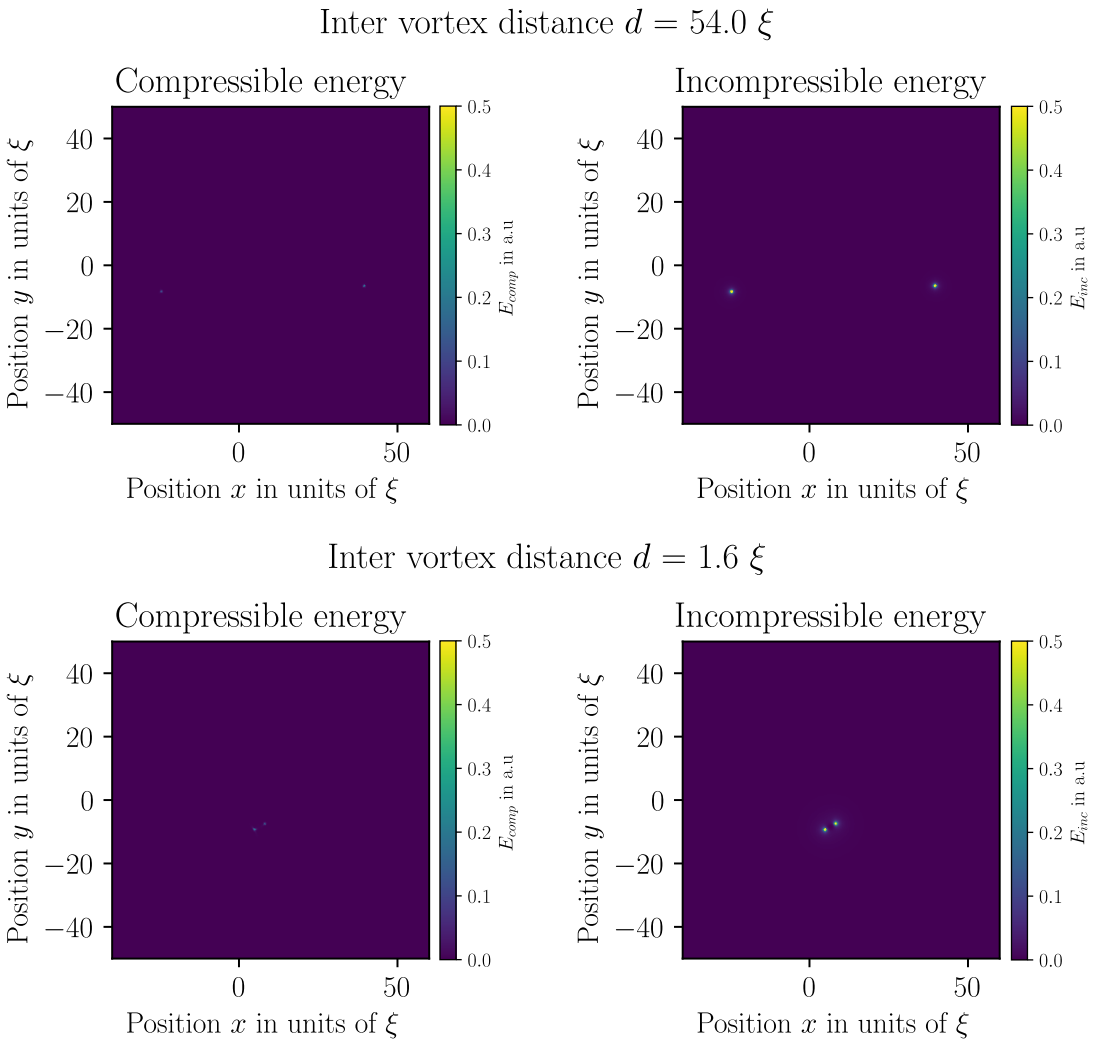

Fig. 5.14 *Compressible and incompressible kinetic energies corresponding to fig.5.13. The two peaks in the incompressible energy on the top panel correspond to the two vortices. In the bottom panel, the vortices remain but have tilted from their initial horizontal axis. The compressible energy does not produce distinguishable patterns.*

We confirm this behavior in the numerical simulations: the two vortices initially emit a sound wave propagating outwards and then orbit each other still forming "ripples" in the phase. This picture is very similar to the dynamics of the gravitational field around a binary system. Looking at the kinetic energies in fig.5.12 confirms that there seems to be a repulsive force between same sign vortices, however the time dynamics displays an orbiting motion of the vortices that indicates some form of stiction between vortices.

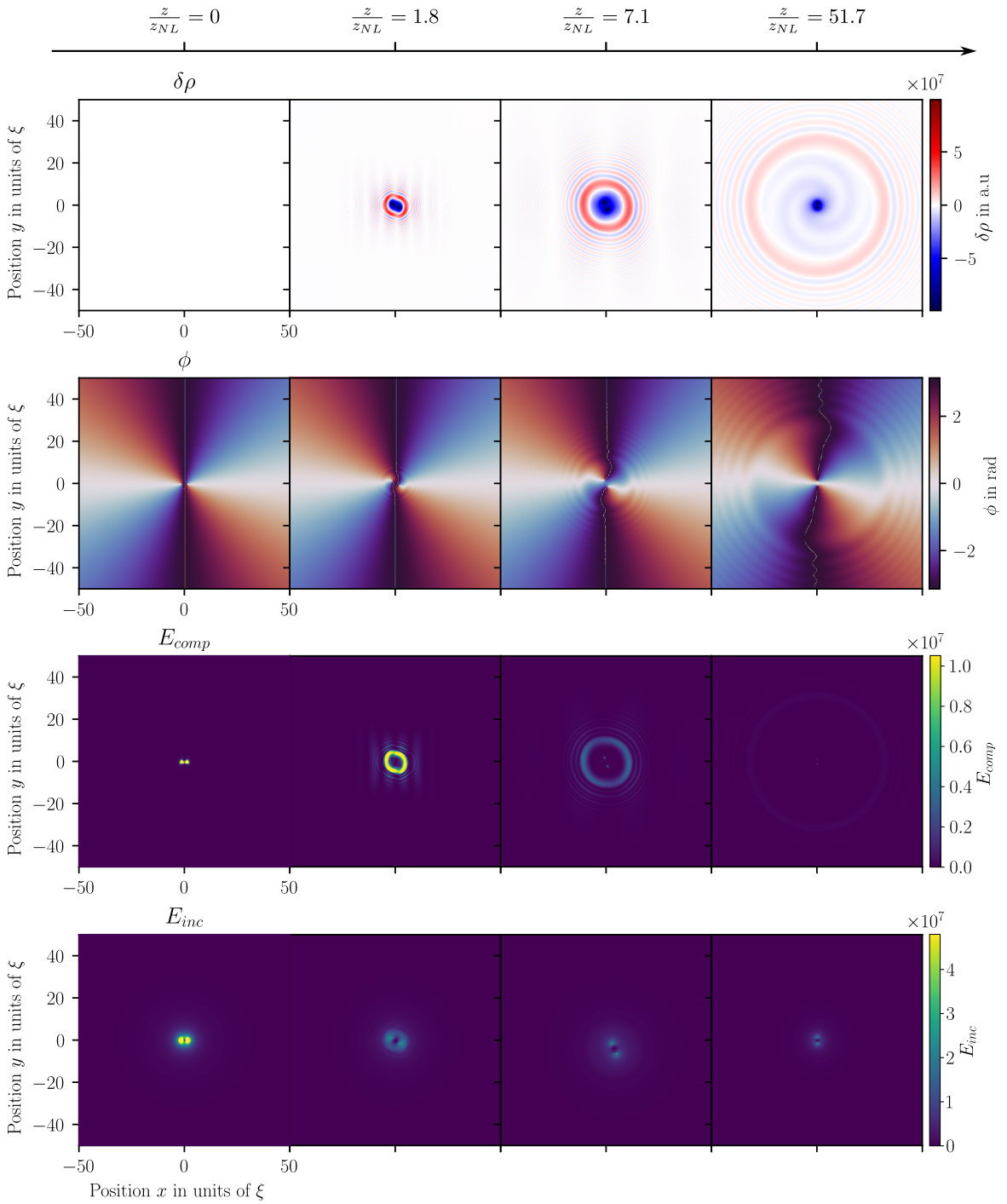

Fig. 5.15 *Numerical simulation of the time evolution of the system. The field is propagated using the* `NLSE` *library. Samples of the field are taken during the propagation through the cell and the density fluctuations, phase, compressible and incompressible kinetic energies are computed. We start with an initial intervortex distance of* $2\langle\xi\rangle$*. At each snapshot, the window is adjusted such as to follow the "instantaneous" healing length in order to remain in the adimensional units. The vortices orbit each other and radiate a sound wave outwards in a dynamics reminiscent of ring down oscillations of binary star systems.*

Importantly, we have seen that this experiment evidences the potential of our platform to probe precisely the vortex-vortex dynamics. In this sense it is similar to [56] and future experiments will allow to replicate this work by taking advantage of our signal-to-noise ratio in order to get a more detailed look at the interplay between vortices and sound modes emission. Having presented elements towards a full characterization of the vortex-vortex interaction, we would like to scale these measurements to a higher and higher number of vortices, towards a thermodynamics setting. I will now present a proposal to continue this experiment to probe the transition to a macroscopic number of vortices.

5.2.3 From microscopic vortex dynamics to macroscopic properties

After having explored the few vortex dynamics, we would like now to look at a large ensemble of vortics as a thermodynamics system in order to potentially observe some form of analogue of the BKT transition in our system. To this extent, we first need to design initial states that are at a thermal equilibrium since we saw in chap.2 that our fluid of light is far from the thermodynamics equilibrium.

In order to probe the dynamics of the vortex binding and unbinding characteristic of the BKT transition, we want to send controlled initial states of vortices at **thermal equilibrium**, and study their evolution with respect to the different system parameter: evolution time, interaction strength or simulated temperature. For this, we can utilize a SLM in order to inject vortices into the fluid as we presented in the previous section 5.1. However, we still have to properly define what is a thermal state of vortices. Assuming a flat fluid i.e flat phase and flat intensity, there is no initial kinetic energy nor interaction energy a part from the one injected by the vortices since the only phase gradients and intensity gradients are due to the vortices. It can be shown [17; 53] that the energy of a vortex pair of charge (l_1, l_2) is:

$$\begin{aligned} E_{pair} &= \pi J l_1^2 \ln\left(\frac{L}{a}\right) + \pi J l_2^2 \ln\left(\frac{L}{a}\right) + 2\pi J l_1 l_2 \ln\left(\frac{R}{a}\right) \\ &= \pi J (l_1 + l_2)^2 \ln\left(\frac{L}{a}\right) - 2\pi J l_1 l_2 \ln\left(\frac{R}{a}\right). \end{aligned} \tag{5.10}$$

Under factorized form, it becomes clear that same charge vortices repell and opposite charge vortices will attract each other:

- if $l_1 = 1$ and $l_2 = 1$, $E_{pair} = 4\pi J \ln\left(\frac{L}{R}\right)$, so the energy will be minimized for $R \to L$
- if $l_1 = 1$ and $l_2 = -1$, $E_{pair} = 2\pi J \ln\left(\frac{R}{a}\right)$, so the energy will be minimized for $R \to a$

Because we know that there should be no net charge for a thermal state with no net angular momentum, we can generate a state vortex by vortex alternating positively and negatively charged vortices (i.e $l_1 = 1$ and $l_2 = -1$), and sorting the relative position $\mathbf{R}$ at random with probability such that:

$$\begin{aligned} p(\mathbf{R}) &= \frac{1}{\mathcal{N}} e^{-\frac{E_{pair}(R)}{k_B T}} \\ \mathcal{N} &= \int_{\xi}^{L} \mathrm{d}\mathbf{R} e^{-\frac{E_{pair}(R)}{k_B T}}. \end{aligned} \tag{5.11}$$

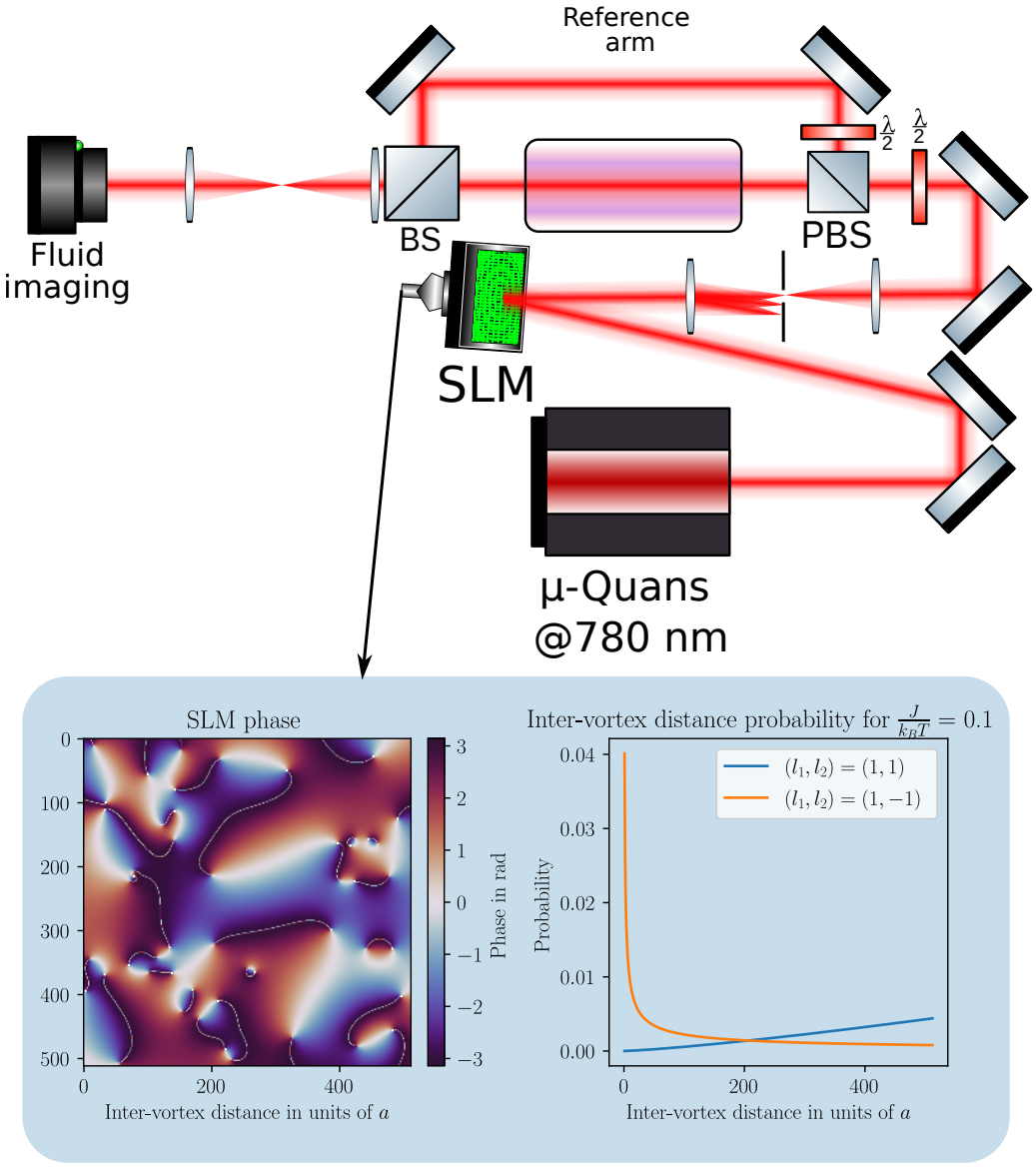

Fig. 5.16 *Experimental setup of the experiment. The input state of the fluid is controlled with the SLM. The distance statistics of the vortex pairs is highlighted in the light blue box (reminiscing of the color code of chapters 1 and 2.) Arbitrary distributions of vortices can be injected into the system in order to study their evolution. Using the off-axis technique, the full field is recovered.*

A vizualization of this type of state is represented in fig.5.16. In the blue panel, the distribution of eq.5.11 is depicted. Note that we do not consider here the effect of the quench at the input face of the cell. Ways to mitigate this quench are presented in the last section 5.3, but in the context where we are interested in the vortices themselves, it seems safe to ignore this in first approach.

Having designed such a state, we can probe the behavior of the vortex ensemble and check the **time evolution** of this system for different **effective temperatures**. In order to get information about the thermodynamics state of the system, we could rely on the following observables:

- Vortex cluster size
- Cluster vortex count
- Pairwise correlation function
- Kinetic energies (compressible and incompressible)

Since the BKT transition is a change of the pairing regime between vortices, there should be a **change in the average number of vortex in a cluster**, from **tightly bound** pairs to **free vortices**. This experiment would also be well suited to a numerical exploration, particularly as our setup currently limits us to values of the evolution time of $\frac{z}{z_{NL}} \approx 200$. Recent developments of our experiments will adress this with higher interactions using the results of chap.3.

I will now conclude this chapter by another proposal that is the subject of ongoing investigations jointly with Clément Duval to probe relaxation and thermalization effects in fluids of light [29].

5.3 Thermalization and condensation

A fundamental question for our system is whether or not the fluid of light will go towards an equilibrium state as time passes. I already explained in chap.1 that in our experiments, the initial state is not an equilibrium state in any sense: it does not follow a thermal distribution, nor some Thomas-Fermi profile as can be found in cold gases [83]. I will now present ways to probe the long time equilibration dynamics of our fluid of light.

5.3.1 Thermalization in fluids of light

In the context of cold atomic gases, inter atomic collisions thermalize very quickly the condensate since only a few number of collisions on average are needed for a condensate to reach thermal equilibrium [83]. In the thermal gas, the Bogoliubov excitations $\hat{b}_{\mathbf{k}_\perp}$ distributed as defined in eq.2.52. The corresponding distribution defined for the fluid of light is then:

$$\left\langle \hat{b}^\dagger_{\mathbf{k}_\perp} \hat{b}_{\mathbf{k}_\perp} \right\rangle = \frac{1}{e^{\Omega_B(\mathbf{k}_\perp)/T} - 1} \tag{5.12}$$

note that in this case the temperature will be defined in terms of the energy scale of the system. In the propagating geometry, since Ω_B has the dimension of a wavenumber, it will also have the dimension of a wavenumber.

In the case of fluids of light however, while there are scattering processes between bogolons as we saw in section 2.5, the time to reach full thermalization is thought to be much larger [60]. Several theoretical works have investigated the preliminary **prethermalization** dynamics following the input quench [60; 70], and their prediction was confirmed experimentally in [3]. I will thus briefly comment on [3] before presenting how we can build on the current experimental setup to overcome the some of this work's limitations.

In [3], the experimental setup before the cell is identical to the one presented in fig.5.16. A SLM is used to superimpose a random speckle to a gaussian background. The induced fluctuations spectrum by this speckle has the following correlation properties (in the photon basis):

$$\left\langle \hat{a}^{\dagger}_{\mathbf{k}_\perp} \hat{a}_{\mathbf{k}_\perp} \right\rangle \propto \frac{1}{\sigma^2}, \tag{5.13}$$

where σ is the speckle "grain" in real space. The narrower the speckle "grain" i.e a small sigma, will mean a larger speckle extent in the Fourier domain. The ratio of these fluctuations to the gaussian background is ϵ^2. The observable use to characterize the fluid after evolution through the cell is the first order coherence function $g^{(1)}(r) = \langle \psi(0)\psi(r) \rangle$. It is predicted (and observed) that in this case this correlation function should follow an algebraic dependance:

$$\begin{aligned} g^{(1)}(r) &\propto \left(\frac{r}{\xi}\right)^{\gamma} \\ \gamma &\propto \epsilon^2 \Phi_{NL} \sigma^2, \end{aligned} \tag{5.14}$$

where $\Phi_{NL} \propto \frac{z}{z_{NL}}$ is the total accumulated non-linear phase. In the case of an initial **thermal state**, this exponent is predicted to scale as $\frac{\epsilon^2}{\sigma^2}$. In order to ascertain this scaling, we impose a thermal state at the input of the cell and then vary the effective temperature in order to check the scaling. However the input state is imposed in the photon basis by the SLM. Due to the **quench** at the input of the cell, if we devise a thermal state, it will be thrown out of equilibrium by this quench. This means we need to compensate this effect. Since the quench can be completely described by the Bogoliubov transform of eq.1.28, we can apply the inverse of this transform to the $\hat{a}_{\mathbf{k}_\perp}$ modes in order to match the state at $z = 0^-$ (just before the quench) to a thermal state for the $\hat{b}_{\mathbf{k}_\perp}$ modes at $z = 0^+$ (just after the quench).

Let us detail a bit the experimental procedure to generate such thermal states: since we impose a classical field with the SLM, we will denote the $\hat{a}_{\mathbf{k}_\perp}$ and $\hat{b}_{\mathbf{k}_\perp}$ modes as classical Fourier amplitudes $a_{\mathbf{k}_\perp}$ / $b_{\mathbf{k}_\perp}$.

- Define the thermal state in terms of the $b_{\mathbf{k}_\perp}$ amplitudes: each $b_{\mathbf{k}_\perp}$ is chosen as a random complex variable with zero mean and variance $\left\langle |b_{\mathbf{k}_\perp}|^2 \right\rangle = \frac{T}{\Omega_B(\mathbf{k}_\perp)}$.
- Transform back to the photon basis: $a_{\mathbf{k}_\perp} = u_{\mathbf{k}_\perp} b_{\mathbf{k}_\perp} + v_{\mathbf{k}_\perp} b^*_{-\mathbf{k}_\perp}$ where the $u_{\mathbf{k}_\perp}$ and $v_{\mathbf{k}_\perp}$ are the Bogoliubov coefficients defined in eq.1.28.
- Fourier transform the $a_{\mathbf{k}_\perp}$ amplitudes back to the real space: $a(\mathbf{r}_\perp) = \int \mathrm{d}\mathbf{k}_\perp a_{\mathbf{k}_\perp} e^{-i\mathbf{k}_\perp \cdot \mathbf{r}_\perp}$

Now that we have detailed the state of the art, theoretical expectations and the experimental procedure to prepare a thermal state, I will now propose a new experiment and new observables in order to probe the relaxation dynamics in fluids of light.

5.3.2 Perturbations from equilibrium states

The experimental setup remains the same as previous proposals, with the setup presented in fig.5.16. In practice the full setup is depicted in fig.4.21, meaning that we have access to the potential engineering presented in chap.4. One first experiment would be to see if a thermal state of phonons is indeed an equilibrium state. One question in the context of thermalization is if the fluid of light thermalizes towards a Bose-Einstein distribution of eq.2.52 or a Rayleigh-Jeans distribution originating from the classical condensation of waves [16]. This could be ascertained by **directly** measuring the **normal** and **anomalous correlators** of the field of eq.2.49. From the field retrieved at the output face of the cell, by applying the Bogoliubov transform, we can extract the bogolon field at $z = L^-$ and then directly compute the correlators. Observing the evolution of these correlators (or lack there of) should confirm or infirm that the thermal state is preserved after evolving inside of the cell.

If the thermal state is indeed shown to be stable, we could slightly perturb the thermal state and measure the relaxation rates of eq.2.53 and 2.54 towards a new thermal equilibrium. Essentially, the goal would be to put ourselves in the assumptions of eqs.2.53 and 2.54. The perturbation would be an additional random speckled added to the thermal state very much like in [3]. By measuring the evolution of the correlators, we could evidence the Landau or Belaiev interaction processes between Bogoliubov particles, which would be the **first indication of effects beyond the Bogoliubov theory**.

Conclusion

I have presented in this chapter the most recent developments of the fluids of light platform. Aided by the system control developed in this thesis, I presented several ongoing or future experiments to evidence effects that go beyond the current modeling of light fluids. Critically, the subject of thermalization and relaxation towards equilibrium has been presented, and the future experiments should be able to go towards controlling thermodynamics properties of the system, designing heating or cooling of the fluid of light. The observation of Bose-Einstein condensation as has been evidenced in polaritons [14] or dye-filled cavities [52], and one could envision that if we are able to build an evaporative trap, it could be within our reach.

Appendices

Appendix A

Numerical tools

A.1 Motivation : why should I learn to code better ?

Modern physics cannot be imagined without computers. Whether it is to run experiments or calculation, coding is ubiquitous and we should strive as a community to develop good practices. This is not only a "pedagogical" issue and making sure that your code is human readable but rather a question of scientific integrity since without repeatability, any study is worthless. This is why I spent vast amounts of time developping libraries in order to streamline many of the generic tools that we use everyday in the team, but more importantly advocate for the **sharing** of these tools, and trying to unify efforts rather than endlessly redevelopping everything from scratch.

There is a big ethical challenge in making science open source, and much improvements can be made into making our results more transparent by sharing our source codes. Furthermore, many recent controversies around data manipulation could have been avoided if publishing code was mandatory.

Another point is that proper programming techniques might allow experiments that were thought impossible before. The first version of the vortex classification algorithm took several hours just to classify a fews hundred vortices. With some clever tricks it now runs in a few ms for several thousand vortices. Too often is there a certain laziness around programming, and many promising ideas are abandoned due to this lack of effort, or knowledge.

Finally, if we should keep only one very cynical reason to mutualize efforts for coding, and publishing our code: **cost**. Of course academia is maybe less inclined to consider this aspect than the private sector, but according to `SlocCount`, the **45195 lines** of codes developped during my thesis would cost a company **1 477 361 $** to develop, employing **8.23 developpers** for **1.33 years**. If this work was to go down the drain due to a lack of knowledge transmission, most of this cost would have to be spent again.

A.2 Numerical measurement tools

A.2.1 Temperature measurement

The temperature is measured by fitting the transmission through the the cell at low intensity with the excellent `Rubidium` code from Andrew Dawes. The laser scans the D_2 line, and we record the transmission through the cell. In order to fit the absolute frequency of the laser, we

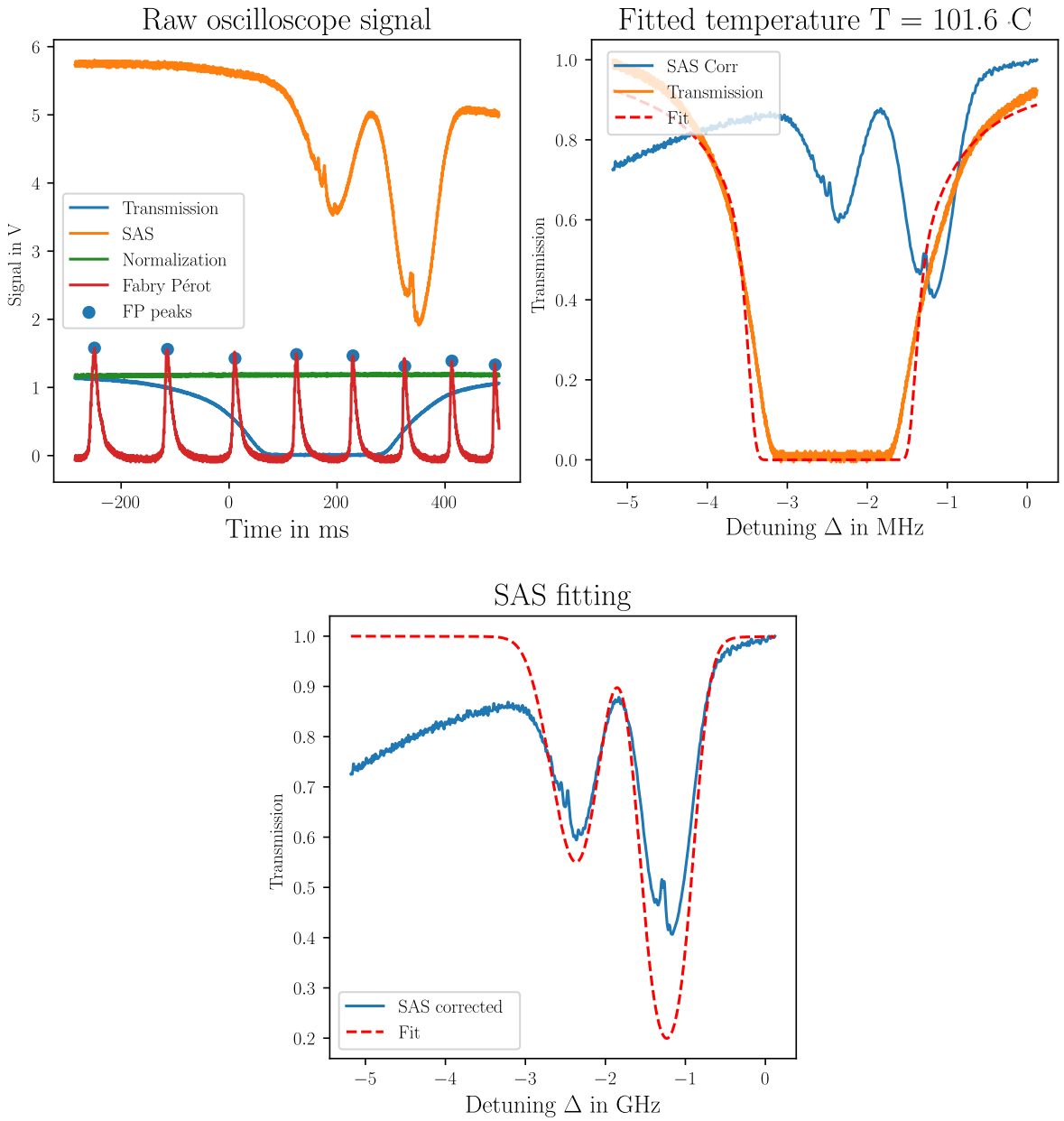

Fig. A.1 *Top left: the raw oscilloscope signal acquired during one frequency scan of the laser. The transmission through the cell is in blue, the saturated absorption (SAS) in orange, the laser power in green and the red signal is from a Fabry-Pérot cavity. Top right: the fitted transmission and temperature. Bottom: the fit of the saturated absorption spectrum used for frequency calibration.*

need a relative measurement of the scan width in frequency, as well as an absolute reference in order to fix the scan offset. The relative reference is given by a Fabry-Pérot cavity. This allows to calibrate the frequency ramp since a linear ramp of the diode current will not lead to a linear ramp in frequency. The offset is then fixed by fitting the SAS spectrum. Note that the detuning use here is defined from the line barycenter, as it is the definition used in the tabulated values of [96]. Finally we use the recivered frequency axis in order to fit the transmission of the cell. The free parameters of the fit are the isotopic fraction, cell length and cell temperature. Since both the length and isotopic fractions are known from the cell manufacturer, this leaves only the temperature as free parameter.

A.2.2 Off-axis interferometry : phase measurements

The experimental setup is presented in fig.3.5.

Interference field Considering a signal beam E_s with a reference beam E_r, we can write the intensity field on a camera:

$$\begin{aligned} &I_{cam}(\mathbf{r}_\perp) \propto |E_s(\mathbf{r}_\perp)e^{i\phi(\mathbf{r},z)} + E_r(\mathbf{r}_\perp)e^{i\mathbf{k}_r\mathbf{r}_\perp}|^2 = \\ &\underbrace{I_s(\mathbf{r}) + I_r(\mathbf{r})}_{\text{DC part}} + \underbrace{2\sqrt{I_s(\mathbf{r}_\perp)I_r(\mathbf{r}_\perp)}\cos\left(\mathbf{k}_r\mathbf{r}_\perp + \phi(\mathbf{r}_\perp) + \phi_0\right)}_{\text{modulated part}} \end{aligned} \tag{A.1}$$

where k_r is the angle of the reference beam. Now we anticipate without too much thinking that in order to demodulate the signal in the cos, we'll need to Fourier transform this expression:

$$\begin{aligned} &\tilde{I}_{\text{cam}}(\mathbf{k}_\perp) = \underbrace{\tilde{I}_{\text{s}}(\mathbf{k}_\perp) + \tilde{I}_{\text{r}}(\mathbf{k}_\perp)}_{0^{th}\ order} + \\ &\underbrace{\mathcal{F}\left[E_s e^{i\phi(\mathbf{r})}\right](\mathbf{k}_\perp) * \left\{\tilde{E}_r(\mathbf{k}_\perp - \mathbf{k}_r) + \tilde{E}_r(\mathbf{k}_\perp + \mathbf{k}_r)\right\}}_{1^{st}\ order} \end{aligned} \tag{A.2}$$

Now we see that the relevant terms are in the first order. The issue is that the convolution term is bothersome. However provided the reference beam is much larger spatially than the signal, its Fourier transform will be much narrower, and thus the convolution will just shift the Fourier transform of the signal since $f(x) * \delta(x - x_0) = f(x - x_0)$ if $\delta(x - x_0)$ is the Dirac delta peaked at x_0. We thus see that the signal in Fourier domain becomes:

$$\begin{aligned} &\tilde{I}_{\text{cam}}(\mathbf{k}_\perp) \approx \underbrace{\tilde{I}_{\text{s}}(\mathbf{k}_\perp) + \tilde{I}_{\text{r}}(\mathbf{k}_\perp)}_{0^{th}\ order} + \\ &\underbrace{\mathcal{F}\left[E_s e^{i\phi(\mathbf{r})}\right](\mathbf{k}_\perp + \mathbf{k}_r) + \mathcal{F}\left[E_s e^{i\phi(\mathbf{r})}\right](\mathbf{k}_\perp - \mathbf{k}_r)}_{1^{st}\ order}. \end{aligned} \tag{A.3}$$

We then have to filter in order to to recover the first order.

Fourier filtering If we filter one of the first order terms, and shift the signal in Fourier domain from $-\mathbf{k}_r$ to get rid of the off-axis term, by back transforming we simply recover:

$$E_s e^{i\phi(\mathbf{r}_\perp)} * \mathcal{F}^{-1}\left[\tilde{T}\right](\mathbf{r}_\perp) \tag{A.4}$$

Where $\tilde{T}(\mathbf{k}_\perp)$ is the function we used to filter the first order in the Fourier domain. If $\tilde{T}(\mathbf{k}_\perp)$ is a circle, $\mathcal{F}^{-1}\left[\tilde{T}\right](\mathbf{r}_\perp)$ will be an Airy function. The meaning of this is that the recovery process is not ideal: it will deteriorate the spatial resolution of the recovered field.

The goal is thus to try and chose the **largest** selection region possible, while still **rejecting** the zeroth order. This leaves only one possibility for the choice of the relative angle between signal and reference: it should be chosen as $\mathbf{k}_r = \frac{1}{\sqrt{2}}\left(\frac{\pi}{d}, \frac{\pi}{d}\right)$ if d is the pixel pitch of the sensor. This corresponds to **half the maximum frequency** which locates the sattelite peaks at the **center** of each quadran.

Efficient FFT implementations The previous process involves two Fourier transforms. Since we have to compute them numerically, and that our images will often be quite large, it is critical to have an efficient implementation of this deconvolution algorithm. Furthermore, since we use this in a real time display, speed is critical. There are two aspects in this case:

- Maximize the speed of the actual transform: this is satisfied using the best FFT libraries like FFTW [37] (for CPU computing) or switching to better hardware like GPU (graphics cards) and using CUDA [78] CUFFT. for instance. Also take care to use fast implementations of the arctangent function since when recovering the phase it can be the leading contribution in terms of time. Since the signal is real, we should also use real FFT (i.e discrete cosine transforms).
- Minimize the memory consumption: this is done by using the proper data types i.e the smallest precision possible, by defining the plans in advance and caching in order to speed up subsequent executions. Also since we crop to a single quadran of the FFT, we can recast the selected satellite peak into a smaller array before back transforming. This means that starting from an initially (N, N) interferogram, we end up with a $(N/2, N/2)$ recovered field.

Actual Python implementation of this routine can be found on the group's GitHub, in the `PhaseUtils` repository.

A.2.3 Non-linear index n_2 measurement

Several methods to measure the non-linear index of refraction have been presented in [5]. However, much work has been devoted in this thesis to develop a reliable **single-shot** measurement. The latest technique we use is to fit the output phase and intensity profiles of the beam that we can extract in a single interferogram. In order to fit the dephasing and intensity, we still need to know the initial beam profile (beam waist) and beam power. We then fit the profile with the solution of the following coupled differential equations involving the absorption α, saturation intensity I_{sat} and non-linear index n_2:

$$\begin{aligned} \frac{\partial \phi}{\partial z} &= k_0 n_2 \frac{I}{1 + \frac{I}{I_{sat}}} \\ \frac{\partial I}{\partial z} &= -\alpha \frac{I}{1 + \frac{I}{I_{sat}}} \end{aligned} \tag{A.5}$$

where the I and ϕ profiles are the azimuthal averages of the intensity and phase in the case where the beam is gaussian to benefit from the cylindrical symmetry to average noise. The

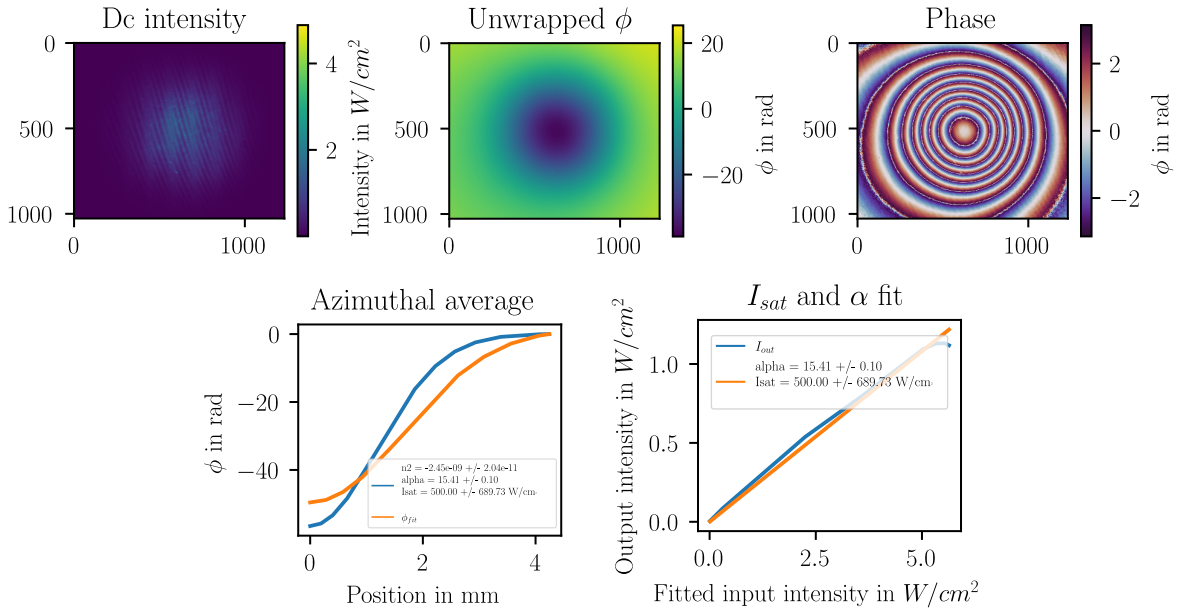

Fig. A.2 *From left to right and top to bottom, the intensity of the beam, unwrapped phase, wrapped phase, azimuthally averaged phase (orange) and fit (blue) and output intensity as a function of the input intensity.*

fitted data is presented in fig.A.2. The fit works well to extract n_2 and α for large beams. However it fails completely to measure I_{sat}. The problem is that even if the beam is large, the fit fails to include self-defocusing. This is why we would like to implement either a fit by the `NLSE` model or use a Physically Informed Neural Network (PINN) as explored in [88].

A.2.4 Vortex clustering algorithm

I will now detail the implementation of the vortex clustering algorithm i.e the `cluster_vortices` function of the `velocity` library that can be found in the `PhaseUtils` repository. The algorithm takes in an array of vortices as $[x_i, y_i, l_i]$ where x / y is are the position of the vortex, and l its charge. We will need two data structures for the algorithm that allow efficient computation: **a R-tree** to represent the spatial distribution of vortices (one for each type of vortices) and a **graph** to represent the hierarchical structure of the clustering. The algorithm is based on the following steps:

- Find mutual nearest neighbors using a global R-tree for all vortices
- Build pairs of mutual nearest neighbors separating between dipoles, pairs of $l = 1$ and $l = -1$
- Initialize clusters with these pairs
- Generate a R-tree for each signs
- Grow clusters by applying rule 2 using the R-tree structure for fast calculation of the n^{th} nearest neighbor. We compute the distance up to the $N/2$ nearest neighbor, where N is the number of vortices (either plus or minus), updating a list of graph edges to connect.
- Extract the minimum spanning tree of the cluster graph
- Extract the clusters as connected components of this tree

A.2.5 Instruments interfacing

A lot of time was spent interfacing with instruments in order to fully automatize the experiments.

PyVisa `PyVisa` is a Python libary that allows to communicate with instruments using the VISA protocol. I used it to design a generic library that allows it to communicate with any instrument and that should be easily extendable: `ScopeInterface`.

Thorlabs Kinesis I wrapped many instruments of the `Kinesis` library. This can be found in the `Piezo` repository, along with a detailed programming guide.

A.3 Numerical simulations

Many results of this thesis were obtained with the help of numerical simulations. I will briefly present the important components that were used to design efficient codes.

A.3.1 Non-linear Schrödinger equation solver

The `NLSE` library is based on the split-step spectral scheme described in chap.1 eq.1.42. It relies heavily on the GPU computing library `CuPy` and `Numba` for just-in-time compilation. It contains three classes that allow simulations of the NLSE in 1D, 2D as well as the couled NLSE in 2D in a vectorized manner (meaning an easy parallelization over many realizations). The code is available on the repository `NLSE` along with extensive documentation.

A.3.2 Monte-Carlo transit simulations

For the simulations of [5], I decided to use the programming language `Julia` for its speed and ease of use. `Julia` is a relatively new language that is designed to be as fast as C while being as easy to use as Python thanks to just-in-time compilation. It also allows easy access to low-level handling of the memory which is critical for performance. The backbone of this code is the `DifferentialEquations.jl` library that provides a native framework to solve differential equations with parallelized realizations. The code is available on the repository `Transit`.

Bibliography

[1] Myrann Abobaker, Wei Liu, Tangui Aladjidi, Alberto Bramati & Quentin Glorieux 2022. "Inverse energy cascade in two-dimensional quantum turbulence in a fluid of light". 2211.08441. Cited pages viii, 15, 85, 120, and 125

[2] Murad Abuzarli 2022. *Out of equilibrium dynamics in a paraxial fluid of light.* Thèse de doctorat Sorbonne Université. URL https://theses.hal.science/tel-03967174. Cited page viii

[3] Murad Abuzarli, Nicolas Cherroret, Tom Bienaimé & Quentin Glorieux 2022. "Non-equilibrium pre-thermal states in a two-dimensional photon fluid". URL https://arxiv.org/abs/2203.07399. Cited pages viii, 23, 141, and 142

[4] G. P. Agrawal. *Nonlinear fiber optics.* Cited page 20

[5] Tangui Aladjidi, Murad Abuzarli, Guillaume Brochier, Tom Bienaimé, Thomas Picot, Alberto Bramati & Quentin Glorieux 2022. "Transit effects for non-linear index measurement in hot atomic vapors". URL https://arxiv.org/abs/2202.05764. Cited pages 61, 67, 148, and 151

[6] C. B. Alcock, V. P. Itkin & M. K. Horrigan 1984. "Vapour pressure equations for the metallic elements: 298–2500k". *Canadian Metallurgical Quarterly* **23**(3), p. 309–313. Cited page 63

[7] A. Amo, S. Pigeon, D. Sanvitto, V. G. Sala, R. Hivet, I. Carusotto, F. Pisanello, G. Lemenager, R. Houdre, E. Giacobino *et al.* . "Polariton superfluids reveal quantum hydrodynamic solitons". *Science* **332**(6034), p. 1167–1170. Cited pages vii, 1, and 7

[8] A. Amo, D. Sanvitto, F. P. Laussy, D. Ballarini, E. del Valle, M. D. Martin, A. Lemaitre, J. Bloch, D. N. Krizhanovskii, M. S. Skolnick *et al.* . "Collective fluid dynamics of a polariton condensate in a semiconductor microcavity". *Nature* **457**(7227), p. 291–295. Cited pages 1 and 83

[9] Alberto Amo, Jérôme Lefrère, Simon Pigeon, Claire Adrados, Cristiano Ciuti, Iacopo Carusotto, Romuald Houdré, Elisabeth Giacobino & Alberto Bramati . "Superfluidity of polaritons in semiconductor microcavities". *Nat. Phys.* **5**(11), p. 805–810. Cited pages vii, 92, and 118

[10] M. H. Anderson, J. R. Ensher, M. R. Matthews, C. E. Wieman & E. A. Cornell 1995. "Observation of bose-einstein condensation in a dilute atomic vapor". *Science* **269**(5221), p. 198–201. Cited pages vii, 13, and 14

[11] Pierre Azam, Adrien Fusaro, Quentin Fontaine, Josselin Garnier, Alberto Bramati, Antonio Picozzi, Robin Kaiser, Quentin Glorieux & Tom Bienaimé

2021. “Dissipation-enhanced collapse singularity of a nonlocal fluid of light in a hot atomic vapor”. *Physical Review A* **104**(1). Cited page 116

[12] Pierre AZAM, Adam GRIFFIN, Sergey NAZARENKO & Robin KAISER 2022. “Vortex creation, annihilation, and nonlinear dynamics in atomic vapors”. *Phys. Rev. A* **105**, p. 043 510. Cited page viii

[13] H.A. BACHOR 1998. *A Guide to Experiments in Quantum Optics*. ISBN 978-3-527-29298-1. URL https://books.google.fr/books?id=6vhAAQAAIAAJ. Cited pages 40, 41, 42, and 48

[14] R. BALILI, V. HARTWELL, D. SNOKE, L. PFEIFFER & K. WEST. “Bose-einstein condensation of microcavity polaritons in a trap”. *Science* **316**(5827), p. 1007–1010. Cited page 142

[15] Stephen M BARNETT & Rodney LOUDON 2006. “On the electromagnetic force on a dielectric medium”. *J. Phys. B: Atomic, Molecular and Optical Physics* **39**(15), p. S671–S684. Cited page 83

[16] K. BAUDIN, A. FUSARO, K. KRUPA, J. GARNIER, S. RICA, G. MILLOT & A. PICOZZI 2020. “Classical Rayleigh-Jeans Condensation of Light Waves: Observation and Thermodynamic Characterization”. *Phys. Rev. Lett.* **125**(24), p. 244 101. Cited page 142

[17] V. L. BEREZINSKIĬ 1971. “Destruction of Long-range Order in One-dimensional and Two-dimensional Systems having a Continuous Symmetry Group I. Classical Systems”. *Soviet Journal of Experimental and Theoretical Physics* **32**, p. 493. Cited pages 125 and 138

[18] T. BIENAIMÉ, M. ISOARD, Q. FONTAINE, A. BRAMATI, A.M. KAMCHATNOV, Q. GLORIEUX & N. PAVLOFF 2021. “Quantitative Analysis of Shock Wave Dynamics in a Fluid of Light”. *Physical Review Letters* **126**(18), p. 183 901. Cited page viii

[19] N. N. BOGOLJUBOV 1958. “On a new method in the theory of superconductivity”. *Journal of Experimental and Theoretical Physics* **34**(1). Cited page 9

[20] C. J. BORDÉ, J. L. HALL, C. V. KUNASZ & D. G. HUMMER 1976. “Saturated absorption line shape: Calculation of the transit-time broadening by a perturbation approach”. *Phys. Rev. A* **14**(1), p. 236–263. Cited page 65

[21] Robert W. BOYD 2008. *Nonlinear Optics, Third Edition* (USA) 3rd édition. ISBN 0123694701. Cited pages 2, 13, and 68

[22] Ashton S. BRADLEY & Brian P. ANDERSON 2012. “Energy Spectra of Vortex Distributions in Two-Dimensional Quantum Turbulence”. *Phys. Rev. X* **2**(4), p. 041 001. Cited pages 86, 123, and 124

[23] Iacopo CARUSOTTO & Cristiano CIUTI 2013. “Quantum fluids of light”. *Rev. Mod. Phys.* **85**(1), p. 299–366. Cited pages 8 and 90

[24] Hugo CAYLA, Salvatore BUTERA, Cécile CARCY, Antoine TENART, Gaétan HERCÉ, Marco MANCINI, Alain ASPECT, Iacopo CARUSOTTO & David CLÉMENT 2020. “Hanbury Brown and Twiss bunching of phonons and of the quantum depletion in an interacting Bose gas”. *Phys. Rev. Lett.* **125**(16), p. 165 301. Cited pages 10 and 26

[25] Jean DALIBARD 2016. “Fluides quantiques de basse dimension et transition de

Kosterlitz-Thouless" . Cited pages vii and 17

[26] Jeffrey A. Davis, Don M. Cottrell, Juan Campos, María J. Yzuel & Ignacio Moreno 1999. "Encoding amplitude information onto phase-only filters". *Appl. Opt., AO* **38**(23), p. 5004–5013. Cited pages 98 and 99

[27] Rémi Desbuquois, Lauriane Chomaz, Tarik Yefsah, Julian Léonard, Jérôme Beugnon, Christof Weitenberg & Jean Dalibard 2012. "Superfluid behaviour of a two-dimensional bose gas". *Nat. Phys.* **8**(99). Cited pages vii, 16, 83, and 102

[28] Jean-Claude Diels & Wolfgang Rudolph 1996. *Ultrashort Laser Pulse Phenomena Fundamentals, Techniques, and Applications an a Femtosecond Time Scale Second Edition.* Cited pages 4 and 6

[29] Clément Duval & Nicolas Cherroret 2023. "Quantum kinetics of quenched two-dimensional bose superfluids". *Phys. Rev. A* **107**, p. 043 305. Cited pages 50, 51, 52, and 140

[30] E.B. Dynkin 1949. "On the representation by means of commutators of the series log(exp(x)exp(y)) for noncommutative x and y". *Matematicheskii Sbornik. Novaya Seriya* **25(67)**, p. 155–162. Cited page 19

[31] G. A. El, A. Gammal & A. M. Kamchatnov. "Oblique dark solitons in supersonic flow of a bose-einstein condensate". *Phys. Rev. Lett.* **97**(18), p. 180 405. Cited page 7

[32] J. Esteve, J.-B. Trebbia, T. Schumm, A. Aspect, C. I. Westbrook & I. Bouchoule 2006. "Observations of density fluctuations in an elongated bose gas: Ideal gas and quasicondensate regimes". *Physical Review Letters* **96**(13), p. 130 403. Cited page 29

[33] U. Fano. "Atomic theory of electromagnetic interactions in dense materials". *Physical Review* **103**(5), p. 1202–1218. Cited page 79

[34] Q. Fontaine, T. Bienaimé, S. Pigeon, E. Giacobino, A. Bramati & Q. Glorieux 2018. "Observation of the bogoliubov dispersion relation in a fluid of light". *Phys. Rev. Lett.* **121**(18). Cited pages 11, 12, and 114

[35] Quentin Fontaine 2019. *Paraxial fluid of light in hot atomic vapor.* Thèse de doctorat Sorbonne Université. URL `https://tel.archives-ouvertes.fr/tel-03402487`. Cited pages viii, 12, 18, 57, 63, 65, 69, 73, 81, and 116

[36] Quentin Fontaine, Pierre-Élie Larré, Giovanni Lerario, Tom Bienaimé, Simon Pigeon, Daniele Faccio, Iacopo Carusotto, Élisabeth Giacobino, Alberto Bramati & Quentin Glorieux 2020. "Interferences between bogoliubov excitations in superfluids of light". *Phys. Rev. Research* **2**, p. 043 297. Cited pages 23, 42, and 81

[37] Matteo Frigo & Steven G. Johnson 2005. "The design and implementation of FFTW3". *Proceedings of the IEEE* **93**(2), p. 216–231. Cited page 148

[38] Dario Gerace & Iacopo Carusotto 2012. "Analog hawking radiation from an acoustic black hole in a flowing polariton superfluid". *Phys. Rev. B* **86**(14), p. 144 505. Cited pages 85 and 111

[39] Quentin Glorieux, Tangui Aladjidi, Paul D. Lett & Robin Kaiser 2023. "Hot atomic vapors for nonlinear and quantum optics". *New Journal of Physics* **25**(5), p. 051 201. Cited page vii

[40] Gilbert Grynberg, Alain Aspect & Claude Fabre. *Introduction to Quantum Optics.*

Cited pages 41 and 57

[41] Zoran HADZIBABIC, Peter KRÜGER, Marc CHENEAU, Baptiste BATTELIER & Jean DALIBARD 2006. "Berezinskii–Kosterlitz–Thouless crossover in a trapped atomic gas". *Nature* **441**(7097), p. 1118–1121. Cited pages 17 and 30

[42] S. E. HARRIS, J. E. FIELD & A. IMAMOĞLU 1990. "Nonlinear optical processes using electromagnetically induced transparency". *Phys. Rev. Lett.* **64**(10), p. 1107–1110. Cited page 70

[43] S. E. HARRIS & Lene Vestergaard HAU 1999. "Nonlinear Optics at Low Light Levels". *Phys. Rev. Lett.* **82**(23), p. 4611–4614. Cited page 70

[44] Chen-Lung HUNG, Victor GURARIE & Cheng CHIN 2013. "From cosmology to cold atoms: Observation of sakharov oscillations in a quenched atomic superfluid". *Science* **341**(6151), p. 1213–1215. Cited pages 30 and 44

[45] Chen-Lung HUNG, Xibo ZHANG, Li-Chung HA, Shih-Kuang TUNG, Nathan GEMELKE & Cheng CHIN 2011. "Extracting density–density correlations from *in situ* images of atomic quantum gases". *New J. Phys.* **13**(7), p. 075 019. Cited page 30

[46] J. HUYNH, M. ALBERT & P.-É. LARRÉ 2022. "Critical velocity for superfluidity in the one-dimensional mean-field regime: From matter to light quantum fluids". *Phys. Rev. A* **105**, p. 023 305. Cited pages 81, 90, 92, 102, 107, 114, and 118

[47] Juliette HUYNH, Frédéric HÉBERT, Mathias ALBERT & Pierre ÉLIE LARRÉ 2023. "Two-dimensional superflow past an obstacle of arbitrary penetrability: Exact results for the critical velocity". 2305.01293. Cited pages 81, 90, 92, 102, 107, 114, and 118

[48] Ted JACOBSON 1996. "Introductory lectures on black hole thermodynamics". Cited page 44

[49] V JOSSE, A DANTAN, A BRAMATI & E GIACOBINO 2004. "Entanglement and squeezing in a two-mode system: theory and experiment". *Journal of Optics B: Quantum and Semiclassical Optics* **6**(6), p. S532–S543. Cited page vii

[50] A. M. KAMCHATNOV & S. V. KORNEEV 2012. "Oblique solitons generated by the flow of a polariton condensate past an obstacle". *J. Exp. Theor. Phys.* **115**(4), p. 579–585. Cited page 7

[51] J. KASPRZAK, M. RICHARD, S. KUNDERMANN, A. BAAS, P. JEAMBRUN, J. M. J. KEELING, F. M. MARCHETTI, M. H. SZYMAŃSKA, R. ANDRÉ, J. L. STAEHLI *et al.* "Bose–einstein condensation of exciton polaritons". *Nature* **443**(7110), p. 409–414. Cited pages vii and 1

[52] Jan KLAERS, Julian SCHMITT, Frank VEWINGER & Martin WEITZ 2010. "Bose–einstein condensation of photons in an optical microcavity". *Nature* **468**(7323), p. 545–548. Cited pages 1 and 142

[53] J. M. KOSTERLITZ 1974. "The critical properties of the two-dimensional xy model". *Journal of Physics C Solid State Physics* **7**(6), p. 1046–1060. Cited pages 125 and 138

[54] R. H. KRAICHNAN & D. MONTGOMERY 1980. "Two-dimensional turbulence". *Reports on Progress in Physics* **43**(5), p. 547–619. Cited page 124

[55] Christian KURTSCHEID, David DUNG, Erik BUSLEY, Frank VEWINGER, Achim ROSCH & Martin WEITZ 2019. "Thermally condensing photons into a coherently split state of

light". *Science (New York, N.Y.)* **366**(6467), p. 894–897. Cited page vii

[56] W. J. Kwon, G. Del Pace, K. Xhani, L. Galantucci, A. Muzi Falconi, M. Inguscio, F. Scazza & G. Roati 2021. "Sound emission and annihilations in a programmable quantum vortex collider". *Nature* **600**(7887), p. 64–69. Cited pages 128, 134, and 138

[57] L. Landau 1941. "Theory of the superfluidity of helium ii". *Phys. Rev.* **60**, p. 356–358. Cited page 81

[58] Renate Landig, Ferdinand Brennecke, Rafael Mottl, Tobias Donner & Tilman Esslinger 2015. "Measuring the dynamic structure factor of a quantum gas undergoing a structural phase transition". *Nat Commun* **6**(1), p. 7046. Cited page 30

[59] Pierre-Élie Larré & Iacopo Carusotto 2015. "Propagation of a quantum fluid of light in a cavityless nonlinear optical medium: General theory and response to quantum quenches". *Phys. Rev. A* **92**(4), p. 043 802. Cited pages 6, 8, 10, 23, 34, and 42

[60] Pierre-Élie Larré & Iacopo Carusotto 2016. "Prethermalization in a quenched one-dimensional quantum fluid of light: Intrinsic limits to the coherent propagation of a light beam in a nonlinear optical fiber". *European Physical Journal D* **70**, p. 45. Cited pages 6, 8, 23, 28, and 141

[61] Pierre-Élie Larré & Iacopo Carusotto 2015. "Optomechanical signature of a frictionless flow of superfluid light". *Phys. Rev. A* **91**(5), p. 053 809. Cited page 83

[62] T. D. Lee, Kerson Huang & C. N. Yang 1957. "Eigenvalues and eigenfunctions of a bose system of hard spheres and its low-temperature properties". *Phys. Rev.* **106**, p. 1135–1145. Cited page 10

[63] E. L. Lewis. "Collisional relaxation of atomic excited states, line broadening and interatomic interactions". *Physics Reports* **58**(1), p. 1–71. Cited page 65

[64] Michael Liebling, Thierry Blu & Michael Unser. "Complex-wave retrieval from a single off-axis hologram". *J. Opt. Soc. Am. A* **21**(3), p. 367. Cited page 123

[65] Andrew D. Ludlow, Martin M. Boyd, Jun Ye, E. Peik & P. O. Schmidt 2015. "Optical atomic clocks". *Rev. Mod. Phys.* **87**, p. 637–701. Cited page vii

[66] Lixia Ma, Xing Lei, Jieli Yan, Ruiyang Li, Ting Chai, Zhihui Yan, Xiaojun Jia, Changde Xie & Kunchi Peng 2022. "High-performance cavity-enhanced quantum memory with warm atomic cell". *Nat Commun* **13**(1), p. 2368. Cited page 70

[67] E. Madelung 1926. "Eine anschauliche Deutung der Gleichung von Schrödinger". *Naturwissenschaften* **14**(45), p. 1004–1004. Cited page 7

[68] KW Madison, F Chevy, W Wohlleben & Jl Dalibard. "Vortex formation in a stirred bose-einstein condensate". *Physical review letters* **84**(5), p. 806. Cited page 7

[69] Giovanni I. Martone, Tom Bienaimé & Nicolas Cherroret 2021. "Spin-orbit-coupled fluids of light in bulk nonlinear media". 2104.11982. Cited page 63

[70] Giovanni I. Martone, Pierre-Élie Larré, Alessandro Fabbri & Nicolas Pavloff 2018. "Momentum distribution and coherence of a weakly interacting Bose gas after a quench". *Phys. Rev. A* **98**(6), p. 063 617. Cited pages 23 and 141

[71] Aaron Meurer, Christopher P. Smith, Mateusz Paprocki, Ondřej Čertík, Sergey B. Kirpichev, Matthew Rocklin, AMiT Kumar, Sergiu Ivanov, Jason K. Moore, Sartaj Singh *et al.* 2017. "Sympy: symbolic computing in python".

PeerJ Computer Science **3**, p. e103. Cited page 61

[72] Claire MICHEL, Omar BOUGHDAD, Mathias ALBERT, Pierre-Élie LARRÉ & Matthieu BELLEC . "Superfluid motion and drag-force cancellation in a fluid of light". *Nat. Comm.* **9**(1), p. 2108. Cited pages vii, 1, 81, 82, 83, 111, and 118

[73] Florent MICHEL, Jean-François COUPECHOUX & Renaud PARENTANI . "Phonon spectrum and correlations in a transonic flow of an atomic bose gas". *Physical Review D* **94**(8). Cited pages vii, 1, and 81

[74] Nir NAVON, Christoph EIGEN, Jinyi ZHANG, Raphael LOPES, Alexander L. GAUNT, Kazuya FUJIMOTO, Makoto TSUBOTA, Robert P. SMITH & Zoran HADZIBABIC 2019. "Synthetic dissipation and cascade fluxes in a turbulent quantum gas". *Science* **366**(6463), p. 382–385. Cited pages 124 and 125

[75] Nir NAVON, Alexander L. GAUNT, Robert P. SMITH & Zoran HADZIBABIC 2016. "Emergence of a turbulent cascade in a quantum gas". *Nature* **539**(7627), p. 72–75. Cited pages 122, 123, and 124

[76] Sergey NAZARENKO & Miguel ONORATO 2006. "Wave turbulence and vortices in Bose–Einstein condensation". *Physica D: Nonlinear Phenomena* **219**(1), p. 1–12. Cited page 124

[77] Ryu NUMASATO & Makoto TSUBOTA 2010. "Possibility of Inverse Energy Cascade in Two-Dimensional Quantum Turbulence". *Journal of Low Temperature Physics* **158**(3-4), p. 415–421. Cited page 124

[78] NVIDIA, Péter VINGELMANN & Frank H.P. FITZEK 2020. "Cuda, release: 10.2.89". URL `https://developer.nvidia.com/cuda-toolkit`. Cited page 148

[79] R A NYMAN, H S DHAR, J D RODRIGUES & F MINTERT 2021. "Phase transitions of light in a dye-filled microcavity: observations and simulations". *Yamada Conference Lx On Research in High Magnetic Fields* **1919**(1), p. 012 006. Cited page vii

[80] R. PANICO, P. COMARON, M. MATUSZEWSKI, A. S. LANOTTE, D. TRYPOGEORGOS, G. GIGLI, M. De GIORGI, V. ARDIZZONE, D. SANVITTO & D. BALLARINI 2023. "Onset of vortex clustering and inverse energy cascade in dissipative quantum fluids". *Nat. Photon.* **17**(5), p. 451–456. Cited pages 123 and 128

[81] Clara PIEKARSKI, Wei LIU, Jeff STEINHAUER, Elisabeth GIACOBINO, Alberto BRAMATI & Quentin GLORIEUX 2021. "Measurement of the static structure factor in a paraxial fluid of light using bragg-like spectroscopy". *Phys. Rev. Lett.* **127**, p. 023 401. Cited pages 11, 114, 115, and 116

[82] S. PIGEON, I. CARUSOTTO & C. CIUTI. "Hydrodynamic nucleation of vortices and solitons in a resonantly excited polariton superfluid". *Phys. Rev. B* **83**(14), p. 144 513. Cited page 7

[83] Lev P. PITAEVSKIJ & Sandro STRINGARI 2016. *Bose-Einstein condensation and superfluidity*. Numéro 164 dans International series of monographs on physics. Reprinted (with corrections) édition. ISBN 978-0-19-875888-4. Cited pages vii, 6, 8, 11, 12, 13, 16, 29, 34, 50, 82, 102, 125, 127, and 140

[84] Anatoli POLKOVNIKOV, Ehud ALTMAN & Eugene DEMLER 2006. "Interference between independent fluctuating condensates". *Proceedings of the National Academy of Sciences* **103**(16), p. 6125–6129.

Cited page 30

[85] N. Pottier 2012. *Physique statistique hors d'équilibre - Processus irréversibles linéaires*. SAVOIRS ACTUELS. ISBN 978-2-7598-0148-0. URL https://books.google.fr/books?id=RcVor7dLy74C. Cited page 28

[86] Jonathan D. Pritchard, Kevin J. Weatherill & Charles S. Adams. *NONLINEAR OPTICS USING COLD RYDBERG ATOMS*. p. 301–350. URL http://dx.doi.org/10.1142/9789814440400_0008. Cited page 79

[87] Christopher Rackauckas & Qing Nie 2017. "DifferentialEquations.jl–a performant and feature-rich ecosystem for solving differential equations in Julia". *Journal of Open Research Software* **5**(1). Cited page 67

[88] M. Raissi, P. Perdikaris & G. E. Karniadakis 2019. "Physics-informed neural networks: A deep learning framework for solving forward and inverse problems involving nonlinear partial differential equations". *Journal of Computational Physics* **378**, p. 686–707. Cited page 150

[89] M. T. Reeves, B. P. Anderson & A. S. Bradley 2012. "Classical and quantum regimes of two-dimensional turbulence in trapped Bose-Einstein condensates". *Phys. Rev. A* **86**(5), p. 053 621. Cited pages 123 and 124

[90] João D. Rodrigues, José T. Mendonça & Hugo Terças 2020. "Turbulence excitation in counterstreaming paraxial superfluids of light". *Phys. Rev. A* **101**(4), p. 043 810. Cited pages 119 and 120

[91] Ralf Schützhold, Michael Uhlmann, Lutz Petersen, Hector Schmitz, Axel Friedenauer & Tobias Schätz 2007. "Analogue of cosmological particle creation in an ion trap". *Physical Review Letters* **99**(20), p. 201 301. Citation Key: schutzholdAnalogueCosmologicalParticle2007. Cited pages 30 and 44

[92] Jiteng Sheng, Xihua Yang, Haibin Wu & Min Xiao 2011. "Modified self-Kerr-nonlinearity in a four-level n-type atomic system". *Phys. Rev. A* **84**(5), p. 053 820. Cited page 71

[93] Paul Siddons, Charles S. Adams, Chang Ge & Ifan G. Hughes. "Absolute absorption on rubidium d lines: comparison between theory and experiment". *J. Phys. B: At. Mol. Opt. Phys.* **41**(15), p. 155 004. Cited pages 55 and 57

[94] Alice Sinatra, Carlos Lobo & Yvan Castin. "The truncated wigner method for bose-condensed gases: limits of validity and applications". *J. Phys. B: At. Mol. Opt. Phys.* **35**(17), p. 3599–3631. Cited page 20

[95] D. V. Skryabin & A. V. Yulin. "Theory of generation of new frequencies by mixing of solitons and dispersive waves in optical fibers". *Phys. Rev. E* **72**(1), p. 016 619. Cited page 7

[96] Daniel A. Steck 2021. "Rubidium d line data". URL http://steck.us/alkalidata. Cited pages 56, 57, 59, and 147

[97] Jeff Steinhauer, Murad Abuzarli, Tangui Aladjidi, Tom Bienaimé, Clara Piekarski, Wei Liu, Elisabeth Giacobino, Alberto Bramati & Quentin Glorieux 2022. "Analogue cosmological particle creation in an ultracold quantum fluid of light". *Nat. Comm.* **13**(1), p. 2890. Cited pages viii, 6, 21, 33, 38, and 42

[98] Giancarlo Calvanese Strinati, Pierbiagio Pieri, Gerd Röpke, Peter Schuck &

Michael URBAN 2018. "The BCS-BEC crossover: From ultra-cold Fermi gases to nuclear systems". *Physics Reports* **738**, p. 1–76. Cited page vii

[99] E. TRIZAC 2021. "Statistical physics, icfp master". URL http://lptms.u-psud.fr/membres/trizac/Ens/iCFP.html. Cited pages 125 and 127

[100] David VOCKE, Thomas ROGER, Francesco MARINO, Ewan M. WRIGHT, Iacopo CARUSOTTO, Matteo CLERICI & Daniele FACCIO . "Experimental characterization of nonlocal photon fluids". *Optica* **2**(5), p. 484. Cited page 118

[101] David VOCKE, Kali WILSON, Francesco MARINO, Iacopo CARUSOTTO, Ewan M. WRIGHT, Thomas ROGER, Brian P. ANDERSON, Patrik ÖHBERG & Daniele FACCIO . "Role of geometry in the superfluid flow of nonlocal photon fluids". *Physical Review A* **94**(1), p. 013 849. Cited pages 97 and 116

[102] P. K. A. WAI, C. R. MENYUK, Y. C. LEE & H. H. CHEN. "Nonlinear pulse propagation in the neighborhood of the zero-dispersion wavelength of monomode optical fibers". *Opt. Lett.* **11**(7), p. 464–466. Cited page 7

[103] D. F. WALLS & G. J. MILBURN. *Quantum optics*. 2nd ed édition. ISBN 978-3-540-28573-1. Cited page 26

[104] Mahmud WASFI 2009. "Optical fiber amplifiers-review". *International Journal of Communication Networks and Information Security* **1**. Cited page vii

[105] G WENDIN 2017. "Quantum information processing with superconducting circuits: a review". *Reports on Progress in Physics* **80**(10), p. 106 001. Cited page vii

[106] V. I. YUKALOV 2007. "Structure factor of bose-condensed systems". *Journal of Physical Studies* **11**(1), p. 55–62. Cited page 30

[107] You-He ZHOU, Dongkeun PARK & Yukikazu IWASA 2023. "Review of progress and challenges of key mechanical issues in high-field superconducting magnets". *National Science Review* **10**(3), p. nwad001. Cited page vii

[108] Fahri Emre ÖZTÜRK, Frank VEWINGER, Martin WEITZ & Julian SCHMITT 2022. "Fluctuation-dissipation relation for a Bose-Einstein condensate of photons" . Cited page vii

Tangui ALADJIDI **2 octobre 2023**

Sujet : Contrôle tout optique de fluides quantiques de lumière en vapeur atomique chaude

Résumé : Les fluides quantiques de lumière présentent une plateform nouvelle et prometteuse dans l'exploration de la physique des particules quantiques en interaction. Ici, nous étudions des fluides constitués de photons dont les interactions sont induites par une vapeur chaude de Rubidium. Pour décrire ces fluides, nous recourrons à un hamiltonien comprenant énergie cinétique, énergie potentielle et énergie d'interaction. Nous présentons dans cette thèse un contrôle tout optique de ces fluides où nous agissons sur chaque terme de ce hamiltonien. Nous avons mis en évidence la générations de corrélations non-classiques induites par le saut des interactions aux interfaces de notre milieu non-linéaire. Le contrôle de la réponse du milieu atomique est ensuite exploré en présentant un cadre numérique extensible qui permet de décrire des structures atomiques arbitraires, que nous utilisons ensuite pour décrire l'effet du pompage optique mis en oeuvre afin de graver optiquement des potentiels dans le fluide de lumière. Nous caractérisons ensuite les propriétés de superfluidité des fluides de lumière et mesurons la vitesse critique autour d'un défaut créé grâce au contrôle du potentiel induit par pompage optique. Nous concluons en étudiant les interactions entre vortex optiques à travers une expérience mettant en lumière un comportement turbulent du fluide, et une expérience de collision de vortex optiques ouvrant la voie à la thermodynamique induite par des effets quantiques au-delà du champ moyen.

Mots clés : Optique quantique, fluides quantiques de lumière, superfluidité, Aladjidi, contrôle tout optique

Subject : Full optical control of quantum fluids of light in hot atomic vapors

Abstract: Quantum fluids of light are a novel and promising platform in the exploration of many-body quantum physics. We study here fluids whose constituants are photons. Their interactions are induced by a hot vapor of Rubidium atoms. In order to describe these fluids, we use a Hamiltonian comprising of three terms: kinetic energy, potential energy and interaction energy. In this thesis, we showcase an all-optical control of each of these terms. We evidenced non-classical correlations induced by the interaction quenches at the interfaces of our non-linear medium. We then explore the control of the atomic response of the vapor, using an easily extendable numerical framework. We then use this framework to study optical pumping, that allows us to realize arbitrary potentials inside the fluid of light. The critical velocity for superfluidity is then mesured, in a scattering experiment against an optical defect using the potential engineering developped in this thesis. Finally, we study vortex-vortex interactions in an experiment showcasing turbulent behavior in a fluid of light as well as a collision experiment between vortices. This paves the way to thermodynamics processes seeded by interactions effects beyond the mean field.

Keywords : Quantum optics, quantum fluids of light, quantum fluids, superfluidity, Aladjidi full optical control